

Grain Boundary Structure and Solute Segregation in Titanium-Doped
Sapphire Bicrystals

by

Seth Thomas Taylor

B.S. (Brown University) 1994

M.S. (University of California, Berkeley) 1998

A dissertation submitted in partial satisfaction of the

requirements for the degree of

Doctor of Philosophy

in

Engineering-Materials Science and Mineral Engineering

in the

GRADUATE DIVISION

of the

UNIVERSITY OF CALIFORNIA, BERKELEY

Committee in charge:

Professor Ron Gronsky, Chair

Professor Andreas Glaeser

Professor Roya Maboudian

Spring 2002

Grain Boundary Structure and Solute Segregation in
Titanium-Doped Sapphire Bicrystals

Copyright © 2002

by

Seth Thomas Taylor

Abstract

Grain Boundary Structure and Solute Segregation in Titanium-Doped Sapphire Bicrystals

by

Seth Thomas Taylor

Doctor of Philosophy in Engineering--Materials Science and Mineral Engineering

University of California, Berkeley

Professor Ron Gronsky, Chair

Solute segregation to ceramic grain boundaries governs material processing and microstructure evolution, and can strongly influence material properties critical to engineering performance. Understanding the evolution and implications of grain boundary chemistry is a vital component in the greater effort to engineer ceramics with controlled microstructures. This study examines solute segregation to engineered grain boundaries in titanium-doped sapphire (Al_2O_3) bicrystals, and explores relationships between grain boundary structure and chemistry at the nanometer scale using spectroscopic and imaging techniques in the transmission electron microscope (TEM). Results demonstrate dramatic changes in solute segregation stemming from small fluctuations in grain boundary plane and structure. Titanium and silicon solute species exhibit strong tendencies to segregate to non-basal and basal grain boundary planes, respectively. Evidence suggests that grain boundary faceting occurs in low-angle twist boundaries to accommodate nonequilibrium solute segregation related to slow specimen cooling rates, while faceting of tilt grain boundaries often occurs to expose special planes of the coincidence site lattice (CSL). Moreover, quantitative analysis of grain boundary

chemistry indicates preferential segregation of charged defects to grain boundary dislocations. These results offer direct proof that static dislocations in ionic materials can assume a net charge, and emphasize the importance of interactions between charged point, line, and planar defects in ionic materials. Efforts to understand grain boundary chemistry in terms of space charge theory, elastic misfit and nonequilibrium segregation are discussed for the Al_2O_3 system.

TABLE OF CONTENTS

Acknowledgments	vi
 1. Introduction	 1
1.1. Background	1
1.2. Ceramic Grain Boundaries	2
1.3. Motivation and Objectives	4
1.4. Ti-Doped Al_2O_3	5
References	8
Figures	10
 2. Overview of Grain Boundary Structure and Chemistry in Ionic Ceramics	11
2.1. Grain Boundaries in Materials	11
2.2. The Structure of Grain Boundaries	12
2.2.1. Geometric Descriptions of Grain Boundaries	12
2.2.1.1. Crystallography and Nomenclature	12
2.2.1.2. The Coincident Site Lattice	13
2.2.2. Dislocation Models of Grain Boundaries	15
2.2.3. Elements of Grain Boundary Structure	16
2.3. The Evolution of Grain Boundary Chemistry	16
2.4. Grain Boundary Chemistry in Ionic Materials	20

2.4.1. Charged Point Defects	20
2.4.1.1. Solute Incorporation and Defect Chemistry in Al_2O_3	21
2.4.2. Space Charge Theory for Ionic Solids	23
2.4.2.1. Intrinsic Case: Pure, Undoped Al_2O_3	24
2.4.2.2. Extrinsic Case	28
2.4.2.2.1. Donor-Doped Al_2O_3	28
2.4.2.2.2. Codoped Al_2O_3	30
2.5. Experimental Studies of Grain Boundary Structure and Segregation in Al_2O_3	32
2.5.1. Grain Boundary Segregation in Al_2O_3	32
2.5.2. Studies of Grain Boundary Chemistry and Structure in Ti-Doped Al_2O_3	35
References	38
Figures	45
 3. Materials and Methods	 53
3.1. Bicrystal Fabrication	53
3.1.1. Twist Boundaries	54
3.1.2. Tilt Boundaries	54
3.1.3. Tricrystal Fabrication	55
3.1.4. Polycrystalline Al_2O_3 Processing	56
3.2. TEM Specimen Preparation	56
3.2.1. Twist Boundaries	56
3.2.2. Tilt Boundaries	57
3.3. Grain Boundary Studies in the TEM	58
3.3.1. Chemical Microanalysis	59

3.3.1.1. Energy Dispersive Spectroscopy	59
3.3.1.2. Electron Energy-Loss Spectroscopy	61
3.3.2. Structure Determination	64
References	65
Figures	66
 4. The Structure and Chemistry of Basal Twist Boundaries	71
4.1. Low-Angle Basal Twist Boundary (S3)	71
4.1.1. Processing Conditions	71
4.1.2. Grain Boundary Structure	71
4.1.3. Grain Boundary Chemistry	73
4.1.4. Evidence for Charged Grain Boundary Dislocations	76
4.2. Medium-Angle Basal Twist Boundary (15b)	79
4.2.1. Processing Conditions	79
4.2.2. Grain Boundary Structure	79
4.2.3. Grain Boundary Chemistry	80
4.3. High-Angle Basal Twist Boundaries (12a and 12b)	82
4.3.1. Processing Conditions	82
4.3.2. Furnace-Cooled Boundary (12a)	83
4.3.2.1. Grain Boundary Structure	83
4.3.2.2. Grain Boundary Chemistry	85
4.3.2.3. Si Segregation to the Basal Plane	87
4.3.2.4. Precipitation on the Off-Basal Facet	92
4.3.2.5. Solute-Induced Grain Boundary Faceting	95
4.3.2.6. Uniformity of Grain Boundary Charge	96

4.3.3. Quenched Boundary (12b)	97
4.3.3.1. Grain Boundary Structure	97
4.3.3.2. Grain Boundary Chemistry	98
4.3.4. Solute Segregation and Specimen Cooling Rate	99
4.4. General Discussion of Solute Segregation to Basal Twist Boundaries ...	100
4.4.1. Measured and Predicted Grain Boundary Solute Concentrations ..	100
4.4.2. Grain Boundary Chemical Width	103
4.4.3. Issues Concerning Solute Valence	105
4.5. Future Work	106
4.6. Summary and Conclusions	108
References	110
Tables	113
Figures	120
 5. The Structure and Chemistry of Basal Tilt Boundaries	 149
5.1. Low-Angle Tilt Boundary (Tilt1)	149
5.1.1. Processing Conditions	149
5.1.2. Grain Boundary Structure	149
5.1.3. Grain Boundary Chemistry	153
5.1.4. Origins of Grain Boundary Faceting	154
5.1.5. The Role of Solute in Grain Boundary Faceting	156
5.1.6. Grain Boundary Dislocations	158
5.1.6.1. Perfect versus partial Dislocations	158
5.1.6.2. Facet Junction Dislocations	159
5.2. High-Angle Tilt Boundaries (Tilts 15b and 15d)	160

5.2.1. Processing Conditions	160
5.2.2. Air-Quenched Tilt Boundary (Tilt15b)	160
5.2.2.1. Grain Boundary Structure	160
5.2.2.2. Grain Boundary Chemistry	161
5.2.3. Vacuum-Quenched Tilt Boundary (Tilt15d)	162
5.2.3.1. Grain Boundary Structure	162
5.2.3.2. Grain Boundary Chemistry	163
5.2.4. Effect of Processing Environment on Ti Solute Segregation	163
5.3. Undoped High-Angle Tilt Boundary (Tilt10)	165
5.3.1. Processing Conditions	165
5.3.2. Grain Boundary Structure	165
5.3.3. Grain Boundary Chemistry	166
5.4. General Discussion of Tilt Boundaries	167
5.4.1. Faceting of Tilt Boundaries	167
5.4.2. Grain Boundary Chemical Width	169
5.5. Future Work	169
5.6. Summary and Conclusions	170
References	172
Figures	173

Appendix A. Issues Concerning Elemental Quantification in Focused-Probe

Microanalysis	199
----------------------------	-----

Appendix B. Calculation of Solute Diffusion Length During Specimen

Cooling	207
----------------------	-----

ACKNOWLEDGMENTS

I would like to thank my research advisor, Professor Ron Gronsby, for his unflagging support, guidance and instruction throughout my tenure here at Berkeley. His teaching and tutelage extend well beyond textbooks and research, and I am grateful to have found such a professional, selfless, dynamic and affable mentor.

I would also like to extend my sincere thanks to Professor Andreas Glaeser for the opportunity to work on an exciting project, and for offering some much-needed guidance and commentary along the way. Thanks also to him and to Professor Roya Maboudian for their service on my qualifying exam committee, and for their review of this final manuscript. I also extend my thanks to the other members of my qualifying exam committee, Professor Gareth Thomas and Professor Tim Sands, for their interest in and support of my research endeavors.

Lawrence Berkeley National Laboratory, and specifically the National Center for Electron Microscopy, has played a major role in supporting my research endeavors throughout these six years. I'd like to extend a special thanks to the staff at NCEM for their instruction, training, and guidance, and for giving me a home at a time when the University offered few opportunities in electron microscopy. Chris Nelson has taught me a great deal about practical microscopy, and ChengYu Song and Doreen Ah Tye have been outstanding resources for overcoming the rigors and frustrations of specimen preparation. I must also acknowledge the support of John Turner and Jane Cavlina, as

well as the contributions of Drs. Mike O’Keefe, Roar Kilaas, Eric Stach, Tamara Radétić and Uli Dahmen.

I must also recognize the invaluable contributions of (soon-to-be Dr.) Robert Marks, who, in making the bicrystals, made my work possible. I also thank Robert and other students (past and present) in the Ceramics Lab for teaching me much about alumina and sapphire.

My dissertation research was financially supported by a Robert Noyce Fellowship from Intel Corporation, whom I would like to thank for their continuing support of university research through various programs, fellowships and industrial work opportunities. Experiments at Lawrence Berkeley National Laboratory were also supported by the Director, Office of Science, Office of Basic Energy Sciences, of the U.S. Department of Energy under Contract No. DE-AC03-76SF00098.

Six years is a long time to devote to the pursuit of an advanced degree, and I am very grateful for the friends and family who have supported me through this long journey and have helped make the trek not only bearable, but rewarding. My parents, Thomas and Barbara, deserve special recognition as the finest teachers I’ve ever had, and I thank them for their unending support and encouragement in all of my pursuits. Thanks also to Todd, Andy, Leslie, Pa, Elena, John, Rosemary, Wyatt, Rey, Jessica, Brian, and (deep breath) Sophie (the niece, not the cat) for helping me to realize and appreciate the finer things in life. And finally, I thank my wife Lourdes for her love, patience and support through these many years, as I devoted myself to pursuits that must have seemed both esoteric and frivolous. The expense of my education is perhaps best measured by the

extent of her sacrifices. Thanks for seeing me through this long journey as my greatest friend and strongest advocate. I love you deeply.

Chapter One

INTRODUCTION

1.1. Background

The discipline of materials science is premised on the notion that a material's physical properties are dictated not merely by its composition, but also by its *microstructure* – the assemblage and organization of its constituent parts. Atoms may be the building blocks of all matter, but their distribution and arrangement at the nanoscopic and/or microscopic levels are what distinguish the panoply of natural and engineered materials. Understanding the relationship between a material's microstructure and its observed properties, be they mechanical, electrical, optical, or magnetic, remains the central focus of materials science and engineering, and the primary pursuit of its practitioners.

The great majority of engineering materials are polycrystalline, meaning their microstructures can be described at the most basic level by a conglomerate of randomly-oriented crystals separated by regions of misorientation known as grain boundaries. These boundaries exhibit a high degree of structural disorder relative to the periodic, crystalline structure of the grain interiors. Consequently, structure, chemistry, and the concentration of point and line defects can be significantly altered at or near grain boundaries, often spawning unique behavior in these regions. Examples can be drawn from all classes of materials. Small amounts of B segregation to Ni_3Al grain boundaries

dramatically increase the cohesive strength and ductility of the alloy by altering the bonding character [1]. Impurities decorating grain boundaries in structural ceramics such as aluminum oxide (Al_2O_3) and silicon nitride (Si_3N_4) facilitate grain boundary sliding at high temperature and weaken the material's resistance to creep deformation [2]. And perhaps most infamous is the temper embrittlement observed in steels as a result of impurity segregation to grain boundaries, adversely affecting mechanical properties and material performance [3].

Indeed, it is well established that material behavior in all classes of polycrystalline solids is often dictated by the character -- notably the chemistry and structure -- of grain boundaries. Understanding the intimate relationship between grain boundaries and macroscopic material properties continues to be a fundamental pursuit of materials science and engineering.

1.2. Ceramic Grain Boundaries

Grain boundaries in ceramics are vitally important because they govern not only material properties, but also material processing and microstructure evolution. Defect chemistry, which describes the concentration and character of various point defects in compound ceramics, and glassy phases at grain boundaries can greatly influence grain boundary diffusion and mobility, and are therefore paramount to the sintering process. Moreover, efforts to optimize engineering performance of ceramic materials typically make use of unique grain boundary behavior to tailor the microstructure for specific applications. Elongated grains in silicon nitride and silicon carbide ceramics impart

significant enhancements in mechanical toughness, and are achieved through careful control of microstructure during material processing.

Ceramics are notoriously impure materials. Unlike metals, where refining techniques can be utilized to remove impurities, even the purest ceramics typically contain a host of impurity species, with concentrations measured at the ppm level. Grain boundary chemistry is often dictated by impurity or solute species that have segregated to the boundary from the bulk. In most ceramic materials, where low solubility for impurities and other solute species is quite typical [2], solute segregation to grain boundaries is inevitable. It has been reported that bulk impurity concentrations as low as 50 parts per million (ppm) can dominate microstructure evolution as a result of intergranular segregation [4]. Given the prominent role played by solute species in both processing and performance, there exists a critical need to identify and understand all relevant parameters affecting impurity segregation to grain boundaries in ceramics. Exploring the critical link between grain boundary structure and chemistry is a vital pursuit in the greater effort to engineer ceramics for optimum performance.

Previous studies reporting on grain boundary segregation in ionic ceramics permeate the literature¹. The majority of these studies have been performed on polycrystalline materials to observe how different solute species affect specific material properties. However, few studies have been conducted with an explicit intent to elucidate the mechanisms of segregation in ionic ceramics, and to correlate segregation behavior with grain boundary structure. This is due partly to the complexity of the segregation

¹ See Chapter 2 for specific references.

process, but is primarily attributed to the experimental difficulties of obtaining spatially-resolved chemical and structural information from grain boundaries.

1.3. Motivation and Objectives

A systematic study of grain boundary segregation in ionic ceramics would ideally permit control of intergranular chemistry and structure, in order to fully assess the role of each parameter on solute segregation. Additionally, quantitative analysis of segregation at an interface, and determination of solute valence and grain boundary atomic structure, must be experimentally feasible. Given these stringent requirements, it is not surprising that our current understanding of the segregation process is so heavily rooted in conjecture and theory.

Recent advances in characterization techniques afford the opportunity to study solute segregation with a new level of clarity and precision. In modern Transmission Electron Microscopes (TEMs), chemical microanalysis is routinely performed with spatial resolution at the nanometer scale, while atomic structure can be resolved at the Angstrom level. Moreover, the recent development of solid-state processing techniques for fabricating ceramic bicrystals, pursued here at UC Berkeley, permits systematic studies of structure-chemistry relationships in controlled grain boundary structures. As discussed in a later chapter, this technique offers the unique ability to control grain boundary orientation and structure (through bicrystal misorientation) and intergranular chemistry (through suitable doping schemes).

The current investigation exploits advances in both processing and characterization techniques to examine the effects of grain boundary orientation and structure on solute

segregation in Ti-doped aluminum oxide (Al_2O_3). Through control of bicrystal processing, the effects of solute valence and specimen cooling rate on grain boundary chemistry are also examined. Results from this work are intended to offer critical feedback concerning the nature and quality of the bicrystal fabrication process, and to aid in the successful fabrication of future bicrystal structures having controlled misorientation and chemistry. Additionally, nanoscale descriptions of intergranular structure and chemistry should shed new light on the continued effort to understand the role of Ti solute in the microstructure evolution and interface thermodynamics of alumina ceramics. Finally, it is hoped that this study will constitute a significant contribution to the current paucity of experimental data linking grain boundary structure and segregation in ceramic materials.

1.4. Ti-Doped Al_2O_3

In the context of microstructure evolution, Ti-doped aluminum oxide is of great interest to the ceramics community. Titanium additions to alumina are known to dramatically enhance grain boundary mobility [5] and sintering rate [6, 7], and to impart unique grain morphologies in sintered polycrystalline compacts [5, 8, 9]. Additionally, it has been shown that Ti-doping can drastically alter Al_2O_3 surface energies, leading to pronounced stabilization of specific crystal faces [10, 11]. Although root cause(s) of this behavior have not been explicitly identified, most theories implicate Ti segregation to the grain boundaries, and subsequent interaction with other impurities, as a likely culprit.

Titanium-doped aluminum oxide offers a model system for studying how changes in solute valence can modify segregation behavior and grain boundary chemistry in an

ionic ceramic. As a solute in Al_2O_3 , titanium can assume two different oxidation states, Ti^{3+} and Ti^{4+} , depending on material processing conditions. The former is common in samples processed in vacuum or in streaming argon gas (reducing environments), while the latter is prevalent for samples fired in air (oxygen-rich environment). Solubility data for these two solutes in Al_2O_3 is fairly limited and quite scattered. As substitutional species, Ti^{3+} ($r_i = 0.74 \text{ \AA}$) and Ti^{4+} ($r_i = 0.67 \text{ \AA}$) replace the smaller Al^{3+} ($r_i = 0.53 \text{ \AA}$), and despite its larger size, isovalent Ti^{3+} is believed to be more soluble than Ti^{4+} since compensating charged defects are not required for Ti^{3+} incorporation. Most experiments to quantify Ti solubility in Al_2O_3 to date have utilized polycrystals of varying impurity content and grain size, and have frequently been performed without direct knowledge of the solute valence² [7, 12-15]. Not surprisingly, results exhibit broad variability, as shown in Figure 1.1, and data concerning the exact solubilities of Ti^{3+} and Ti^{4+} in Al_2O_3 as a function of temperature remain elusive and subject to interpretation.

Dopant effects on defect structure and interfacial energy, and related processes such as grain boundary diffusion and mobility, should depend sensitively on solute valence. Cahoon and Christensen [6] demonstrated enhanced sintering rates in TiO_2 -doped alumina fired in air – a result verified later in separate studies by Bagley et al. [7] and Ikegami et al. [16]. Studies of microstructure evolution in Ti-doped Al_2O_3 by Horn and Messing revealed anisotropic grain growth and modest increases in grain boundary mobility for samples annealed in air above 1350°C [8]. Recently, Powers showed that Ti additions enhance grain boundary mobility in air-annealed Al_2O_3 by nearly two orders of magnitude relative to undoped alumina [5]. Samples annealed in air always exhibited

² Titanium valence is often inferred based on the processing environment, but is rarely confirmed using spectroscopy techniques. In single crystal Al_2O_3 (sapphire), Ti valence is usually inferred based on

higher grain boundary mobilities than those annealed in vacuum, suggesting a possible valence effect. Comparing grain boundary chemistry for the two different solutes (Ti^{3+} and Ti^{4+}) on nominally the same boundary structures will help to understand differences in microstructure evolution between Ti^{3+} and Ti^{4+} .

material color: Ti^{3+} introduces a pink coloration, while Ti^{4+} results in no coloring.

Chapter 1 References

1. D.A. Muller, S. Subramanian, P.E. Batson, J. Silcox, and S.L. Sass, "Structure, Chemistry and Bonding at Grain Boundaries in Ni_3Al . I. The Role of Boron in Ductilizing Grain Boundaries," *Acta Materialia* **44** (4) 1637-45 (1996).
2. W.D. Kingery, H.K. Bowen, and D.R. Uhlmann, *Introduction to Ceramics*. New York: J. Wiley and Sons, 1976.
3. G.E. Dieter, *Mechanical Metallurgy*. New York: McGraw-Hill, Inc., 1986.
4. I.J. Bae and S. Baik, "Abnormal Grain Growth in Alumina," *Materials Science Forum* **204-206** 485-90 (1996).
5. J.D. Powers, "Titanium Effects on Microstructure Development in Alumina," Ph.D. Dissertation, University of California, Berkeley, 1997.
6. H.P. Cahoon and C.J. Christensen, "Sintering and Grain Growth of Alpha-Alumina," *Journal of the American Ceramic Society* **39** (10) 337-44 (1956).
7. R.D. Bagley, I.B. Cutler, and D.L. Johnson, "Effect of TiO_2 on Initial Sintering of Al_2O_3 ," *Journal of the American Ceramic Society* **53** (3) 136-41 (1970).
8. D.S. Horn and G.L. Messing, "Anisotropic Grain Growth in TiO_2 -Doped Alumina," *Materials Science and Engineering A* **A195** 169-78 (1995).
9. A. Kebbede, J. Parai, and A.H. Carim, "Anisotropic Grain Growth in $\alpha\text{-Al}_2\text{O}_3$ with SiO_2 and TiO_2 Additions," *Journal of the American Ceramic Society* **83** (11) 2845-2851 (2000).
10. J.D. Powers and A.M. Glaeser, "High-Temperature Healing of Cracklike Flaws in Titanium Ion-Implanted Sapphire," *Journal of the American Ceramic Society* **76** (9) 2225-34 (1993).
11. M. Kitayama, "The Wulff Shape of Doped and Undoped Alumina," Ph.D. Dissertation, University of California, Berkeley, 1996.
12. E.R. Winkler, J.F. Sarver, and I.B. Cutler, "Solid Solution of Titanium Dioxide in Aluminum Oxide," *Journal of the American Ceramic Society* **49** (12) 634-637 (1966).
13. S.K. Roy and R.L. Coble, "Solubilities of Magnesia, Titania, and Magnesium Titanate in Aluminum Oxide," *Journal of the American Ceramic Society* **51** (1) 1-6 (1968).

14. J.M. Tsaui and F.A. Kröger, "Electrical Conductivity and Creep of Polycrystalline α -Al₂O₃ Doped with Titanium or Iron Plus Titanium," *Journal of Materials Science* **22** 2332-2340 (1987).
15. K. Hamano, C. Hwang, Z. Nagagawa, and Y. Ohya, "Effects of TiO₂ on Sintering of Alumina Ceramics," *Yogyo-Kyokai Shi* **94** (5) 505-11 (1986).
16. T. Ikegami, K. Kotani, and K. Eguchi, "Some Roles of MgO and TiO₂ in Densification of Sinterable Alumina," *Journal of the American Ceramic Society* **70** (12) 885-90 (1987).

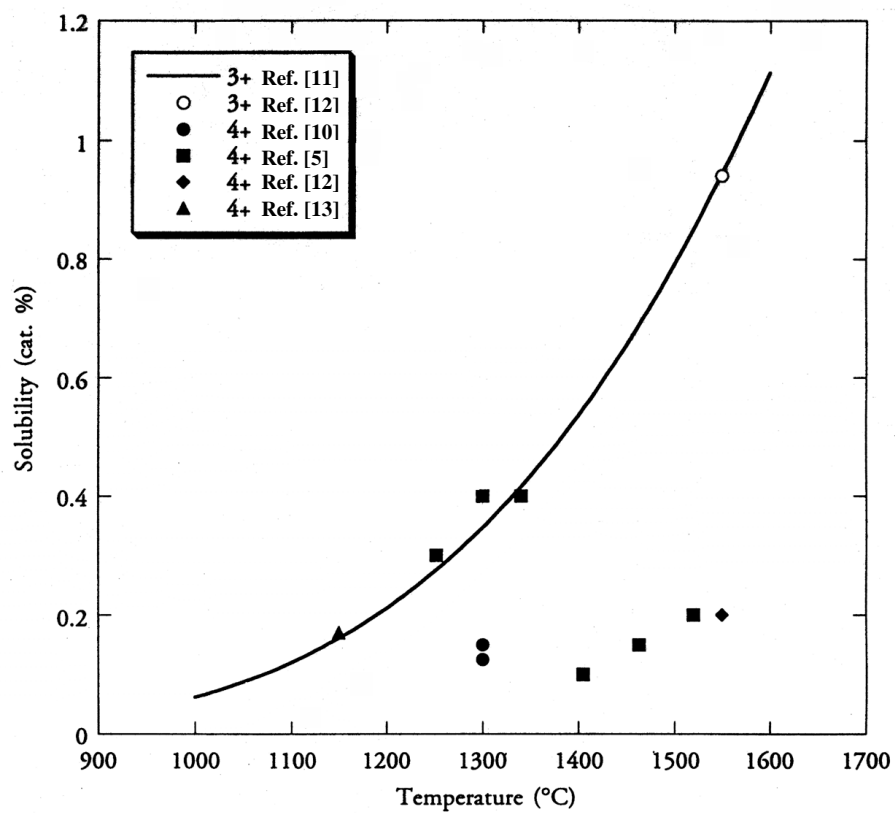


Figure 1.1. Compendium of solubility data for Ti^{3+} and Ti^{4+} in Al_2O_3 as a function of temperature. (Reproduced from [3]).

Chapter Two

OVERVIEW OF GRAIN BOUNDARY STRUCTURE AND CHEMISTRY IN IONIC CERAMICS

2.1. Grain Boundaries in Materials

A grain boundary describes the interface between two crystals (grains) of the same phase having different orientations. The misorientation is accommodated at the grain boundary, and so some amount of structural disorder is a characteristic (basic feature) of all grain boundaries in materials. This structural disorder imparts unique properties and behavior to grain boundaries relative to the interior or bulk crystal. Because grain boundaries are structural defects, they are usually high-energy sites relative to the perfect lattice. As such, they represent metastable structures prone to chemical attack and thermal modification. Vacant sites at the boundary represent potential host sites for larger solute species, while also permitting enhanced diffusion due to facile vacancy formation (and elimination). Bonding across the grain boundary can be significantly altered due to adsorbed solute species and/or modified atomic coordination and spacing, so basic properties such as mechanical strength and thermal and electronic conductivity can be quite different at grain boundaries. In essence, all parameters that dictate how a material behaves – namely structure, bonding, and chemistry – can be dramatically transformed at grain boundaries in materials. Efforts to understand basic grain boundary behavior, and to link material behavior with grain

boundary structure, chemistry and bonding, have been a major focus of materials science and engineering research for the past sixty years. The fact that these efforts remain a critical component of fundamental materials research underscores the complexity of grain boundary behavior.

This chapter reviews some of the fundamental concepts of grain boundary science and engineering, and explores the linkage between grain boundary structure and chemistry. Issues specific to the study of grain boundaries in ionic ceramics are discussed, and reviews of previous investigations are presented.

2.2. The Structure of Grain Boundaries

2.2.1. Geometric Descriptions of Grain Boundaries

2.2.1.1. Crystallography and Nomenclature

The geometric character of a grain boundary is uniquely determined by five macroscopic degrees of freedom (DOFs). To define the misorientation between two grains, three DOFs are needed to specify the proper rotation: two for the unit vector along the rotation axis \mathbf{p} , and one for the rotation angle θ [1]. Two more DOFs are required to specify the interface normal, \mathbf{n} . In some instances, it is more desirable and perhaps more convenient to use the five DOFs to characterize the interface plane normal rather than the misorientation. Here, the creation of an interface is treated as the sum of two operations: a joining of two crystal surfaces with normal vectors \mathbf{n}_1 and \mathbf{n}_2 , followed by a rotation of one of the crystals about \mathbf{n}_1 or \mathbf{n}_2 by an angle θ . Two DOFs are consumed by each vector \mathbf{n}_1 and \mathbf{n}_2 , and the fifth DOF is the angle θ .

The misorientation of any grain boundary can generally be expressed as a sum of tilt and twist components. We imagine that any grain boundary can be created by two successive rotations about perpendicular axes. First a tilt rotation is introduced, in which the rotation axis is parallel to the boundary plane. Then a twist rotation is performed about an axis perpendicular to the boundary plane. Pure tilt and twist rotations are illustrated schematically in Figure 2.1 (a) and (b), respectively. A unique specification of the tilt and twist components of a general grain boundary does not exist, because equivalent axis/angle descriptions can be found which yield the same final misorientation [1].

A pure tilt boundary is defined by the condition that the rotation axis \mathbf{p} lies in the boundary plane. A symmetric tilt boundary is one in which the grain boundary plane has the same family of Miller indices in both crystals, while an asymmetric tilt boundary plane has different Miller index forms in either crystal. A pure twist boundary lies normal to its axis of rotation \mathbf{p} . A symmetric twist boundary is, by definition, a pure twist boundary, whereas an asymmetric twist boundary is essentially an asymmetric tilt boundary that has been subjected to a further twist rotation about the grain boundary normal [1].

More detailed and formal descriptions of grain boundary geometry and terminology can be found in references [1] and [2].

2.2.1.2. The Coincident Site Lattice

A popular formalism for describing the geometry and structure of grain (and interphase) boundaries is offered by the coincident site lattice (CSL) construction.

When two interpenetrating lattices are rotated from a condition of initial coincidence, specific rotation angles can lead to situations where lattice points from both crystals coincide. Figure 2.2 shows the particular case where two cubic lattices have been rotated 36.9° about the [001] axis, normal to the page. The CSL describes the lattice of coincident sites in both grains formed by a particular rotation. The reciprocal density of coincident sites is defined by the parameter Σ . A grain boundary with $\Sigma = 5$, such as the one shown in Figure 2.2, indicates that one out of every five atoms in each crystal represents a coincidence site. A grain boundary with a high density of coincidence points implies good matching of adjacent grains, with little structural disorder. Highly-ordered grain boundaries occur at “special” orientations and are characterized by low Σ values.

It should be pointed out that the CSL is a purely geometric model which does not account for changes in interatomic bonding, dislocation content, and solute chemistry --factors known to affect grain boundary behavior. Nonetheless, the CSL has proven to be a useful construction because it helps to explain some empirical observations concerning grain boundary behavior in materials. Various studies in metal and ceramic systems have demonstrated that low- Σ CSL boundaries exhibit unique behavior relative to non-CSL boundaries. A classic study by Aust and Rutter showed that CSL boundaries in Sn-doped Pb had higher mobilities than non-CSL boundaries because their highly-ordered structures did not permit segregation of Sn solute [5]. Roshko and Kingery demonstrated that Ca segregation to a non-CSL boundary in MgO was nearly twice that observed at two different CSL boundaries [6]. And experiments by various workers have shown that special CSL orientations lead to minima in plots of

grain boundary energy versus misorientation angle, as reviewed by Randle [3]. The utility of the CSL stems from its ability to offer a relative measure of grain boundary structural order, which is essential to a basic understanding of grain boundary phenomena such as segregation, diffusivity, and mobility.

2.2.2. Dislocation Models of Grain Boundaries

It has been shown that for small differences in misorientation, grain boundary structure is accurately described by a periodic row or array of dislocations [7-10]. The structural misfit of low-angle symmetric tilt boundaries (i.e. those having a misorientation angle θ less than or equal to 15°) is accommodated by a row of edge dislocations with periodic spacing D , as shown schematically in Figure 2.3. Such an arrangement represents a low-energy configuration because the structural disorder is generally confined to the periodic dislocations, and so the overall structural disorder is minimized. For an asymmetric tilt boundary, a second set of edge dislocations with extra planes normal to those of the original set are formed [11].

Similarly, low-angle twist boundaries can be described as an array of screw dislocations. More than one set of dislocations is required to form the boundary, however, since a single set of parallel screw dislocations would only lead to a shear strain in the crystal [12]. In cubic materials, the boundary is formed by two intersecting sets of screw dislocations lying along perpendicular axes. In hexagonal materials, three sets of dislocations combine to form a hexagonal array which accommodates misfit at the grain boundary. Figure 2.4 illustrates how structural disorder caused by the twist

rotation of two cubic crystals can be accommodated by a crossed-grid of screw dislocations, separated by regions of good atomic matching.

The dislocation spacing D varies with the crystal misorientation θ and the magnitude of the dislocation Burgers vector \mathbf{b} , according to Frank's rule:

$$\sin \theta = \frac{b}{D} \quad (2.1)$$

At larger angles of misorientation, dislocations become so closely-spaced that interactions between individual dislocations may prevent their periodic spacing. Thus, dislocation-based descriptions of grain boundary structure are typically not valid at misorientation angles greater than $\approx 15^\circ$. The structure of high-angle grain boundaries is more commonly described using repeat polyhedral structural units along the boundary plane [13-16].

2.2.3. Elements of Grain Boundary Structure

Descriptions of grain boundary structure span several length scales, from Ångstroms to microns, and incorporate various elements of structure. These include atomic arrangements spanning perhaps a few Ångstroms or nanometers in scale; defect or dislocation structure, spanning tens to perhaps hundreds of nanometers; and planar faceting, which can occur over much larger length scales (tens of nanometers to several microns). Attempting to establish relationships between solute segregation and each element of grain boundary structure is a motive that will be discussed and revisited throughout this study.

2.3. The Evolution of Grain Boundary Chemistry

As discussed in Section 2.1, grain boundaries are inherently disordered, high-energy structures relative to the grain interior(s), and are therefore susceptible to both structural and chemical modifications which serve to reduce the overall grain boundary energy and impart greater thermodynamic stability. In many ways, a grain boundary's chemistry is dictated by its structure.

As part of his seminal work on the thermodynamics of fluids and surfaces, Gibbs demonstrated that adsorption of chemical species could modify the energy of a surface via the expression

$$d\sigma = -\sum_i \Gamma_i d\mu_i \quad (2.2)$$

where $d\sigma$ is the change in boundary energy at constant temperature, μ_i is the chemical potential of the i^{th} component, and Γ_i is the excess amount of component i per unit area [17]³. Equation 2.2 establishes a driving force for equilibrium segregation of solute species to (or away from) an interface. In doing so, it predicts an enrichment of solute species that lower the surface energy γ , or conversely, a depletion of species that increase γ . Reduction in interfacial energy is believed to result from an increase in atomic coordination with solute adsorption, making the boundary more bulk-like in terms of bonding and packing density. Despite the broad applicability of the Gibbs' equation, its practical use in predicting solute segregation (adsorption) has been very limited, primarily because the parameters σ , Γ and μ (or their equivalents) are not easily measured.

³ Gibbs' original work on surface adsorption has since been applied to segregation at grain boundaries; see for example the adaptation by Cahn and Hilliard [18].

A more fruitful and perhaps tenable approach is to consider segregation in terms of the distortion energy surrounding solute atoms in the grain interior. Incorporating solute atoms of different size into the solvent matrix requires considerable strain energy. If that strain energy can be relieved by segregation to a region that is already distorted, then a large driving force for segregation exists. McLean derived an expression relating the grain boundary solute concentration (C_{gb}) to the driving force for segregation (Q) and to the bulk solute concentration in the lattice (C_l) [19]:

$$C_{gb} = \frac{C_l \exp\left(\frac{Q}{RT}\right)}{1 + C_l \exp\left(\frac{Q}{RT}\right)} \quad (2.3)$$

According to Equation 2.3, the grain boundary solute concentration should have a strong dependence on C_l , T , and Q . Higher bulk solute concentrations and lower temperatures promote greater grain boundary concentrations. Additionally, solute atoms with larger misfit will have larger values for Q , leading to more pronounced segregation behavior. McLean showed that large grain boundary concentrations can be produced even for small values of C_l if the solute species are strongly misfitting. Moreover, because most all solute atoms introduce some amount of elastic misfit, equilibrium grain boundary segregation should occur in nearly all solid solutions.

Assuming that the strain energy introduced by a solute atom at the grain boundary is small, most of a solute's distortion energy in the grain interior can be relieved by segregation to the boundary. McLean expressed the distortion energy W around a solute atom in an elastic matrix as [19]:

$$W = \frac{24\pi K G r_1 (r_2 - r_1)^2}{3K + 4G \left(\frac{r_1}{r_2} \right)} \quad (2.4)$$

Here, the solute atom is modeled as a sphere occupying a vacant site in the matrix, where K is the bulk modulus of the solute, G is the shear modulus of the matrix, r_1 is the radius of the void, and r_2 is the radius of the solute atom. This model, in concert with Equation 2.3, has proven quite expedient to the prediction of grain boundary solute concentrations in various material systems because, unlike Gibbs' thermodynamic expression, the relevant parameters (K and G) can be easily measured for most materials. Clearly, since it is assumed that $Q \approx W$, the model is most accurate in describing grain boundary segregation in systems with strongly-misfitting solute species.

The role of grain boundary structure in solute segregation should not be overlooked. While large elastic driving forces (W) promote segregation of solute species, grain boundary structure ultimately determines the extent to which the boundary can accommodate those species. This is because a particular grain boundary has a limited number of available sites capable of hosting misfitting solutes – a fact often overlooked or neglected by many segregation models. The presence of dislocations and facets at a grain boundary can greatly modify the concentration of accommodating sites, and should therefore have an important effect on solute segregation.

The ability of grain boundary dislocations to accommodate excess solute has been demonstrated by recent Monte Carlo studies of solute segregation in cubic alloys [20-23]. Calculations on pure twist boundaries show that grain boundary solute concentrations increase linearly with twist angle up to about $\approx 35^\circ$, at which point

saturation occurs. This behavior is attributed to increasing dislocation density in the twist boundary, and not to any particular value of Σ . Moreover, experimental studies of solute segregation in Fe-Au (alloy) bicrystals offer conclusive evidence that Au segregates heavily to the cores of grain boundary dislocations [24]. Other studies showing changes in solute concentration at different grain boundary facets further demonstrate that grain boundary structure plays a critical role in the evolution of grain boundary chemistry [25, 26].

2.4. Grain Boundary Chemistry in Ionic Materials

In addition to elastic driving forces, solute segregation and the evolution of grain boundary chemistry in ionically-bonded materials such as ceramic oxides are subject to electrostatic forces. This section details the critical link between charged defects and solute segregation in ionic materials – a very important feature that distinguishes ceramic oxides from metallic and covalent materials.

2.4.1. Charged Point Defects

Ceramic oxides are composed of two distinct sublattices of metal cations and oxygen anions, the latter usually being a close-packed structure [27]. Point defects, be they vacancies or impurity species, are electrically charged, and their concentrations are subject to the constraint of electroneutrality throughout the crystal. If an aliovalent⁴ cation impurity is introduced into the lattice, the crystal must compensate for the charge

⁴ Substitutional impurities having the same charge as a host lattice ion are termed isovalent, otherwise they are aliovalent. A donor impurity has a positive charge, and an acceptor impurity is negatively-charged, with respect to the lattice ion it is replacing.

imbalance by creating a defect of the opposite sign, but of the same magnitude. Typical charge compensation mechanisms involve the creation of charged vacancies or interstitials, depending on the specific charge imbalance and the relative defect formation energies of the crystal. Consequently, point defect concentrations vary not only with temperature (the so-called intrinsic concentration), but also with the incorporation of dopant species (extrinsic concentration).

Ceramic oxides have very large point defect formation energies relative to metals, semiconductors, and even other ionic compounds (such as the metal halides). Although individual point defect formation energies have proven very difficult to measure experimentally, calculations suggest cation vacancy formation energies on the order of 5 eV in aluminum oxide [28, 29]. As a result, the intrinsic vacancy concentration n_v , given by the expression

$$n_v = N \exp\left(\frac{-g_v}{2kT}\right) \quad (2.5)$$

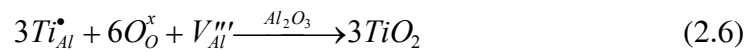
where N is the total number of ions and g_v is the vacancy formation energy, is typically quite low in ceramic oxides, even at fairly high temperatures. Extrinsic point defect concentrations are typically much larger, as minor solute additions (such as those due to residual impurities in ceramic materials) generate cation and/or anion vacancies through charge-compensating defect reactions. The specific case of solute incorporation in aluminum oxide, and its effect on vacancy concentrations, is discussed below.

2.4.1.1. Solute Incorporation and Defect Chemistry in Al_2O_3

Before discussing in detail how charged defects form and behave in Al_2O_3 , it is first necessary to introduce the Kröger-Vink notation – a favored method for describing

point defects in ionic materials. This notation fully describes a point defect in three parts. The main body of the notation describes if the defect is a vacancy “V” or an ion such as “Al”. The subscript denotes the site that the defect occupies, either an ion site in the lattice or an interstitial site “i”. Finally, the superscript describes the effective charge of the defect relative to the perfect lattice. Here, dashes (') represent negative charge, dots (•) signify positive charge, and x's are used to show neutrality. Using this notation, an aluminum vacancy in Al_2O_3 would be expressed as V_{Al}''' , while an oxygen vacancy is denoted by $V_{\text{O}}^{\bullet\bullet}$. Similarly, $\text{Ti}_{\text{Al}}^{\text{x}}$ denotes an isovalent substitutional Ti^{3+} impurity, while $\text{Ti}_{\text{Al}}^{\bullet}$ describes a Ti^{4+} donor impurity.

If we consider introducing a small concentration of Ti^{4+} solute (via TiO_2 additions) to an ideally-pure Al_2O_3 lattice, charge neutrality must be maintained by the generation of negatively-charged point defects. This means that oxygen interstitials (O_i'') and/or aluminum vacancies (V_{Al}''') must form to accommodate the positive charge of the solute. Mackrodt [29] and Grimes [28] have independently shown that the preferred (low-energy) mechanism for the incorporation of Ti^{4+} occurs via substitution for Al^{3+} and concurrent creation of aluminum vacancies. The mechanism describing Ti^{4+} incorporation is formally given as



with the important condition that

$$[\text{Ti}_{\text{Al}}^{\bullet}] = 3[V_{\text{Al}}'''] \quad (2.7)$$

Equation 2.7 establishes the relationship between the solute concentration and the compensating point defect concentration. For 100 ppm TiO_2 -doped Al_2O_3 , the extrinsic

aluminum vacancy concentration is 40% larger than the intrinsic concentration at 1200°C. At most all temperatures realized in practice, the extrinsic concentration can exceed intrinsic concentrations by orders of magnitude, even for fairly minor impurity concentrations. Thus, extrinsic point defect concentrations typically dominate in ceramic oxides.

The ability to acquire an electric charge is not limited to point defects in ionic materials; line defects (dislocations) and planar defects (grain boundaries and surfaces) can also be electrically charged. To understand the physical origins of these charged defects, and the resulting effect on grain boundary chemistry, a detailed description of space charge theory is required.

2.4.2. Space Charge Theory for Ionic Solids

The presence of charged line and planar defects in ionic solids is one outstanding characteristic that distinguishes this class of solids from metals and alloys. The existence of such charged defects, and their equilibration with other charged species, have serious implications for grain boundary and dislocation behavior in ionic materials.

As demonstrated by Frenkel [30] and Lehovec [31], and later by Eshelby [32], surfaces, grain boundaries and dislocations in ionic materials can carry an electric charge as a result of local nonstoichiometry, characterized by excess ions of one sign⁵. This charge is compensated by an adjacent space-charge cloud of the opposite sign, which decays with distance into the crystal on a length scale that is typically a few to

⁵ The remainder of this discussion will trace the evolution of charge at a grain boundary. However, the derivation is equally valid for surfaces and dislocations and any other defects that act as vacancy sources. The reader is referred to [33] and [34-35] for detailed descriptions of charged surfaces and dislocations, respectively, in ionic materials.

several hundred angstroms [36]. Electroneutrality is preserved throughout the bulk of the crystal despite the redistribution of charged defects near the boundary. Consequently, at equilibrium there exists an electrostatic (space charge) potential difference between the grain boundary and the crystal interior. The origin and nature of this space charge potential ultimately depend on material purity. Three specific examples detailing the evolution of ionic space charge at a grain boundary for an ideally pure, a donor-doped, and a co-doped (acceptors and donors) Al_2O_3 bicrystal are discussed below. Note that these derivations assume the grain boundary acts as a perfect vacancy source/sink.

2.4.2.1. Intrinsic Case: Pure, Undoped Al_2O_3

The evolution of a space charge potential at a grain boundary in ideally pure Al_2O_3 can be understood by considering the equilibration of charged defects with the boundary, characterized by the following reactions:

$$Al_{Al}^x = Al_{boundary}^{\bullet\bullet\bullet} + V_{Al}^{\prime\prime\prime} \quad (2.8)$$

$$O_O^x = O_{boundary}^{\prime\prime} + V_O^{\bullet\bullet} \quad (2.9)$$

$$null \leftrightarrow 2V_{Al}^{\prime\prime\prime} + 3V_O^{\bullet\bullet} \quad (2.10)$$

The first two expressions describe the interaction of a lattice ion with the grain boundary to form a vacancy, while the last expression represents a fundamental condition of stoichiometry.

For most oxide ceramics characterized by a close-packed anion sublattice, the energy required to form an anion vacancy is typically larger than that to form a cation vacancy. In aluminum oxide, and indeed many of the oxide ceramics, exact vacancy

formation energies have proven quite difficult to determine accurately, but this general trend (i.e., $g_{v_{cation}} < g_{v_{anion}}$) is still anticipated. Thus, upon heating the crystal, excess cation vacancies form at the grain boundary and are injected into the adjacent crystal, leaving the boundary enriched in Al^{3+} cations (and hence positively charged). According to Eq. 2.10 above, an excess in V_{Al}''' will also suppress creation of $V_O^{..}$ near the boundary. The concentration of each type of vacancy then varies with distance in the space charge layer according to a spatially-varying potential $\phi(x)$.

The potential $\phi(x)$ can be calculated using the method set forth by Kliever and Koehler [33]. At any point in the crystal, the concentration of cation (or anion) vacancies is governed by the vacancy formation energy ($g_{v_{Al}}$ or g_{v_O}), the effective vacancy charge z and the electrostatic potential $\phi(x)$. For Al_2O_3 , these concentrations can be expressed as

$$[V_{Al}'''](x) = 2 \exp \left[-\frac{(g_{v_{Al}} - 3e\phi(x))}{kT} \right] \quad (2.11)$$

$$[V_O^{..}](x) = 3 \exp \left[-\frac{(g_{v_O} + 2e\phi(x))}{kT} \right] \quad (2.12)$$

Far away from the grain boundary (at $x=\infty$), the vacancy concentrations are given as

$$[V_{Al}''']_{\infty} = 2 \exp \left[-\frac{(g_{v_{Al}} - 3e\phi_{\infty})}{kT} \right] \quad (2.13)$$

$$[V_O^{..}]_{\infty} = 3 \exp \left[-\frac{(g_{v_O} + 2e\phi_{\infty})}{kT} \right]. \quad (2.14)$$

The condition of electrical neutrality requires that

$$3[V_{Al}''']_{\infty} = 2[V_O^{..}]_{\infty}, \quad (2.15)$$

which yields an expression for the electrostatic potential ϕ_∞ at the interior of the crystal

$$\phi_\infty = \frac{1}{5e} (g_{V_{Al}} - g_{V_O}). \quad (2.16)$$

Equation 2.16 shows that the sign and magnitude of the space charge potential for pure Al_2O_3 , far away from the boundary, is determined solely by the difference in cation and anion vacancy formation energies, and is independent of temperature. In this derivation, the potential is referenced to zero at the grain boundary, and since $g_{V_{Al}} < g_{V_O}$, the space charge potential will be negative in the crystal interior. This corresponds to a boundary with excess cations (positively charged) adjacent to a region enriched in cation vacancies, and depleted in anion vacancies.

Equations 2.11 and 2.12 show that the vacancy concentrations adjacent to the grain boundary are dependent on the spatially-varying space charge potential $\phi(x)$, whose form has not yet been discussed. Kliewer and Koehler have shown that $\phi(x)$ approximates an exponentially-decaying function over some characteristic distance away from the grain boundary when the quantity $|(e\phi_\infty/kT)|$ is unity or less, and decays somewhat faster as its value increases beyond unity [33]. The expression for $\phi(x)$ is then given as

$$\phi(x) = \phi_\infty \left[1 - \exp\left(-\frac{x}{\delta}\right) \right] \quad (2.17)$$

where δ is a characteristic length (the Debye length) whose magnitude is determined primarily by the dielectric strength of the crystal and the overall defect concentration. The Debye length is given as

$$\delta = \left[\frac{\epsilon \epsilon_0 kT}{e^2 \sum_i (N_i z_i^2)} \right] \quad (2.18)$$

where ϵ_0 is the permittivity of free space, ϵ is the static relative dielectric constant of Al_2O_3 , and N_i and z_i are the concentration and effective charge, respectively, of each species i . Vacancy concentrations adjacent to the grain boundary are therefore more easily expressed as functions of (x/δ) , and are given as

$$[V_{Al}''']_{(x/\delta)} = 2 \exp \left[-\frac{(g_{V_{Al}} - 3e\phi(x/\delta))}{kT} \right] \quad (2.19)$$

$$[V_O^{\bullet\bullet}]_{(x/\delta)} = 3 \exp \left[-\frac{(g_{V_O} + 2e\phi(x/\delta))}{kT} \right]. \quad (2.20)$$

These last two equations are used to plot the vacancy concentrations adjacent to a grain boundary in pure Al_2O_3 at 1600°C , as shown in Figure 2.5a. Values for $g_{V_{Al}}$ and g_{V_O} calculated in [29] for Shottky disorder have been used for these calculations, although the applicability of bulk defect formation energies to a grain boundary is clearly suspect⁶. As expected, enrichment of cation vacancies, and depletion of anion vacancies, are observed adjacent to the positively charged grain boundary, which exists in the plot at $x/\delta=0$. Figure 2.5b is a plot of the spatially-varying space-charge potential, showing a negative potential that reaches a fixed value in the crystal interior.

In reality, pure ceramic crystal can never be achieved because all ceramics contain residual solute species, so the intrinsic case is not a plausible scenario. It is perhaps more constructive to consider the origin and description of the space charge

potential for a doped solid, since solute concentrations ultimately dictate point defect concentrations in real materials. First we consider the case of a single aliovalent dopant, and then expand the treatment to include two dopants of different charge (a co-doped scenario).

2.4.2.2. Extrinsic Case

2.4.2.2.1. Donor-doped Al_2O_3

Whereas the space-charge potential near a grain boundary in ideally-pure Al_2O_3 is determined solely by the (difference in) vacancy formation energies, the potential in a doped material with aliovalent solute varies with solute concentration and temperature. This is because aliovalent solute concentrations in the bulk alter the vacancy concentrations and ultimately affect the equilibration of charged defects with ions at the grain boundary. Dopant effects on the grain boundary charge, and the associated space charge potential, can be understood and quantified with reference to equations describing the defect chemistry in the crystal interior and near the boundary.

We consider the specific case where an appreciable concentration of donor impurities (e.g. Ti^{4+} in Al_2O_3 , more commonly expressed as $\text{Ti}_{\text{Al}}^\bullet$) exists in the bulk. Donor impurities introduce a positive charge when they substitute for Al^{3+} cations, so compensating defects must be created to preserve charge neutrality in the crystal. Previous studies have shown that the preferred compensating defect mechanism for

⁶ Ikeda and co-workers have demonstrated that vacancy formation energies in TiO_2 can vary by as much as 1 eV between different types of grain boundaries [37]. Differences in defect formation energies between a grain boundary and the bulk could be even larger.

Al_2O_3 is the creation of negatively charged cation vacancies [28, 29]. Electroneutrality requires that

$$[Ti_{Al}^\bullet]_o = 3[V_{Al}''']_o \quad (2.21)$$

so that, in accordance with Eq. 2.13, far away from the surface the defect concentrations are given as

$$[Ti_{Al}^\bullet]_o = 3[V_{Al}''']_o = 6 \exp \left[-\frac{(g_{V_{Al}} - 3e\phi_\infty)}{kT} \right]. \quad (2.22)$$

Solving for the potential in the crystal interior yields

$$\phi_\infty = \frac{1}{3e} \left(g_{V_{Al}} + kT \ln \left(\frac{[Ti_{Al}^\bullet]_o}{6} \right) \right) \quad (2.23)$$

Following a derivation analogous to the intrinsic case, the space charge potential close to the grain boundary in the doped crystal is expressed as

$$\phi(x/\delta) = \frac{1}{3e} \left(g_{V_{Al}} + kT \ln \left(\frac{[Ti_{Al}^\bullet]_o}{6} \right) \left(1 - \exp \left(-\frac{x}{\delta} \right) \right) \right) \quad (2.24)$$

while the concentration(s) of charged defects are given as

$$[Ti_{Al}^\bullet](x/\delta) = 3[V_{Al}'''](x/\delta) = 6 \exp \left[-\frac{(g_{V_{Al}} - 3e\phi(x/\delta))}{kT} \right] \quad (2.25)$$

Several important facts can be gleaned from Eqs. 2.23-2.25. First, Eq. 2.23 shows that the sign and magnitude of the extrinsic potential depends on the vacancy formation energy $g_{V_{Al}}$, the bulk solute concentration $[Ti_{Al}^\bullet]_o$, and the temperature. Second, the sign of the grain boundary charge exists independent of the relative values of $g_{V_{Al}}$ and g_{V_O} .

For donor-doped Al_2O_3 , $g_{V_{Al}}$ is so large that ϕ_∞ is positive for nearly all (practical)

temperatures. This implies an accumulation of positive defects Ti_{Al}^\bullet , and a depletion of V_{Al}''' , adjacent to a negatively-charged grain boundary -- a result very different than that observed for the intrinsic case. Figure 2.6a shows the space charge potential calculated for 1000 ppm TiO_2 -doped Al_2O_3 at $1600^\circ C$, assuming an aluminum vacancy formation energy of 3.08 eV as calculated by Grimes [28]. Figure 2.6b is the affiliated plot of major defect concentrations in the space charge region.

2.4.2.2.2. Codoped Al_2O_3

We now consider the situation where a significant concentration of donor (Ti^{4+}) and acceptor (Ca^{2+}) solute species exist in the bulk. In codoped compositions of Al_2O_3 , donor and acceptor solutes are able to charge-compensate for each other. So while the complete electroneutrality condition is given as

$$[Ti_{Al}^\bullet] + 2[V_O^{\bullet\bullet}] = [Ca'_{Al}] + 3[V_{Al}'''] \quad (2.26)$$

it is the net doping that determines the lattice defect structure and grain boundary potential [38]. For the specific case where $[Ti_{Al}^\bullet]_o \gg [Ca'_{Al}]_o$, Eq. 2.26 reduces to

$$[Ti_{Al}^\bullet] - [Ca'_{Al}] = 3[V_{Al}'''] \quad (2.27)$$

and the potential in the crystal interior is given as

$$\phi_\infty = \frac{1}{3e} \left(g_{V_{Al}'''} + kT \ln \left(\frac{[Ti_{Al}^\bullet]_o - [Ca'_{Al}]_o}{6} \right) \right). \quad (2.28)$$

The individual defect concentrations in the space charge region are then

$$[Ti_{Al}^\bullet](x/\delta) = [Ti_{Al}^\bullet]_o \exp \left[-\frac{(e\phi(x/\delta) - e\phi_\infty)}{kT} \right] \quad (2.29)$$

$$[Ca'_{Al}](x/\delta) = [Ca'_{Al}]_{\infty} \exp\left[\frac{e\phi(x/\delta) - e\phi_{\infty}}{kT}\right] \quad (2.30)$$

$$[V'''_{Al}](x/\delta) = 2 \exp\left[-\frac{(g_{V_{Al}} - 3e\phi(x/\delta))}{kT}\right] \quad (2.31)$$

Plots of the space-charge potential and the defect concentrations near the grain boundary are shown in Figure 2.7a and 7b, respectively, for 1000 ppm TiO₂- and 300 ppm CaO-doped Al₂O₃ at 1600°C. A negatively-charged grain boundary, and a positive potential in the crystal, are still observed despite the Ca²⁺ additions, although the concentration of Ti solute at the boundary has now decreased.

Of course, the space charge potential alone does not determine the distribution of solute species at the grain boundary. Strongly-misfitting solute species will still segregate to the grain boundary (and other defect sites) to relieve elastic strain energy, regardless of their effective charge and/or interaction with the space charge potential. But it is not clear in such instances how or if the different driving forces interact or superimpose to yield the ultimate segregation profile.

Yan, Cannon and Bowen [39] developed models to examine the coupled effects of elastic and electrostatic driving forces for solute segregation. Their work demonstrates that elastic interactions between solute and grain boundary can significantly modify the electrostatic potential, and thus the overall distribution of space charge, near the boundary. However, their derivation assumes all solutes have the same charge (they consider only divalent donor solutes in KCl), so their models may not be appropriate for describing Ca²⁺ and Ti⁴⁺ segregation in Al₂O₃. Interestingly, though, they show that minority solutes with large elastic interaction energies (such as Ca in MgO-doped Al₂O₃) segregate strongly to grain boundaries, and in doing so strongly

diminish segregation of the majority solute. They conclude that when more than one aliovalent solute is present, the segregation of one species can significantly modify the segregation of other species due to electrostatic considerations.

Ceramics usually contain a variety of impurity species. These solutes are likely to have different radii -- and therefore different elastic interaction energies with grain boundaries -- as well as different valences, so their individual segregation profiles are expected to be very different indeed. Because of electrostatic coupling in ionic ceramics, the segregation profiles of the various solute species should be inter-dependent. To date, however, few if any theoretical studies have attempted to model the segregation behavior of multi-valent, multi-solute systems.

2.5. Experimental Studies of Grain Boundary Structure and Segregation in Al_2O_3

This section recounts relevant studies on the structure and chemistry of grain boundaries in aluminum oxide. Summary papers by Johnson [40] and Kingery [41, 42] offer more detailed and comprehensive reviews of solute segregation to ceramic grain boundaries. Pertinent studies of grain boundary segregation in MgO [6, 43-48], TiO_2 [37, 38, 49] and other ceramic oxides [50-58] may also be of interest to the reader, but are not discussed here.

2.5.1. Grain Boundary Segregation in Al_2O_3

Kingery's seminal papers describing various grain boundary phenomena in ceramics catalyzed a lengthy and ambitious pursuit to understand the nature and behavior of ceramic grain boundaries [59, 60]. Subsequent studies sought to reveal the evolution of grain boundary chemistry in ceramics, and to offer some insight as to how boundary structure governs solute segregation. Unfortunately, experimental techniques at that time did not afford sufficient spatial resolution to reveal a detailed picture of structure-chemistry relations. Indeed, most reports of grain boundary segregation in polycrystalline alumina ceramics were motivated by a need to explain observed grain boundary behavior, and did not involve direct observations of grain boundary chemistry. Westbrook inferred Mg segregation to grain boundaries based on hardness profiles acquired near the boundary in MgO-doped Al_2O_3 [61]. Jorgensen attributed reduced grain growth behavior in the same material system to a drag effect caused by grain boundary segregation of Mg solute [62, 63].

The ensuing development of spatially-resolved spectroscopy techniques allowed more direct measurements of grain boundary chemistry. The first direct observations of impurity segregation to alumina grain boundaries were made by Tong and Williams, who found enhanced concentrations of Mg, Si, Ca, Na and Fe in Al_2O_3 using spark-source mass spectroscopy, illustrating the ubiquitous nature of impurity segregation in alumina [64]. Later studies made use of Auger electron spectroscopy (AES) on fractured (exposed) grain boundary surfaces to examine and quantify solute segregation. A study by Marcus and Fine showed the surprising result that Ca, but not Mg, could be detected at fractured grain boundaries in MgO-doped alumina [65]. Here, the bulk Ca concentration was reported as 5-15 ppm, while MgO was present at the 1000-ppm level,

clearly demonstrating the strong dependence of impurity segregation on ionic radius. Reports by Taylor [66] and Johnson [67] using similar techniques confirmed the initial finding by Marcus and Fine: namely, that Ca is a much stronger segregant than Mg in Al_2O_3 , even at very minor bulk concentrations. Despite the successes of spectroscopy-based techniques in exposing grain boundary chemistry, there was still no viable method for correlating structure and chemistry.

The advent of TEM-based microanalysis techniques permitted grain boundary studies with new clarity and precision, as direct examination of intergranular chemistry and structure could be performed at nanometer resolution on buried (non-fractured) interfaces. Krivanek [68], Clarke [69], and Li [70] all utilized x-ray microanalysis in a scanning transmission electron microscope (STEM) to quantify grain boundary concentrations of various impurities in polycrystalline Al_2O_3 . The latter study clearly demonstrated that grain boundary concentrations of isovalent solutes Cr^{3+} , Ga^{3+} , Ti^{3+} , Sc^{3+} and Y^{3+} are generally consistent with values predicted from a modified form of McLean's elastic-misfit expression (Equation 2.4), given as

$$\ln \frac{C_{gb}}{C_l} = \frac{\Delta S}{k} + \frac{24\pi K G r_1^3}{3K + 4G \left(\frac{r_1}{r_2} \right)} \left(\frac{r_2 - r_1}{r_1} \right)^2 \frac{1}{kT} \quad (2.32)$$

Here, all variables are the same as in Eq. 2.4, and ΔS is the entropy change stemming from solute segregation to the boundary. In a plot of $\ln(C_{gb}/C_l)$ versus $((r_2 - r_1)/r_1)^2$, reproduced in Figure 2.8, the authors verified the validity of Equation 2.32 in describing the segregation behavior of isovalent impurities in alumina.

But these early TEM-based investigations of solute segregation in alumina made no effort to correlate grain boundary structure and chemistry. In fact, experiments to

explore grain boundary structure-chemistry relationships in alumina have surfaced only recently [71-78]. As a result of so few studies, our understanding of how solute segregation varies with grain boundary structure is very minimal, and limited to only a few solute species in Al_2O_3 .

2.5.2. Studies of Grain Boundary Chemistry and Structure in Ti-doped Al_2O_3

Krivanek [68] used x-ray microanalysis in a STEM to quantify solute segregation in Al_2O_3 doped with 0.1 wt% TiO_2 , and observed a ten-fold increase in Ti concentration (1.0 wt%) at the grain boundary relative to the bulk. No second phases were observed at or near the grain boundary. Specific details concerning material processing were not reported.

Li and Kingery [70] also used x-ray microanalysis in a STEM to measure grain boundary segregation in polycrystalline Al_2O_3 samples doped with TiO_2 . In 0.2 wt% TiO_2 -doped samples fired in oxygen at 1525°C , some grain boundary regions were wet by a liquid phase, while some segments were ostensibly free of second phases. The former showed pronounced enrichment of Ti, Ca and Si, while in the latter, Ti segregation occurred at levels 60-80 times greater than the bulk concentration. However, in 0.5 wt% TiO_2 -doped samples fired at 1775°C in hydrogen, Ti enrichment at the grain boundary was only twice the bulk concentration.

Swiatnicki and co-workers [77, 78] examined intergranular segregation in alumina co-doped with 1.8 wt% TiO_2 and 0.46 wt% MgO , and sintered at 1400°C in an oxidizing atmosphere. They observed substantial grain boundary enrichment of Ti (and impurities such as Si and Ca), but found no evidence of Mg segregation. Solute

segregation varied strongly with grain boundary crystallography, depending primarily on grain boundary plane orientation and, to a lesser degree, on the grain misorientation. However, as the authors report, the dependence of solute segregation on grain boundary crystallography is quite complex:

“In the coherent $\Sigma 3$ grain boundaries with symmetrical GB plane, the segregation was not detected. In the other boundaries the segregation is important and rather insensitive to the special misorientations corresponding to a “plane matching” model. Moreover, the CSL misorientations, (others than $\Sigma 3$), seem not to diminish significantly the segregation level. However, these boundaries present a high Σ value or are strongly deviated from the exact CSL misorientation. On the other hand the segregation is very weak in some cases where the boundary plane is parallel to dense lattice planes for both grains . . . In these cases the segregation may be altered by the GB microstructure (facets, dislocations) or by the deviation of the plane from the exact crystallographic plane. Some influence can arise also from the proximity of titanate precipitates or adjoining boundaries with a strong segregation, which can play a significant role if the material is in a non-equilibrium state”. [77]

The significance of grain boundary plane was born out by segregation data for Ti and Si. Silicon was found to segregate preferentially to intergranular planes lying parallel to dense lattice planes (such as (0001)) for one of the adjacent grains, while Ti exhibited stronger segregation to boundaries that do not expose any dense planes. No intergranular films were observed at any of the grain boundaries.

Most recently, Kebbede and Carim [76] have examined solute segregation in 0.6 wt% TiO₂-doped Al₂O₃ sintered in air at 1450°C, and containing 0.05 wt% Si impurity. They too observe that Ti segregation varies according to grain boundary plane. Minor Ti segregation is observed to (0001)-type grain boundary planes, but strong Ti enrichment is found at curved or faceted boundary segments that deviate from (0001).

A shortcoming shared by all previous studies of Ti-doped Al_2O_3 is an inability to directly determine Ti valence. In fact, only one study [70] even acknowledged the importance of solute valence on segregation behavior. In that study, Ti valence was inferred based on processing conditions, but was not actually measured. Moreover, all previous studies of Ti segregation in Al_2O_3 utilized polycrystalline samples, which are advantageous in terms of yielding a great variety of different boundary orientations, but are plagued by the fact that segregation behavior at a particular boundary can be greatly affected by the structure, energy and chemistry of neighboring boundaries.

Chapter 2 References

1. A.P. Sutton and R.W. Balluffi, *Interfaces in Crystalline Materials*. Oxford: Oxford University Press, 1995.
2. D. Wolf and S. Yip, eds. *Materials Interfaces*. London: Chapman and Hall, 1992.
3. V. Randle, *The Role of the Coincident Site Lattice in Grain Boundary Engineering*. Cambridge: University Press, 1996.
4. R.W. Balluffi, "Grain Boundary Structure and Segregation," in *Interfacial Segregation*, W.C. Johnson and J.M. Blakely, Editors. American Society for Metals: Metals Park, 1979.
5. K.T. Aust and J.W. Rutter, "Grain Boundary Migration in High-Purity Lead and Dilute Lead-Tin Alloys," *Transactions of the American Institute of Mining and Metallurgical Engineers* **215** (1) 119-27 (1959).
6. A. Roshko and W.D. Kingery, "Segregation at Special Boundaries in MgO," *Journal of the American Ceramic Society* **68** (12) C331-C333 (1985).
7. J.M. Burgers, "Geometrical Considerations Concerning the Structural Irregularities to be Assumed in a Crystal," *Proceedings of the Physical Society* **52** 23-33 (1940).
8. W.L. Bragg, "Discussion," *Proceedings of the Physical Society* **52** 54-5 (1940).
9. W.T. Read and W. Shockley, "Dislocation Models of Crystal Grain Boundaries," *Physical Review* **78** (3) 275-89 (1950).
10. W. Shockley and W.T. Read, "Quantitative Predictions from Dislocation Models of Crystal Grain Boundaries," *Physical Review* **75** (4) 692 (1949).
11. J.M. Howe, *Interfaces in Materials*. New York: John Wiley and Sons, Inc., 1997.
12. A.H. Cottrell, *Dislocations and Plastic Flow in Crystals*. Oxford: Oxford University Press, 1953.
13. M.F. Ashby, F. Spaepen, and S. Williams, "The Structure of Grain Boundaries Described as a Packing of Polyhedra," *Acta Metallurgica* **26** 1647-63 (1978).
14. A.P. Sutton and V. Vitek, "On the Structure of Tilt Grain Boundaries in Cubic Metals. I. Symmetrical Tilt Boundaries," *Philosophical Transactions of the Royal Society of London A* **309** (1506) 1-36 (1983).

15. A.P. Sutton and V. Vitek, "On the Structure of Tilt Grain Boundaries in Cubic Metals. II. Asymmetrical Tilt Boundaries," *Philosophical Transactions of the Royal Society of London A* **309** (1506) 37-54 (1983).
16. A.P. Sutton and V. Vitek, "On the Structure of Tilt Grain Boundaries in Cubic Metals. III. Generalizations of the Structural Study and Implications for the Properties of Grain Boundaries," *Philosophical Transactions of the Royal Society of London A* **309** (1506) 55-68 (1983).
17. J.W. Gibbs, *Collected Works*. New Haven: Yale University Press, 1948.
18. J.W. Cahn and J.E. Hilliard, "On the Equilibrium Segregation at a Grain Boundary," *Acta Metallurgica* **7** 219-221 (1959).
19. D. McLean, *Grain Boundaries in Metals*. Oxford: Oxford University Press, 1957.
20. S.M. Foiles, "Calculation of Grain-Boundary Segregation in Ni-Cu Alloys," *Physical Review B* **40** (17) 11502-6 (1989).
21. A. Seki, D.N. Seidman, Y. Oh, and S.M. Foiles, "Monte Carlo Simulations of Segregation at [001] Twist Boundaries in a Pt(Au) Alloy - I. Results," *Acta Metallurgica et Materialia* **39** (12) 3167-77 (1991).
22. A. Seki, D.N. Seidman, Y. Oh, and S.M. Foiles, "Monte Carlo Simulations of Segregation at [001] Twist Boundaries in a Pt(Au) Alloy - II. Discussion," *Acta Metallurgica et Materialia* **39** (12) 3179-85 (1991).
23. H.Y. Wang, R. Najafabadi, D.J. Srolovitz, and R. Lesar, "Segregation to and Structure of [001] Twist Grain Boundaries in Cu-Ni Alloys," *Acta Metallurgica et Materialia* **41** (9) 2533-46 (1993).
24. J.R. Michael, C.H. Lin, and S.L. Sass, "High Resolution Detection of Solute Segregation to the Cores of Dislocations in Grain Boundaries," *Scripta Metallurgica* **22** 1121-4 (1988).
25. M. Menyhard, B. Rothman, and C.J. McMahon, Jr., "Observations of Segregation and Grain-Boundary Faceting by Tellurium and Oxygen in Iron," *Scripta Metallurgica et Materialia* **29** (8) 1005-9 (1993).
26. A.M. Donald and L.M. Brown, "Grain Boundary Faceting in Cu-Bi Alloys," *Acta Metallurgica* **27** 59-66 (1979).
27. W.D. Kingery, H.K. Bowen, and D.R. Uhlmann, *Introduction to Ceramics*. New York: J. Wiley and Sons, 1976.

28. R.W. Grimes, "Solution of MgO, CaO, and TiO₂ in α -Al₂O₃," *Journal of the American Ceramic Society* **77** (2) 378-84 (1994).
29. W.C. Mackrodt, "Calculated Point Defect Formation, Association, and Migration Energies in MgO and α -Al₂O₃," in *Structure and Properties of MgO and Al₂O₃ Ceramics*, W.D. Kingery, Editor. The American Ceramic Society: Columbus, 1984.
30. J. Frenkel, *Kinetic Theory of Liquids*. New York: Oxford University Press, 1946.
31. K. Lehovc, "Space-Charge Layer and Distribution of Lattice Defects at the Surface of Ionic Crystals," *Journal of Chemical Physics* **21** (7) 1123-1128 (1953).
32. J.D. Eshelby, C.W.A. Newey, P.L. Pratt, and A.B. Lidiard, "Charged Dislocations and the Strength of Ionic Crystals," *Philosophical Magazine* **3** (25) 75-89 (1958).
33. K.L. Kliewer and J.S. Koehler, "Space Charge in Ionic Crystals. I. General Approach with Application to NaCl," *Physical Review* **140** (4A) A1226-A1240 (1965).
34. J.S. Koehler, D. Langreth, and B. von Turkovich, "Charged Dislocations in Ionic Crystals," *Physical Review* **128** (2) 573-80 (1962).
35. R.A. Menezes and W.D. Nix, "High Temperature Dislocation Mobility in LiF Part I. Charged Dislocations in Ionic Crystals," *Materials Science & Engineering* **16** 57-66 (1974).
36. Y.M. Chiang, D. Birnie III, and W.D. Kingery, *Physical Ceramics. Principles for Ceramic Science and Engineering*. New York: John Wiley and Sons, Inc., 1997.
37. J.S. Ikeda, Y.M. Chiang, A.J. Garratt-Reed, and J.B. Vander Sande, "Space Charge Segregation at Grain Boundaries in Titanium Dioxide: II, Model Experiments," *Journal of the American Ceramic Society* **76** (10) 2447-59 (1993).
38. J.S. Ikeda and Y.M. Chiang, "Space Charge Segregation at Grain Boundaries in Titanium Dioxide: I, Relationship Between Lattice Defect Chemistry and Space Charge Potential," *Journal of the American Ceramic Society* **76** (10) 2437-46 (1993).

39. M.F. Yan, R.M. Cannon, and H.K. Bowen, "Space Charge, Elastic Field, and Dipole Contributions to Equilibrium Solute Segregation at Interfaces," *Journal of Applied Physics* **54** (2) 764-778 (1983).
40. W.C. Johnson, "Grain Boundary Segregation in Ceramics," *Metallurgical Transactions A* **8A** 1413-1422 (1977).
41. W.D. Kingery, "Distribution and Influence of Minor Constituents on Ceramic Formulations," in *Ceramic Microstructures '86: Role of Interfaces*, J.A. Pask and A.G. Evans, Editors. Plenum Press: New York, 1987.
42. W.D. Kingery, "The Chemistry of Ceramic Grain Boundaries," *Pure and Applied Chemistry* **56** (12) 1703-14 (1984).
43. W.D. Kingery, T. Mitamura, J.B. Vander Sande, and E.L. Hall, "Boundary Segregation of Ca, Fe, La and Si in Magnesium Oxide," *Journal of Materials Science* **14** 1766-7 (1979).
44. M.H. Leipold, "Addenda to Impurity Distribution in MgO," *Journal of the American Ceramic Society* **50** (11) 628-9 (1967).
45. T. Mitamura, E.L. Hall, W.D. Kingery, and J.B. Vander Sande, "Grain Boundary Segregation of Iron in Polycrystalline Magnesium Oxide Observed by STEM," *Ceramurgia International* **5** (4) 131-6 (1979).
46. W.H. Gourdin, W.D. Kingery, and J. Driear, "The Defect Structure of MgO Containing Trivalent Cation Solutes: The Oxidation-Reduction Behavior of Iron," *Journal of Materials Science* **14** 2074-82 (1979).
47. Y.M. Chiang, A.F. Henriksen, and W.D. Kingery, "Characterization of Grain Boundary Segregation in MgO," *Journal of the American Ceramic Society* **64** (7) 385-89 (1981).
48. T.A. Yager and W.D. Kingery, "The Equilibrium Defect Structure of Iron-Doped MgO in the Range 600-1200°C," *Journal of Materials Science* **16** 489-94 (1981).
49. C.D. Terwilliger and C. Yet-Ming, "Size-Dependent Solute Segregation and Total Solubility in Ultrafine Polycrystals: Ca in TiO₂," *Acta Metallurgica et Materialia* **43** (1) 319-28 (1995).
50. D.B. Kingery, J.B. Vander Sande, and T. Mitamura, "A Scanning Transmission Electron Microscopy Investigation of Grain-Boundary Segregation in a ZnO-Bi₂O₃ Varistor," *Journal of the American Ceramic Society* **62** (3-4) 221-2 (1979).

51. M.H. Leipold, "Grain Boundary Impurities," in *Ceramic Microstructures*, R.M. Fulrath and J.A. Pask, Editors. John Wiley and Sons, Inc.: New York, 1968.
52. B. Bender, D.B. Williams, and M.R. Notis, "Investigation of Grain-Boundary Segregation in Ceramic Oxides by Analytical Scanning Transmission Electron Microscopy," *Journal of the American Ceramic Society* **63** (9-10) 542-6 (1980).
53. Y.M. Chiang and T. Takagi, "Grain Boundary Chemistry of Barium Titanate and Strontium Titanate: I, High-Temperature Equilibrium Space Charge," *Journal of the American Ceramic Society* **73** (11) 3278-85 (1990).
54. D.M. Duffy and P.W. Tasker, "A Calculation of the Interaction Between Impurity Ions and Grain Boundaries in NiO," *Philosophical Magazine A* **50** (2) 155-69 (1984).
55. D.M. Duffy and P.W. Tasker, "Space-Charge Regions Around Dipolar Grain Boundaries," *Journal of Applied Physics* **56** (4) 971-977 (1984).
56. M. Aoki, Y.M. Chiang, I. Kosacki, L.J. Lee, H. Tuller, and Y. Liu, "Solute Segregation and Grain Boundary Impedance in High-Purity Stabilized Zirconia," *Journal of the American Ceramic Society* **79** (5) 1169-80 (1996).
57. S.J. Pennycook, E.C. Dickey, P.D. Nellist, M.F. Chisholm, Y. Yan, and S.T. Pantelides, "A Combined Experimental and Theoretical Approach to Atomic Structure and Segregation at Ceramic Interfaces," *Journal of the European Ceramic Society* **19** (13-14) 2211-2216 (1999).
58. S.H. Yoon and H. Kim, "Experimental Evidence for Space Charge Segregation in Nb-Doped BaTiO₃," *Journal of Materials Research* **16** (5) 1479-86 (2001).
59. W.D. Kingery, "Plausible Concepts Necessary and Sufficient for Interpretation of Ceramic Grain-Boundary Phenomena: I, Grain Boundary Characteristics, Structure, and Electrostatic Potential," *Journal of the American Ceramic Society* **57** (1) 1-8 (1974).
60. W.D. Kingery, "Plausible Concepts Necessary and Sufficient for Interpretation of Ceramic Grain-Boundary Phenomena. II. Solute Segregation, Grain-Boundary Diffusion, and General Discussion," *Journal of the American Ceramic Society* **57** (2) 74-83 (1974).
61. J.H. Westbrook, "Analysis of the Nature of Grain Boundaries in Ceramics," in *Ceramic Microstructures*, R.M. Fulrath and J.A. Pask, Editors. John Wiley and Sons, Inc.: New York, 1968.

62. P.J. Jorgensen and J.H. Westbrook, "Role of Solute Segregation at Grain Boundaries During Final-Stage Sintering of Alumina," *Journal of the American Ceramic Society* **47** (7) 332-8 (1964).
63. P.J. Jorgensen, "Modification of Sintering Kinetics by Solute Segregation in Al_2O_3 ," *Journal of the American Ceramic Society* **48** (4) 207-10 (1965).
64. S.S.C. Tong and J.P. Williams, "Chemical Analysis of Grain Boundary Impurities in Polycrystalline Ceramic Materials by Spark Source Mass Spectrometry," *Journal of the American Ceramic Society* **53** (1) 58-9 (1970).
65. H.L. Marcus and M.E. Fine, "Grain-Boundary Segregation in MgO-Doped Al_2O_3 ," *Journal of the American Ceramic Society* **55** (11) 568-570 (1972).
66. R.I. Taylor, J.P. Coad, and R.J. Brook, "Grain Boundary Segregation in Al_2O_3 ," *Journal of the American Ceramic Society* **57** (12) 539-40 (1974).
67. W.C. Johnson and D.F. Stein, "Additive and Impurity Distributions at Grain Boundaries in Sintered Alumina," *Journal of the American Ceramic Society* **58** (11-12) 485-488 (1975).
68. O.L. Krivanek, M. Harmer, and R. Geiss, "Electron Microscopy Studies of Grain Boundary Segregation in $\alpha\text{-Al}_2\text{O}_3$," in *Ninth International Congress on Electron Microscopy*. Toronto: Microscopical Society of Canada, 1978.
69. D.R. Clarke, "Grain-Boundary Segregation in an MgO-Doped Al_2O_3 ," *Journal of the American Ceramic Society* **63** (5-6) 339-341 (1980).
70. C.W. Li and W.D. Kingery, "Solute Segregation at Grain Boundaries in Polycrystalline Al_2O_3 ," in *Structure and Properties of MgO and Al_2O_3 Ceramics*, W.D. Kingery, Editor. American Ceramic Society: Columbus, 1984.
71. D. Bouchet, F. Dupau, and S. Lartigue-Korinek, "Structure and Chemistry of Grain Boundaries in Yttria Doped Aluminas," *Microscopy Microanalysis Microstructures* **4** (6) 561-573 (1993).
72. J. Bruley, T. Hoche, H.J. Kleebe, and M. Rühle, "Recent Attempts to Detect Magnesium in a Heavily Doped Sapphire Bicrystal by Spatially Resolved Electron Energy-Loss Spectroscopy," *Journal of the American Ceramic Society* **77** (9) 2273-76 (1994).
73. J. Bruley, J. Cho, H.M. Chan, M.P. Harmer, and J.R. Rickman, "Scanning Transmission Electron Microscopy Analysis of Grain Boundaries in Creep-Resistant Yttrium- and Lanthanum-Doped Alumina Microstructures," *Journal of the American Ceramic Society* **82** (10) 2865-70 (1999).

- 74. K. Kaneko, T. Gemming, I. Tanaka, and H. Müllejans, "Analytical Investigation of Random Grain Boundaries of Zr-Doped Sintered α -Al₂O₃ by Transmission Electron Microscopy and Scanning Transmission Electron Microscopy," *Philosophical Magazine A* **77** (5) 1255-72 (1998).
- 75. W.D. Kaplan, H. Müllejans, M. Ruhle, J. Rodel, and N. Claussen, "Ca Segregation to Basal Surfaces in Alpha-Alumina," *Journal of the American Ceramic Society* **78** (10) 2841-2844 (1995).
- 76. A. Kebbede and A.H. Carim, "Segregation of Si and Ti in Alpha-Alumina," *Materials Letters* **41** (4) 198-203 (1999).
- 77. W. Swiatnicki, S. Lartigue-Korinek, A. Dubon, and J.Y. Laval, "Intergranular Segregation and Grain Boundary Crystallography in Al₂O₃," *Materials Science Forum* **126-128** 193-6 (1993).
- 78. W. Swiatnicki, S. Lartigue-Korinek, and J.Y. Laval, "Grain Boundary Structure and Intergranular Segregation in Al₂O₃," *Acta Metallurgica et Materialia* **43** (2) 795-805 (1995).

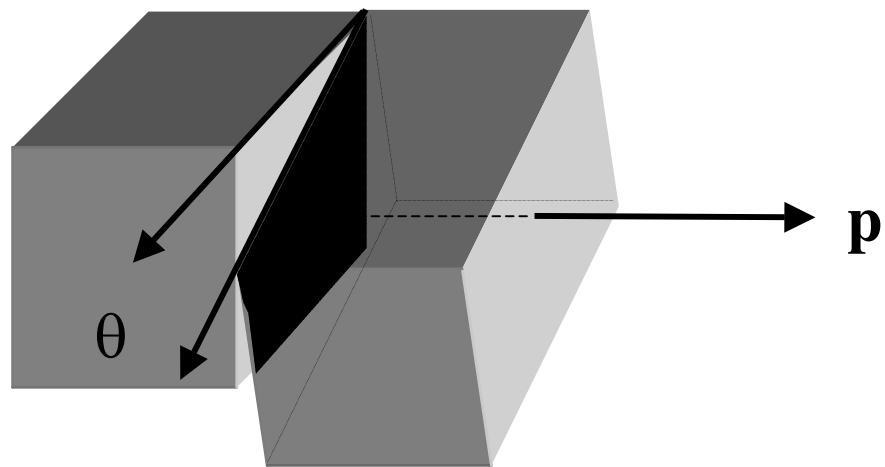
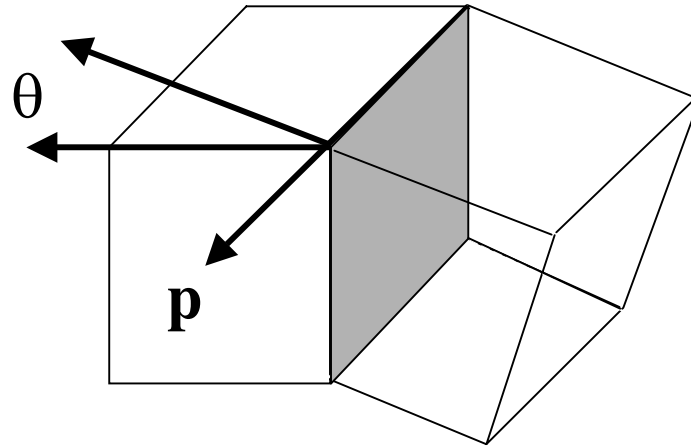


Figure 2.1. Rotation of two crystals about a common axis \mathbf{p} to form a (a) tilt and (b) twist boundary. In the former, \mathbf{p} is contained in the boundary plane, but is normal to the plane in the latter.

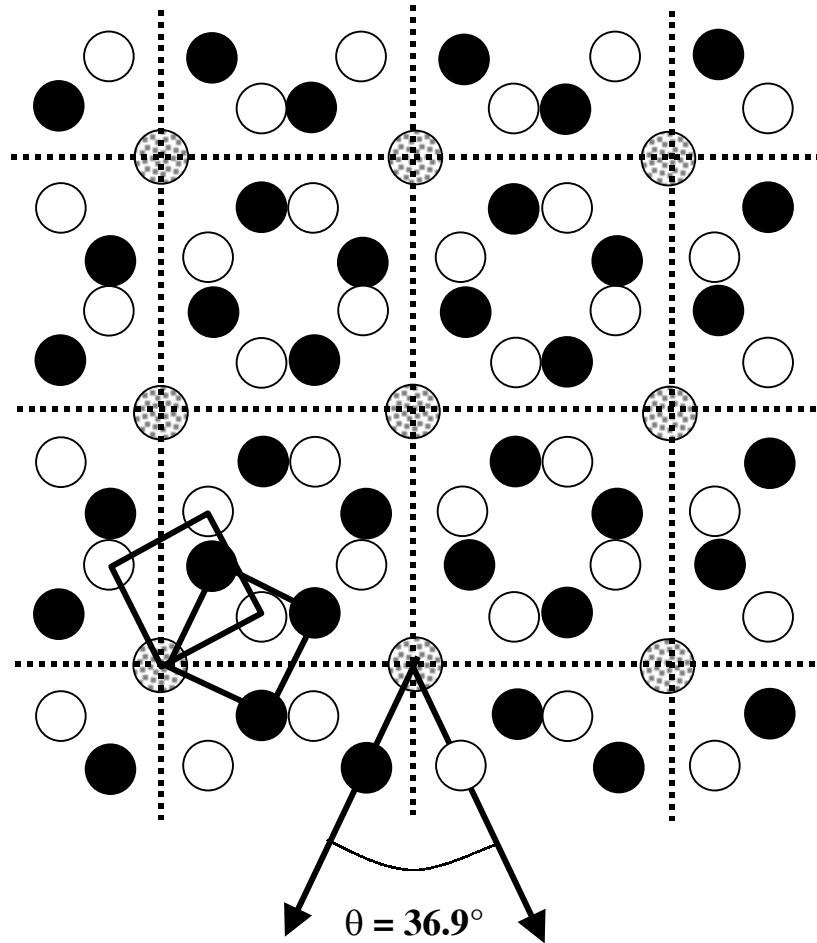


Figure 2.2. Rotation of two cubic lattices by 36.9° about a common axis results in a $\Sigma 5$ CSL. Dashed lines indicate the lattice of coincidence sites.

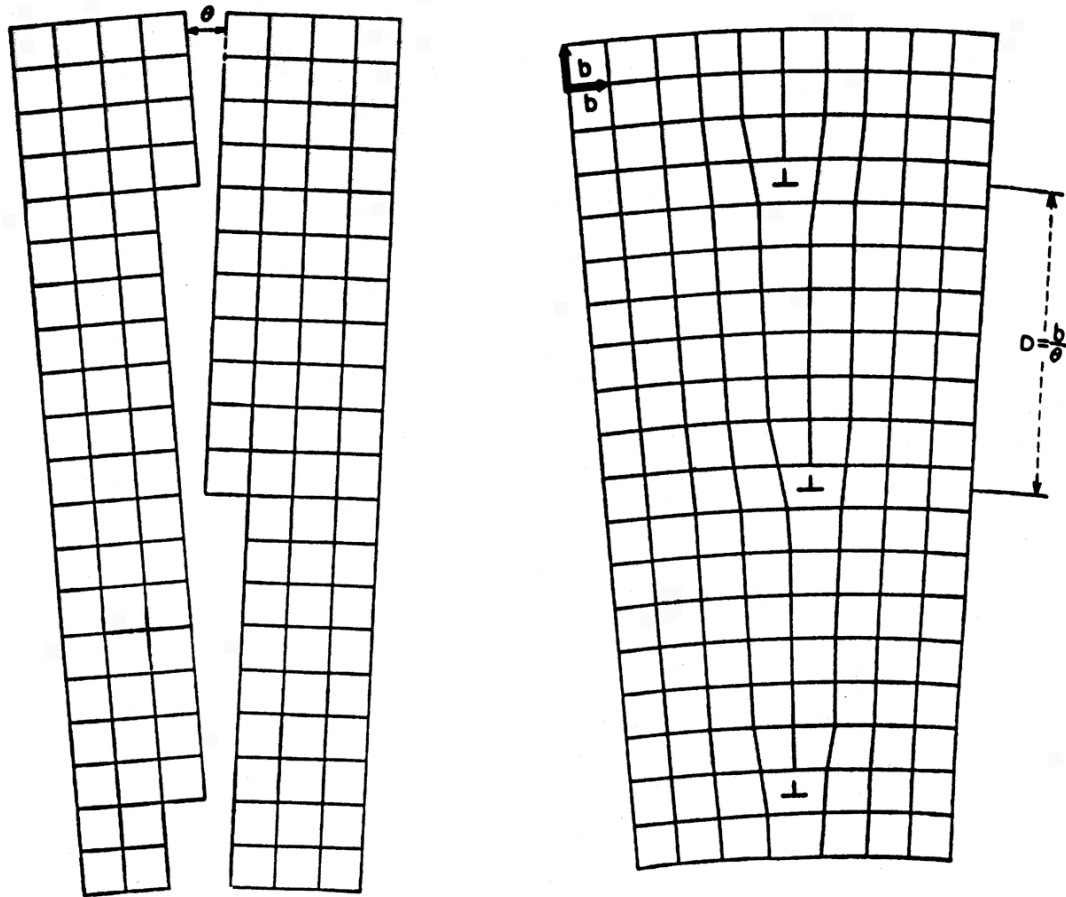


Figure 2.3. Formation of a low-angle tilt boundary from two crystals misoriented by a small angle θ . The tilt boundary is characterized by a row of edge dislocations with periodic spacing D . (Reproduced from [9]).

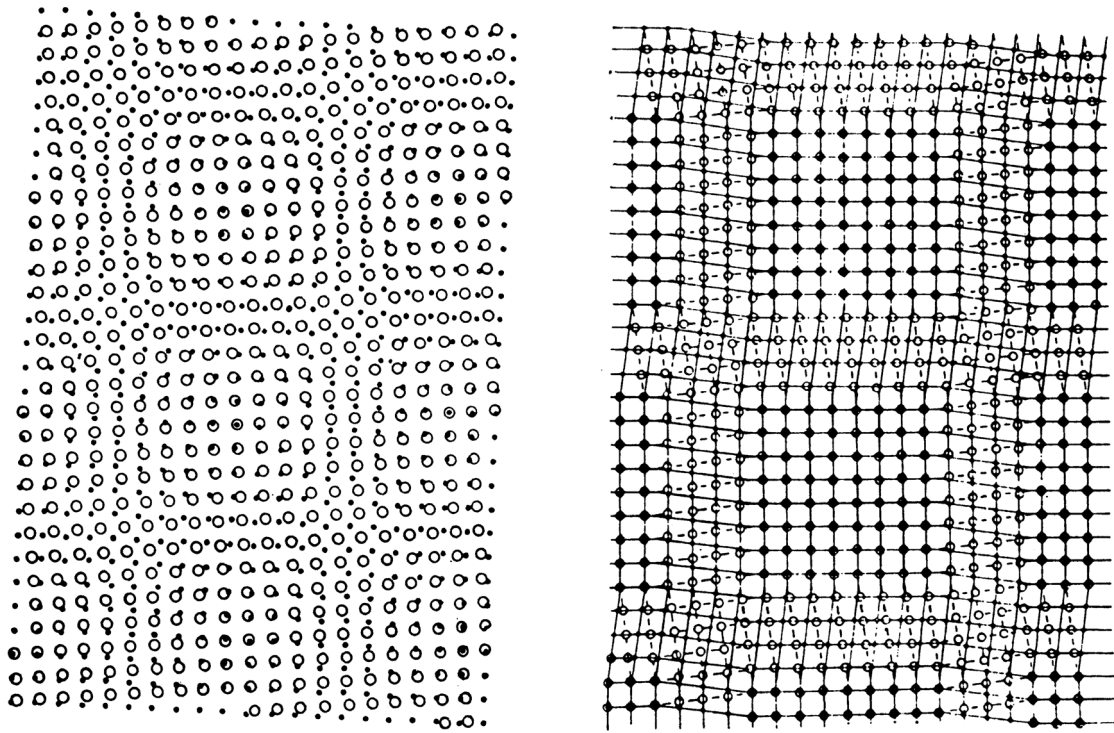
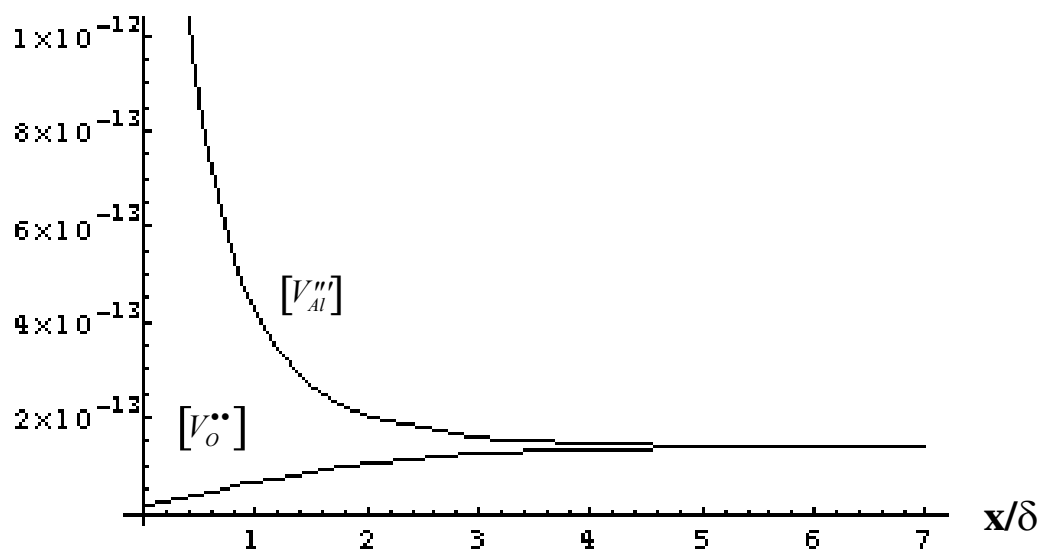


Figure 2.4. (a) Rotation of two cubic crystals about their common normal leads to formation of a twist boundary. (b) Small displacements of atoms lead to large areas of registry separated by screw dislocations. Open circles represent atoms above the boundary plane, and closed circles are atoms beneath the plane. (From [9]).

Conc. (mol)



ϕ (V)

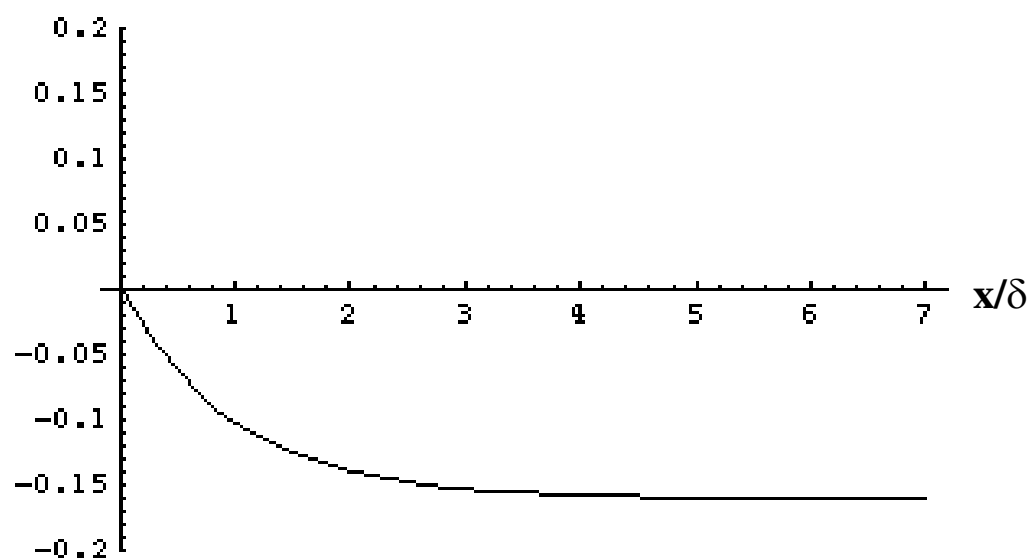


Figure 2.5. (a) Intrinsic defect concentrations and (b) spatially-varying potential near a charged grain boundary in undoped Al_2O_3 at 1600°C . Grain boundary positioned at $x/\delta = 0$. ($\delta = 3$ nm at 1600°C).

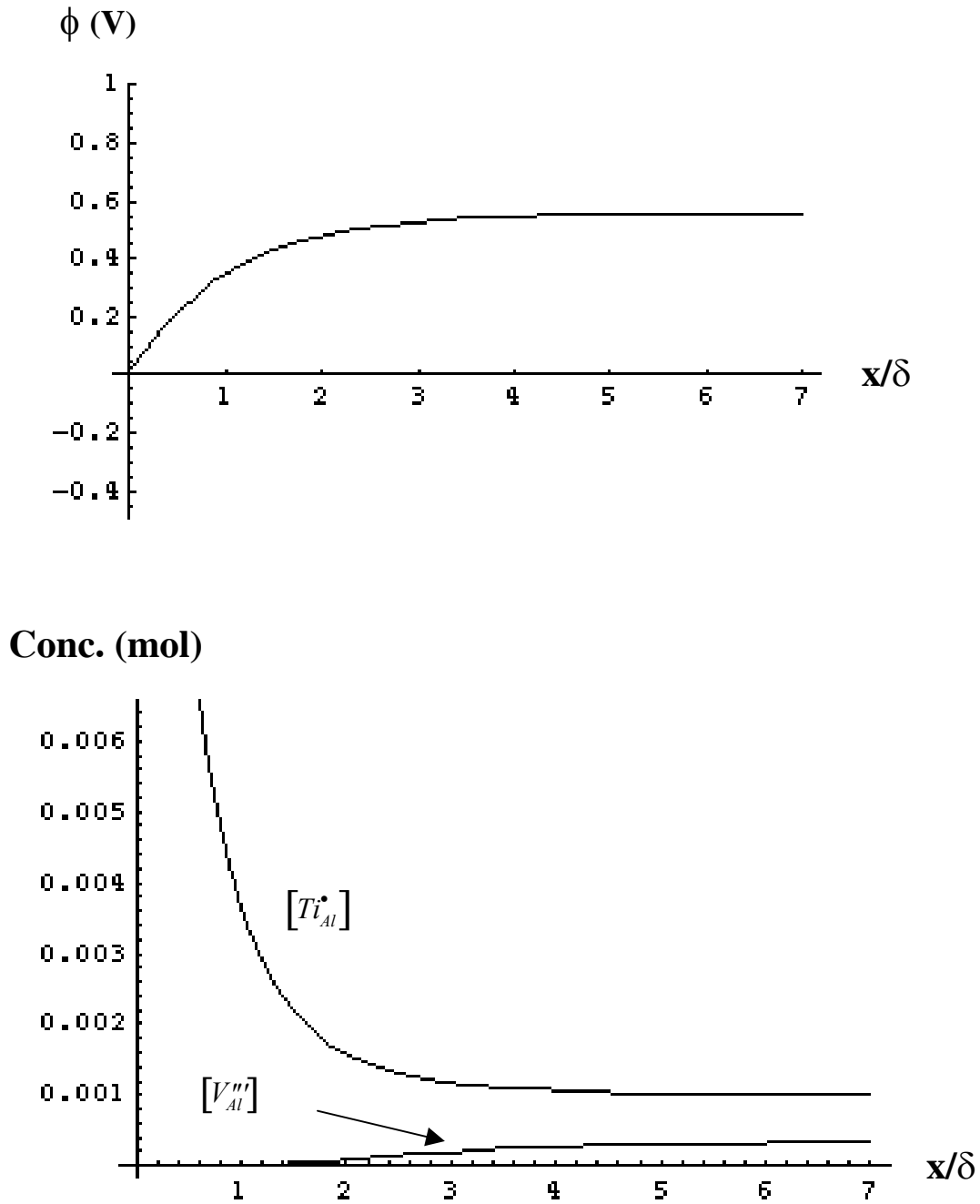


Figure 2.6. (a) Extrinsic space charge potential and (b) charged defect concentrations adjacent to grain boundary in 1000 ppm TiO_2 -doped Al_2O_3 at 1600°C. Grain boundary positioned at $x/\delta = 0$. ($\delta = 3$ nm at 1600°C).

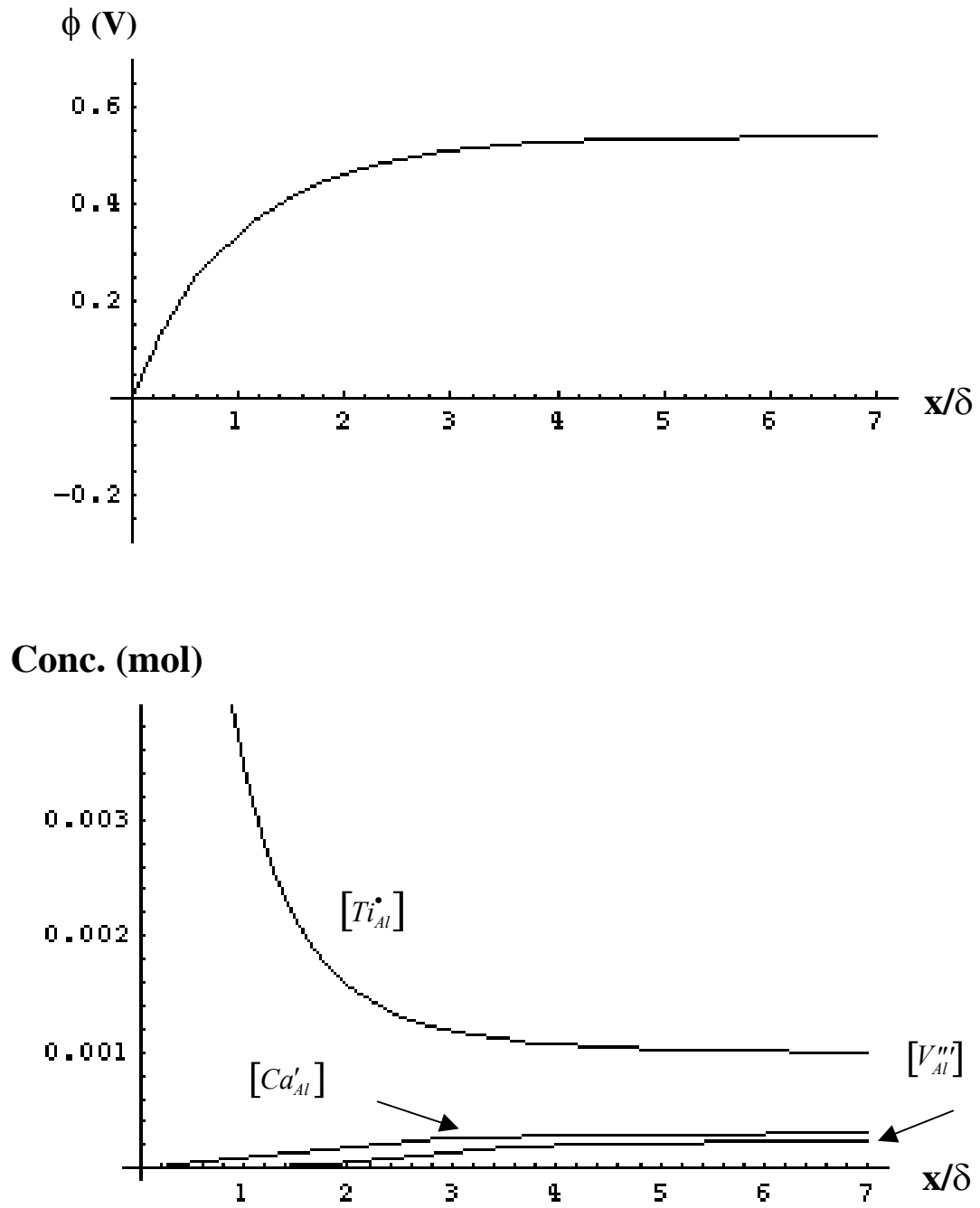


Figure 2.7. (a) Extrinsic space charge potential and (b) charged defect concentrations near a grain boundary in codoped (1000 ppm TiO_2 , 300 ppm CaO) Al_2O_3 at 1600°C.

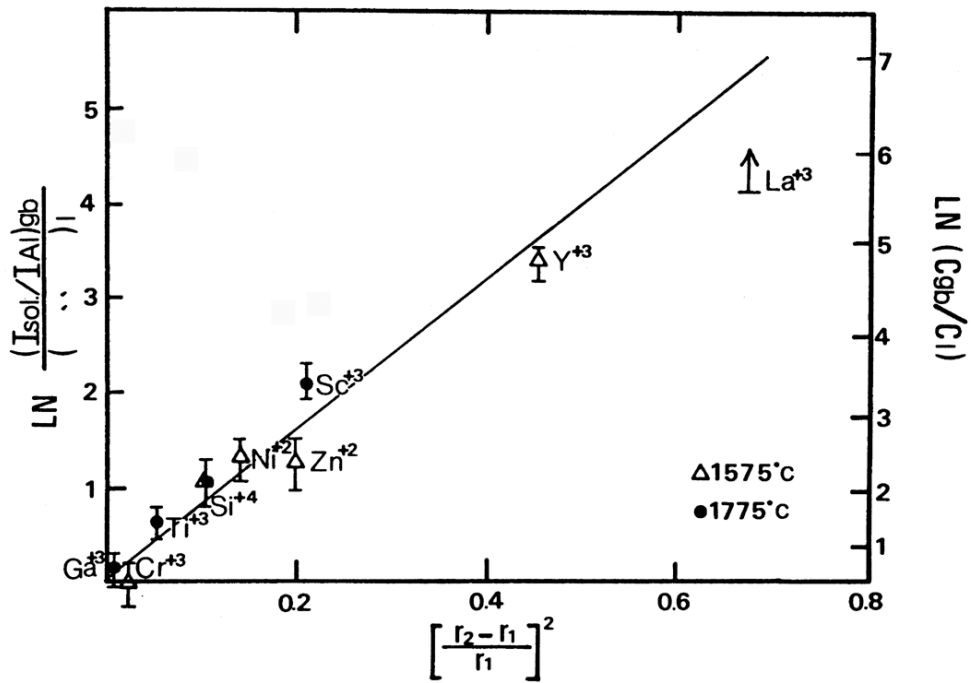


Figure 2.8. Plot of solute enrichment versus ionic misfit for various divalent and trivalent solutes in Al_2O_3 shows a linear fit, in agreement with Eq. 2.32. (From [70]).

MATERIALS AND METHODS

3.1. Bicrystal Fabrication

Bicrystal and tricrystal specimens have been fabricated using a solid state processing technique that exploits the tendency for larger grains to grow at the expense of smaller ones. Misoriented sapphire seed crystals are separated by a thin slab of fine-grained Ti-doped polycrystalline alumina. As the assembly is annealed at high temperature, the sapphire seeds -- acting as extremely large grains -- grow into the adjacent polycrystal by consuming its smaller grains. Continued growth of the misoriented seed crystals ultimately results in complete consumption of the polycrystalline layer, yielding a single grain boundary where the two growth fronts impinge.

Application of this templated grain growth technique to the fabrication of controlled-misorientation tilt and twist boundaries is briefly reviewed here. The reader is referred to Marks' work [1] for a more detailed description of specific processing procedures and viable grain boundary geometries.

3.1.1. Twist Boundaries

A basal twist boundary is formed by inserting a thin (100-200 μm) polycrystalline slab between two sapphire wafers that have been rotated about their common [0001] axis, as shown in Figure 3.1, and then diffusion bonding the sandwich structure in a hot press. The arrows in the figure indicate the growth direction of each sapphire seed crystal during the thermal treatment. A pure, symmetric twist boundary results when the two growth fronts collide to form a grain boundary that is perpendicular to the [0001] misorientation axis. Tilt components are introduced if the grain boundary plane is not exactly perpendicular to the rotation axis. The initial misorientation of the two sapphire seed crystals ultimately determines the orientation of the bicrystal grain boundary, while boundary chemistry will depend sensitively on the solute content of the polycrystalline alumina.

3.1.2. Tilt Boundaries

A schematic illustrating the various steps in tilt boundary fabrication is shown in Figure 3.2 [1]. To introduce a tilt misorientation, an [0001]-oriented sapphire substrate is cut in half along its length, and the cut piece is folded over onto the other half as shown in (a). A second cut is made at an angle θ to the first cut, as in (b), and the pieces are unfolded to produce the structure shown in (c). The result is two sapphire crystals misoriented by an angle 2θ . The two cut edges are now placed in contact with each other (forming a symmetric tilt boundary seed), and a doped polycrystal is placed on top, as in (d). The assembled structure is diffusion bonded in a hot press and subsequent anneals at high temperature are employed to grow each side of the tilt seed into the

polycrystal. Impingement of the parallel growth fronts results in formation of a tilt boundary, as shown in (e). If the boundary plane is parallel to [0001], then a pure tilt boundary is formed, otherwise the boundary is characterized by some finite amount of twist component. The chemistry of the tilt boundary is determined by the solute content of the polycrystalline alumina.

3.1.3. Tricrystal Fabrication

An alternate technique for the fabrication of controlled-misorientation grain boundaries incorporates three crystals rather than two. Tricrystal fabrication utilizes a combination of the different bicrystal processing steps mentioned above to form tilt and twist boundary structures in the same assembly. As shown in Figure 3.3a, this technique involves nothing more than a basic tilt boundary assembly (consisting of a tilt boundary seed and a thin polycrystalline slab) with an added [0001]-oriented sapphire substrate on top of the polycrystal. After diffusion bonding the stack structure, high temperature anneals will cause the (parallel) growth fronts emanating from the tilt boundary seed to collide with the growth front proceeding from the top crystal. The result, shown schematically in Figure 3.3b, is a tricrystal having three distinct grain boundaries – two of twist character, and one of tilt character – in the same sample. After processing, tricrystal samples are sectioned into three different pieces, each containing a distinct grain boundary for subsequent analysis in the TEM.

3.1.4. Polycrystalline Al₂O₃ Processing

Polycrystalline alumina compacts were made by Marks using various batches of alumina powder. Details concerning powder processing and subsequent densification to form polycrystalline material can be found in [1]. The current study incorporated only undoped or 1000 ppm (500 ppm cationic) TiO₂-doped Al₂O₃ powders that were later hot- or cold-pressed and/or sintered to near-theoretical density. Specific information concerning the processing of each bicrystal grain boundary examined in this work is included in Chapters 4 and 5 immediately before results from each sample are presented.

3.2. TEM Specimen Preparation

3.2.1. Twist Boundaries

Bicrystal twist boundaries were typically quite thick (1200-2000 μm depending on the exact structure), and therefore required extensive mechanical thinning for the preparation of electron-transparent foils for TEM analysis. A surface grinder was used to remove sapphire at a rate of 3-5 $\mu\text{m}/\text{min}$ down to about 500 μm total thickness – 250 μm on either side of the twist boundary. The bicrystals were then sectioned into rectangular pieces using a low-speed diamond saw. Dimensions of the cut pieces were nominally 2 mm x 10 mm x 500 μm (W x L x t). In this geometry, the grain boundary plane is perpendicular to the specimen thickness direction. Each piece was thinned from both sides down to 300 μm thickness using a 30 μm diamond-impregnated grinding plate, with the twist boundary situated half way between the top and bottom surfaces.

The specimen was then glued⁷ into an alumina tube (3 mm outer diameter) with the grain boundary plane parallel to the length of the tube, as shown in Figure 3.4a. After curing at 135°C, the tube was sectioned into thin discs with dimensions 3 mm x 500 μm (D x t) using a low-speed diamond saw. One side of each disc was polished to a 3 μm finish, while the other side was thinned (down to 120 μm thickness), dimpled (to 20 μm thickness) and then polished to a 3 μm finish⁸. These thin foils (nominally 15 μm thick at the dimple center) were then perforated using an Ar ion-mill operating at low incident angles (< 6 degrees) to maximize thin area for TEM analysis. The geometry of a perforated twist boundary sample is illustrated in Figure 3.4b. Samples were (indirectly) cooled with liquid nitrogen during the ion milling process to mitigate specimen heating and damage. The ion-milling process typically required 8-10 hours to generate a thin hole at the dimple center.

3.2.2. Tilt Boundaries

A surface grinder was used to thin processed tilt boundary bicrystals down to 400 μm thickness. Bicrystals were then sectioned into thin squares with nominal dimensions 2 mm x 2 mm x 400 μm (W x L x t). Here, the grain boundary plane is parallel to the specimen thickness direction, and the grain boundary does not extend all the way through the thickness. Additional material removal is achieved using a 30 μm diamond-impregnated plate to “expose” the tilt boundary on the top and bottom surfaces of each piece.

⁷ M-Bond 610 adhesive

⁸ The dimple was centered on the grain boundary plane; precise alignment was facilitated by optical microscopy.

The bottom side is now polished to a 3 μm finish, while the top side is dimpled to 20 μm thickness and polished to a 3 μm finish. The thin (15 μm at the dimple center) square foil is mounted onto a 3 mm-diameter slotted Cu grid (for mechanical support), cured at 135°C, and then perforated in a low-angle Ar ion mill.

3.3. Grain Boundary Studies in the TEM

The transmission electron microscope is a powerful tool for the study of grain boundary structure and chemistry, with modern instruments yielding chemical information at nanometer resolution and structural information resolved at close to one Angstrom. Quantitative and qualitative chemical microanalysis are afforded by spectroscopic techniques such as energy dispersive x-ray spectroscopy (EDS) and electron energy-loss spectroscopy (EELS), while studies of a material's atomic-, defect-, and micro-structure are made possible by electron diffraction and various imaging techniques. Despite the rigors of preparing thin, electron-transparent specimens, TEM-based studies are unrivaled in their ability to probe the structure and chemistry of buried, unexposed interfaces in materials.

Comprehensive reviews highlighting the basic principles of analytical electron microscopy, and the common microanalysis techniques such as EDS and EELS, can be found in [2, 3]. This section merely summarizes some of the salient experimental parameters pertinent to the present study.

3.3.1. Chemical Microanalysis

A Philips CM200 FEG-(S)TEM microscope was utilized for all studies of grain boundary chemistry. This microscope operates at 200 kV accelerating voltage and is capable of producing focused electron probes as small as one nanometer in diameter – an essential feature for the study of interfaces where chemistry can vary significantly over very short length scales. The microscope is equipped with a Gatan Imaging Filter housing an electron spectrometer for EELS studies, and a solid-state Si-Li detector with an ultra-thin beryllium window for x-ray detection. Quantitative studies of grain boundary chemistry were performed using EDS, while EELS was utilized for solute valence determination as well as qualitative studies of solute segregation.

3.3.1.1. Energy Dispersive Spectroscopy

High-energy incident electrons striking a thin TEM foil undergo inelastic collisions and cause the ejection of core-shell electrons from constituent atoms. Characteristic x-rays are emitted from the sample when valence electrons fill the vacancy left behind by the core ionization event. Energy dispersive x-ray spectroscopy makes use of these characteristic x-rays to identify and quantify specimen chemistry. A detector positioned immediately above the thin TEM specimen collects x-rays emitted from the thin foil, permitting plots of x-ray intensity versus energy.

Studies of grain boundary chemistry and solute segregation were performed in (S)TEM mode using a focused 1.0 nm electron probe. Grain boundaries were positioned in an edge-on condition in which the boundary plane was parallel to the incident beam direction. The focused probe was then stepped across (or sometimes along) the grain

boundary at discrete spatial intervals and an energy-dispersed x-ray spectrum was acquired for a period of approximately 15-30 seconds at each step. Computer-controlled positioning of the probe was facilitated by annular dark-field (ADF) imaging in (S)TEM mode. Images acquired in between spectra allowed for the correction of specimen drift, which can be quite significant in insulating materials exposed to strong beam currents.

Accurate quantification of elemental concentrations requires knowledge of specimen thickness at the exact locations where EDS spectra have been acquired. Specimen thickness was determined at those locations using low-loss EELS spectra, according to the technique described by Egerton [4].

Elemental composition can be quantified using the well-known Cliff-Lorimer equation [5],

$$\frac{C_A}{C_B} = k_{AB} \frac{I_A}{I_B} \quad (3.1)$$

where $C_{A/B}$ is the concentration of element A/B, $I_{A/B}$ is the characteristic x-ray intensity (above background) of element A/B, and k_{AB} is a proportionality factor. Equation 3.1 requires empirical determination of k-factors from standards of known composition to relate x-ray intensities to elemental compositions. Alternately, one can employ standardless techniques which rely heavily on principles of solid state physics to quantify elemental concentrations from measured x-ray intensities.

In the current study, quantification of grain boundary solute concentration(s) has been performed using a standardless technique included in the data acquisition software package (ESVision, EmiSpec Systems, Tempe, AZ)⁹. The accuracy of this technique in

⁹ Although k-factors were experimentally determined for Ti/Al, Si/Al and Ca/Al, efforts to perform standard quantification were complicated by a bug in the software package preventing calculation of

quantifying small elemental concentrations (less than 1.0 at. %) in Al_2O_3 has not yet been determined, but is an ongoing endeavor. Nonetheless, elemental quantification of ceramic oxides such as sapphire, mullite and titania using the standardless technique yielded results consistently within 5% error. Moreover, the main interest in the current study is to compare *relative* solute concentrations¹⁰, so the accuracy of absolute concentrations is not critical to useful interpretation of the data.

All quantitative EDS analyses utilized the major K_α peaks for Al, Ti, Si and Ca. Background subtraction of the relevant peaks in all spectra was performed using a third-order polynomial to remove continuum counts. Specimen thickness data was used to allow absorption correction for each spectrum, ensuring the “thin foil criterion” for quantitative microanalysis.

3.3.1.2. Electron Energy-Loss Spectroscopy

As mentioned previously, incident electrons striking a thin TEM foil undergo inelastic collisions and cause the ejection of core-shell electrons from constituent atoms. The energy lost through inelastic scattering of incident electrons by core shell electrons is characteristic of the ionized atom, producing sharp (ionization) edges in plots of electron intensity versus energy loss, which can be used to determine specimen chemistry. Additionally, because the ionization process can impart more than the critical energy needed to eject a core electron from the attraction of the nucleus, some core electrons leave the atom as electromagnetic waves [3]. Ensuing interactions between the

elemental ratios. A newer version of the software promises a solution to this problem, and should permit direct comparison of standard and standardless quantification.

¹⁰ These should be very consistent since all studies have been performed on the same microscope operating at fixed, known settings.

excited electron and neighboring atoms are manifested as intensity variations in the ionization edge. Known collectively as energy-loss near-edge structure (ELNES), these intensity fluctuations provide valuable information about the local atomic and electronic structure of the probed atoms. Changes in chemical valence and/or atomic coordination are reflected as subtle changes in the ELNES and energy threshold of the ionization edge. The energy loss spectrum can therefore be used to identify the elements and their valence states in the specimen.

The main application of EELS in the current investigation is to determine Ti valence in Ti-doped Al_2O_3 . Valence determination of $3d$ transition metal ions utilizes the L_2 and L_3 ionization edges, or “white lines”, which represent electron transitions to unoccupied $3d$ states. Because EELS probes the unoccupied density of states, the character of transition metal white lines is intimately related to d -band filling. Changes in titanium ion valence should therefore be reflected as changes in the Ti $L_{2,3}$ edge. Previous investigators have examined Ti $L_{2,3}$ edges from various Ti-containing ceramics and minerals [6-10], and qualitative differences in Ti $L_{2,3}$ ELNES have been discerned among the different bulk materials. These differences can be exploited for the unambiguous determination of Ti valence in other materials.

Reference Ti $L_{2,3}$ spectra were acquired from thin-foil TiO_2 (Ti^{4+}), CaTiO_3 (Ti^{4+}), and Ti_2O_3 (Ti^{3+}) standards at an energy dispersion of 0.1 eV/channel, and are shown in Figure 3.5. Since all three materials have octahedrally-coordinated Ti cations, variations in the Ti $L_{2,3}$ ELNES can be attributed directly to changes in Ti valence. The Ti $L_{2,3}$ edges from tetravalent Ti compounds TiO_2 and CaTiO_3 are qualitatively different than trivalent Ti_2O_3 as the L_2 and L_3 peaks are split in the former, reflecting the

symmetry of the $3d$ orbitals in these compounds [11]. Moreover, the edge onset in Ti_2O_3 occurs at a slightly lower energy (456 eV) than in the other two compounds (458.3 eV), as might be expected given their different $3d$ occupancies. These pronounced differences in the near-edge structure of Ti^{3+} - and Ti^{4+} -containing compounds is utilized in the following chapters to determine the valence of Ti solute at bicrystal grain boundaries in Al_2O_3 .

Prior to performing EELS studies on doped Al_2O_3 bicrystals, TEM foils were cleaned in an oxygen-argon plasma immediately before loading them into the microscope to remove surface hydrocarbon contamination. Parallel electron energy-loss spectra were acquired in STEM mode with a focused 1.0 or 1.2 nm electron probe. Positioning of the focused probe was facilitated by annular dark-field images acquired in STEM mode. After orienting the boundary to an edge-on position, a series of energy loss spectra were acquired using computer software to step the probe across the grain boundary at fixed spatial and temporal intervals (typically 1-2 nm per step, 2-5 seconds per acquisition). Drift-correction software was also utilized during these acquisitions to minimize the deleterious effects of specimen drift. Energy-loss spectra had to be acquired at an energy dispersion no greater than 0.1 eV/channel in order to resolve the peak-splitting of the Ti $L_{2,3}$ edge.

In some samples containing Ca and Ti solute at the grain boundary, quantitative measurements of Ca/Ti elemental ratios could be extracted from EELS spectra acquired at 0.3 eV/channel. To extract elemental counts, a power-law background was fit to each edge. Counts above the background were integrated up to 40 eV beyond the edge onset to yield the total elemental counts in a spectrum.

3.3.2. Structure Determination

The various elements of grain boundary structure, identified and described in Chapter 2, were assessed using a variety of techniques in the TEM. Conventional imaging and electron diffraction techniques allowed determination of grain boundary facet structure and crystal misorientation, respectively. Grain boundary dislocations were imaged and analyzed using two-beam imaging techniques – namely bright field (BF) and centered dark field (CDF) -- which utilize diffraction contrast to parameterize the dislocation strain field, ultimately permitting determination of dislocation Burgers vectors. And finally, grain boundary atomic structure was revealed using phase contrast imaging in a high-resolution transmission electron microscope (HRTEM) having 1.6 Å point-to-point resolution. Prior to imaging and diffraction work, TEM samples were coated with a thin layer of amorphous carbon in order to minimize charging and radiation damage in the microscope.

Chapter 3 References

1. R.A. Marks, "Fabrication and Thermal Grooving of Controlled Misorientation Grain Boundaries in Titanium-Doped and Undoped Alumina," Ph.D. Dissertation, University of California, Berkeley, 2002.
2. D.B. Williams, *Practical Analytical Electron Microscopy in Materials Science*. Mahwah: Philips Electron Optics Publishing Group, 1987.
3. D.B. Williams and C.B. Carter, *Transmission Electron Microscopy*. New York: Plenum Press, 1996.
4. R.F. Egerton and S.C. Cheng, "Thickness Measurement by EELS," in *Proceedings of the 43rd Annual Meeting of the Electron Microscopy Society of America*, G.W. Bailey, Editor. San Francisco Press, Inc.: San Francisco, 1985.
5. G. Cliff and G.W. Lorimer, "The Quantitative Analysis of Thin Specimens," *Journal of Microscopy* **103** 203-7 (1975).
6. N.J. Zaluzec, "Electron Energy Loss Spectroscopy in Advanced Materials," in *Transmission Electron Energy Loss Spectrometry in Materials Science*, M.M. Disko, C.C. Ahn, and B. Fultz, Editors. The Minerals, Metals and Materials Society: Warrendale, 1992.
7. R. Brydson, H. Sauer, and W. Engel, "Electron Energy Loss Near-Edge Structure as an Analytical Tool -- The Study of Minerals," in *Transmission Electron Energy Loss Spectrometry in Materials Science*, M.M. Disko, C.C. Ahn, and B. Fultz, Editors. The Minerals, Metals and Materials Society: Warrendale, 1992.
8. M.T. Otten, B. Miner, J.H. Rask, and P.R. Buseck, "The Determination of Ti, Mn and Fe Oxidation States in Minerals by Electron Energy-Loss Spectroscopy," *Ultramicroscopy* **18** 285-290 (1985).
9. M. Sankararaman and D. Perry, "Valence Determination of Titanium and Iron Using Electron Energy Loss Spectroscopy," *Journal of Materials Science* **27** 2731-2733 (1992).
10. S. Suzuki, M. Tomita, S. Okada, and H. Arai, "Valence Analysis of Transition Metal Ions in Spinel LiMnMO_4 ($M=\text{Ti, V, Mn, Co}$) by Electron Energy Loss Spectroscopy," *Journal of Physics and Chemistry of Solids* **57** (12) 1851-1856 (1996).
11. R. Brydson, H. Sauer, W. Engel, J.M. Thomas, E. Zeitler, N. Kosugi, and H. Kuroda, "Electron Energy Loss and X-Ray Absorption Spectroscopy of Rutile and Anatase: A Test of Structural Sensitivity," *Journal of Physics: Condensed Matter* **1** 797-812 (1989).

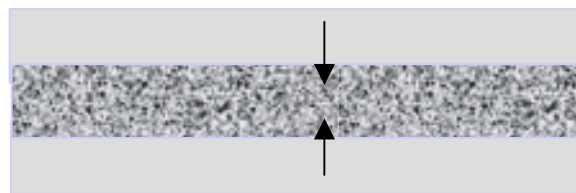
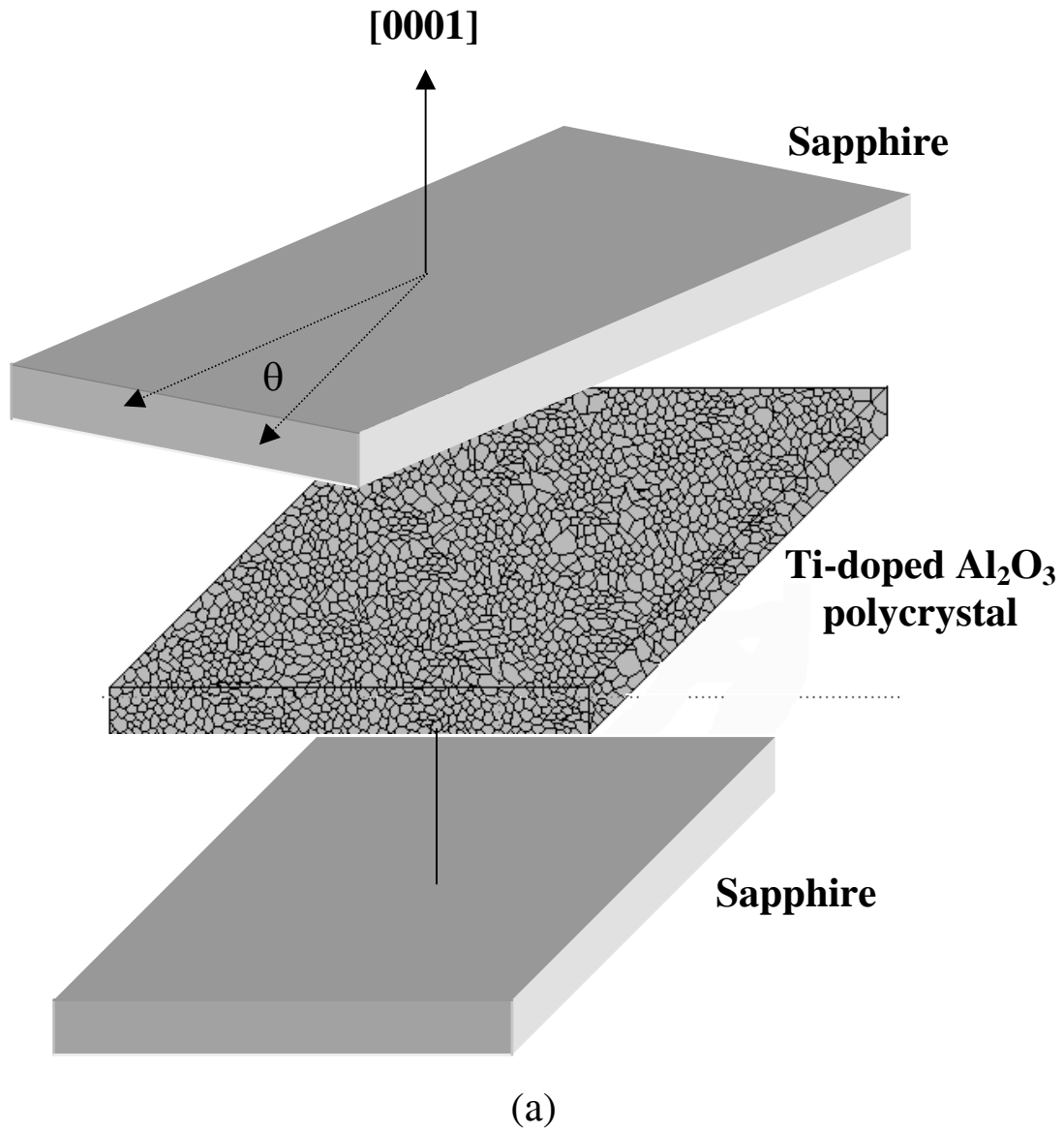


Figure 3.1. Formation of a basal twist boundary by rotation of two sapphire crystals about their common $[0001]$ axis. In (b), the arrows indicate growth directions of the seed crystals when viewed in cross-section.

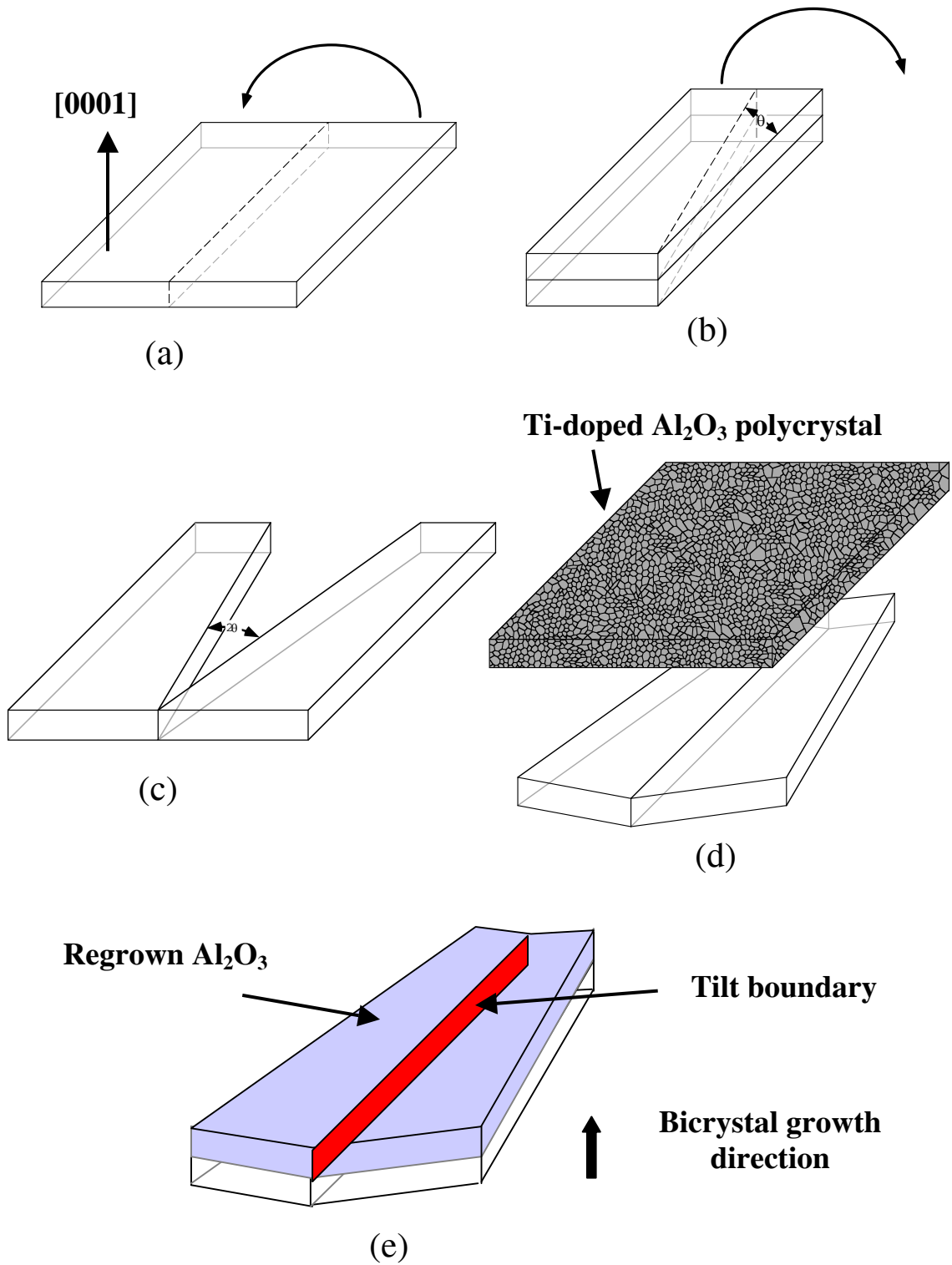


Figure 3.2. The various steps involved in bicrystal tilt boundary fabrication via templated grain growth. (Drawings courtesy of Marks [1]).

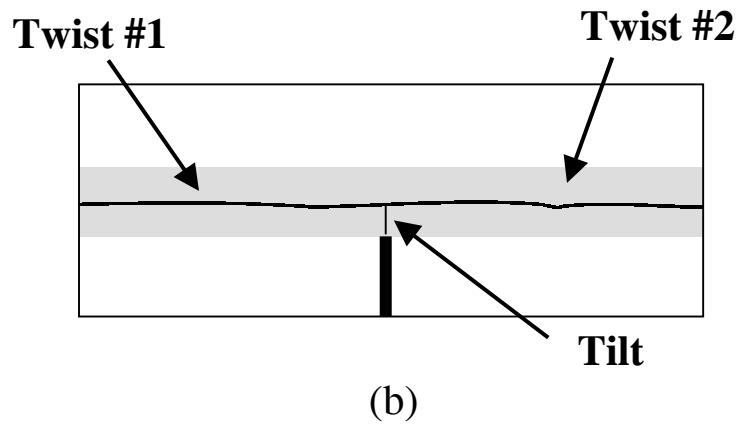
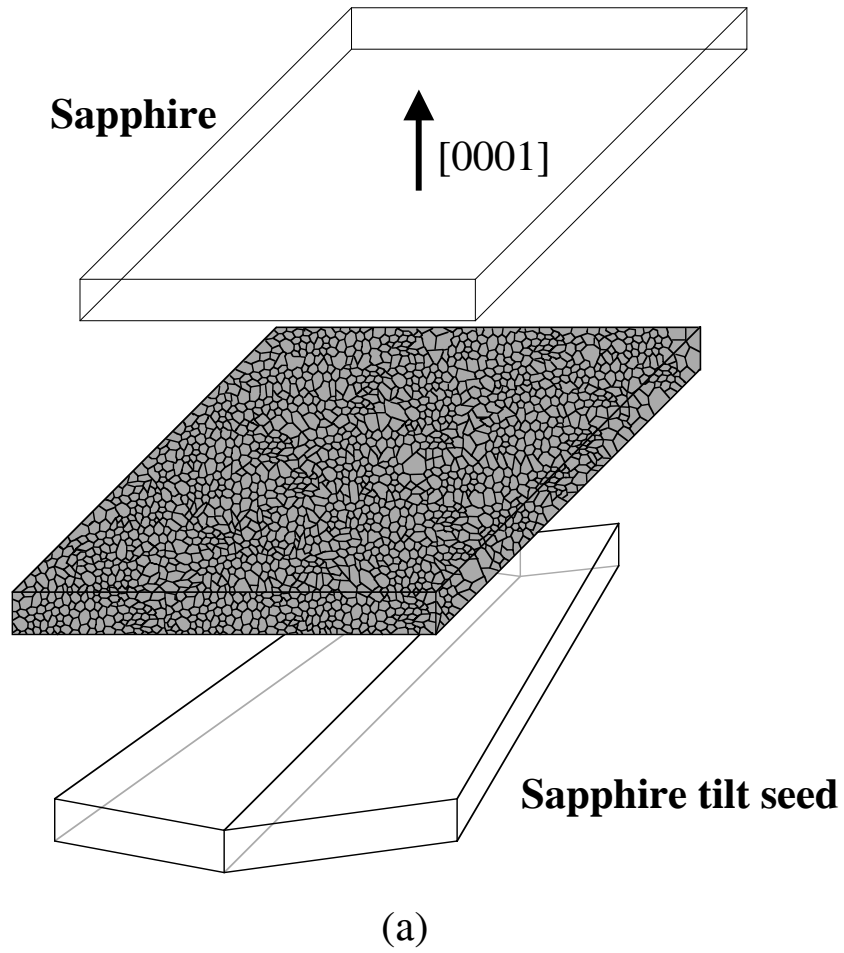


Figure 3.3. Fabrication of a tricrystal results in two distinct twist boundaries (having different character) and a tilt boundary.

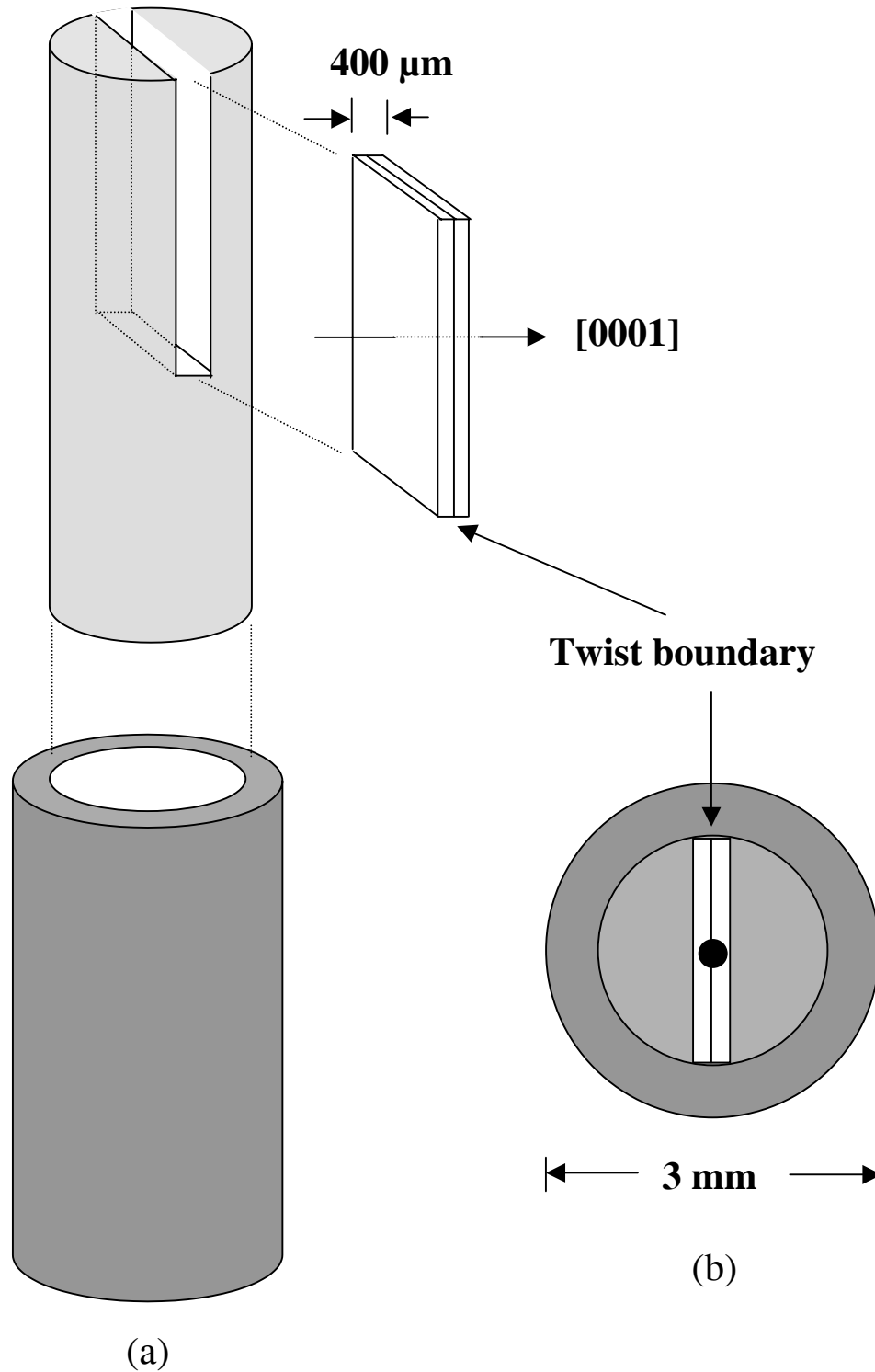


Figure 3.4. (a) TEM specimen preparation of bicrystal twist boundaries using an alumina tube to position and support the boundary. (b) Schematic of an ion-milled sample, with the perforation centered on the grain boundary.

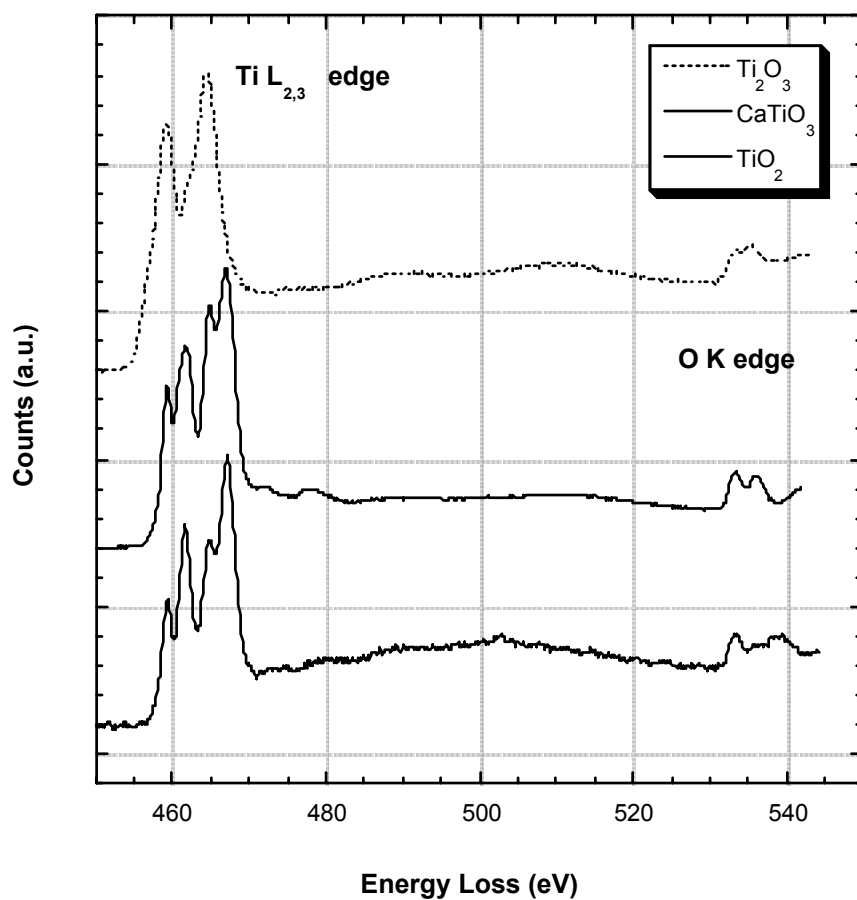


Figure 3.5. Comparison of energy-loss spectra from various oxides with octahedrally-coordinated Ti cations. Variations in Ti L_{2,3} edge structure are due to differences in Ti valence.

Chapter Four

THE STRUCTURE AND CHEMISTRY OF BASAL TWIST BOUNDARIES

4.1. Low-Angle Basal Twist Boundary (S3)

4.1.1. Processing Conditions

This basal twist boundary represents one of the first efforts to fabricate bicrystals using the directed assembly growth process [1]. The alumina powder was doped with 500 ppm (cationic) Ti and cold pressed in air to form a polycrystalline compact. Two sapphire crystals were misoriented by nominally 2.0° about [0001] and separated by a thin polycrystalline slab. The stack was diffusion bonded at elevated temperature in a reducing environment for an unknown period of time. A 24-hour growth anneal in air at 1600°C was followed by an anneal in argon at the same temperature, for the same duration. Details regarding the exact specimen cooling rate are not available, although furnace-cooling is assumed.

4.1.2. Grain Boundary Structure

Convergent beam electron diffraction (CBED) was performed on the grain boundary to determine the misorientation angle between the two crystals. Analysis of the shift in Higher Order Laue Zones (HOLZ) from the CBED patterns reveals a small misorientation angle of 0.3° .

Cursory examination at low-magnification in the TEM reveals that the boundary plane is not straight, but meanders significantly along its length. Changes in boundary plane are gradual and do not occur via micro-scale faceting.

Figure 4.1 shows a conventional TEM image of the low-angle twist boundary. The left grain has been oriented in the $[10\bar{1}0]$ zone axis, as evidenced by the inset diffraction pattern; its (0001) plane is parallel to the boundary plane. Features exhibiting strong contrast can be observed with periodic spacing (158 ± 10 nm) along the grain boundary plane. These features could be indicative of contrast associated with the strain fields of grain boundary dislocations, or might also be attributed to small precipitates that have formed heterogeneously at the twist boundary, or could perhaps stem from both.

Diffraction contrast imaging of the twist boundary region was performed in an effort to resolve the grain boundary dislocation structure. Two diffraction contrast images of the inclined grain boundary are shown in Figures 4.2 and 4.3. Included with each image is a stereographic projection for the relevant zone axis, showing the crystallographic orientations of the operative \mathbf{g} -vector and the (0001) plane. An hexagonal array of dislocations can be seen in the bright-field (BF) image of Figure 4.2. The average spacing between the primary dislocations (arrowed) is measured as 160 ± 15 nm. In the centered dark-field (CDF) image of Figure 4.3, however, the same dislocation set shows only residual contrast because an invisibility criterion ($\mathbf{g} \cdot \mathbf{b} = 0$) has been satisfied. In both figures, the orientation of the boundary plane in the image closely matches that of the basal plane on the stereographic projection, confirming an (0001) grain boundary plane for the bicrystal. Moreover, similarities in spacing between the

periodic grain boundary dislocations imaged in Fig 4.2 and the contrast features of Fig. 4.1 confirm that the dislocations are, in fact, the structural features giving rise to the contrast.

The magnitude of the dislocation Burgers vector $|\mathbf{b}|$ can be predicted from Frank's equation for a low-angle grain boundary,

$$|\mathbf{b}| = D \sin \theta \quad (4.1)$$

since the misorientation angle θ and dislocation spacing D are both known. Equation 4.1 predicts a Burgers vector magnitude of 8.25 Å for this low-angle boundary.

Experimental determination of the primary¹¹ dislocation Burgers vector has been achieved by applying the $\mathbf{g} \cdot \mathbf{b}$ visibility criterion to various dislocation images acquired with different \mathbf{g} -vectors. Table 4.1 shows a compendium of visibility conditions for a series of diffraction-contrast images of the primary grain boundary dislocations. A $\langle 10\bar{1}0 \rangle$ -type Burgers vector is consistent with all visibility/invisibility data measured for the primary dislocations. The magnitude of a $\frac{1}{3}[10\bar{1}0]$ Burgers vector is 8.24 Å, consistent with predictions from Frank's rule for this sample.

Finally, neither diffraction contrast nor phase contrast imaging revealed the presence of any second phases at the grain boundary or in the bulk of the grains.

4.1.3. Grain Boundary Chemistry

A series of EDS and EELS line profiles were acquired along (parallel to) and across (perpendicular to) the low angle twist boundary to examine spatial variations in

the grain boundary chemistry. Figure 4.4 shows qualitative results from an EELS line profile performed along the grain boundary (a), and the accompanying ADF-STEM image showing where the profile was acquired (b). The line profile shows integrated Ti counts as a function of position along the twist boundary, where three distinct peaks in Ti intensity can be seen. The spacing between the first and second peaks is 150 nm, while the spacing between the second and third peaks is 149 nm. The source of the Ti peaks is believed to be the cores of primary grain boundary dislocations, as revealed by the ADF-STEM image, which shows three regions of strain contrast equally-spaced along the boundary.

Attempts to acquire EDS line profiles along the grain boundary for quantitative analysis were ultimately thwarted by specimen drift. The longer acquisition times (20-30 seconds) required for quantitative EDS are not amenable to insulating materials, whose charge build-up leads to pronounced specimen displacements under the electron beam. Here, software routines to correct specimen drift are not always useful as the drift can be non-linear over such long acquisition times. Moreover, line profiles parallel to the grain boundary accommodated little, if any, specimen drift normal to the boundary plane before the probe deviated from the region of interest.

EDS line profiles *across* the grain boundary were more feasible, and ultimately permitted quantitative analysis of grain boundary chemistry near dislocation cores, and in non-dislocated (perfect) grain boundary segments. A characteristic concentration

¹¹ For a fixed misorientation, dislocations with larger spacing must necessarily have higher-magnitude Burgers vectors; “primary” dislocations are those with the largest Burgers vector, typically a perfect lattice displacement vector.

profile from a perfect boundary region is presented in Figure 4.5a. Both Ti and Ca¹² are observed to segregate to the grain boundary, reaching peak boundary concentrations of approximately 0.31 and 0.16 atomic percent, respectively, while showing no measurable concentrations far away (≈ 50 nm) from the grain boundary in either grain.

Figure 4.5b shows a representative concentration profile obtained through a primary dislocation core. A dramatic increase in Ti concentration is observed in the plane of the grain boundary relative to the surrounding grains. Segregation of Ca is also observed, though not as strongly as Ti, and only slightly more concentrated than at the perfect boundary. No other solute species were seen to segregate appreciably to the grain boundary region. These results were reproduced several times from different segments of the grain boundary, and always through the primary dislocation cores detectable in the ADF-STEM image.

Due to their small Burgers vectors, the secondary grain boundary dislocations could not be discerned in edge-on imaging of the boundary. Line profiles through these secondary dislocations were therefore not feasible.

Solute profiles at the different grain boundary sites were also examined using EELS line scans. Figure 4.6a shows solute concentration data from the perfect grain boundary, while Figure 4.6b shows concentration data obtained from a grain boundary dislocation. The elemental ratio Ca/Ti has been determined for each point in the line profiles, and average values for the grain boundary region are shown in Table 4.2 for the two defect sites. The grain boundary dislocation exhibits a much smaller Ca/Ti elemental ratio (0.21) than does the perfect region of grain boundary (0.43). These results are

¹² Though not an intentionally-added dopant, Ca exists in minor quantities (≥ 5 ppm) in most all alumina

consistent with calculated Ca/Ti ratios from EDS data, also shown in Table 4.2, so both techniques indicate greater relative amounts of Ti in the dislocation core region than at non-dislocated portions of the boundary.

Electron energy loss spectra were acquired from the grain boundary to directly determine Ti valence. A typical spectrum showing the Ti $L_{2,3}$ edge is shown in Figure 4.7, along with edges acquired from other Ti-containing compounds with known Ti valence, and having octahedral cation coordination. Comparison of the different spectra reveals that Ti^{4+} is the dominant species in this bicrystal twist boundary.

Finally, the chemical width of the grain boundary -- the distance over which a discernable chemical signal can be detected above background -- can be more accurately measured from these EELS spectra, since the step size is much smaller than for EDS profiles. The grain boundary Ti signal appears to have a spatial width of 12 nm, as measured from Figure 4.6b, which implies a space charge region extending 60 Å on either side of the grain boundary.

4.1.4. Evidence for Charged Grain Boundary Dislocations

Results from twist boundary S3 show that both Ca^{2+} and Ti^{4+} segregate to the grain boundary. However, the measured Ca/Ti ratio is smaller at the dislocated regions than at the “perfect” boundary, implying that Ti^{4+} solute has a greater preference to segregate to the grain boundary dislocations than does Ca^{2+} . Since Ti^{4+} ($r = 0.67$ Å) is significantly smaller than Ca^{2+} ($r = 0.99$ Å), excess Ti at the dislocation cores cannot be attributed to elastic misfit. Rather, the mechanism responsible for variations in Ca/Ti at

powders. It is known to be a strong segregant to surfaces and grain boundaries due to its large size

different grain boundary sites probably relates to the ionic character of Al_2O_3 , and can be explained with reference to space charge theory.

When Ti^{4+} substitutes for Al^{3+} , it introduces a positive charge into the lattice, while substitutional Ca^{2+} cations behave as negatively-charged defects in Al_2O_3 . In a heavily donor-doped material, grain boundaries and dislocations should acquire an overall negative charge, according to predictions of space charge theory discussed in Chapter 2. Segregation of donor impurities to these sites occurs in an effort to neutralize their intrinsic charges. Indeed, the high concentration of Ti^{4+} seen at this twist boundary is consistent with those predictions. Pronounced segregation of Ca^{2+} is not anticipated by space charge calculations, but as discussed later, probably stems from elastic misfit of the larger Ca^{2+} cations substituting for smaller Al^{3+} . Inferences regarding the magnitude of the intrinsic grain boundary (or dislocation) charge can be made from the measured $\text{Ca}^{2+}/\text{Ti}^{4+}$ concentration ratio at each site. The present results therefore indicate the dislocation core is more negatively charged than the perfect boundary and attracts the Ti^{4+} preferentially in an effort to achieve local charge neutrality.

Why might the perfect grain boundary have a charge that's different from the dislocated region? One possible explanation is that the vacancy formation energies differ between the two defect sites. If, in fact, the perfect grain boundary has a less negative intrinsic charge, then a smaller aluminum vacancy formation energy is anticipated at the grain boundary core relative to the dislocation core, in accordance with Eq. 2.25.

Investigators have long hypothesized that vacancy formation energies in ionic materials should vary from one defect site to another, but to the author's knowledge, only one study has ever experimentally verified and quantified a difference. Ikeda and colleagues inferred changes in defect formation energies as large as 1 eV between grain boundaries in a single polycrystalline sample of TiO_2 [2]. Links between defect formation energies and fundamentally different defect sites are expected based on the defect's ability to create (or destroy) vacancies. A more efficient cation vacancy source, in which the cation vacancy formation energy is quite low, should acquire a greater (intrinsic) positive charge in an undoped crystal, and a lesser (intrinsic) negative charge in a donor-doped crystal, than a defect site having a larger cation vacancy formation energy. In this particular situation, it is not immediately clear why the grain boundary core acts as a more efficient vacancy source than the dislocation core, but presumably the open structure of the boundary is responsible at some level.

To explain the variation in measured Ca/Ti ratio at the different grain boundary sites, we might also consider the possibility that dislocation cores serve as nucleation sites for precipitates which never actually grow beyond small nuclei. However, if the solute decorating the dislocation cores does in fact represent stable nuclei, then the observed Ca/Ti ratio should be consistent with an anticipated precipitate phase. Unfortunately, no Al_2O_3 - TiO_2 -CaO ternary phase diagram exists to suggest possible equilibrium precipitate phases. The only known ternary phase is $\text{CaTiAl}_2\text{O}_6$, with a Ca/Ti ratio of unity. Results from chemical microanalysis at the dislocation cores suggests that the Ca/Ti ratio is significantly less than one, meaning that a stoichiometric precipitate phase does not appear to be nucleating at the core.

4.2. Medium-Angle Basal Twist Boundary (15b)

4.2.1. Processing Conditions

Polycrystalline alumina compacts were made by cold-pressing 500 ppm (cat. %) Ti-doped Al_2O_3 powder, followed by firing at 1400°C for three hours in air. The polycrystal was placed atop a sapphire tilt seed (nominally 40° misorientation about $[0001]$), and then this layered structure was sandwiched between two sapphire crystals. This stack arrangement, the precursor for a tricrystal structure, was diffusion bonded at 1250°C for 15 hours at 15 MPa. A series of anneals to grow the grain boundaries ensued: 1600°C for 40 hours (vacuum), 1600°C for 115 hours (argon), 1700°C for 12 hours (vacuum), 1800°C for 48 hours (vacuum), and 1850°C for 15 hours (argon). At this point, the tricrystal was cut in half along its length to yield two tricrystal pieces with (nominally) the same misorientations. One of the samples was given a final anneal at 1600°C for 40 hours in air, then air-quenched to room temperature at a rate of approximately $800^\circ\text{C}/\text{sec}$.

4.2.2. Grain Boundary Structure

The misorientation angle was determined using two different techniques. A rough estimate was attained using $[0001]$ Laue back reflection patterns acquired individually from the two crystals forming the twist boundary. The misorientation angle, calculated from the relative rotation of their Laue patterns, was found to be $11.3 \pm 2^\circ$. A more precise measure of misorientation is yielded by the Johari and Thomas technique

which makes use of Kikuchi electron diffraction in the TEM [3]. Analysis using this technique suggests a misorientation angle of 12.4° , on the cusp between a low-angle and high-angle grain boundary.

Figure 4.8, a conventional TEM image of the twist boundary viewed edge-on, reveals no obvious faceting of the boundary plane. Diffraction data (inset in figure) is used to position the [0001] crystallographic direction, from which it is determined that the boundary plane is a few degrees off of the basal plane. Diffraction data indicates that neither grain is oriented with its basal plane parallel to the grain boundary. Rather, the grain boundary plane is roughly 3 to 8 degrees off of the basal plane of both crystals. Slight changes in the grain boundary plane are observed along its length, but these do not occur via faceting.

Diffraction contrast imaging of the inclined grain boundary using several independent **g**-vectors produced no evidence of grain boundary dislocations. If dislocations do exist in the grain boundary plane, their spacing may be too fine to resolve with centered dark field imaging.

No continuous or discrete grain boundary phases were observed in this specimen.

4.2.3. Grain Boundary Chemistry

Chemical microanalysis of the twist boundary region reveals strong segregation of Ti solute and relatively weak Ca segregation, as shown in Figure 4.9a. Peak grain boundary Ti concentrations are just over 1.0 atomic %, while Ca concentrations reach approximately 0.25 atomic %. These results were obtained from a region where the grain boundary plane was approximately 8° off of the basal plane of one of the crystals;

an exact grain boundary plane was not determined. The grain boundary chemical width is consistently between 15 and 17 nm, as shown in Figure 4.9b for Ti measured in an EELS line profile across the grain boundary.

Electron energy-loss studies to determine Ti valence indicate the presence of both Ti^{3+} and Ti^{4+} in the grain boundary vicinity, although Ti^{3+} appears to be the majority species. The Ti $L_{2,3}$ edges of two spectra acquired near the grain boundary are presented in Figure 4.10a. Both spectra have been aligned (in energy) to the onset of the O K edge at 532 eV. Spectrum A (solid line) was obtained from the grain boundary near a thin edge, immediately adjacent to a perforation in the TEM foil. This spectrum does not exhibit any structural features (such as spin-orbit splitting) in the Ti $L_{2,3}$ ELNES that are characteristic of octahedral Ti^{4+} cations. Spectrum B (dashed-line) was also acquired on the grain boundary, but many tens of nanometers away from the edge in a slightly thicker region. Here, stunted or frustrated peak-splitting is faintly discerned. Figure 4.10b compares Spectrum A to a representative spectrum from Ti_2O_3 . The two main peaks are closely matched in energy, shape and relative intensity, suggesting a match to Ti^{3+} . Figure 4.10c compares Spectrum B to a representative TiO_2 spectrum. Despite significant noise in the former, one can see that the relevant peaks in the Ti $L_{2,3}$ ELNES seem to be shifted to lower energies in the twist boundary spectrum relative to the TiO_2 edge. These results suggest that predominantly Ti^{3+} exists near the grain boundary at the specimen edge, while a combination of Ti^{3+} and Ti^{4+} exists at the boundary further away from the edge. Attempts to measure Ti valence at distances very far removed from the edge (i.e. hundreds of nanometers) were unsuccessful due to a steep gradient in specimen thickness.

Results similar to these, in which Ti valence is observed to vary over relatively short length scales (tens of nanometers), have been found in other quenched bicrystal samples as well. The prevalence of Ti^{3+} is quite surprising given the bicrystal's lengthy final anneal in air at 1600°C – conditions which should hasten conversion to oxidized Ti^{4+} . Possible explanations for prevalence of Ti^{3+} will be discussed later in this chapter.

4.3. High-Angle Basal Twist Boundaries (12a and 12b)

4.3.1. Processing Conditions

Titanium-doped (500 ppm cat.) polycrystalline alumina compacts were cold-pressed and fired as described previously. A polished polycrystalline slab was placed atop a sapphire tilt seed (with nominal misorientation of 40°), and a sapphire crystal was positioned atop the polycrystalline layer to yield the scaffold for a tricrystal specimen. Sapphire crystals were oriented to produce nominal 30° basal twist boundaries (where $[2\bar{1}\bar{1}0] // [10\bar{1}0]$) on either side of a 40° basal tilt boundary. The stack was diffusion bonded at 1250°C for 15 hours at 15 MPa, followed by a series of anneals to grow the boundaries through the doped polycrystal: 1250°C for 25 hours (air), 1400°C for 15 hours (air), 1600°C for 32 hours (air), 1575°C for 36 hours (air), 1700°C for 40 hours (vacuum), 1800°C for 36 hours (vacuum), 1850°C for 8 hours (vacuum), 1850°C for 24 hours (argon), 1900°C for 16 hours (argon), and 1600°C for 8 hours in vacuum. The tricrystal was cut in half along its length, and both sections were given one final anneal at 1600°C for 50 hours in air – a step intended to convert all Ti^{3+} to Ti^{4+} . One of the tricrystals (12a) was kept in the furnace and cooled at a rate of $30^\circ\text{C}/\text{min}$ to room temperature. The other section (12b) was quenched in air to room temperature at a rate

of 800°C/sec. Results from twist boundaries of each piece are presented separately below.

4.3.2. Furnace-Cooled Boundary (12a)

4.3.2.1. Grain Boundary Structure

A high-resolution phase-contrast image of the grain boundary is presented in Figure 4.11. Although both crystals are oriented close to low-index zone axes, the grain boundary plane is not perfectly parallel to the viewing direction (i.e. it is not in an “edge-on” viewing condition), indicating a slight inclination of the grain boundary relative to (0001). The fringes resolved in the left, $[10\bar{1}0]$ -oriented crystal represent the (0003) planes with interplanar spacing 4.33 Å. A basal (0001) boundary plane should be parallel to these (0003) fringes, but as the figure shows, the trace of the boundary plane deviates from (0001) by about $8.0 \pm 0.6^\circ$ in this region of the boundary.

Kikuchi diffraction patterns were utilized to quantify the exact misorientation of the two crystals forming the twist boundary. To simplify calculation of the misorientation angle, it has been assumed that the crystals are crystallographically related by a pure twist rotation about their common [0001] directions. Analysis of the diffraction data yields a misorientation angle of $29.4 \pm 0.3^\circ$.

Figure 4.12 shows conventional TEM micrographs of the twist boundary viewed edge-on. Diffraction data has been used to determine the proper orientation of the (0001) basal plane and $\langle 0001 \rangle$ crystallographic directions. The image clearly demonstrates that segments of the grain boundary have faceted off of the primary (0001) grain boundary plane. Measurements from TEM images indicate a facet angle of $8.6^\circ \pm$

0.5° away from the basal plane. Analysis over an extended length of grain boundary (several μm) confirms that these facets occur at multiple intervals along the grain boundary, though not necessarily with periodic spacing.

Close inspection of Figure 4.12 reveals isolated regions of contrast along the off-basal facets. Diffraction-contrast imaging of the inclined grain boundary reveals the presence of small ($\approx 10\text{ nm}$) precipitates in the same general area of the off-basal facet, as shown in Figure 4.13. These precipitates appear to be faceted, and do not extend through the entire thickness of the specimen. Other off-basal facets of the grain boundary were decorated with small precipitates like these, but precipitate formation was not observed anywhere along the basal plane. Dislocations were not detected at any portion of the off-basal facet.

Further examination of the twist boundary revealed one very large (100 nm), highly-faceted precipitate located in a different part of the boundary, and shown in Figure 4.14a. Adjacent to it is a smaller (40 nm) faceted precipitate. Although both precipitates have formed on the off-basal facet, the precipitates themselves have faceted along the basal planes of the matrix phase, as seen in the phase-contrast image of Figure 4.14b. Convergent beam electron diffraction patterns were acquired from the larger precipitate (see Figure 4.14c) using a focused nanometer probe. Structural analysis indicates that the large precipitate is the rutile (tetragonal) phase of TiO_2 , oriented with its c-axis parallel to the $[2\bar{1}\bar{1}0]$ and $[10\bar{1}0]$ zone axes of the sapphire bicrystal grains. The orientation relationship between precipitate and matrix is given (for one of the crystals) as

$$(100)_{\text{rutile}} // (0001)_{\text{sapphire}}$$

$$[001]_{\text{rutile}} // [10\bar{1}0]_{\text{sapphire}}$$

Chemical data presented in the following section confirms the identity of the precipitate as TiO_2 .

Periodic grain boundary dislocations, such as those seen in the low-angle twist boundary, were not observed in this specimen. Application of Frank's rule to a pure twist boundary with $\approx 30^\circ$ misorientation predicts a periodic dislocation spacing of 8-16 Å, assuming a dislocation Burger's vector magnitude of 4-8 Å. Such fine spacing between dislocations is not easily resolved in conventional diffraction-contrast imaging modes, and may be the reason why dislocations were not detected here.

4.3.2.2. Grain Boundary Chemistry

EDS line profiles were acquired from the different grain boundary facets to investigate the effect (if any) of grain boundary plane on the distribution and concentration of segregated solute species. Figures 4.15a and 4.15b show representative EDS line profiles obtained from the basal and off-basal¹³ grain boundary facets, respectively. The presence of Si solute on both grain boundary facets is immediately recognized from these plots¹⁴. Variations in grain boundary solute concentrations are quite dramatic between the two boundary facet planes. On the basal facet, Si is by far the most prevalent solute, with peak concentrations approaching 1.0 atomic percent, while peak Ti and Ca concentrations are significantly lower at 0.50 and 0.38 at. %, respectively.

¹³ The off-basal profile was acquired tens of nanometers away from any small precipitates occupying the boundary plane.

respectively. The situation is quite different for the off-basal facet, however, where strong Ti segregation is observed with significantly less Si segregation (peak concentrations of 0.94 and 0.33 at. %, respectively). The peak Ca concentration is measured as 0.30 at. %, similar to its peak value on the basal facet.

Measurements of solute segregation to the different facet planes consistently showed dramatic changes in Si and Ti concentrations between the two facets. Although absolute solute concentrations measured quantitatively from EDS spectra were somewhat variable, the normalized solute concentrations were very consistent for a given facet plane. Here, the normalized concentration of solute i is defined as

$$C_{norm}^i = \frac{C_i}{C_{Si} + C_{Ti} + C_{Ca}} \quad (4.2)$$

where C_i is the (absolute) peak grain boundary concentration of solute i as measured quantitatively from EDS spectra. Table 4.3 shows the normalized solute concentrations measured for each solute as a function of the facet plane. An average 50% decrease in Si concentration is observed between the basal and off-basal facet, while Ti concentration increases by more than 66%. The Ca concentration is not significantly affected by boundary facet type.

Line profiles were acquired through the small precipitates decorating the off-basal facets to determine precipitate chemistry. Figure 4.16 illustrates that these precipitates are strongly enriched in Ti solute over many nanometers (there is no spike or Gaussian distribution to the concentration), with very little Ca or Si enrichment. In fact, the Ca and Si concentrations are unchanged with respect to their values for the off-basal

¹⁴ Silicon, like Ca, is a common residual impurity in alumina powders. Although not detected in previous bicrystal samples, its presence in this specimen can be attributed to a different batch of alumina powder

grain boundary facet. Chemical profiles from these precipitate suggest a Ti-rich second-phase that is approximately 15-20 nm wide, and which does not occupy the entire specimen thickness (i.e., bicrystal grain boundary exists above and below the precipitate). In light of this limited chemical data, the small precipitates are assumed to be TiO_2 , though in the absence of any structural data, an exact phase cannot be concretely determined.

Microanalysis data from one of the large grain boundary precipitates, identified previously from structural data as the rutile phase of TiO_2 , is presented in Figure 4.17. The measured titanium and oxygen concentrations are approximately 33 and 66 at. %, respectively, consistent with a TiO_2 precipitate phase.

Finally, Figure 4.18 shows Ti $L_{2,3}$ edges of electron energy loss spectra acquired from a large rutile precipitate, a small precipitate, and a region of the off-basal facet free of precipitates. Comparing these edges to the Ti $L_{2,3}$ edge obtained from a TiO_2 powder standard confirms the prevalence of Ti^{4+} solute at the grain boundary in this specimen. Unfortunately, Ti $L_{2,3}$ edges recorded from the basal facets do not permit Ti valence determination because the signal-to-noise ratio is too large and features in the energy-loss near edge structure cannot be discerned. Weak edges and poor counting statistics are presumably due to the lower concentration of Ti solute on the basal boundary facet.

4.3.2.3. Si Segregation to the Basal Plane

Silicon solute concentrations play an important role in the microstructure evolution of polycrystalline alumina. Additions of SiO_2 can promote the formation of

used to fabricate the polycrystalline growth layer.

liquid phases which dictate grain growth behavior, and may ultimately determine grain size and grain morphology. Myriad studies testify to the prevalence of platelike grains, characterized by high aspect-ratios with long boundary planes parallel to (0001), in SiO₂-doped materials containing a liquid phase. Evidence suggests a possible link between microstructures exhibiting a prevalence of basal boundary planes, and enrichment by Si solute. Susnitzky and Carter showed that basal twist boundaries formed by pressure sintering of two sapphire crystals were strongly faceted on (0001) planes when a thin film of SiO₂ was sandwiched between the two sapphire crystals, but did not exhibit strong faceting in the absence of SiO₂ additions [4]. Although chemical microanalysis was not performed on these basal facets, they attributed the faceting behavior to the presence of SiO₂ impurities.

Observations of preferred Si segregation to the basal plane in polycrystalline Al₂O₃ have been reported previously by several investigators [5-7]. Swiatnicki et al. report strong enrichment of Ti dopant, as well as Si and Ca impurities, at nearly all Al₂O₃ grain boundaries examined in their study [6]. They observe large variations in solute concentrations from one boundary to another, with the Si/Ti grain boundary concentration ratio exhibiting an acute dependence on grain boundary crystallography. Specifically, Si was found to segregate preferentially on boundary planes lying parallel to (0001), while Ti segregation was greater (relative to Si) on all other planes. A striking example of the acute dependence of solute segregation on boundary plane is reproduced from their work in Figure 4.19, where Ti and Si solute concentrations are measured at various points along a curved grain boundary whose plane orientation changes from (0001) basal to $(01\bar{1}2)$ rhombohedral. The Si/Ti concentration ratio approaches three at

the basal plane, but quickly drops to near unity just 5° off of (0001). The extent of calcium segregation did not vary significantly with changes in grain boundary plane or orientation.

In the same study, quantitative measurements of grain boundary solute concentrations were reported for the (0001) boundary plane. This data has been used to calculate normalized solute concentrations at the basal grain boundary, to permit comparison with basal plane segregation results of the present study. As evidenced by Table 4.4, one finds very good agreement between normalized solute concentrations measured at (0001) boundaries in Swiatnicki's work, and the high-angle twist boundary studied here.

In a different study, Bouchet and co-workers observed Si segregation to most all grain boundaries in a large-grained yttrium-doped alumina sample [7]. Interestingly, yttrium was found to be the dominant solute at all grain boundaries except those that were parallel to the (0001) basal plane of one of the grains, in which case Si was the solute in greatest abundance. The authors hypothesize that the formation of basal type grain boundary planes may result from a preferential segregation of Si on these planes, and further suggest that epitaxial growth of a Si-rich compound (mullite, SiAl_2O_5) may be the mechanism responsible for Si enrichment. They propose an epitaxial relationship in which the densely-packed (310) mullite plane grows atop (0001) alumina. However, while Si-rich amorphous phases were detected at a few of the basal-plane boundaries, no evidence for a Si-rich *crystalline* phase was reported.

Preferential segregation of Si solute to basal grain boundary planes has also been reported by Kebbede and Carim in 0.6 wt% TiO_2 -doped Al_2O_3 with anisotropic

microstructure consisting of alumina platelets in an equiaxed matrix [5]. Strong Si segregation was observed at grain boundaries containing an amorphous aluminosilicate layer, but was not detected at other (equiaxed) grain boundaries free of a continuous phase. The authors could not accurately quantify the amount of Si segregation due to the presence of the glassy phase at the basal boundaries. Ti was found to segregate more heavily to curved and/or pyramidal planes of platelet grains than to basal planes. Ti concentrations at the former were quantified as 5.2 wt% while those at the basal planes were estimated to be 1.2 wt% (they had to estimate due to the glassy phase issue). By comparison, the measured Ti concentration at boundaries separating equiaxed grains was fairly consistent at 3.3 wt%.

The authors hypothesize that preferred Ti segregation to pyramidal planes (and lack thereof to basal planes) may be attributed to grain boundary crystallography and preferred anion/cation stacking. Basal planes are more densely packed, so the larger Ti^{4+} ions introduce more strain energy when replacing Al^{3+} than do the smaller Si^{4+} ions ($r_i = 0.41 \text{ \AA}$). However, pyramidal planes and other random boundaries generally have more open structures and can more readily accommodate the tensile misfit of Ti^{4+} .

Although a detailed description of the grain boundary atomic structure via HRTEM has not been obtained for the twist boundary in this study, hypothetical models of the grain boundary structure can be constructed based strictly on knowledge of the grain boundary plane and orientation. Figure 4.20 shows two rudimentary structural models for the basal-plane boundary (a), and a grain boundary plane $\left(1 \ 0 \ \bar{1} \ 20\right)$ that is 8.6° off-basal (b). It should be noted that these models have been constructed from purely geometric considerations, and as such do not represent ‘minimum-energy’

configurations. We simply consider the joining of two grains with no reconstruction of the grain boundary structure. Though unrealistic, the purpose of the models is to provide a very simple comparison of ionic packing and free volume at the different facet planes. Both models have top crystals oriented along $[2\bar{1}\bar{1}0]$ and bottom crystals oriented along $[10\bar{1}0]$.

The most obvious distinction between the two grain boundary models pertains to the density of cation sites. The Al-terminated basal plane model (Fig. 4.20a) shows cations in close proximity to each other at the boundary core, leading to a high density of cation sites not observed in either of the bulk grains. This model represents a worst-case scenario for elastic strain energy accumulation at the grain boundary, as substitution of Ti^{4+} on closely-spaced cation sites will undoubtedly cause large tensile stresses to develop. However, substitution by smaller Si^{4+} cations is not expected to cause any appreciable strain energy.

The structural model for the off-basal facet (Fig. 4.20b) shows little if any increase in the cation density at the boundary plane. In fact, the density of cation sites actually decreases at the grain boundary relative to the basal plane in either grain. Presumably, then, substitution of Ti^{4+} for Al^{3+} should only be limited by saturation of available sites, and not by large elastic strain energies induced by cation substitution. According to the termination of each grain at the boundary, it's plausible that the off-basal facet is better able to accommodate Ti solute due to a lower density (and less close packing) of cation sites at the grain boundary.

Finally, differences in preferred cation coordination should not be overlooked as a possible explanation for the acute boundary-plane dependence of Si^{4+} and Ti^{4+}

segregation in Al_2O_3 . Silicon cations generally prefer tetrahedral coordination by oxygen anions [8], while Ti^{4+} prefers octahedral coordination. Indeed, the low solubility limit of Si^{4+} in bulk α - Al_2O_3 has previously been attributed to cation coordination, since cation sites in Al_2O_3 are octahedrally-coordinated [9, 10]. But if Si^{4+} is a (fully) substitutional defect in the bulk and at the boundary, then its solubility should be limited at both locations by coordination, since it is replacing an octahedrally-coordinated Al^{3+} cation. Without detailed knowledge of the grain boundary atomic structure, it's impossible to know if the local coordination of cation sites at the basal grain boundary deviates from six-fold to four-fold. However, the basal-plane model in Fig. 4.20a certainly suggests reduced coordination of cation sites at the grain boundary core. Silicon's preference to coordinate tetrahedrally with oxygen could conceivably explain its strong segregation to these reduced-coordination sites at the basal boundary plane.

4.3.2.4. Precipitation on the Off-Basal Facet

Several issues regarding the nature of precipitate formation in this sample are worthy of discussion. Specifically, why is this the only grain boundary (of all the tilt and twist boundaries examined) to exhibit precipitation? And is there any significance to the fact that precipitate formation only occurs on the off-basal facet?

The slow cooling rate experienced by this sample is most certainly a root cause of grain boundary precipitation. At the annealing temperature of 1600°C , solute solubility is higher, and the space charge potential is lower, than their expected values at 1200°C or 1000°C . Therefore, as the bicrystal cools from 1600° , changes in solubility and space charge potential should both serve to increase the driving force for solute

segregation to the boundary. In samples that are quenched to room temperature, cooling occurs so quickly that diffusion is effectively inhibited, preserving the grain boundary solute distribution established at high temperature. In contrast, slow cooling rates (which accompany furnace cooling) provide the opportunity for solute species to attempt to equilibrate at the lower temperatures. At temperatures where bulk and boundary diffusion are still kinetically viable (i.e., $T \geq 1200^{\circ}\text{C}$), the solute distribution is constantly trying to adjust to equilibrium conditions, but the cooling rate is too fast for equilibration to occur. As a result, we observe nonequilibrium segregation of solute to the grain boundary in samples that have been slow-cooled. The grain boundary chemistry observed in these samples is not representative of an equilibrium condition at 1600°C , nor at room temperature, but may represent a pseudo-equilibrium condition for some intermediate temperature (perhaps 1200°C).

In his seminal paper detailing grain boundary phenomena in ceramic materials, Kingery emphasized the importance of specimen cooling rate on solute segregation to grain boundaries, and discussed how slow cooling can promote nonequilibrium segregation and even phase separation (precipitation) [11]. Experimental studies by other investigators support Kingery's initial assertions. Paulus showed significantly higher Ca and Y solute concentrations at grain boundaries in slow-cooled ferrite samples as compared to quenched ones [12]. Leipold similarly found that MgO samples quenched from 2000°C in water showed much less boundary segregation than furnace-cooled samples [13].

In the present study, precipitation of TiO_2 on the off-basal facets is presumably a consequence of slow-cooling and associated nonequilibrium segregation. Indeed,

precipitates were not found in any of the quenched grain boundary samples. More surprising, however, is that other doped bicrystal grain boundaries (including the low angle twist boundary S3, and a low-angle tilt boundary discussed in the next chapter) furnace-cooled to room temperature showed no signs of precipitate formation. One explanation is that the alumina powder used to make the doped polycrystal for directed assembly of this bicrystal contained a higher concentration of Ti dopant, or at least a higher concentration of Ti^{4+} solute. An alternative theory might incriminate the off-basal facet as a critical component in the onset of precipitation.

There are two outstanding reasons why precipitation might be favored on the off-basal facet rather than the basal plane. First, the Ti^{4+} concentration is much higher on the off-basal plane, and may actually exceed the solubility limit of Ti^{4+} in Al_2O_3 , leading to TiO_2 precipitation. This would represent a chemically-induced precipitation scenario. Second, large vacant sites at the grain boundary core, as seen in Fig. 4.20b, may permit the nucleation and subsequent growth of a second phase by minimizing the strain energy associated with precipitate evolution. Realizing that the basal plane has neither a large Ti concentration nor a preponderance of vacant sites, one or perhaps both of these arguments may explain why precipitation is only observed on the off-basal facet.

One other feature that distinguished the high-angle twist boundary from others examined in this study is its high Si concentration at the grain boundary. If Si^{4+} and Ti^{4+} are competing for available cation sites at the basal plane, then Si solute may be indirectly responsible for TiO_2 precipitation by hastening the saturation of available sites.

4.3.2.5. Solute-Induced Grain Boundary Faceting

If grain boundary precipitation occurs in response to nonequilibrium segregation of excess Ti solute, then the same driving force could be responsible for grain boundary faceting. Morrissey and Carter have demonstrated that the basal grain boundary plane is extremely stable in Al_2O_3 [14]. Faceting is not expected based on grain boundary energy considerations alone. Moreover, because the facet plane is high-index, its repeated occurrence along the grain boundary length is unexpected. Given the low-energy of the basal plane, faceting would not be an energy-minimizing transition based solely on structural considerations, unless the high-index plane represents a special (high-density) plane of the CSL. Regardless, the off-basal facet may be energetically favorable if one also considers the accommodation of excess solute.

Donald and Brown were the first to suggest that grain boundary faceting in alloy systems could be attributed to strongly misfitting solutes at the boundary plane [15]. Their seminal work on Bi-doped Cu showed that greater size differences between solute and host atoms lead to stronger tendencies for faceting. Significantly, they also showed that faceting does not always occur along high-density planes of the CSL, implying structural stabilization by grain boundary solute species.

Many other studies in metals and alloys have established relationships between grain boundary faceting and solute enrichment at the boundary [16-19]. A particularly eloquent display of solute-induced faceting was offered by Ference and Balluffi, who showed that grain boundary faceting in Bi-doped Cu is a reversible process that can be

augmented or suppressed by addition or removal of Bi solute [19]. An initially-faceted boundary in doped Bi roughens to form a flat boundary upon removal of the Bi, and then re-facets along the same planes as Bi is once again introduced. Reversibility implies that faceting is an equilibrium process – as described by Cahn [20] -- signaling a phase transition from a flat (single-phase) interface to a faceted structure consisting of facets (phases) which coexist along lines of intersection.

To date, studies linking grain boundary faceting to solute segregation in ceramics have not been reported. Morrissey and Carter studied faceted grain boundaries in Al_2O_3 and attempted to correlate favored boundary planes with low-energy planes of sapphire and/or special planes of the CSL [14]. While the authors noted the importance of solute species in determining grain boundary energies, their analysis gave no consideration to possible effects of solute segregation or bulk impurity concentrations on grain boundary structure.

4.3.2.6. Uniformity of Grain Boundary Charge

As discussed previously, variations in vacancy formation energies are predicted to occur with changes in grain boundary structure [21-23]. In this study, the ratio of donor/acceptor species at a grain boundary can be used as a rough measure of grain boundary charge¹⁵. Comparing measured ratios from different facets may yield some clues regarding the intrinsic charge of each facet, thus exposing possible differences in vacancy formation energies between two fundamentally different boundary structures.

¹⁵ This assumption may not be valid, however, since equilibrium conditions were not maintained upon furnace cooling. Qualitative comparisons of intrinsic charge should be possible, but quantitative comparisons are most certainly erroneous due to nonequilibrium segregation.

Using average grain boundary solute concentrations, and assuming all Ti solute at the boundary is tetravalent, the ratio $([\text{Si}^{4+}] + [\text{Ti}^{4+}]) / [\text{Ca}^{2+}]$ was calculated as 3.95 for the basal facet, and 4.23 for the off-basal facet. One might infer that the off-basal facet has a more negative intrinsic charge, implying a higher aluminum vacancy formation energy. However, the measured difference is probably not statistically significant given the accuracy of solute quantification. Also, TiO_2 precipitation on the off-basal facet may introduce errors in the determination of an “average” donor concentration on that plane. In light of these issues, a legitimate claim cannot be made regarding the relative defect formation energies for the two facets. Nonetheless, controlled bicrystal structures afford the unique opportunity to evaluate, indirectly, possible differences in vacancy formation energies between different grain boundaries.

4.3.3. Quenched Boundary (12b)

4.3.3.1. Grain Boundary Structure

Kikuchi electron diffraction data confirms that this twist boundary has the same misorientation angle (i.e. measured to within the experimental error of the technique) as the furnace-cooled twist boundary described in the previous section. This result is anticipated since both twist boundaries came from the same tricrystal specimen.

A phase contrast image of the quenched twist boundary is shown in Figure 4.21. The top crystal is oriented very close to a $[2\bar{1}\bar{1}0]$ zone axis and exhibits prominent $(0\bar{1}14)$ fringes, while the bottom crystal is oriented along $[10\bar{1}0]$ to clearly expose the (0003) fringes. Despite the low-index orientation of both crystals, the grain boundary is clearly not in an exact edge-on orientation. Moreover, the image reveals that the grain

boundary plane is not exactly parallel to the (0003) fringes of the bottom crystal.

Diffraction data illustrates that both crystals have their basal planes parallel to each other, so the grain boundary plane is slightly off of (0001) for each crystal.

Conventional TEM and electron diffraction confirm the off-basal character of the grain boundary plane. Figure 4.22 shows the grain boundary imaged edge-on with the right crystal oriented along $[10\bar{1}0]$. The $[0001]$ direction and (0001) plane are included in the image to demonstrate the slight deviation, measured as $3.0 \pm 0.5^\circ$, off of the basal plane. This image also serves to illustrate the straight, non-faceted nature of the twist boundary. No grain boundary faceting was observed in any of the thinned regions of this specimen, nor were any second phases detected along the grain boundary or in the bulk.

4.3.3.2. Grain Boundary Chemistry

A representative EDS line profile across the quenched twist boundary is shown in Figure 4.23. Pronounced segregation of Ti, Si and Ca solute is observed at the grain boundary, with peak concentrations of 0.36, 0.33, and 0.16 at. %, respectively. Average peak grain boundary concentrations, as determined from a series of line profiles, are shown in Table 4.5 for the three solute species. To facilitate comparison with segregation data from the furnace-cooled twist boundary having the same misorientation, average normalized solute concentrations, defined by Eq. 4.2, are also reported in the table. The chemical width of the grain boundary consistently measured between 10-12 nm

Electron energy loss spectra acquired from the grain boundary region could not conclusively identify a unique Ti valence in this specimen. Evidence from multiple

TEM samples suggests that both Ti^{3+} and Ti^{4+} exist in measurable quantities near the grain boundary. Figure 4.24a shows the Ti $L_{2,3}$ edge of two spectra acquired only a few nanometers apart and close to the grain boundary. Differences in the near-edge structure between the two spectra are easily discerned, and are consistent with reference spectra for Ti^{3+} and Ti^{4+} . A more graphic display of the change in Ti valence over such short length scales is presented in Figure 4.24b, which shows a series of energy loss spectra acquired near the thin edge of a grain boundary pore. The spacing between each spectrum is 7.9 nm; the transition from Ti^{3+} to Ti^{4+} occurs within approximately 30 nm.

4.3.4. Solute Segregation and Specimen Cooling Rate

Unfortunately, direct comparison of solute segregation data for the quenched and furnace-cooled twist boundaries is complicated by variations in the grain boundary plane. The two prominent boundary planes in the furnace-cooled specimen are (0001) and a plane 8.6° off-basal, while the quenched specimen has a grain boundary plane roughly 3.0° off-basal. The cooling rate and the grain boundary plane should both affect the *absolute* grain boundary concentrations of all solute species. The former is predicted by reduced solute solubility at lower temperatures, while the latter has been demonstrated in this study for the furnace-cooled twist boundary, where solute concentrations changed considerably with grain boundary facet plane. It is therefore not practical to compare absolute grain boundary solute concentrations for different boundary planes in samples that have experienced very different cooling rates.

Still, it is not immediately clear how or if the *normalized* grain boundary solute concentrations should vary with cooling rate. If one makes the bold assumption that all

solutes are equally affected by changes in cooling rate, then one can directly compare the normalized concentrations of solute species at different boundary planes in samples that have experienced different cooling rates¹⁶. Such a comparison is made in Figure 4.25, where the normalized grain boundary solute concentrations are shown for the two boundary planes in the furnace-cooled specimen and the off-basal plane in the quenched sample. Here, the Ti and Si peak boundary concentrations for the 3.0° off-basal plane are seen to be intermediate between values measured for the basal plane and the 8.6° off-basal plane. These results are consistent with the hypothesis that Ti segregation increases, and Si segregation decreases, as the grain boundary plane begins to deviate from (0001).

4.4. General Discussion of Solute Segregation to Basal Twist Boundaries

4.4.1. Measured and Predicted Grain Boundary Solute Concentrations

All twist boundaries examined in this study show pronounced segregation of Ti and Ca solute to the grain boundary. Cosegregation of Ca and Ti is not consistent with solute profiles predicted from space charge theory (see, for example, Figure 2.7b), which forecast a depletion of Ca^{2+} immediately adjacent to the boundary. Therefore, we might assume that elastic misfit of the large Ca^{2+} cations is responsible for their segregation to the negatively charged grain boundary.

As discussed in Chapter 2, Kingery modified McLean's equation to permit calculation of grain boundary solute enrichment, given as

¹⁶ In theory, the segregation of each solute should vary with temperature due to changes in bulk solubility, and due to changes in the space charge potential and grain boundary charge with temperature. Si^{4+} and Ti^{4+} both have very low solubilities in Al_2O_3 , and they both behave as positively-charged substitutional

$$\ln\left(\frac{C_{gb}}{C_{lattice}}\right) = \frac{\Delta S}{k} + \frac{24\pi K G r_1^3}{3K + 4G\left(\frac{r_1}{r_2}\right)} \left(\frac{r_2 - r_1}{r_1}\right)^2 \frac{1}{kT} \quad (4.3)$$

Ignoring the entropy term¹⁷, this equation can be used to compare predicted and experimentally-measured grain boundary solute concentrations. Experimental data can also be compared with estimates of solute enrichment (or depletion) predicted from space charge calculations. Figures 4.26 (a) and (b) show calculated Ti solute profiles for 1200° and 1600°C, respectively, predicting peak Ti concentrations of 8.0 and 1.6 at. %.

Table 4.6 compares measured grain boundary solute concentrations with those predicted by elastic-misfit and space charge models. Observed grain boundary solute concentrations are not consistent with predictions from space charge theory, nor do they match the elastic misfit model. Measured Ti⁴⁺ concentrations are always less than those predicted by space charge theory. The same is true for measured Ca²⁺ concentrations relative to predictions from elastic misfit. Moreover, discrepancies between theory and experiment are significantly greater at 1200°C than at 1600°C.

Inconsistencies between experiment and prediction might be attributed to several factors, including inherent limitations of each theory (elastic and space charge) in describing the empirical situation. First, neither theory accounts for the fact that there are a limited number of vacant (accommodating) sites at the grain boundary available to the solute species. Accordingly, both models should over-estimate the amount of solute segregation observed in practice. Also, neither model on its own accounts for interactions between elastic and electrostatic driving forces. For instance, the elastic

impurities in Al₂O₃. Thus, it may not be completely outlandish to assume that their nonequilibrium segregation profiles would be similarly affected by cooling rate.

model does not account for the fact that Ca^{2+} should be repelled from the negatively charged grain boundary in donor-doped Al_2O_3 , so it may again over-estimate the amount of segregated solute.

Beyond limitations with the models, we should also assess the accuracy of our assumptions concerning defect chemistry. All twist boundaries, with the exception of S3, received final anneals in air, and it has been assumed that Ti valence should be primarily 4^+ in each of these samples. It is more likely, however, that both Ti^{3+} and Ti^{4+} exist in the processed bicrystals as a result of sluggish and incomplete oxidation. The presence of Ti^{3+} would reduce the intrinsic negative charge on the grain boundary (according to Eq. 2.23) leading to lower $[\text{Ti}^{4+}]$ concentrations at the grain boundary. Additionally, neutral defect clusters (such as $\text{Ti}^{4+}\text{-Ca}^{2+}$) could form in the bulk, reducing the driving force segregation, as well as the concentration of charged solute species. The net result would be less solute segregated to the grain boundary.

And finally, issues concerning the accuracy of quantitative microanalysis must be addressed when scrutinizing how accurately predictions match experiments¹⁸.

Quantitative microanalysis using a focused-probe in the (S)TEM typically under-estimates the actual grain boundary solute concentration, especially if the chemical width of the grain boundary is smaller than the probe diameter. This is because the volume of the probed area far exceeds the grain boundary core volume, effectively diluting the extrapolated solute concentration at the boundary core. For the specific case considered here, the grain boundary chemical width is quite large (>10 nm), but the peak boundary

¹⁷ Li and Kingery's plot of $\ln(C_{\text{gb}}/C_{\text{I}})$ vs. $(r_2-r_1/r_1)^2$, shown in Figure 2.8, passes through the origin, suggesting a negligible ΔS term.

¹⁸ A more detailed discussion of the accuracy of quantitative grain boundary microanalysis can be found in Appendix A.

concentration is highly localized to less than one nanometer in width. Ultimately, this is the solute concentration that we are trying to compare to theory. Because the peak concentration is so localized (see Figs. 2.5 and 2.6 to discern how quickly the Ti solute concentration falls away from the boundary core), focused-probe microanalysis utilized in these studies will always underestimate the peak solute concentration at the grain boundary core.

4.4.2. Grain Boundary Chemical Width

Predictions from space charge theory show a Ti-enriched region extending approximately 80 Å away from the grain boundary at 1600°C, and 56 Å away from the grain boundary at 1200°C, for 0.001 mol TiO₂-doped Al₂O₃ (refer to Fig. 4.26).

Measurements of the grain boundary chemical width using line profiles across the various twist boundaries are therefore consistent with predictions of space charge theory¹⁹, as shown in Table 4.7.

An interesting feature observed in all samples is how closely the Ca solute profile spatially mirrors the Ti profile; similar chemical widths are observed for both solutes. This result is not consistent with the expectation that strongly-misfitting solutes should adsorb very close to the grain boundary core, where the structural disorder is most heavily concentrated. Previous studies of solute segregation to grain boundaries in ionic ceramics have demonstrated the tendency for elastically-misfitting solutes to adsorb near the boundary core, regardless of their relative charge, while charged solute species having little size misfit tend to adsorb over much larger distances [24]. An example of

this is shown in Figure 4.27 for various solutes in MgO. Here, misfitting Si^{4+} and Ca^{2+} adsorb close to the boundary core, while Sc^{4+} , similar in size to Mg^{2+} , exhibits a much broader chemical width, consistent with predictions from space charge theory.

Due to significant size differences between Ti^{4+} and Ca^{2+} , we might expect different adsorption behavior for the two solutes, with Ca^{2+} accumulating close to the boundary core and Ti^{4+} occupying a broader region. Clearly this trend is not replicated in our data. Kingery has suggested that the segregation profile can be spatially modified by thermal stress fields which develop adjacent to the grain boundary during cooling [22]. He postulates that a stress-field effect like this could be significant in many ceramic oxides possessing a high degree of anisotropy in both elastic constants and thermal expansion coefficients. If such a mechanism were to induce appreciable lattice strain, the distortion should be measurable in HRTEM images of the grain boundary. Examination of phase-contrast images from twist boundaries (Figures 4.11 and 4.21) reveals no measurable changes in interplanar spacing near the grain boundary, as seen in Figure 4.28²⁰. This would seem to suggest that thermal stress fields are not responsible for the close matching of Ti and Ca solute profiles.

Defect association between Ti^{4+} and Ca^{2+} might also be implicated as a possible explanation for their matching profiles, but if they were associated as a neutral defect, then their segregation to the boundary should be driven by strain relief, and the adsorption should be localized to the grain boundary core. Alternately, more complex defect clusters involving Ca^{2+} and Ti^{4+} may have formed. Grimes has suggested that Ca^{2+}

¹⁹ In furnace-cooled samples, we would expect the final “quench” temperature to be somewhere near 1200°C, where diffusion becomes kinetically limited and the segregation profile is effectively frozen-in.

impurities may self-compensate in Al_2O_3 by forming interstitial-substitutional defect clusters, such as $\{\text{Ca}_i^{\bullet\bullet} : 2\text{Ca}'_{\text{Al}}\}^x$ [25]. The possible existence of Ca^{2+} interstitials in Ti-doped Al_2O_3 offers numerous possibilities for neutral and charged defect clusters, some of which may lead to the observed solute profiles. It would seem that such a defect cluster would have to be positively charged, and would have to contain Ti^{4+} and Ca^{2+} species to be consistent with observed data.

4.4.3. Issues Concerning Solute Valence

The presence of Ti^{3+} in quenched bicrystal samples 12b and 15b is somewhat surprising given their lengthy (40-50 hour) exposure to air at 1600°C . Previous work has demonstrated that a 10-15 hour anneal at 1600°C in air is sufficient to convert Ti^{3+} to Ti^{4+} in polycrystalline compacts [26], though little data regarding the kinetics of valence conversion exists. The bicrystals would presumably require more time and/or higher temperatures to achieve the same conversion, since oxygen diffusivity is limited by a severe paucity of grain boundaries. However, results from the furnace-cooled twist boundary (12a) clearly illustrate that conversion from Ti^{3+} to Ti^{4+} can be accomplished at reasonable times and temperatures. Thus, attributing the prevalence of Ti^{3+} to insufficient diffusion kinetics during the high-temperature anneal would not appear to be a valid explanation.

The only major difference between the processing of 12a and 12b is the rate at which the specimens were cooled from the final annealing temperature. Yet there is no

²⁰ Quantitative measurements have also been performed on phase contrast images of tilt boundaries (see, for example, Figures 5.1 and 5.11 in the ensuing chapter) in an effort to detect changes in interplanar spacing. No lattice strain adjacent to the grain boundary could be detected.

obvious mechanism to explain how, why, or to what extent the cooling rate should affect Ti valence. Assuming higher diffusivity along the grain boundary, Ti solute near the boundary should be the most readily oxidized, presumably existing as Ti^{4+} . And even if residual Ti^{3+} still exists away from the grain boundary, it should not have sufficient time to segregate to the boundary during the rapid quench. A rough estimate of the diffusion length of Ti^{3+} during a fast quench suggests this solute should move no more than a few Angstroms (see Appendix B). Seemingly, the only logical explanation is that Ti^{4+} is reduced to Ti^{3+} during the ion-milling process in TEM specimen preparation. Although samples are chilled to near liquid-nitrogen temperatures during ion-milling, they are also exposed to a heavily reducing environment which may facilitate conversion from Ti^{4+} to Ti^{3+} .

To investigate this hypothesis, attempts were made to prepare TEM specimens of quenched twist boundaries with minimum exposure to ion-milling. This requires more mechanical thinning on the dimpler, but unfortunately sapphire's brittle behavior limits the extent to which it can be mechanically thinned (approximately 10 μm), so a certain amount of ion-milling is always required. Because electrochemical thinning is not an option for sapphire, the issue of milling-induced solute valence modification appears to be an ongoing conundrum not easily solved.

4.5. Future Work

A major effort should be to understand why Si^{4+} solute prefers segregation to the basal plane, while Ti^{4+} favors off-basal facets. This is clearly an important issue governing the microstructure evolution of polycrystalline alumina, and yet one for which

very little is known. If the different segregation behaviors is related to atomic structure and/or cation coordination at the grain boundary, then electron microscopy may be the only tool capable of addressing the problem. High angle annular dark field imaging in a STEM, in concert with atomic-column spectroscopy, offers the unique ability to image and chemically map materials simultaneously at atomic resolution. Here, incredibly small ($< 5 \text{ \AA}$) electron probes offer the distinct advantage of high signal-to-noise ratios, so crisp energy-loss spectra can be acquired even from very small volumes. In theory, such an instrument should be able to resolve the cationic structure at the grain boundary, while spectroscopy can be used to determine not only chemical species, but also details regarding site-specific electronic structure and coordination. If Si^{4+} prefers segregation to the basal plane due to local tetrahedral coordination with oxygen anions, then changes in the near edge structure of electron energy-loss spectra should reflect differences between octahedrally- and tetrahedrally-coordinated Si^{4+} . The National Center for Electron Microscopy at LBNL will soon be installing a STEM instrument with these advanced capabilities, so opportunities to resolve this fundamental issue in alumina ceramics are imminent.

Another area of study might explore the concept of solute-induced grain boundary faceting in ceramics. Bicrystal fabrication via directed assembly is an ideal technique for investigating relationships between grain boundary chemistry and structure, since grain boundary geometries can be closely replicated, but with very different chemistries. Towards this end, it would be interesting to examine the tendency for grain boundary faceting as a function of Ti dopant concentration, while maintaining the same grain boundary geometry (misorientation and plane) and specimen cooling rate.

Alternately, one could also examine faceting as a function of solute misfit (or valence), using dopants with varying sizes (or valency), but having a fixed concentration and valence (size). To investigate the role of solute misfit on grain boundary faceting, we could compare samples separately doped with 500 ppm Si^{4+} ($r = 0.41 \text{ \AA}$), Ti^{4+} ($r = 0.67 \text{ \AA}$), and Zr^{4+} ($r = 0.79 \text{ \AA}$). Or, to examine the role of solute valence, compare samples individually doped with 500 ppm Li^+ , Mg^{2+} , Ti^{3+} , Zr^{4+} and Nb^{5+} -- all of which have similar ionic radii ($r = 0.75\text{-}0.80 \text{ \AA}$). If grain boundary faceting is indeed solute-induced, we would expect to see faceting in samples doped with the more strongly-misfitting solutes, and also in samples doped with strong charge-misfitting solutes, such as Li^+ and Nb^{5+} .

More efforts should also be directed towards understanding the relationship between bicrystal processing and Ti valence. The current study shows that oxidation of Ti^{3+} to Ti^{4+} is quite sluggish in bicrystal structures even at temperatures as high as 1600°C . If future studies hope to exert control over solute valence, the kinetics of oxidation-reduction reactions must be clarified for the relevant furnace environments and processing conditions.

4.6. Summary and Conclusions

Sapphire twist boundaries of varying misorientations have been successfully fabricated via a directed-assembly growth process, with fairly stringent control of grain boundary crystallography. Structural and chemical characterization of a low-angle twist boundary reveals dramatic changes in solute concentrations between grain boundary dislocations, and adjacent segments of “perfect” grain boundary. Solute variability is

believed to result from different intrinsic charges on the two defect sites, and seems to imply unique values for aluminum vacancy formation energy ($g_{v_{Al}}$) at each site.

Twist boundaries with the same misorientation but different cooling rates exhibit very different grain boundary structure and chemistry. The furnace-cooled sample shows faceting of the grain boundary plane, as well as second-phase (TiO_2) precipitation. Both of these phenomena are attributed to nonequilibrium solute segregation that accompanies slow-cooling from 1600°C , as evidenced by the absence of faceting and precipitation in the quenched sample. Dramatic changes in grain boundary chemistry (specifically Ti^{4+} and Si^{4+} solute) between the different facets are consistent with previous studies of solute segregation in polycrystalline Al_2O_3 . A demonstrated preference for Si^{4+} to adsorb on the basal plane, and for Ti^{4+} to adsorb on non-basal planes, may also be responsible for grain boundary faceting in the slow-cooled sample.

Grain boundary solute enrichment occurs over a fairly large region ($< 10\text{ nm}$) in all samples. Titanium enrichment is consistent with predictions from space charge theory, while Ca segregation occurs as a result of elastic misfit in the bulk grain(s). However, Ca adsorption at the grain boundary is not confined to the structurally-disordered core, as might be expected for strongly-misfitting solute species. Discrepancies between measured and predicted grain boundary solute concentrations suggest mixed Ti valence at the grain boundary, and highlight fundamental limitations of quantitative analysis using focused probe techniques.

Chapter 4 References

1. E. Mammana, *unpublished work*, 1998.
2. J.S. Ikeda, Y.M. Chiang, A.J. Garratt-Reed, and J.B. Vander Sande, "Space Charge Segregation at Grain Boundaries in Titanium Dioxide: II, Model Experiments," *Journal of the American Ceramic Society* **76** (10) 2447-59 (1993).
3. O. Johari and G. Thomas, *The Stereographic Projection and its Applications*. New York: Interscience, 1969.
4. D.W. Susnitzky and C.B. Carter, "Structure of Alumina Grain Boundaries with and without a Thin Amorphous Intergranular Film," *Journal of the American Ceramic Society* **73** (8) 2485-93 (1990).
5. A. Kebbede and A.H. Carim, "Segregation of Si and Ti in alpha-Alumina," *Materials Letters* **41** (4) 198-203 (1999).
6. W. Swiatnicki, S. Lartigue-Korinek, and J.Y. Laval, "Grain Boundary Structure and Intergranular Segregation in Al_2O_3 ," *Acta Metallurgica et Materialia* **43** (2) 795-805 (1995).
7. D. Bouchet, F. Dupau, and S. Lartigue-Korinek, "Structure and Chemistry of Grain Boundaries in Yttria Doped Aluminas," *Microscopy Microanalysis Microstructures* **4** (6) 561-573 (1993).
8. A. Salleo, "High Power Laser Damage in Fused Silica," Ph.D. Dissertation, University of California, Berkeley, 2001.
9. C.H. Lee and F.A. Kröger, "Electrical Conductivity of Polycrystalline Al_2O_3 Doped with Silicon," *Journal of the American Ceramic Society* **68** (2) 92-9 (1985).
10. E.R. Winkler, J.F. Sarver, and I.B. Cutler, "Solid Solution of Titanium Dioxide in Aluminum Oxide," *Journal of the American Ceramic Society* **49** (12) 634-637 (1966).
11. W.D. Kingery, "Plausible Concepts Necessary and Sufficient for Interpretation of Ceramic Grain-Boundary Phenomena. II. Solute Segregation, Grain-Boundary Diffusion, and General Discussion," *Journal of the American Ceramic Society* **57** (2) 74-83 (1974).
12. M. Paulus, "Properties of Grain Boundaries in Spinel Ferrites," in *The Role of Grain Boundaries and Surfaces in Ceramics*, W.W. Kriegel and H. Palmour III, Editors. Plenum Press: New York, 1966.

13. M.H. Leipold, "Addenda to Impurity Distribution in MgO," *Journal of the American Ceramic Society* **50** (11) 628-9 (1967).
14. K.J. Morrissey and C.B. Carter, "Faceted Grain Boundaries in Al₂O₃," *Journal of the American Ceramic Society* **67** (4) 292-301 (1984).
15. A.M. Donald and L.M. Brown, "Grain Boundary Faceting in Cu-Bi Alloys," *Acta Metallurgica* **27** 59-66 (1979).
16. J.R. Michael and D.B. Williams, "An Analytical Electron Microscope Study of the Kinetics of the Equilibrium Segregation of Bismuth in Copper," *Metallurgical Transactions A* **15A** 99-105 (1984).
17. G.H. Bishop, W.H. Hartt, and G.A. Bruggeman, "Grain Boundary Faceting of <1010> Tilt Boundaries in Zinc," *Acta Metallurgica* **19** 37-47 (1971).
18. M. Menyhard, B. Rothman, and C.J. McMahon, Jr., "Observations of Segregation and Grain-Boundary Faceting by Tellurium and Oxygen in Iron," *Scripta Metallurgica et Materialia* **29** (8) 1005-9 (1993).
19. T.G. Ference and R.W. Balluffi, "Observation of a Reversible Grain Boundary Faceting Transition Induced by Changes of Composition," *Scripta Metallurgica* **22** (12) 1929-34 (1988).
20. J.W. Cahn, "Transitions and Phase Equilibria Among Grain Boundary Structures," *Journal de Physique Colloque* **C6-43** 199-213 (1982).
21. J.D. Eshelby, C.W.A. Newey, P.L. Pratt, and A.B. Lidiard, "Charged Dislocations and the Strength of Ionic Crystals," *Philosophical Magazine* **3** (25) 75-89 (1958).
22. W.D. Kingery, H.K. Bowen, and D.R. Uhlmann, *Introduction to Ceramics*. New York: J. Wiley and Sons, 1976.
23. Y.M. Chiang, D. Birnie III, and W.D. Kingery, *Physical Ceramics. Principles for Ceramic Science and Engineering*. New York: John Wiley and Sons, Inc., 1997.
24. Y.M. Chiang, A.F. Henriksen, and W.D. Kingery, "Characterization of Grain Boundary Segregation in MgO," *Journal of the American Ceramic Society* **64** (7) 385-89 (1981).
25. R.W. Grimes, "Solution of MgO, CaO, and TiO₂ in α -Al₂O₃," *Journal of the American Ceramic Society* **77** (2) 378-84 (1994).

26. S.K. Mohapatra and F.A. Kröger, "Defect Structure of α -Al₂O₃ Doped with Titanium," *Journal of the American Ceramic Society* **60** (9-10) 381-387 (1977).

Table 4.1. Visibility data for grain boundary dislocations in the low-angle twist boundary (S3) under various imaging conditions.

g-vector	Zone axis	Visible?
$[5 \bar{1} 5 10 4]$	$[4 0 \bar{4} 1]$	yes
$[1 \bar{2} 1 0]$	$[4 0 \bar{4} 1]$	no
$[\bar{1} 0 5 5 6]$	$[2 \bar{2} 0 1]$	yes
$[5 0 \bar{5} 8]$	$[4 0 \bar{4} 1]$	yes
$[0 \bar{5} 5 4]$	$[4 0 \bar{4} 1]$	yes
$[5 0 \bar{5} 3]$	$[\bar{1} 1 4 7 6]$	yes
$[5 \bar{1} 0 5 2]$	$[\bar{1} 1 4 7 6]$	no
$[5 \bar{1} 5 10 4]$	$[4 0 \bar{4} 1]$	yes

Table 4.2. Measured Ca/Ti elemental ratios for different defect sites at the low-angle twist boundary (S3), as revealed by EDS and EELS line profiles.

	Perfect Grain Boundary	Grain Boundary Dislocation
EDS	0.52	0.32
EELS	0.43	0.21

Table 4.3. Normalized grain boundary solute concentrations (in %) measured for the two facet planes in a slow-cooled high-angle twist boundary (12a).

	Basal Facet	Off-Basal Facet
Si ⁴⁺	54 ± 5	27 ± 7
Ti ⁴⁺	31 ± 6	55 ± 6
Ca ²⁺	16 ± 4	18 ± 1

Table 4.4. Normalized solute concentrations (in %) for (0001) grain boundaries reported in [6], and for the furnace-cooled high-angle twist boundary of this study.

	Swiatnicki [6]	This Study
Si ⁴⁺	51	54 ± 5
Ti ⁴⁺	27	31 ± 6
Ca ²⁺	22	16 ± 4

Table 4.5. Solute concentration data for the quenched high-angle twist boundary (12b).

	Grain Boundary Solute Concentration (at. %)	Normalized Solute Concentration (%)
Si	0.31 ± 0.12	33 ± 6
Ti	0.40 ± 0.08	43 ± 6
Ca	0.22 ± 0.06	24 ± 5

Table 4.6. Measured and predicted grain boundary solute concentrations (at. %) as a function of temperature for twist boundaries examined in this study.

Solute	1200°C	1600°C
Ti ⁴⁺ (space charge [§])	8.0	1.6
Ti ⁴⁺ (elastic misfit [§])	0.06	0.05
Ti ⁴⁺ (S3 – measured [†])	0.30	--
Ti ⁴⁺ (15b – measured)	--	1.0
Ti ⁴⁺ (12b – measured)	--	0.36
Ca ²⁺ (space charge [§])	0	0
Ca ²⁺ (elastic misfit [§])	13.6	1.26
Ca ²⁺ (S3 – measured [†])	0.25	--
Ca ²⁺ (15b – measured)	--	0.25
Ca ²⁺ (12b – measured)	--	0.16

[§] Assumes 0.02 at. % Ti⁴⁺ and 0.0002 at. % Ca²⁺ in the bulk

[†] Measured at a non-dislocated region of grain boundary

Table 4.7. Predicted and measured grain boundary chemical widths (in nm) for Ti solute at twist boundaries in this study.

Sample	Temp (°C)	Measured Width	Predicted Width [§]
S3	1200	12	10.6
15b	1600	15-17	16.1
12b	1600	12	16.1

[§] Assumes 0.02 at. % Ti⁴⁺ in the bulk

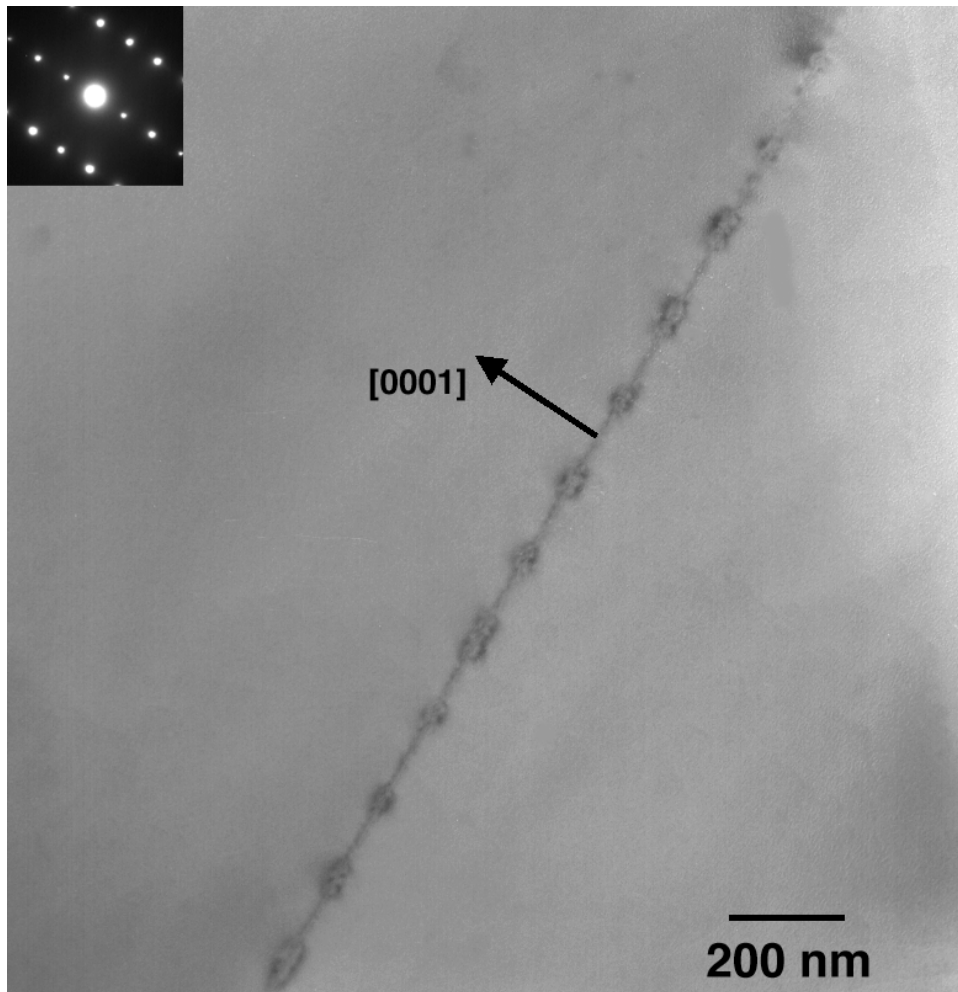


Figure 4.1. Conventional TEM image of twist boundary S3 viewed edge-on, showing periodic dislocation strain contrast.

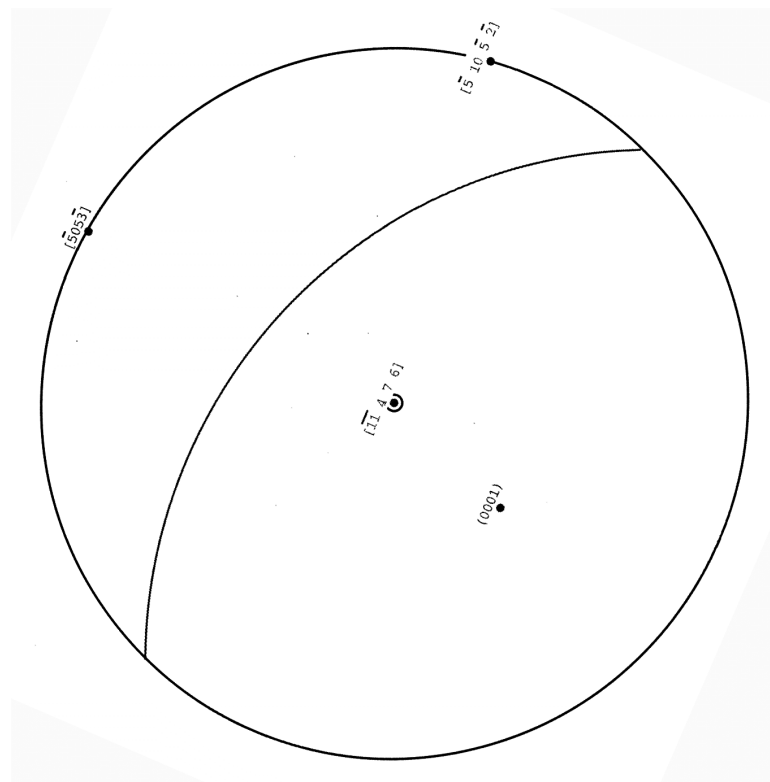
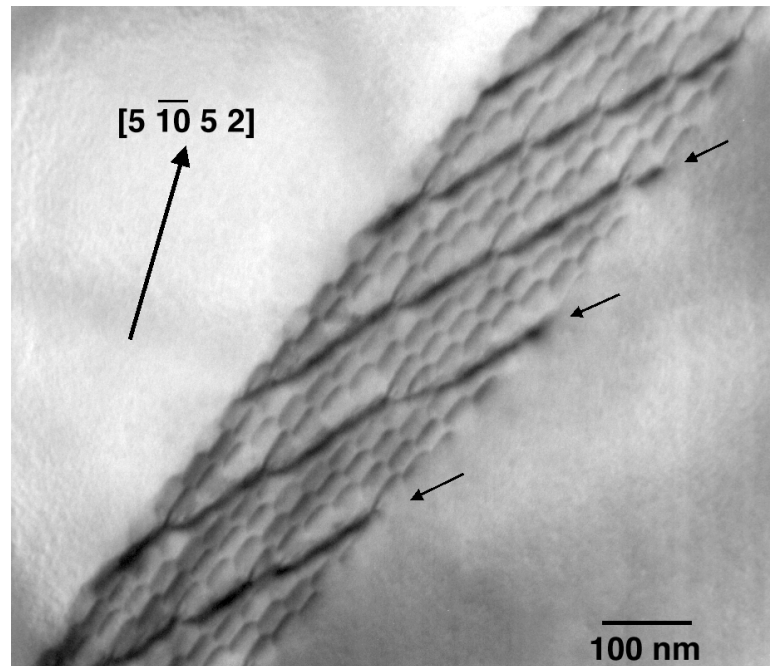


Figure 4.2. (a) Bright field (BF) image of inclined twist boundary showing periodic networks of screw dislocations. (b) Stereogram for the high-index zone index showing proper orientation of the (0001) basal plane.

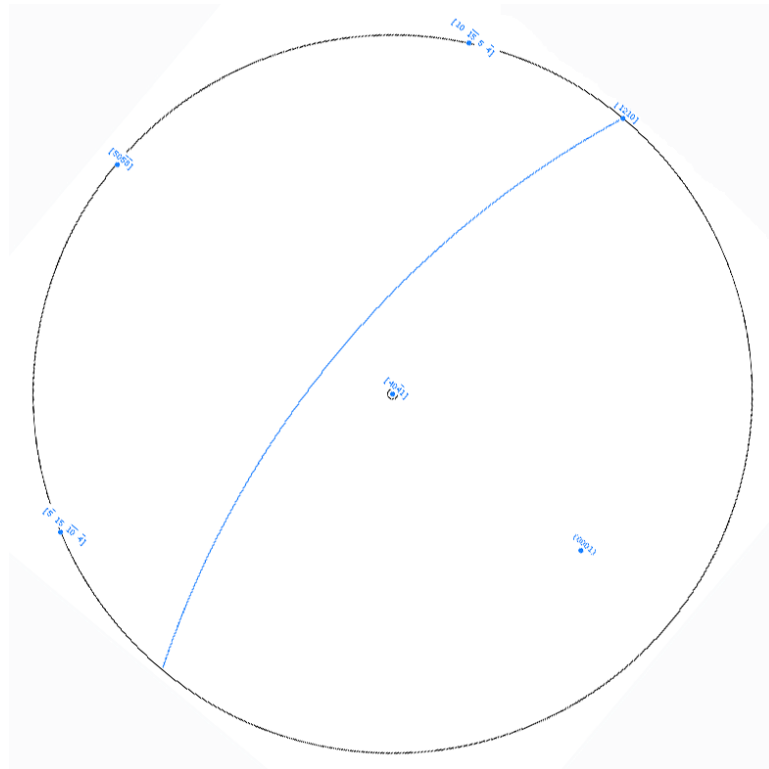
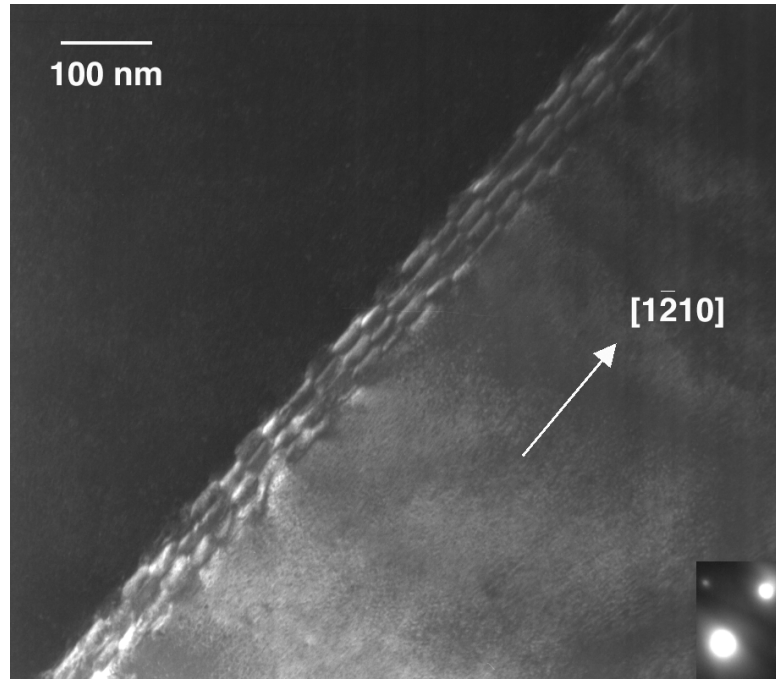


Figure 4.3. (a) Centered dark-field (CDF) image of inclined twist boundary S3 with primary dislocations in a ($g_b=0$) invisibility condition. (b) Stereogram shows orientation of the basal plane.

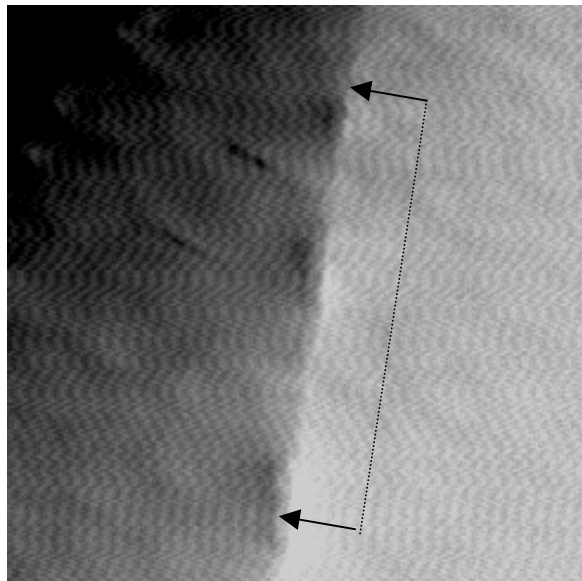
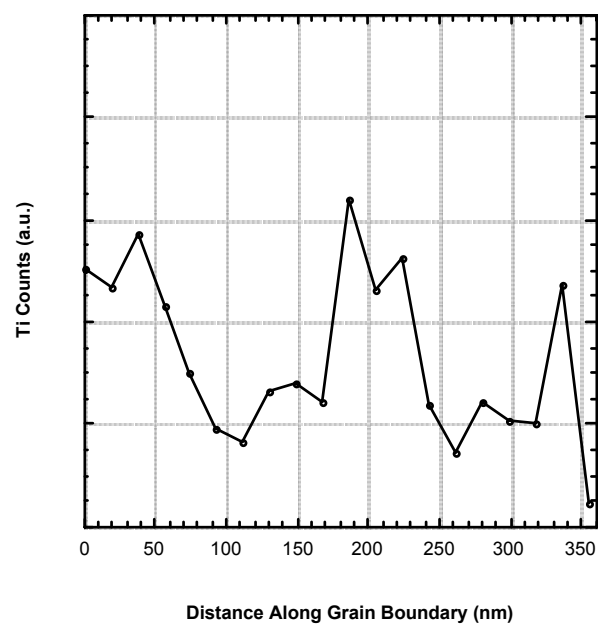


Figure 4.4. (a) EELS chemical profile along twist boundary S3 shows distinct Ti peaks at regions of strain contrast, as seen in (b) the annular dark-field image.

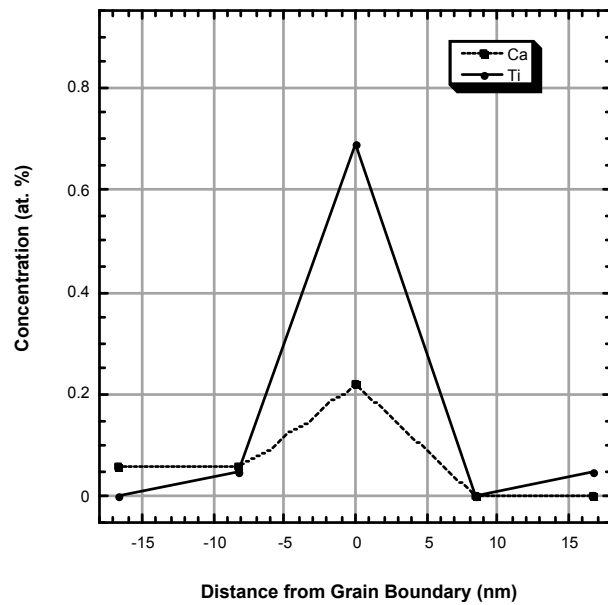
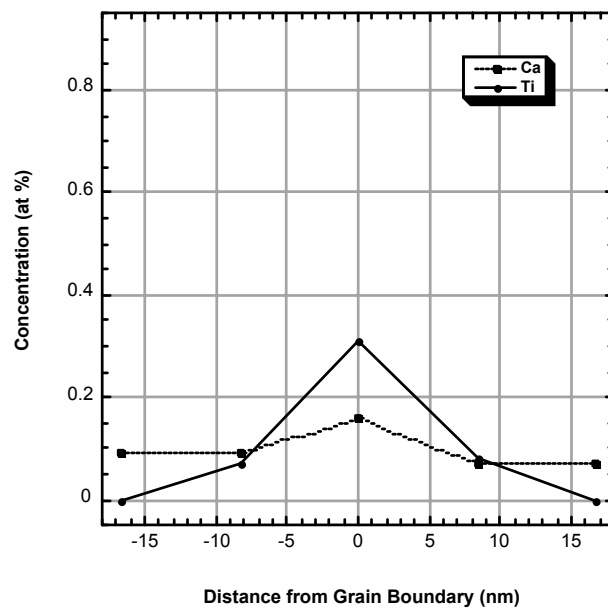


Figure 4.5. EDS line profiles across (a) perfect and (b) dislocated grain boundary regions in S3 show dramatic changes in Ti concentration between the two sites.

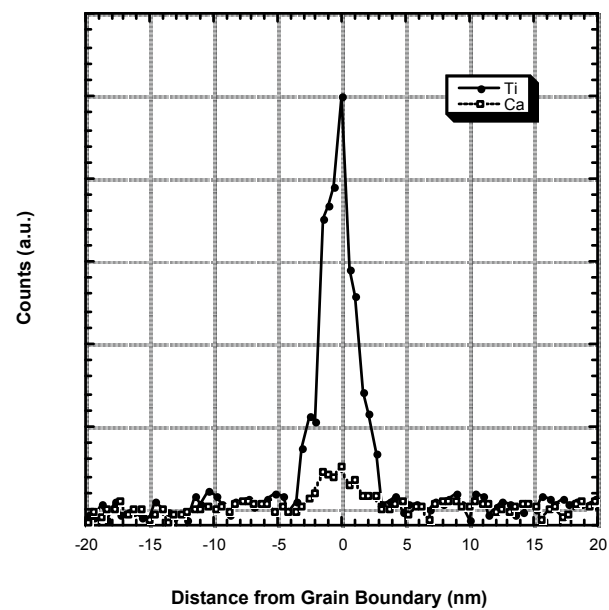
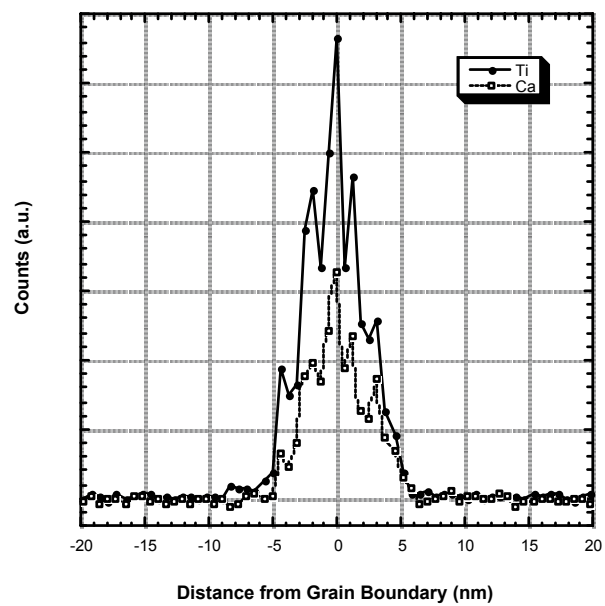


Figure 4.6. EELS line profiles across (a) perfect and (b) dislocated grain boundary regions in S3 show dramatic changes in Ti concentration between the two sites.

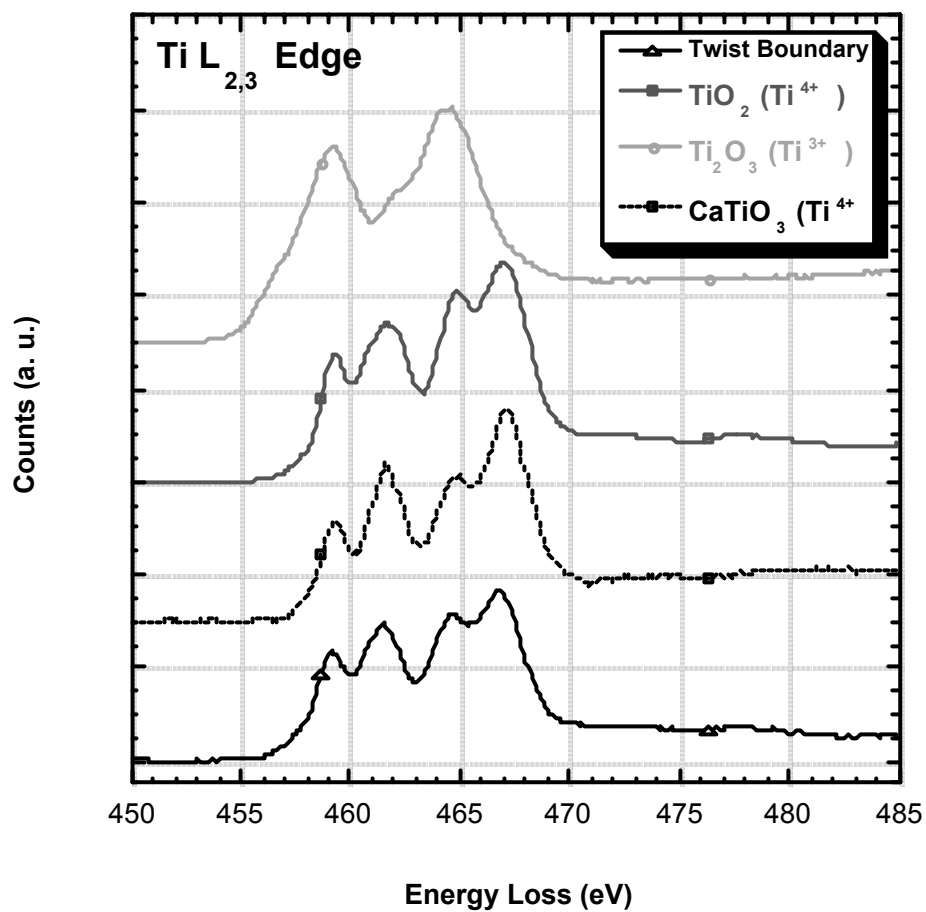


Figure 4.7. Comparison of Ti $L_{2,3}$ edges from various Ti-based oxides (all with octahedral cation coordination) shows that energy-loss near-edge structure can be used to fingerprint Ti valence. Here, Ti solute from the low-angle twist boundary (S3) is identified as Ti^{4+} .

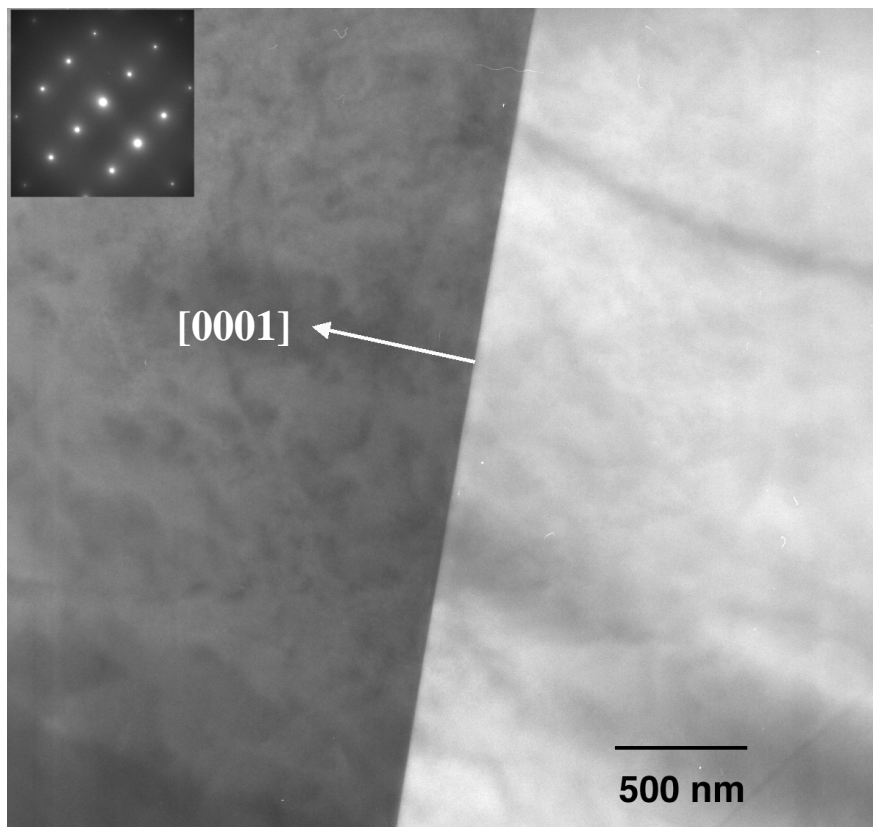


Figure 4.8. Conventional TEM image of high-angle twist boundary (15b) shows a very straight grain boundary plane with no signs of faceting.

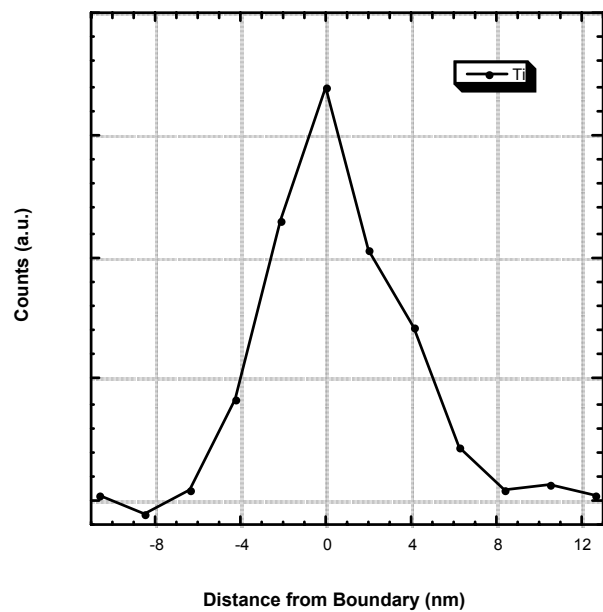
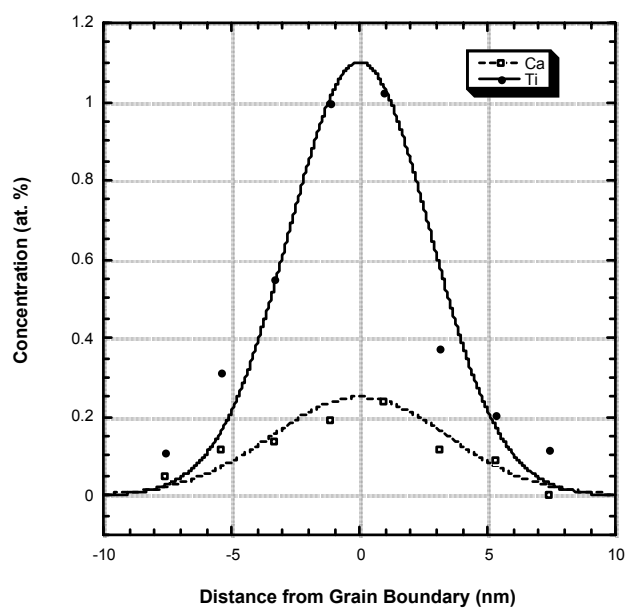


Figure 4.9. (a) EDS line profile across high-angle twist boundary 15b shows strong Ti enrichment. EELS profile in (b) gives an accurate measure of the grain boundary chemical width.

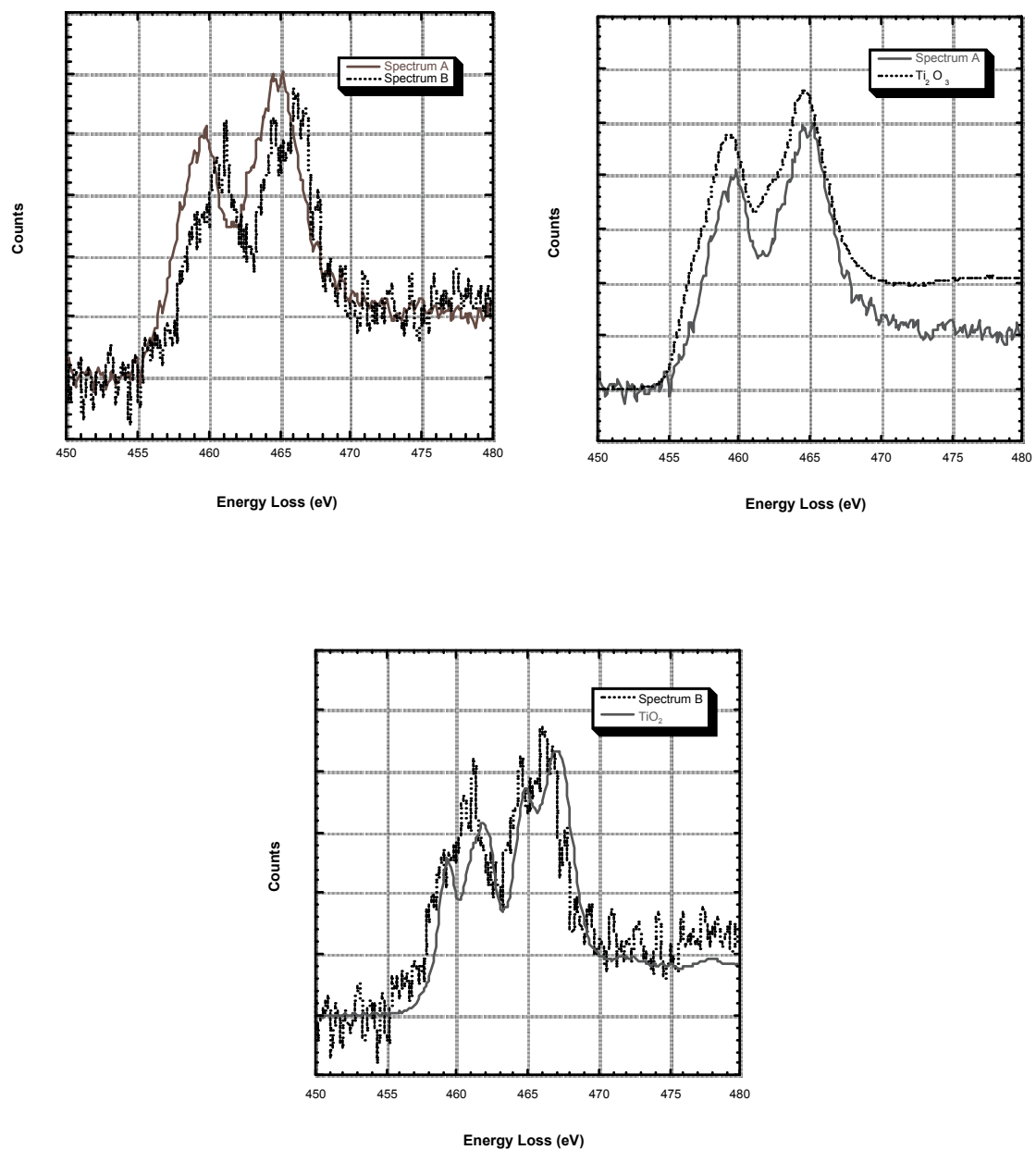


Figure 4.10. (a) Ti L_{2,3} edges acquired near the grain boundary show different near-edge structure. Comparison with spectra from (b) Ti₂O₃ and (c) TiO₂ demonstrates mixed valence in twist boundary 15b.

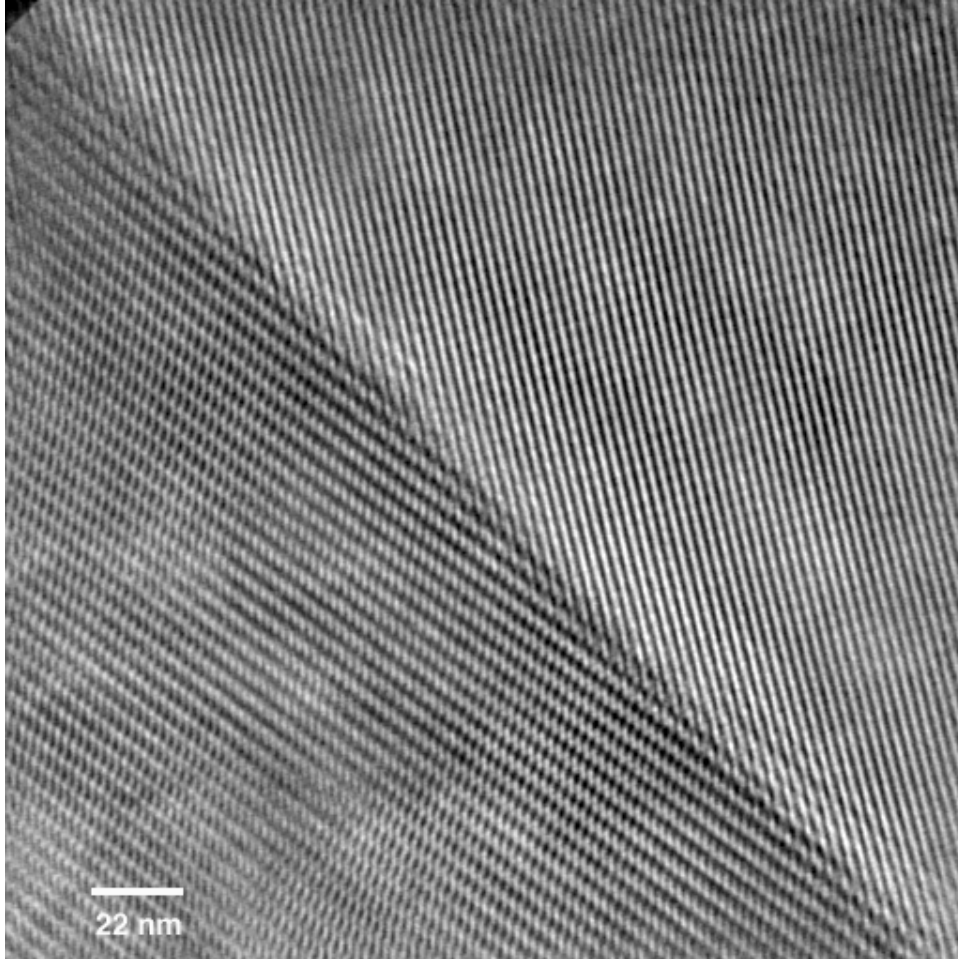


Figure 4.11. Phase contrast image of twist boundary 12a reveals a grain boundary plane that is $\approx 8^\circ$ off of (0001) in both crystals. The left crystal is close to a $[10\bar{1}0]$ zone axis while the right crystal is close to $[2\bar{1}\bar{1}0]$.

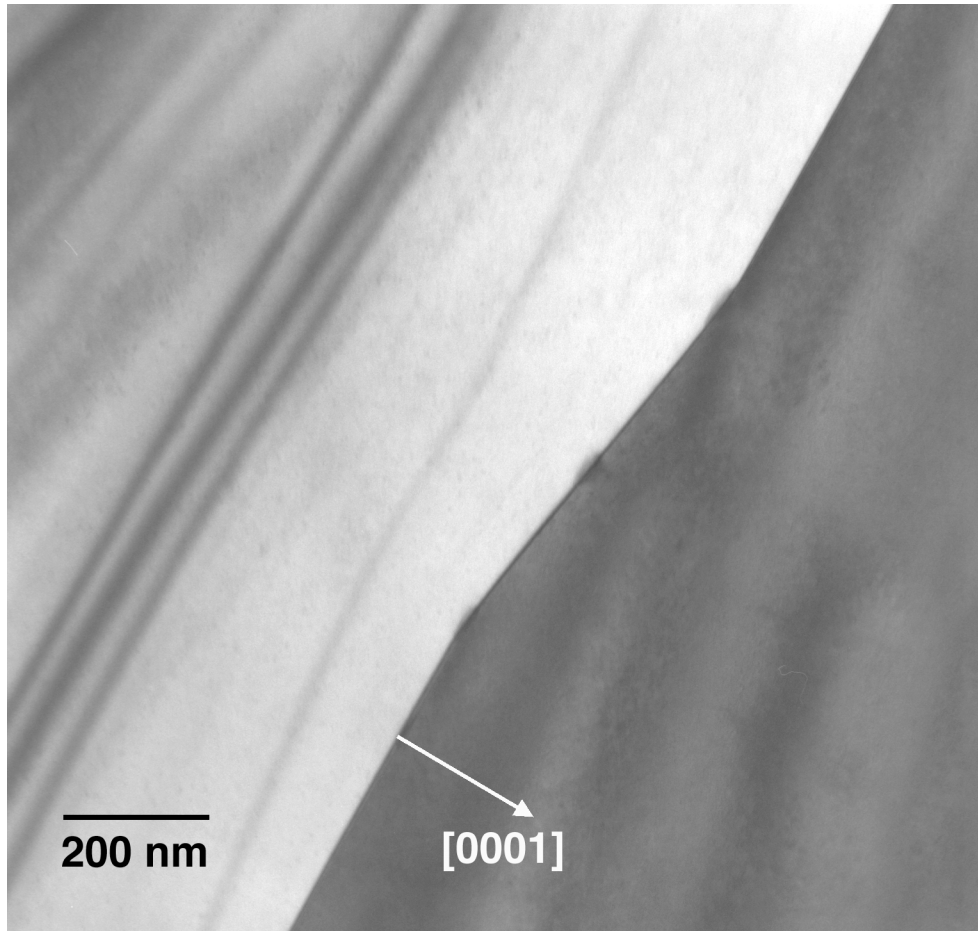


Figure 4.12. Conventional TEM image of twist boundary 12a shows grain boundary faceting off of (0001) onto a high-index plane. The angle between facet planes is 8.6° .

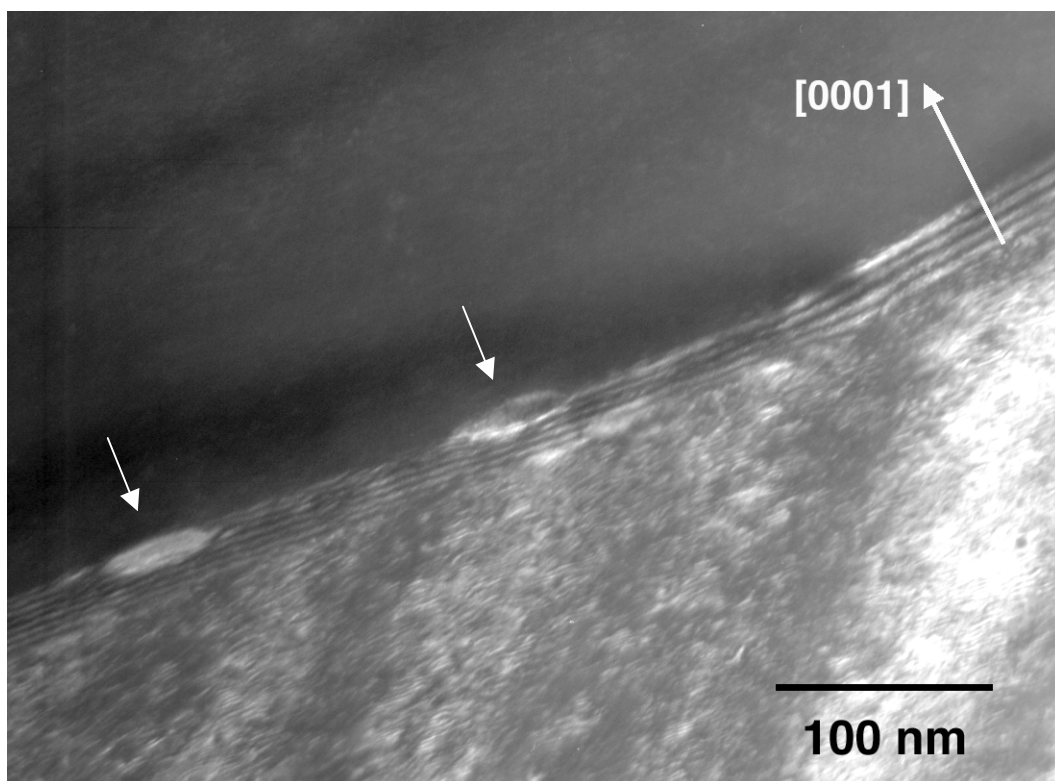
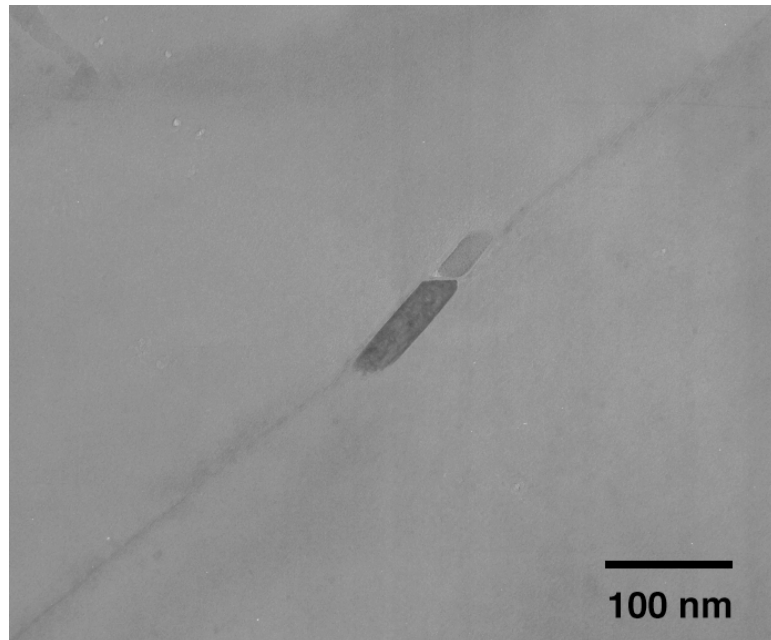
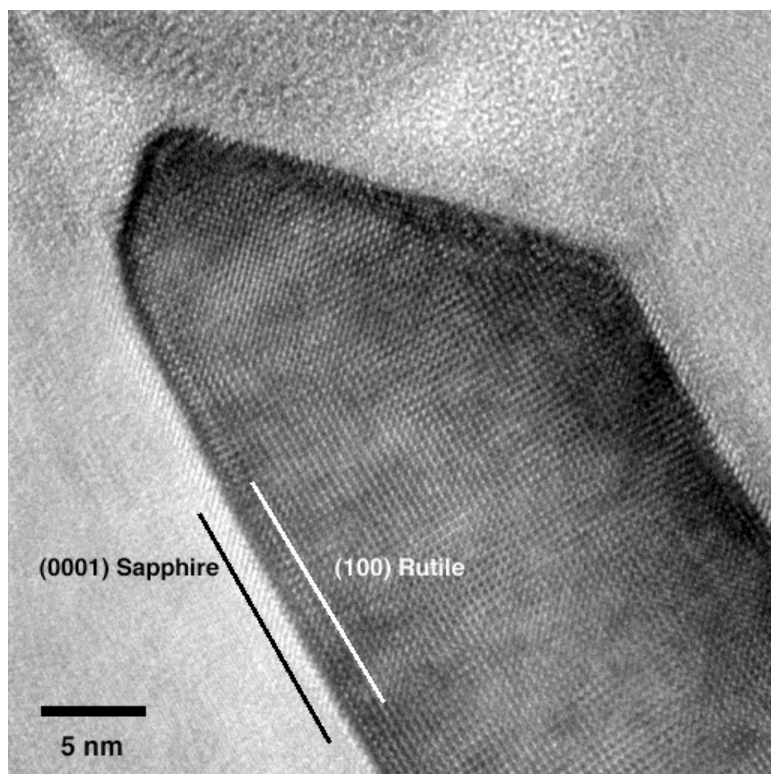


Figure 4.13. Dark-field image of inclined twist boundary 12a reveals small faceted precipitates on the off-basal boundary facet.

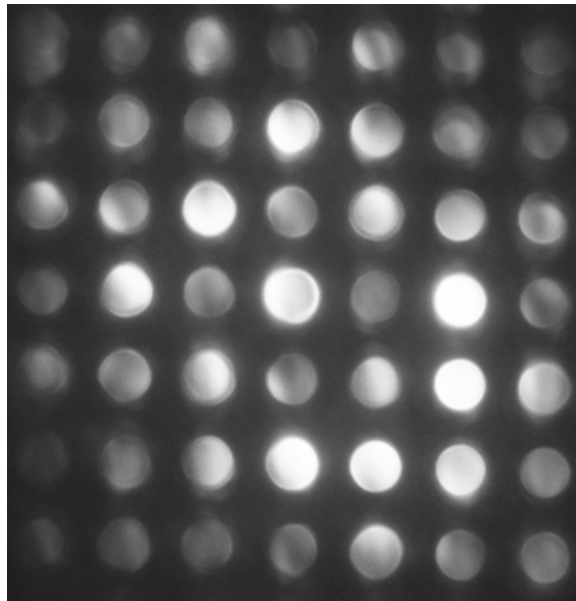


(a)



(b)

Figure 4.14. (a) Conventional and (b) phase contrast TEM images of large precipitate on off-basal facet of 12a. (c) CBED diffraction pattern shows precipitate is rutile TiO_2 phase.



(c)

Figure 4.14 (continued)

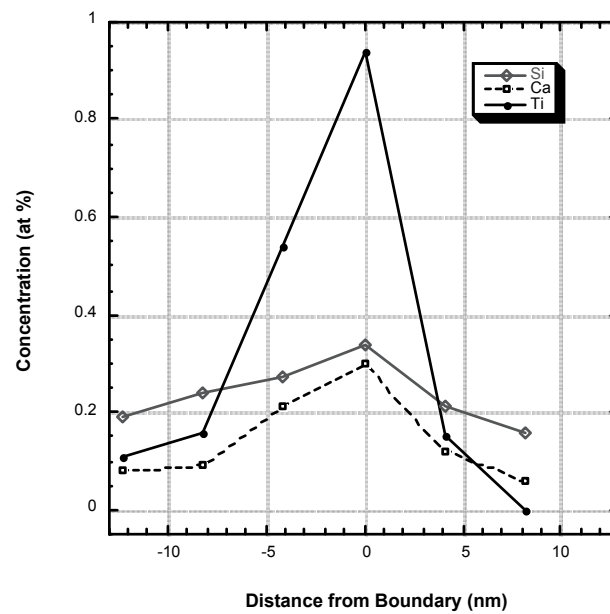
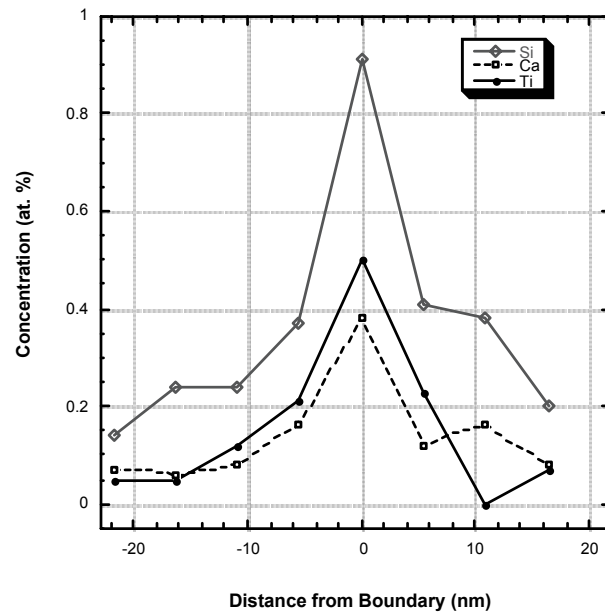


Figure 4.15. EDS line profiles across (a) basal and (b) off-basal facets of twist boundary 12a show pronounced changes in grain boundary chemistry.

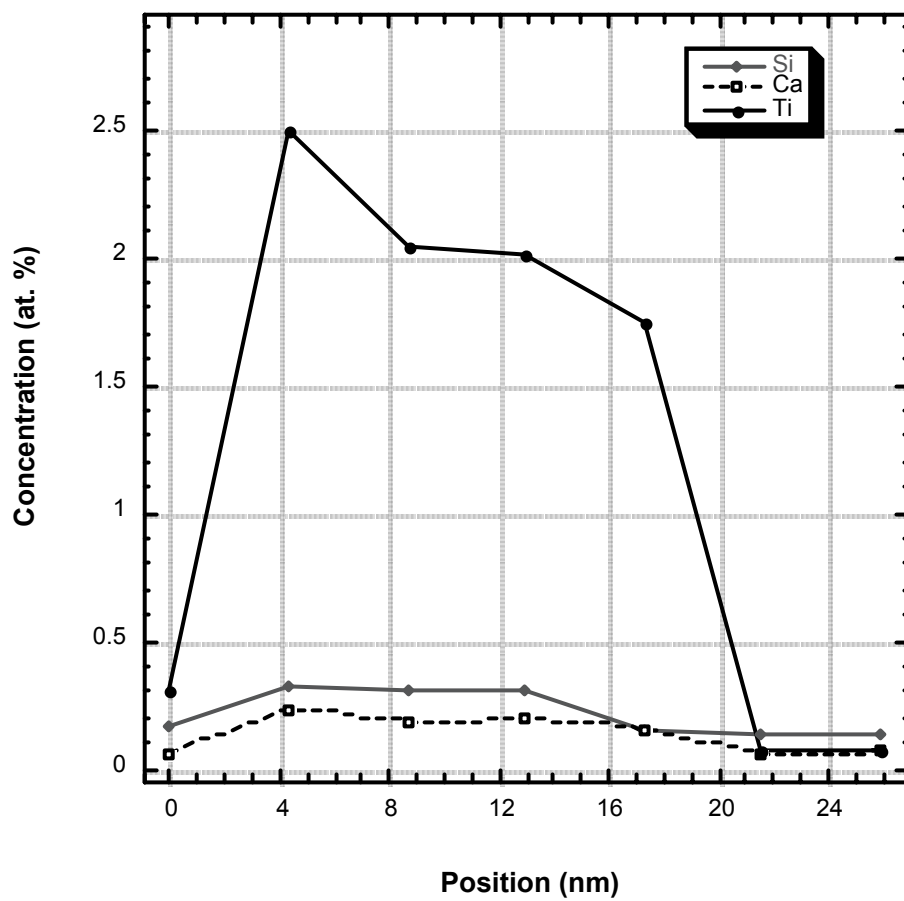


Figure 4.16. EDS line profile through a small precipitate on off-basal facet of twist boundary 12a shows very strong Ti enrichment over 15-20 nm.

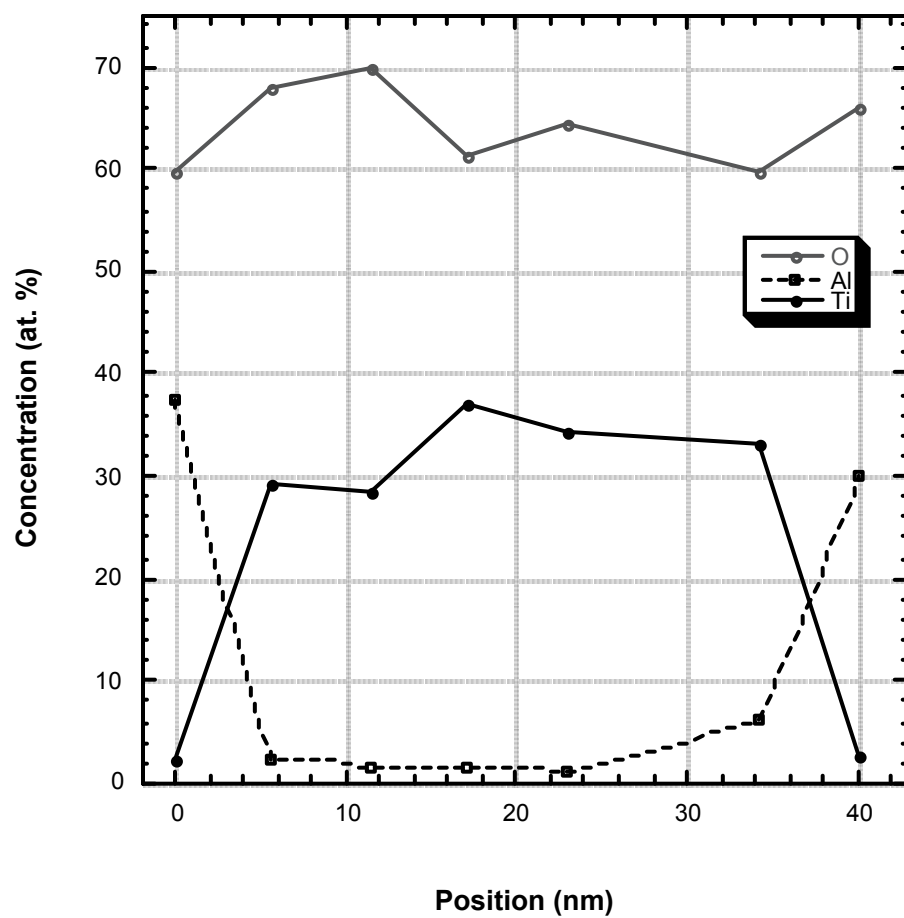


Figure 4.17. EDS line profile through large precipitate on off-basal facet of twist boundary 12a confirms TiO_2 stoichiometry.

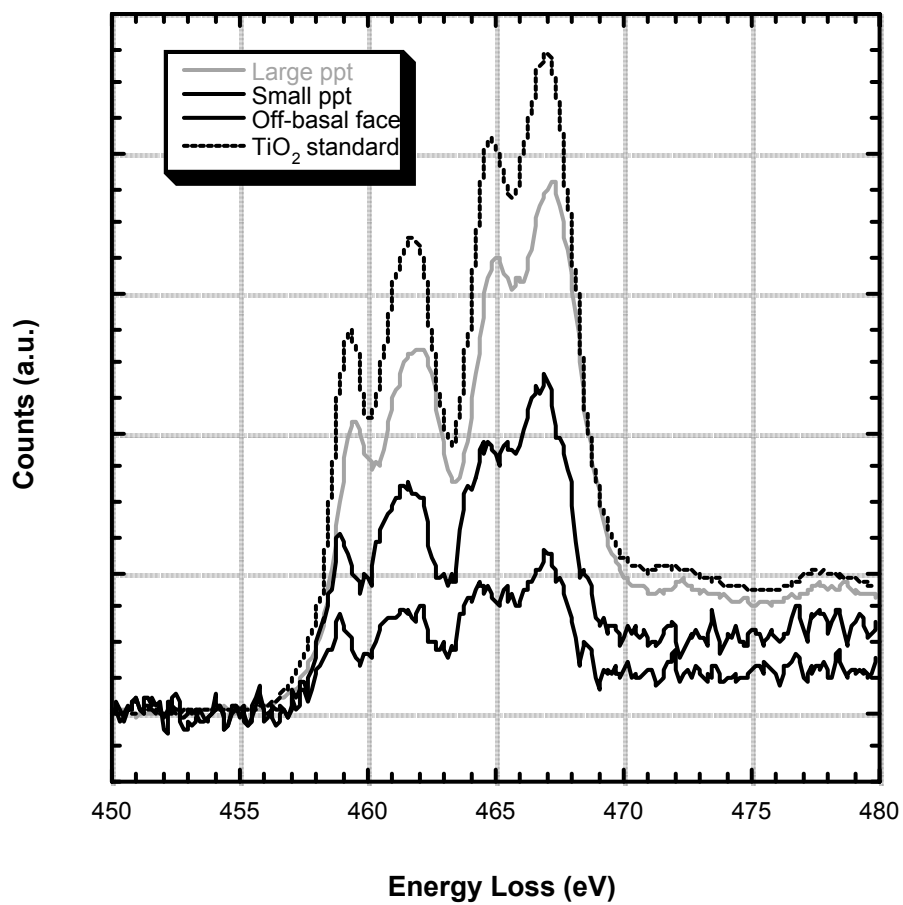


Figure 4.18. Ti $L_{2,3}$ edges acquired at various locations along the off-basal facet of twist 12a all show evidence for Ti^{4+} .

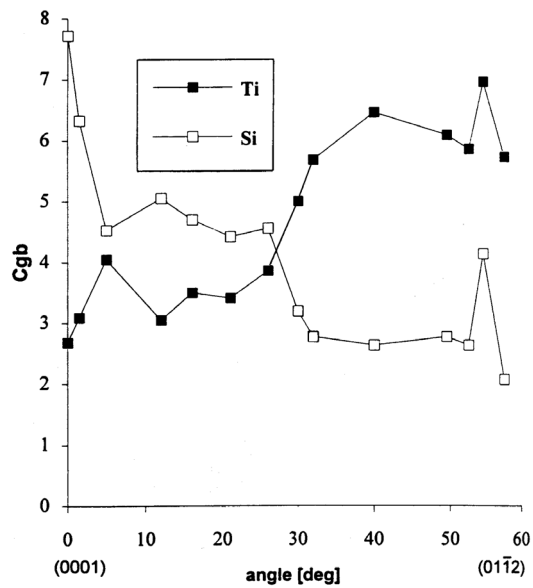
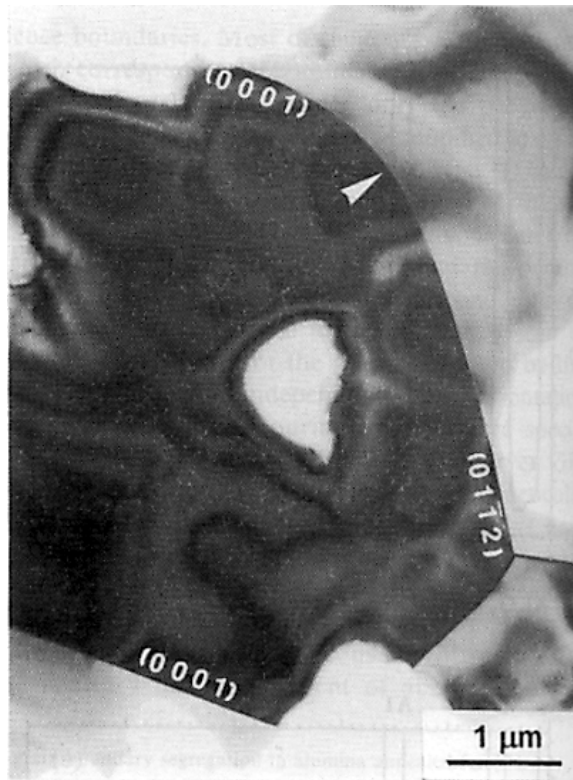


Figure 4.19. (a) TEM image shows a curved grain boundary which changes from (0001) to rhombohedral $(01\bar{1}2)$. (b) Grain boundary chemistry data illustrates dramatic changes in Si/Ti ratio with boundary plane orientation. (Figure reproduced from [6]).

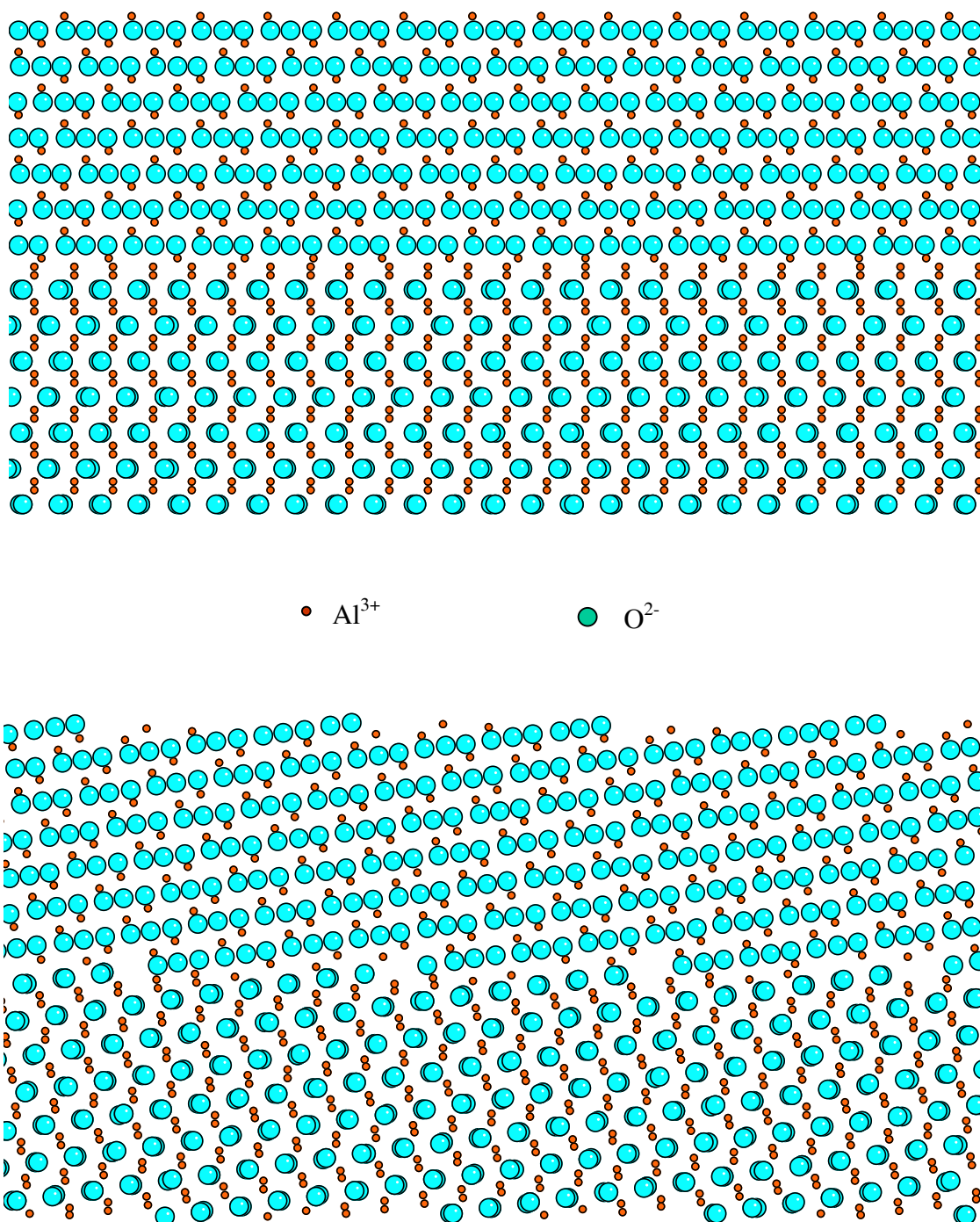


Figure 4.20. Simple structural models of (a) basal and (b) off-basal facets in twist boundary 12a may help explain the acute dependence of grain boundary chemistry on structure.

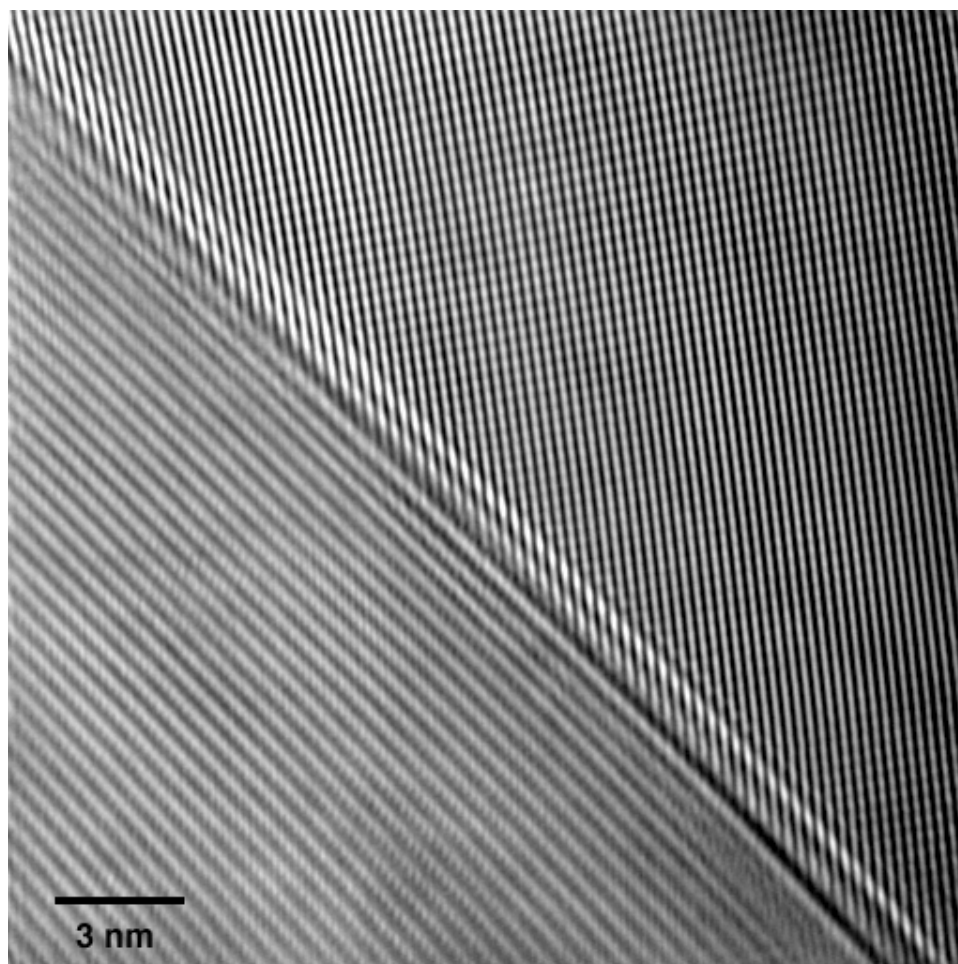


Figure 4.21. Phase contrast image of the quenched twist boundary 12b.

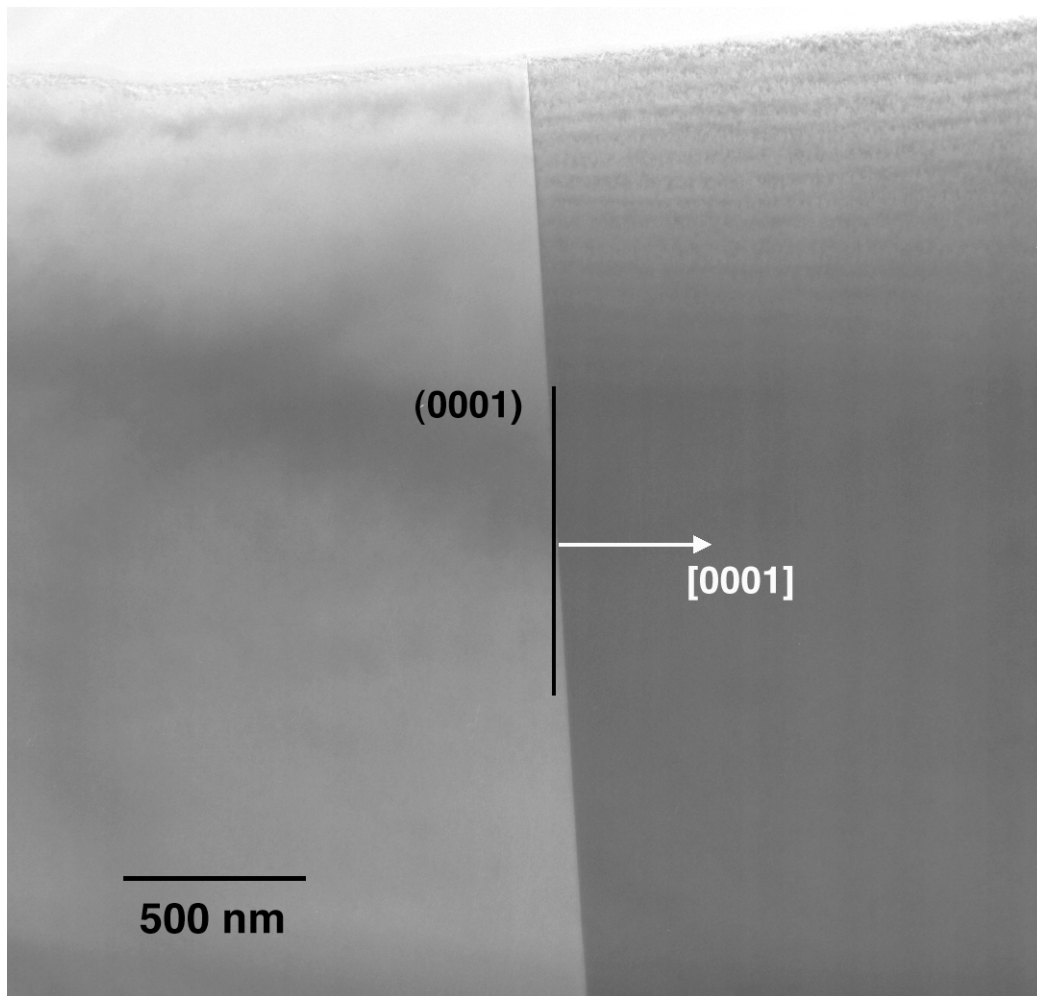


Figure 4.22. Conventional TEM image of the quenched twist boundary 12b shows the grain boundary plane is 3° off of (0001) .

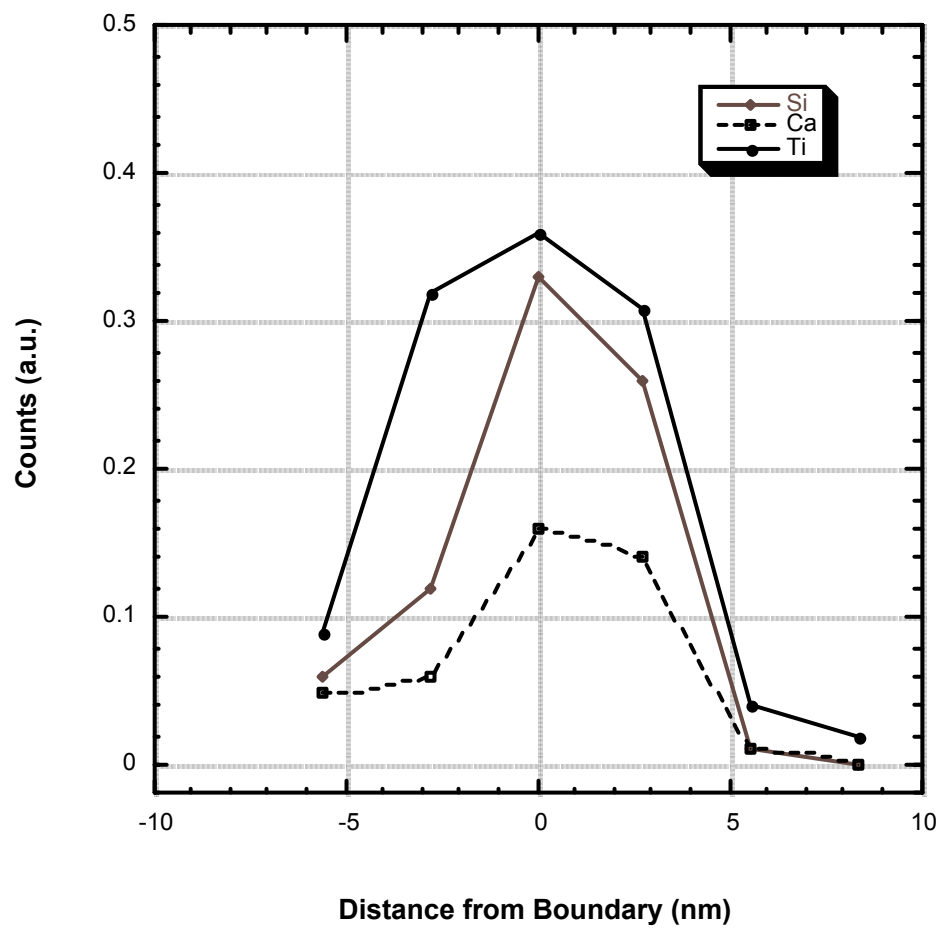


Figure 4.23. EDS line profile across twist boundary 12b shows strong Ti and Si solute enrichment.

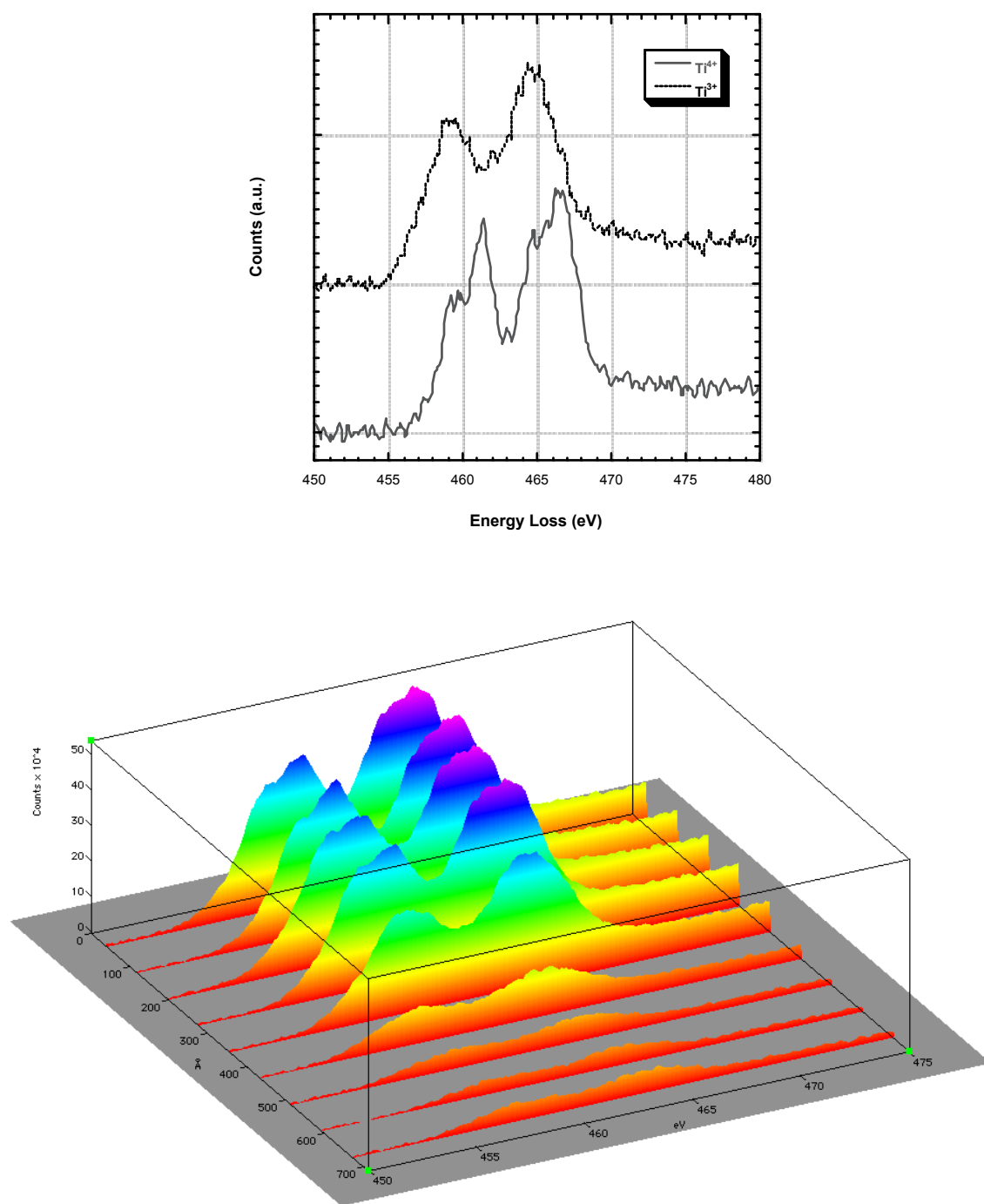


Figure 4.24. (a) Ti L_{2,3} edges acquired just a few nanometers apart show very different near edge structure. (b) A series of spectra acquired near the boundary illustrate a clear change from Ti³⁺ to Ti⁴⁺ over a range of 30 nm.

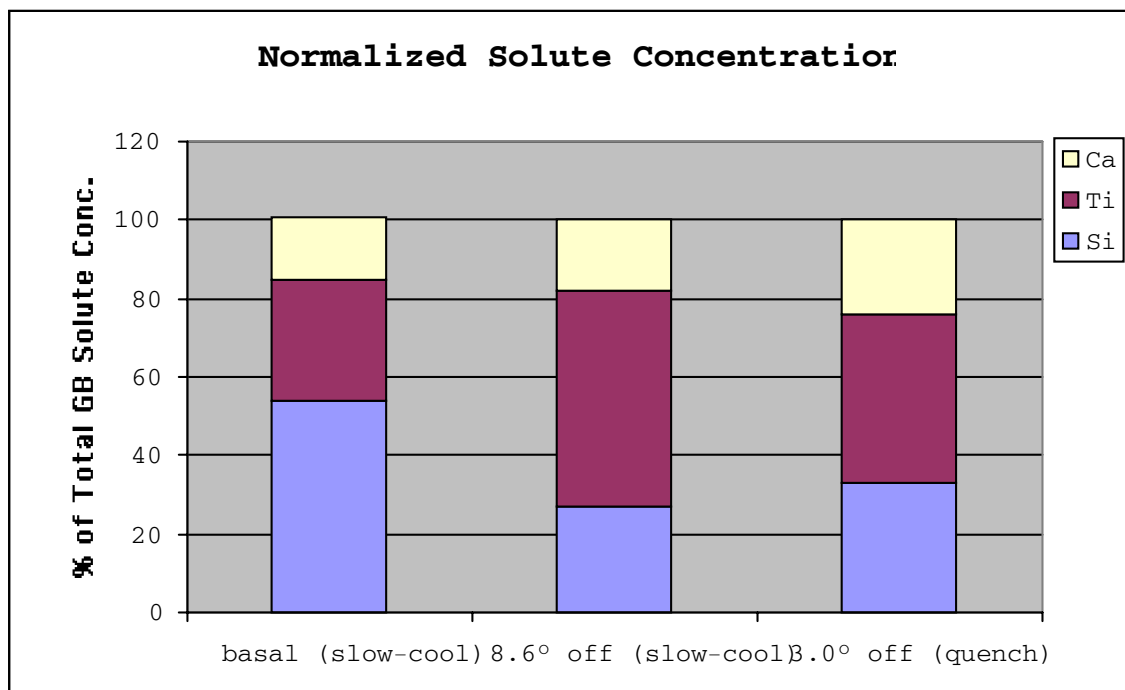


Figure 4.25. Comparison of normalized solute concentration for the various grain boundary planes in twist boundaries 12a and 12b.

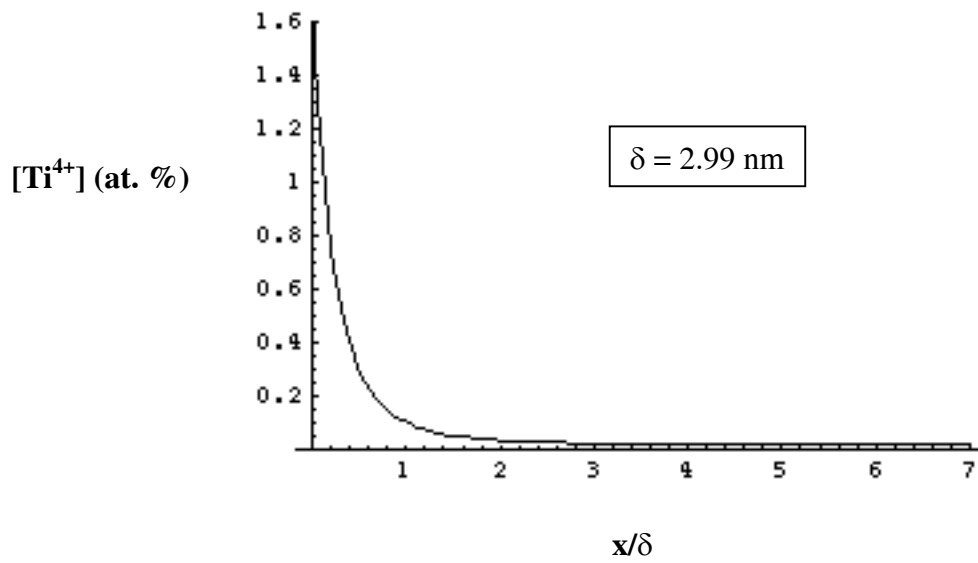
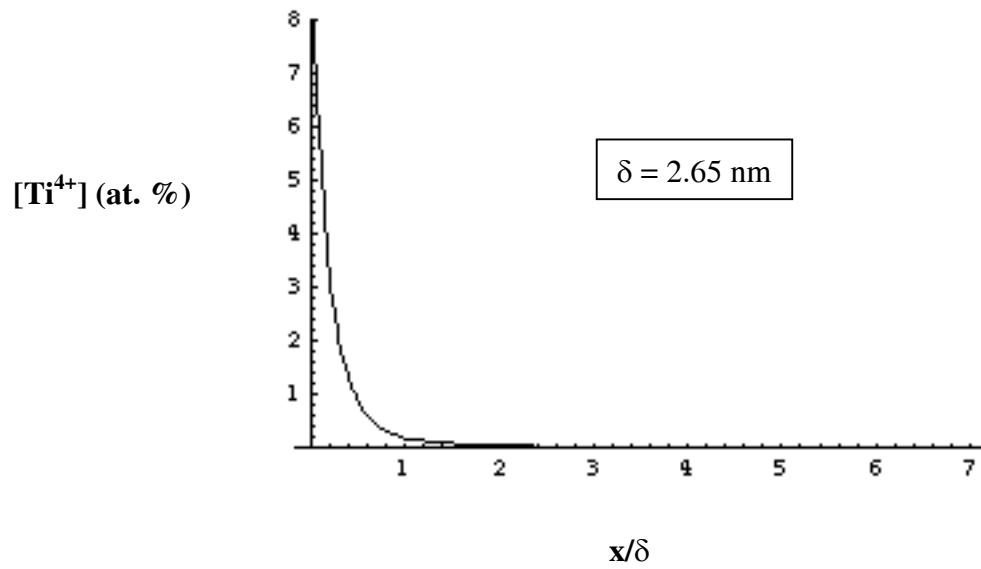


Figure 4.26. Grain boundary solute profiles for Ti^{4+} at (a) 1200°C and (b) 1600°C calculated from space charge theory, assuming 500 ppm (cationic) Ti-doped Al_2O_3 . Solute concentrations are given in at. %.

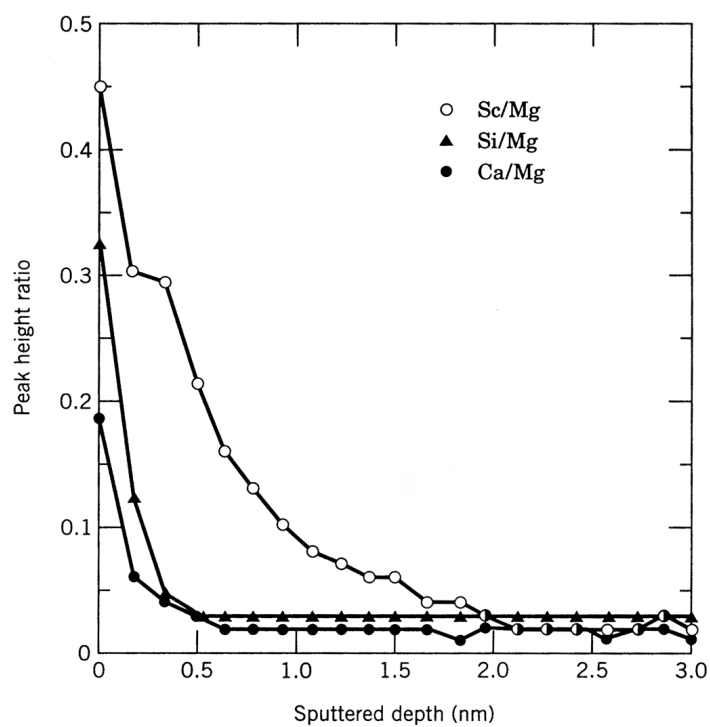


Figure 4.27. Solute profile in MgO demonstrates the tendency for strongly-misfitting solute species (Ca, Si) to adsorb close to the grain boundary core. (Figure reproduced from [24]).

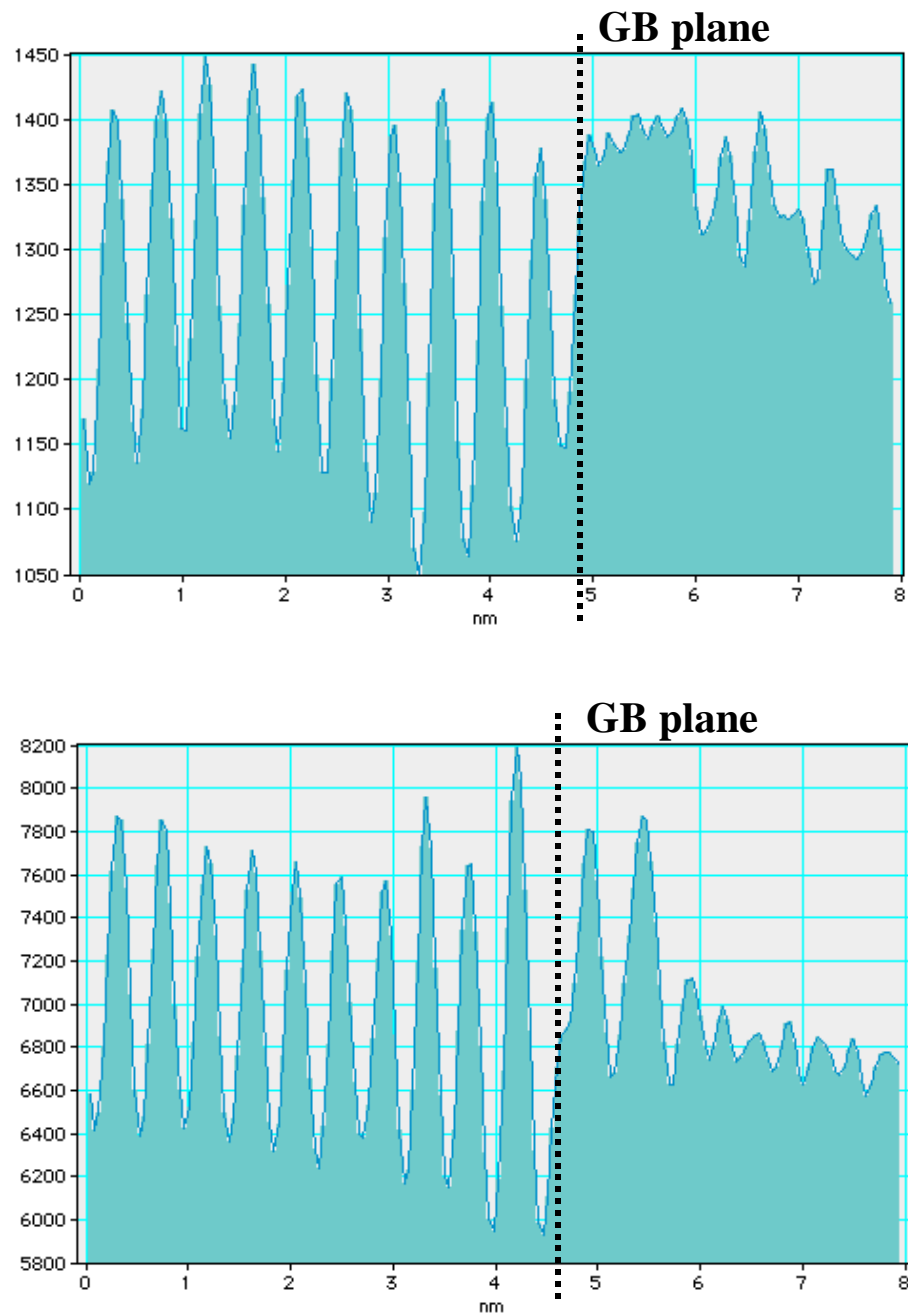


Figure 4.28. Intensity profiles reveal extremely consistent spacing of (0003) planes near the grain boundary in (a) twist boundary 12a (Figure 4.11) and (b) twist boundary 12b (Figure 4.21), refuting the idea that thermally-induced lattice distortion adjacent to the grain boundary is responsible for extensive segregation of Ca solute.

Chapter Five

THE STRUCTURE AND CHEMISTRY OF BASAL TILT BOUNDARIES

5.1. Low-Angle Tilt Boundary (Tilt1)

5.1.1. Processing Conditions

Alumina powder was Ti-doped (500 ppm cat.) and cold-pressed to form a polycrystalline compact. A polished slice of polycrystalline material was placed on top of a sapphire tilt seed (with nominal 10° misorientation), and the stack was diffusion-bonded at 1300°C for 2 hours at 10 MPa. To promote growth of the tilt boundary, the stack was annealed at 1600°C for 375 hours in air, then at 1800°C for 125 hours in vacuum before a final treatment at 1600°C for 5 hours in vacuum. The bicrystal assembly was furnace-cooled to room temperature at approximately $30^\circ\text{C}/\text{min}$.

5.1.2. Grain Boundary Structure

A phase-contrast image of the low-angle tilt boundary is shown in Figure 5.1. The grain boundary is atomically-sharp and free of any continuous or discrete second phases. Quantitative analysis of the angle between $(11\bar{2}0)$ planes at the grain boundary allows accurate determination of the misorientation angle, measured here as $9.8 \pm 0.5^\circ$ -- just slightly off of the intended misorientation of 10° . The grain boundary plane in this particular region is approximately 4.9° off of a low-index $(11\bar{2}0)$ plane of each crystal,

illustrating its symmetric tilt character. According to Marks [1], each sapphire seed crystal was cut at an angle of $\approx 5^\circ$ off of a straight $\{1\bar{1}20\}$ edge, so the original interface plane for the tilt boundary seed appears to have been preserved fairly accurately in the final processed bicrystal.

Periodic regions of mottled contrast can be seen along the grain boundary plane of Figure 5.1. These regions represent edge dislocations that form at the grain boundary to accommodate the geometric misfit between the two grains. Interactions between the incident electrons and the dislocation strain field cause the mottled contrast at the dislocation cores. To verify that these features are in fact dislocations, a Burgers circuit has been constructed around the dislocation core as shown in the figure. The resulting closure failure suggests a $\frac{1}{3}[1\bar{1}20]$ perfect Burgers vector with magnitude 4.76 Å.

A processed Moiré image, formed using Fourier components of periodic $\{1\bar{1}20\}$ planes, clearly exposes the grain boundary dislocations and their periodic spacing, as shown in Figure 5.2. For low angle tilt boundaries, the spacing of periodic edge dislocations, D , should depend on the misorientation angle θ and the magnitude of the dislocation Burgers vector \mathbf{b} , according to Frank's formula:

$$\theta = \frac{|\mathbf{b}|}{D} \quad (5.1)$$

Equation 5.1 predicts a periodic dislocation spacing of 28.0 Å, compared to a measured spacing of 27.5 Å.

Structural models of the tilt boundary were constructed to determine the grain boundary plane, and to permit comparison between experimental images and HRTEM image simulations. The latter is required to determine the origin and nature of the

contrast – either white columns of atoms on a black background, or black columns on a white background -- observed in Figure 5.1. Phase contrast images represent complex interference patterns between electron waves and the crystal lattice. As such, the relationship between an experimental HRTEM image and the atomic (or ionic) structure of the crystal is typically neither obvious nor intuitive. To accurately determine this relationship, HRTEM images are usually calculated over a range of objective lens defocus and specimen thickness values to obtain a suitable match with the experimental image. Then, the model structure is superimposed on the calculated image to determine how crystal structure and phase-contrast image are related.

A structural model of the tilt boundary region is shown in Figure 5.3a. Aluminum cations are the small blue circles, while oxygen anions are the larger yellow circles. The grain boundary plane in the model is a symmetric $(3\bar{7}40)$ plane. Figure 5.3b compares a “best match” simulated image (inset) to the experimental image of Figure 5.1. The close matching of these images confirms a $(3\bar{7}40)$ grain boundary plane. Indeed, the angle between $(3\bar{7}40)$ and $(1\bar{1}20)$, calculated from known crystallographic equations, is 4.72° , consistent with measurements from the HRTEM image. In Figure 5.3c, the structural model is superimposed on the calculated image to illustrate that the white columns observed in both images coincide with the positions of Al^{3+} cation columns. Oxygen anions cannot be resolved in either image.

In other regions of the specimen, experimental images reveal grain boundary faceting off of the original $(3\bar{7}40)$ plane, as illustrated in Figure 5.4. Although one of the crystals is tilted slightly off of $[0001]$, the facet plane can still be identified as

$\{10\bar{1}0\}$ -type, and the adjoining boundary planes both appear to be $\{3\bar{7}40\}$ -type. Facets along $\{10\bar{1}0\}$ were found to occur periodically along this particular segment of the boundary, but unfortunately, the spacing between faceted segments was not quantified.

Conventional TEM images acquired from thicker regions of the specimen show more pronounced faceting of the grain boundary plane. Figure 5.5a is a bright-field image of the grain boundary, with the [0001] diffraction pattern from the bottom (dark) crystal inset for crystallographic labeling. One set of facets is observed to be perfectly parallel to $(10\bar{1}0)$, while the other set of facets deviates slightly from $(11\bar{2}0)$. As Figure 5.5b demonstrates, these results were reproducible at various locations along the grain boundary. That is, one set of facets is always parallel to $(10\bar{1}0)$, while the other set is a few degrees off of $(11\bar{2}0)$. For the latter, estimates of the exact deviation from a perfect $(11\bar{2}0)$ plane ranged between 4.3 and 4.9° (with a measuring error of approximately 0.5°), as measured from numerous facets in various images acquired at different locations. This data suggests that $(3\bar{7}40)$ is a stable grain boundary facet; $(11\bar{2}0)$ facets are not observed at the tilt boundary, even though these might be anticipated due to their low-index and, presumably, low energy.

Diffraction-contrast images of the inclined grain boundary suggest a possible link between grain boundary dislocations and the faceting process. Careful inspection of Figure 5.6a, a dark-field image of the inclined grain boundary, reveals the presence of grain boundary dislocations (exhibiting white contrast) at the junction of two facet planes. The $(3\bar{7}40)$ and $(10\bar{1}0)$ planes are labeled in the figure as A and B, respectively. As illustrated in the schematic of Figure 5.6b, dislocations are only

observed at the convex transition from A to B, and are not seen at the concave transition from B to A. Two-beam imaging using various g-vectors did not yield evidence of any other types of dislocations at the facet junctions.

5.1.3. Grain Boundary Chemistry

Chemical microanalysis was performed at the different facet planes to quantitatively measure solute concentrations. Figure 5.7a shows a representative EDS line profile from the $(3\bar{7}40)$ grain boundary plane. The peak Ti concentration is measured at just over 1.0 at. %, while the Ca and Si concentrations do not exhibit any appreciable concentrations. Figure 5.7b, an EDS line profile across the faceted $(10\bar{1}0)$ plane, reveals a dramatic decrease in Ti solute concentration relative to the original boundary plane. The peak Ti concentration has dropped approximately 50%, while Ca and Si concentrations still seem to be negligible. Quantitative microanalysis of the two grain boundary planes was repeated on several different facets, and results were reproducible within 10% error. The grain boundary chemical width was consistently measured as 15-17 nm from EDS line profiles.

Despite significant concentrations of Ti solute at the grain boundary, crisp energy-loss spectra proved difficult to acquire, complicating determination of Ti valence. Figure 5.8 shows a characteristic Ti $L_{2,3}$ edge acquired near the tilt boundary, compared with the Ti $L_{2,3}$ edge from Ti_2O_3 . Despite a low signal-to-noise ratio in the tilt boundary spectrum, qualitative matching of the near-edge structural features suggests predominantly Ti^{3+} exists at the tilt grain boundary. This finding is consistent with the fact that the sample was annealed extensively at high-temperature in reducing

atmospheres. Attempts to measure Ti valence at the different facet planes were thwarted by very weak Ti $L_{2,3}$ edge signals, but given the processing environment, Ti^{3+} is assumed to exist throughout the specimen.

5.1.4. Origins of Grain Boundary Faceting

A number of reasons could be set forth to explain the grain boundary faceting observed in the low-angle tilt boundary. A simple explanation is energy minimization: the boundary could facet along low-index (and presumably low-energy) planes in one of the grains to minimize the total grain boundary energy. In a similar fashion, the grain boundary could facet along planes of the CSL possessing high planar coincidence site density (PCSD), which are also known to be low-energy grain boundary planes [2]. An alternative hypothesis is that excess Ti solute has segregated to the boundary in a nonequilibrium fashion as a result of slow-cooling, ultimately leading to grain boundary faceting. The validity of each argument in describing the grain boundary structure of this sample will now be examined.

According to calculations by Grimmer [3] and Bruggeman [4], the $9.8^\circ[0001]$ basal tilt boundary is not predicted to be a “special” grain boundary in Al_2O_3 , which is to say that the number of coincidence lattice sites shared by both grains should be quite low. However, geometric analysis of the interpenetrating lattices, using two hexagonal arrays rotated by 9.8° about their common $[0001]$ axis as shown in Figure 5.9, suggests that this misorientation is very close to a $\Sigma 37$ grain boundary. Several unit cells of the $\Sigma 37$ CSL are included in the figure to demonstrate the translational periodicity of the CSL. The repeat distance between any two coincident sites lying on the same plane

(referenced to the original hexagonal lattice) is found to be 37 atoms, consistent with a $\Sigma 37$ CSL. Also shown in the figure is the $(10\bar{1}0)$ plane for each crystal (dashed lines), as well as the $(3\bar{7}40)$ grain boundary plane (bold line).

Figure 5.10 depicts a structural model of the faceted tilt boundary. The two primary grain boundary facets, $(3\bar{7}40)$ and $(10\bar{1}0)$ are, respectively, parallel to a high PCSD plane of the CSL, and parallel to a low-energy plane in one of the grains. The $(10\bar{1}0)$ plane does not coincide with any high-PCSD planes of the CSL. Each plane represents a distinct type of low-energy structure (either for one of the crystals, or for both), but it is not immediately clear which facet plane is more energetically favorable. The relative stability of each facet plane ultimately depends on temperature and the grain boundary solute concentration. Attempts to understand the evolution of grain boundary faceting in this tilt-boundary sample therefore require consideration of both parameters.

Little is known about the equilibrium grain boundary structure of the tilt boundary at high temperature. Is the boundary faceted? Direct observation of ceramic grain boundaries at high temperature has, to the author's knowledge, not been reported. Work by Hsieh and Balluffi on low- Σ tilt boundaries in pure Al and Au demonstrates that initially-faceted boundaries tend to roughen (de-facet) at high temperature [5]. However, highly stable faceted boundaries require homologous temperatures close to unity before the onset of roughening. Intuitively, one might anticipate grain boundary roughening to occur at higher temperatures in an effort to reduce the extra energy associated with facet edges. Moreover, higher-entropy grain boundary phases might be anticipated at high temperatures [2], which would also favor curved or roughened grain boundary structures as opposed to faceted ones. But extremely long times may be

required to permit sufficient motion of the boundary in its evolution towards a “structural” equilibrium.

Regardless of the equilibrium grain boundary structure at high temperature, faceting might be expected upon cooling due to surface energy considerations. Kitayama [6] has shown that relative surface energies in sapphire exhibit greater anisotropy as temperature decreases from 1800°C to 1600°C²¹. If the trend towards greater anisotropy in surface energy continues with further cooling, large differences in surface energies should promote faceting onto low-energy planes. But since thermal equilibrium is not maintained during cooling in this study, faceting may not occur along the overall lowest-energy planes, but rather along planes which *locally* have the lowest-energy. This obviously follows from kinetic constraints on grain boundary mobility, and the boundary’s inability to adopt any plane of its choosing.

5.1.5. The Role of Solute in Grain Boundary Faceting

As discussed in Chapter 4, grain boundary faceting in a furnace-cooled twist boundary appears to be driven by the accommodation of excess grain boundary solute. The grain boundary facets off of a very stable (0001) plane onto a high-index plane in an effort to accommodate Ti^{4+} solute. Since a quenched sample of the exact misorientation and solute content does not exhibit this behavior, it is presumed that slow-cooling of the bicrystal is responsible for nonequilibrium solute segregation to (and hence faceting of) the grain boundary. The tilt boundary under consideration was also slow-cooled from

²¹ This effect is attributed to enhanced solute segregation to surfaces at lower temperature, as well as to intrinsic differences in a surface’s ability to accommodate the solute.

1600°C and may have resorted to a similar faceting mechanism to accommodate nonequilibrium solute enrichment.

In the absence of solute, we might expect certain crystallographic planes to be favored facet planes, but in the presence of solute, is it valid to assume that these planes would still be preferred? Unfortunately, detailed information regarding possible effects of solute on the relative stability of *grain boundary planes* in Al_2O_3 is lacking.

However, previous studies measuring the Wulff shape in doped and undoped sapphire crystals may offer some insight regarding the effects of solute segregation on relative grain boundary energies. Kitayama [6, 7] examined how various dopants (Mg^{2+} , Ca^{2+} , Ti^{3+} and Ti^{4+}) modified the Wulff shape of sapphire at high temperature. He demonstrated that solute segregation to surfaces can have a significant effect on surface energy anisotropy. In this regard, Ti^{3+} appeared to make the Wulff shape more isotropic, while Ti^{4+} was found to promote surface energy anisotropy, disproportionately affecting the surface energy of different planes.

Extending these results to internal interfaces, there is reason to believe that grain boundary solute content could stabilize a facet plane that is not energetically favored in undoped material. Consequently, the accumulation of solute species should not be overlooked as a factor affecting the final grain boundary structure. Based strictly on surface energy considerations, one might expect the tilt boundary to facet along low-index $\{10\bar{1}0\}$ and $\{11\bar{2}0\}$ planes upon cooling. Accounting for strong Ti enrichment, however, may explain why the grain boundary adopts a $(3\bar{7}40)$ facet. Perhaps the boundary tries to facet along $(11\bar{2}0)$, but its mobility is restricted by a high solute concentration, and its structure is therefore kinetically frustrated. Or perhaps the $(3\bar{7}40)$

plane is favored because its atomic structure can better accommodate Ti solute. Or maybe that facet's stability is imparted by a combination of efficient solute accommodation and a high density of coincident sites. The exact mechanism responsible for stabilizing the $(3\bar{7}40)$ plane is not currently known, but it presumably relates in some manner to its high Ti concentration.

5.1.6. Grain Boundary Dislocations

5.1.6.1. Perfect versus Partial Dislocations

Ikuhara and co-workers have studied the dislocation structure in low-angle grain boundaries of undoped sapphire bicrystals [8, 9]. They found evidence for perfect (non-dissociated) $\frac{1}{3}[11\bar{2}0]$ dislocations at very low-angle tilt boundaries ($\theta < 1^\circ$), whereas higher-angle tilt boundaries ($1^\circ < \theta < 10^\circ$) contained $\frac{1}{3}[10\bar{1}0]$ partial dislocations separated by ribbons of faulted material. Calculations of total grain boundary energy revealed that for misorientation angles greater than $\approx 0.5^\circ$, the faulted grain boundaries (containing partial dislocations) have lower energies than those containing perfect dislocations [10], as shown in Figure 5.11. These calculations suggest that perfect grain boundary dislocations should only be energetically-favored at very small tilt misorientations in undoped sapphire, consistent with their experimental findings.

Results from this study show that perfect $\frac{1}{3}[11\bar{2}0]$ grain boundary dislocations are favored at fairly high misorientation angles (9.8°) in Ti-doped sapphire bicrystals – a clear departure from the findings of Ikuhara et al. The implication is that Ti solute may play a role in stabilizing the perfect dislocations to higher misorientations in basal tilt

boundaries. The presence of Ti solute could conceivably reduce the grain boundary core energy and/or the associated strain energy of the perfect dislocations, or could possibly increase the stacking fault energy associated with dislocation dissociation into partials, relative to the undoped case²². Nonetheless, these results demonstrate the striking effect of solute on grain boundary structure and behavior in alumina, and underscore the importance of continued efforts to understand grain boundary structure-chemistry relationships in ceramics.

5.1.6.2. Facet Junction Dislocations

The observed facet junction dislocations seen in Figure 5.6 probably result from a change in the grain boundary structure from curved to faceted. At the onset of faceting, different relative displacements of the two lattices across adjacent facets will result in dislocations at the facet junction, as shown schematically in Figure 5.12. Interestingly, Balluffi has shown that coincidence or near-coincidence grain boundaries (i.e. those marked by a fairly high degree of periodic matching) are capable of supporting grain boundary dislocations with large (and therefore distinguishable) Burgers vectors [2]. The fact that the facet dislocations of Figure 5.6 exhibit such strong contrast is consistent with the boundary's near-coincidence orientation, and seems to support Balluffi's claim.

5.2. High-Angle Tilt Boundaries (Tilts 15b and 15d)

5.2.1. Processing Conditions

²² Although direct evidence of Ti segregation to tilt boundary dislocations has not been obtained in this study, results from Chapter 4 certainly demonstrate the strong tendency for Ti (and other solutes) to decorate twist boundary dislocations. Similar behavior is expected for tilt boundaries.

Details concerning alumina processing and tricrystal fabrication are given in Section 4.2.1. Tilt boundary 15b was given a final anneal at 1600° C for 40 hours in air before quenching at 800°C/sec. Tilt 15d was given the same final anneal and quench, but these were performed in vacuum. Tilt boundaries were fabricated with nominal 40° misorientations about [0001].

5.2.2. Air-Quenched Tilt Boundary (Tilt15b)

5.2.2.1. Grain Boundary Structure

A high-resolution phase contrast image of the tilt boundary is presented in Figure 5.13a. The misorientation angle between the two grains, as measured from this image and from electron diffraction data, is $39.0 \pm 1.8^\circ$. A processed Moiré image of the grain boundary, shown in Figure 5.13b, demonstrates that while dislocations do exist at the boundary, their spacing is not periodic.

Closer analysis of the HRTEM image indicates that the tilt boundary is not perfectly symmetric. The measured angle between the grain boundary and $(11\bar{2}0)$ in the left crystal is 18.9° , while the same angle measured in the right crystal is 20.1° . Referenced to the left grain, the boundary plane is $(14\bar{5}0)$, but appears to be of slightly higher index in the right grain, at least in the region where the HRTEM image was acquired. The angle between $(14\bar{5}0)$ and $(11\bar{2}0)$ is calculated as 19.1° from crystallographic equations for the sapphire system, in fine agreement with the measured angle.

A misorientation angle of 38.2° about [0001] is known to produce a special $\Sigma 7$ grain boundary in Al_2O_3 [3], so this tilt boundary is close to an exact coincidence

orientation. Simple geometric analysis of hexagonal cation arrays can once again be utilized to examine the significance of the seemingly arbitrary $(14\bar{5}0)$ grain boundary plane. Figure 5.14 shows two interpenetrating hexagonal lattices rotated 39.0° with respect to each other. One unit cell of the CSL is included to highlight the coincident sites and their periodicity. The figure also shows the $(11\bar{2}0)$ planes for each grain (dashed lines), as well as the grain boundary plane (bold line). Here, the boundary plane is clearly parallel to a CSL plane having the highest density of planar coincident sites.

Translation of the CSL unit cell reveals that the lattice of coincident sites is not truly periodic over large distances. This is consistent with the boundary not being in an exact coincidence orientation. In practice, the slight deviation from an exact $\Sigma 7$ orientation is probably accommodated structurally by dislocations in the boundary plane²³. The simple geometric model does not account for this structural misfit accommodation, and so the CSL appears to be non-periodic over large distances.

Figure 5.15 shows a lower-magnification image of the tilt boundary, illustrating a fairly straight boundary plane with no pronounced faceting. Neither conventional nor HRTEM imaging revealed any evidence of second phases at the grain boundary.

5.2.2.2. Grain Boundary Chemistry

Grain boundary chemistry studied using EDS line profiles shows strong enrichment of Ti and Ca solute, as shown in Figure 5.16. Average grain boundary solute concentrations were approximately 0.43 at. % for Ti and 0.15 at. % for Ca. These values

²³ Efforts to identify and characterize these dislocations are ongoing.

were very consistent at different positions along the boundary. No measurable Si signal was detected in this sample.

Electron energy-loss spectra acquired from the grain boundary show primarily Ti^{3+} , as illustrated in Figure 5.17. This is somewhat surprising considering the boundary's lengthy final anneal at 1600°C in air, but is nonetheless consistent with results from other air-quenched boundaries, which show a prevalence of Ti^{3+} near the boundary region. Given this sample's lengthy exposure to an oxidizing atmosphere at high temperature, some fraction of the Ti solute concentration should have been converted to Ti^{4+} . Unfortunately, accurate identification of Ti valence is sensitive to solute concentration, so an inability to detect Ti^{4+} in this sample might be attributed to low Ti boundary concentrations. EELS line profiles across the boundary, such as the one seen in Figure 5.18, show a Ti-enriched region approximately 15 nm wide -- consistent with the grain boundary chemical widths measured from EDS line profiles for Ca and Ti.

5.2.3. Vacuum-Quenched Tilt Boundary (Tilt15d)

5.2.3.1. Grain Boundary Structure

Electron diffraction patterns recorded from the boundary indicate a misorientation angle of $39.3 \pm 1.0^{\circ}$ between the two grains, consistent with the angle measured from the air-quenched sample (15b).

Figure 5.19 shows an image of the grain boundary at fairly low magnification. The boundary plane is quite straight and does not exhibit any marked faceting.

Efforts to perform HRTEM on this sample were thwarted by significant deviation of the grain boundary plane from (hki0). That is, the grain boundary plane normal has a non-zero component in the c-direction. Consequently, low-index [0001] poles in the crystals could not be maintained parallel to the beam while aligning the grain boundary to an edge-on condition.

5.2.3.2. Grain Boundary Chemistry

Microanalysis near the grain boundary region shows peak Ti and Ca solute concentrations averaging 0.32 and 0.13 at. %, respectively, as illustrated in Figure 5.20. Although this particular line profile indicates a narrow Ca-enriched zone (relative to Ti) at the boundary, other profiles acquired from the boundary show similar chemical widths for Ca and Ti (approximately 13-16 nm). Solute concentrations were very consistent along the grain boundary, and no measurable Si signal was detected in any of the spectra.

Electron energy-loss spectra show only Ti^{3+} at the boundary, as seen in Figure 5.21. This result is consistent with the sample's extensive high-temperature anneals in a reducing environment.

5.2.4. Effect of Processing Environment on Ti Solute Segregation

Similarities in misorientation angle, bulk chemistry, annealing temperature, and specimen cooling rate between tilt boundaries 15b and 15d permit direct analysis of the effect of processing environment on Ti solute segregation. Unfortunately, Ti valence in sample 15b appears to be a mixture of Ti^{3+} and Ti^{4+} , complicating comparisons of grain boundary solute concentrations between the air-anneal and vacuum-annealed samples.

Larger grain boundary solute concentrations are predicted for aliovalent Ti^{4+} than for isovalent Ti^{3+} , due to an extrinsic space charge potential in donor-doped Al_2O_3 . Space charge calculations suggest concentrations approaching 1.6 at.% Ti^{4+} at the boundary for 500 ppm (cat.) Ti-doped Al_2O_3 at 1600°C (in air), while elastic-misfit models predict only 0.2 at.% Ti^{3+} for the same doping conditions in a reducing environment. We therefore expect, and in fact observe, greater Ti concentrations in the air-annealed sample (15b) than in the vacuum-annealed sample (15d). The large discrepancy between predicted and measured Ti^{4+} solute concentrations in tilt boundary 15b suggests that a significant portion of the Ti solute has remained isovalent. Apparently, complete conversion of Ti^{3+} to Ti^{4+} is hindered by a lack of grain boundaries in the bicrystal sample at 1600°C in air.

Measured Ca concentrations at the two tilt boundaries are very similar, as are the grain boundary chemical widths; changing from Ti^{4+} to Ti^{3+} has no apparent effect on the Ca solute profile. These observations seem to imply that defect association between Ti and Ca cations is not responsible for those species having similar chemical widths, as the preferred defect association reactions should be very sensitive to solute content. Currently, no explanation can be offered as to why elastically-misfitting Ca^{2+} and Ti^{3+} solute species adsorb over such a broad region at the grain boundary.

5.3. Undoped High-Angle Tilt Boundary (Tilt10)

5.3.1. Processing Conditions

Undoped Al_2O_3 powder was hot-pressed initially at 875°C for 3 hours at 20 MPa, and then additionally at 1400°C for one hour at 35 MPa to form a polycrystalline compact. A sapphire tilt seed with nominally 40° misorientation was placed in contact with a polished slice of undoped polycrystal ($300\text{ }\mu\text{m}$ thick) and diffusion-bonded at 1250°C for 50 hours at 10 MPa. Growth of the tilt boundary was encouraged via three separate anneals: 1800°C for 56 hours in vacuum, followed by 1600°C for 12 hours in air, followed by 0.75 hours at 1400°C in vacuum. The bicrystal assembly was then furnace-cooled at approximately $30^\circ\text{C}/\text{min}$ to room temperature.

5.3.2. Grain Boundary Structure

Diffraction patterns acquired from the tilt boundary indicate a misorientation angle of $41.7 \pm 1.5^\circ$, which is also consistent with measurements from phase-contrast images. Figure 5.22 shows a phase-contrast image that has been processed to remove non-periodic Fourier components. The image reveals a symmetric $(51\bar{6}0)$ tilt boundary plane oriented 20.9° with respect to the $(11\bar{2}0)$ plane of each crystal.

Conventional TEM images reveal faceting along the undoped bicrystal grain boundary, as shown in Figure 5.23 (a)²⁴ and (b). According to the inset diffraction pattern, the short facet segments (marked A) are nearly parallel to the $(10\bar{1}0)$ plane of one of the crystals, but the long facets (marked B) do not match any obvious low-index planes. The angle between the two facet planes is approximately $11.5 \pm 1.0^\circ$.

²⁴ TEM images of Figure 5.23a exhibit rather anomalous contrast and texture due to sputtering and re-deposition of Cu from the support grid during ion-milling.

Two interpenetrating hexagonal (cation) arrays rotated by 41.8° about $[0001]$, shown in Figure 5.24a, are very close to a special $\Sigma 31$ orientation. A coincident site lattice is included in the figure to demonstrate the periodicity of coincident points. Also shown is the symmetric $(51\bar{6}0)$ plane, which perfectly bisects the angle between cation close-packed $(11\bar{2}0)$ planes. A schematic of the bicrystal grain boundary structure is shown in Figure 5.24b, where both facet planes are included in addition to the CSL. Here, the non-indexed facet has been positioned relative to $(51\bar{6}0)$ using angle measurements from TEM images. It is clear from this figure that the $(51\bar{6}0)$ facet occupies a high PCSD plane of the CSL, while the other facet is parallel to a CSL plane with slightly lower PCSD. The second facet is not actually parallel to $(10\bar{1}0)$, but is in fact very high index $\left(15 \ 8 \ \bar{23} \ 0\right)$.

5.3.3. Grain Boundary Chemistry

EDS analysis of the tilt boundary revealed no significant solute concentrations along either of the facet planes. The lack of a measurable Ca signal is somewhat surprising given its omnipresence in Al_2O_3 powders, and its observed tendency to strongly segregate. However, the low angle tilt boundary (Tilt1) also showed no signs of Ca solute accumulation at the grain boundary, so it may be possible that different batches of alumina powder had varying purities.

5.4. General Discussion of Tilt Boundaries

5.4.1. Faceting of Tilt Boundaries

Of the four tilt boundaries examined in this study, only two showed pronounced grain boundary faceting, and both of these were furnace-cooled from 1600°C. Significantly, one of the faceted boundaries (Tilt10) was undoped and showed no signs of solute enrichment at the grain boundary, suggesting that solute segregation may not be the (only) impetus for grain boundary faceting. Instead, the tilt boundaries may (also) facet as a result of slow-cooling. As the temperature drops below 1600°C, grain boundary energies may become more anisotropic, so that certain boundary planes become energetically favored. The exact planes would of course depend critically on solute concentration and temperature. Nonetheless, these conditions would promote faceting of the grain boundary in order to expose lower energy planes. Diffusion kinetics (i.e., cooling rate) would presumably determine to what extent the equilibrium structure is achieved in practice. Moreover, in doped-samples, high grain boundary solute concentrations could inhibit boundary mobility and prevent fruition of the equilibrium structure.

The notion that a grain boundary can assume more than one distinct phase structure, and that grain boundaries can undergo phase transformations in the same manner as bulk phases, was delineated first by Hart [11] and later by Cahn [12]. An important implication of their work is that equilibrium grain boundary phases are dictated by thermodynamic variables such as temperature and composition. Cahn asserts that each grain boundary in a polycrystalline specimen may have one or more phase transitions, but these occur at different temperatures for different boundaries. Transitions between equilibrium phases generally occur by the appearance of new grain

boundary orientations. Thus, the onset of faceting, which can be induced by changes in chemical composition as well as temperature, must be interpreted as a phase change.

Studies by Hsieh and Balluffi on grain boundary roughening/faceting in alloys clearly demonstrate the tendency for grain boundaries to facet upon cooling, and to roughen upon heating [5]. These structural changes are reversible and appear to represent equilibrium phases. Other work by Ference and Balluffi has shown that solute content plays a critical role in fixing the equilibrium grain boundary phase [13]. Grain boundaries in Bi-doped Cu roughen (de-facet) upon removal of Bi, but re-facet upon addition of Bi. The structural phase transformation is reversible, suggesting equilibrium behavior.

Results from this study show that regardless of chemistry or cooling rate, tilt boundaries tend to adopt grain boundary planes that lie parallel to high -- though not necessarily the highest -- PCSD planes of the coincident site lattice. The degree to which solute concentration determines these planes is unclear, but should be the subject of future work comparing grain boundary structures in doped and undoped bicrystals having the same misorientation. The importance of the CSL in dictating the grain boundary plane emphasizes that comparisons between equilibrium Wulff shapes of crystal surfaces, and grain boundary structure of bicrystals are not always valid. That is, application of surface energy data to the prediction of grain boundary structure cannot account for the role of the CSL in “special” boundaries.

5.4.2. Grain Boundary Chemical Width

As mentioned previously, the grain boundary chemical width for elastically-misfitting solutes such as Ca^{2+} and Ti^{3+} is expected to be fairly narrow, if segregation is confined to the structurally-disordered grain boundary core region. All tilt boundary samples exhibit fairly broad solute-enriched grain boundary regions -- a result that cannot be explained at present, but is nonetheless consistent with results for twist boundary samples discussed in Chapter 4.

5.5. Future Work

Efforts to understand the origin and nature of faceting in slow-cooled tilt boundaries should focus on the effects of solute content and temperature. To elucidate the role of solute, one must compare grain boundary structures in undoped bicrystals to those in Ti-doped bicrystals having the same misorientation and cooling rate. Moreover, comparison of the dislocation structure in these different bicrystals as a function of misorientation angle could help to explain the role of Ti solute in stabilizing certain dislocation and boundary structures.

Meanwhile, quenching tilt boundaries with the same misorientation and solute content from different temperatures should help to elucidate the role of temperature and/or cooling rate on grain boundary structure. *In-situ* heating studies in the TEM could also prove invaluable for directly assessing the effects of temperature on boundary structure. Unfortunately, most TEM heating stages are limited to a maximum temperature of 1200-1300°C. These temperatures may not be sufficient to permit extensive grain boundary structural changes in Al_2O_3 . Nonetheless, thermal cycling

experiments should shed some light on the nature of equilibrium grain boundary structure in Al_2O_3 .

5.6. Summary and Conclusions

Successful fabrication of low- and high-angle symmetric tilt boundaries via the directed-assembly growth process has been demonstrated. The boundaries are atomically sharp and free of second phases. Specimen cooling rate appears to have a marked effect on the final grain boundary structure: pronounced faceting has been observed in grain boundaries furnace-cooled from high temperature, while quenched boundaries do not exhibit this type of behavior.

Faceting of a slow-cooled, low-angle, near- $\Sigma 37$ tilt boundary occurs along two distinct planes. One facet is shown to be parallel to the $(10\bar{1}0)$ plane of one crystal, while the other facet is parallel to a high-density plane of the CSL. Large variations in Ti solute concentration between the different facets suggest that excess solute may play a significant role in determining the ultimate grain boundary structure, though a specific mechanism has not yet been determined. The low-angle tilt boundary can be successfully described as an array of periodic edge dislocations with perfect Burgers vector $\frac{1}{3}[11\bar{2}0]$, whereas a periodic dislocation model cannot accurately describe the structure of high-angle grain boundaries.

Faceting of a slow-cooled, high-angle, near- $\Sigma 31$ tilt boundary occurs along two distinct planes of the CSL. One of the facet planes has a higher PCSD than the other, but changes in solute content on the different facets could not be discerned. A high-angle,

near- $\Sigma 7$ tilt boundary quenched in air has a boundary plane parallel to the highest density plane of the CSL, and exhibits no faceting.

Grain boundary chemistry comparisons between air-quenched and vacuum-quenched samples with the same nominal misorientation were thwarted by an inability to quantify relative concentrations of Ti^{3+} and Ti^{4+} in each sample.

Chapter 5 References

1. R. Marks, *private communication*, 2001.
2. R.W. Balluffi, "Grain Boundary Structure and Segregation," in *Interfacial Segregation*, W.C. Johnson and J.M. Blakely, Editors. American Society for Metals: Metals Park, 1979.
3. H. Grimmer, R. Bonnet, S. Lartigue, and L. Priester, "Theoretical and Experimental Descriptions of Grain Boundaries in Rhombohedral Alpha-Al₂O₃," *Philosophical Magazine A-Defects and Mechanical Properties* **61** (3) 493-509 (1990).
4. G.A. Bruggeman, G.H. Bishop, and W.H. Hartt, "Coincidence and Near-Coincidence Grain Boundaries in HCP Metals," in *The Nature and Behavior of Grain Boundaries*, H. Hu, Editor. Plenum Press: New York, 1972.
5. T.E. Hsieh and R.W. Balluffi, "Observations of Roughening/De-faceting Phase Transitions in Grain Boundaries," *Acta Metallurgica* **37** (8) 2133-9 (1989).
6. M. Kitayama, "The Wulff Shape of Doped and Undoped Alumina," in Ph.D. Dissertation, University of California, Berkeley, 1996.
7. M. Kitayama, J.D. Powers, L. Kulinsky, and A.M. Glaeser, "Surface and Interface Properties of Alumina via Model Studies of Microdesigned Interfaces," *Journal of the European Ceramic Society* **19** 2191-2209 (1999).
8. Y. Ikuhara, N. Shibata, T. Watanabe, F. Oba, T. Yamamoto, and T. Sakuma, "Grain Boundary Characters and Structures in Structural Ceramics," *Proceedings of 7th JFMSS* (2001).
9. Y. Ikuhara, T. Watanabe, T. Yamamoto, T. Saito, H. Yoshida, and T. Sakuma, "Grain Boundary Structure and Sliding of Alumina Bicrystals," *Proceedings of the Materials Research Society* **601** 125-32 (1999).
10. Y. Ikuhara, F. Oba, and N. Shibata, *unpublished work*, (2002).
11. E.W. Hart, "Grain Boundary Phase Transformations," in *The Nature and Behavior of Grain Boundaries*, H. Hu, Editor. Plenum Press: New York, 1972.
12. J.W. Cahn, "Transitions and Phase Equilibria Among Grain Boundary Structures," *Journal de Physique Colloque* **C6-43** 199-213 (1982).
13. T.G. Ference and R.W. Balluffi, "Observation of a Reversible Grain Boundary Faceting Transition Induced by Changes of Composition," *Scripta Metallurgica* **22** (12) 1929-34 (1988).

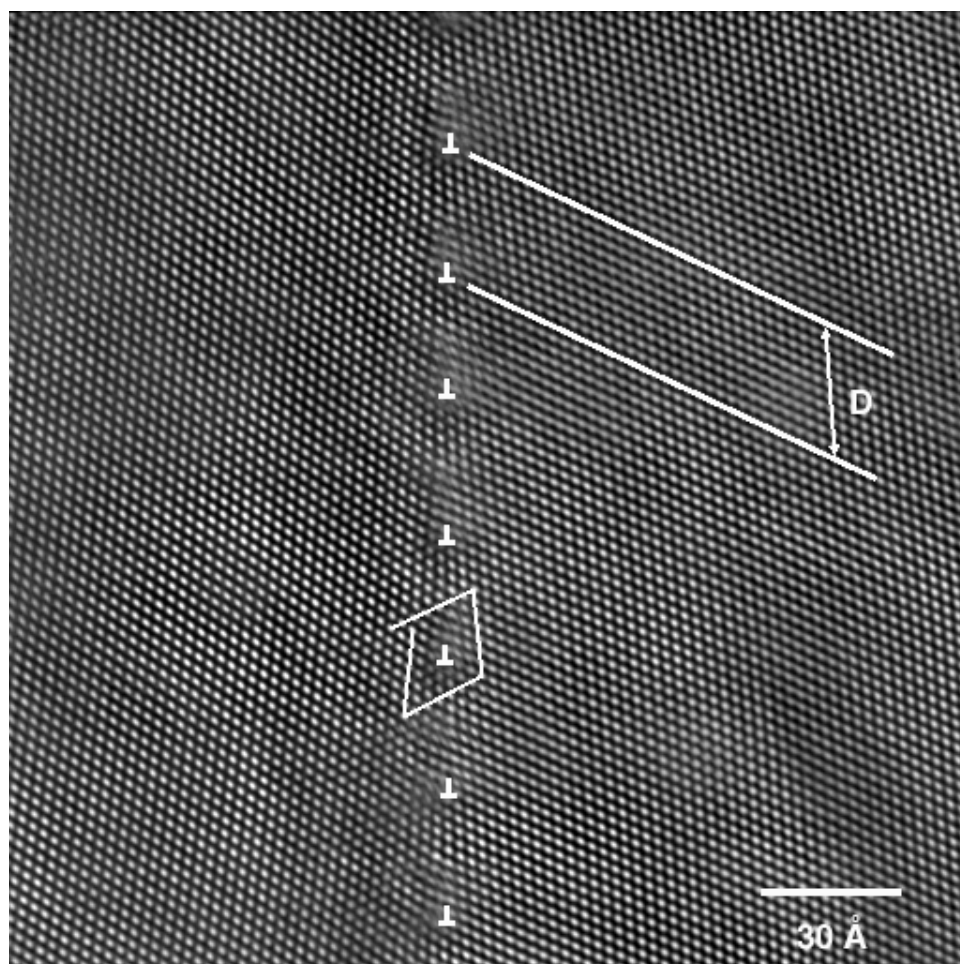


Figure 5.1. High-resolution phase contrast image of low-angle tilt boundary reveals edge dislocations with perfect Burgers vector $\frac{1}{3}[1\bar{1}20]$ and periodic spacing $D = 27.5 \text{ \AA}$.

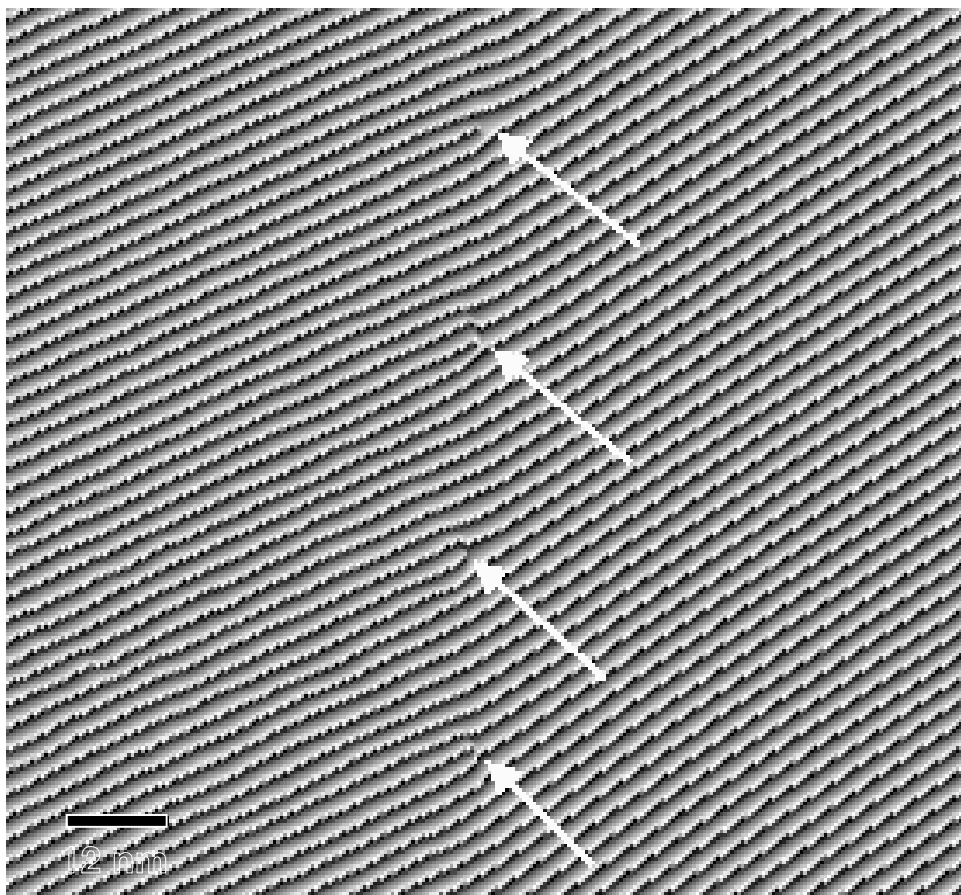


Figure 5.2. Processed Moiré image of tilt boundary reveals periodic grain boundary dislocations (arrowed) at the intersection of $(11\bar{2}0)$ planes.

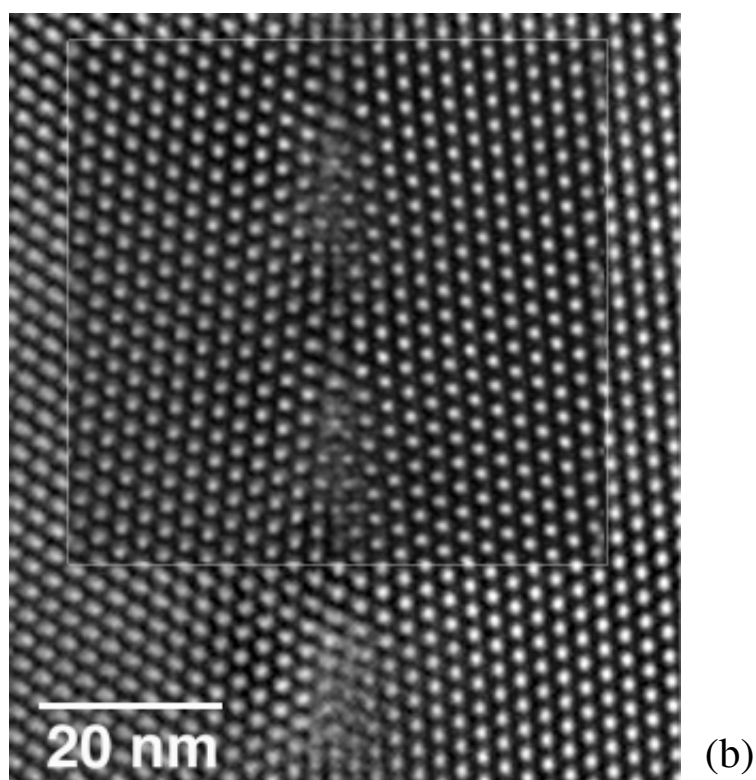
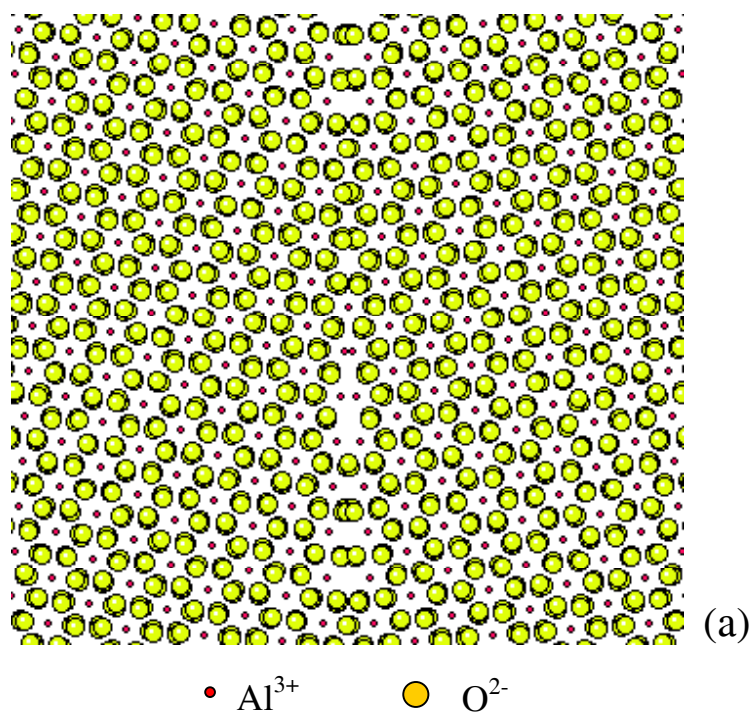
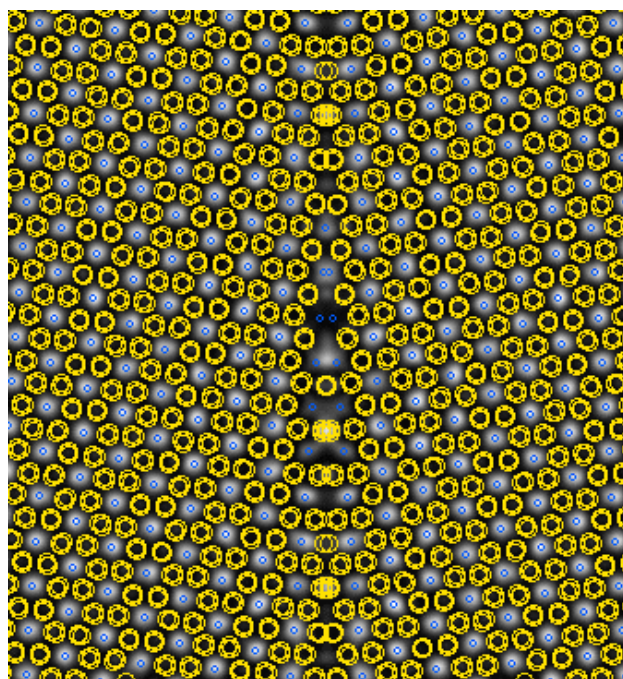


Figure 5.3. (a) Structural model of tilt boundary used to generate a calculated image of grain boundary structure. (b) Comparison of simulated (inset) and experimental images shows outstanding agreement. (c) Structural model superimposed on simulated image.



(c)

Figure 5.3 (continued)

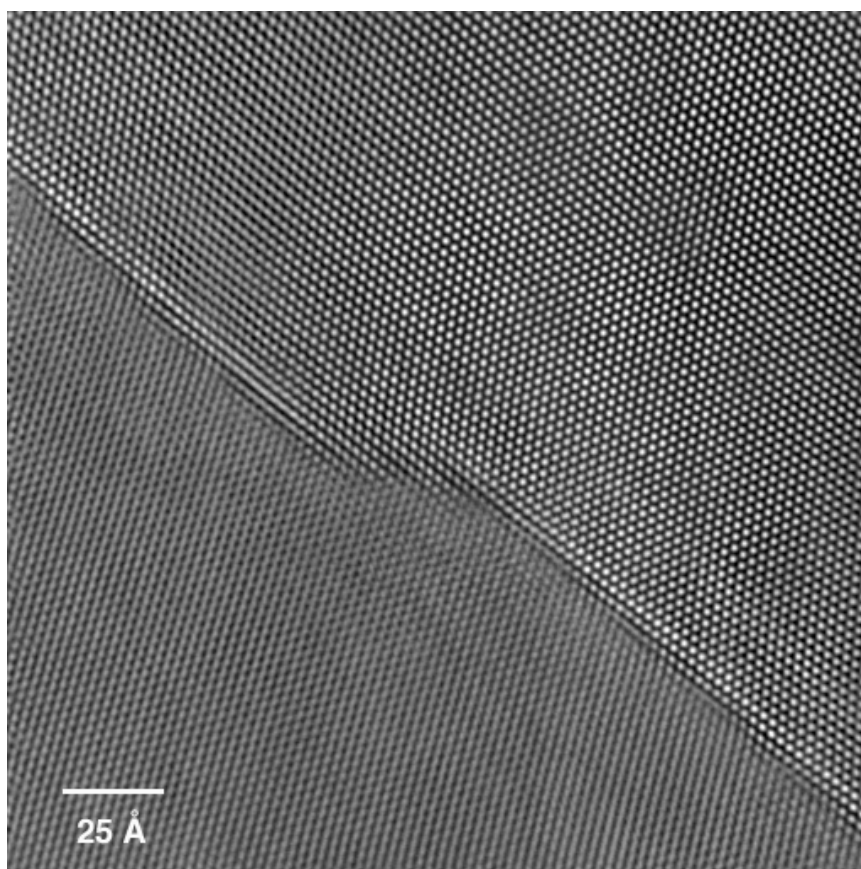


Figure 5.4. Phase contrast image of faceted low-angle tilt boundary. The long facets are parallel to $(3\bar{7}40)$.

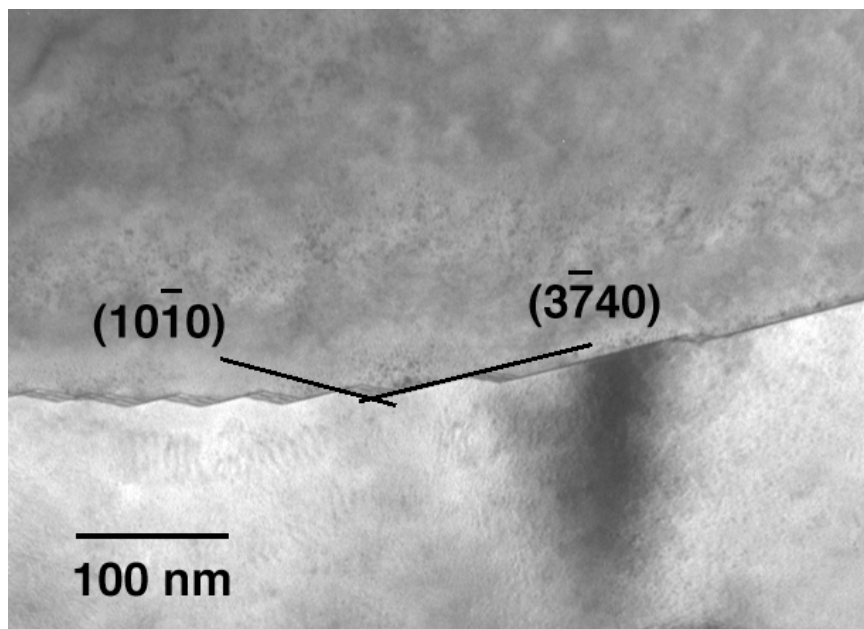
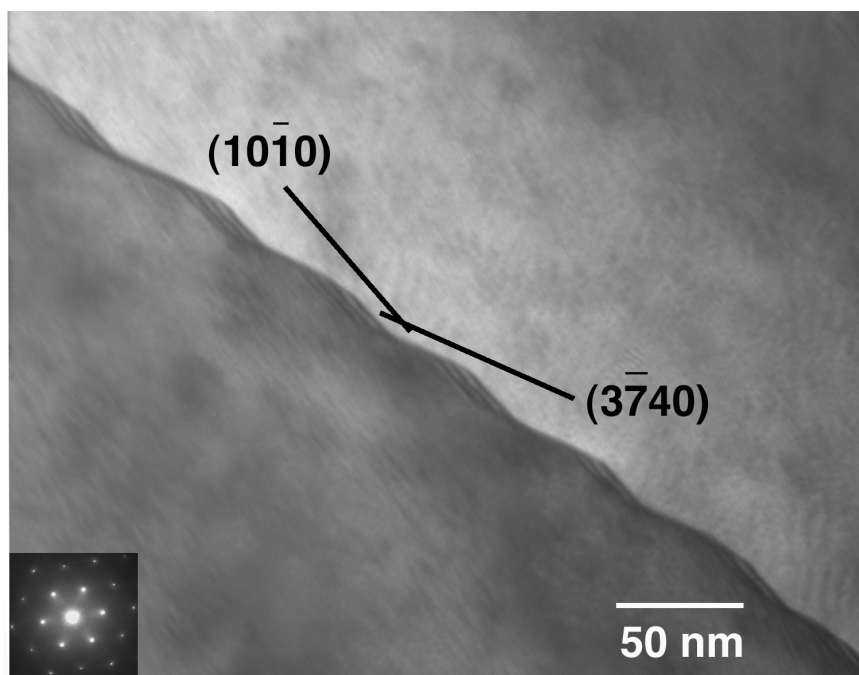
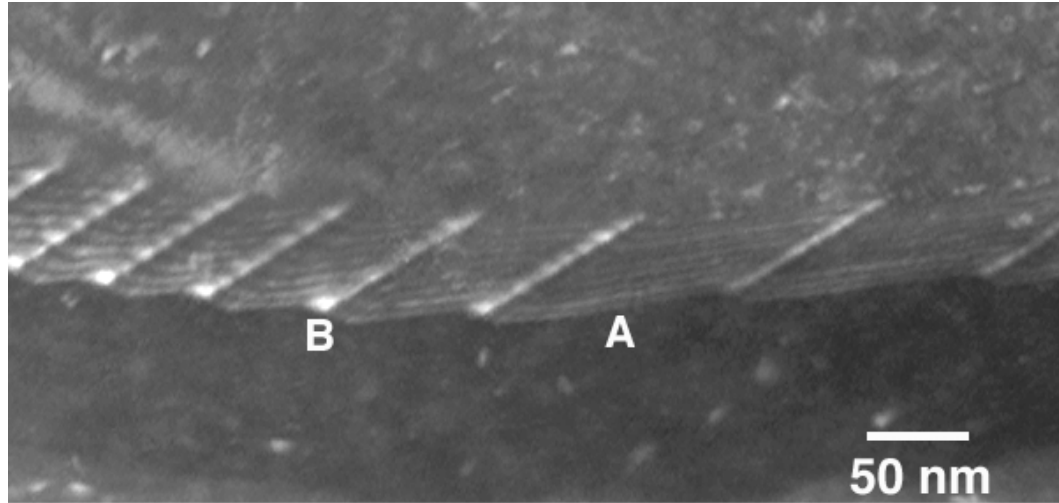


Figure 5.5. Conventional TEM images of faceted tilt boundary show pronounced faceting along $(10\bar{1}0)$ and $(3\bar{7}40)$ planes.



A: $\{3\bar{7}40\}$

B: $\{10\bar{1}0\}$

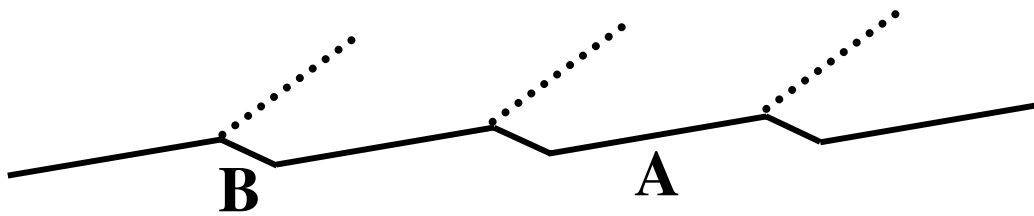


Figure 5.6. (a) Dark-field image shows dislocations with strong contrast at junction between two facet planes. (b) Corresponding schematic shows that dislocations are only observed at one of the facet junction sites.

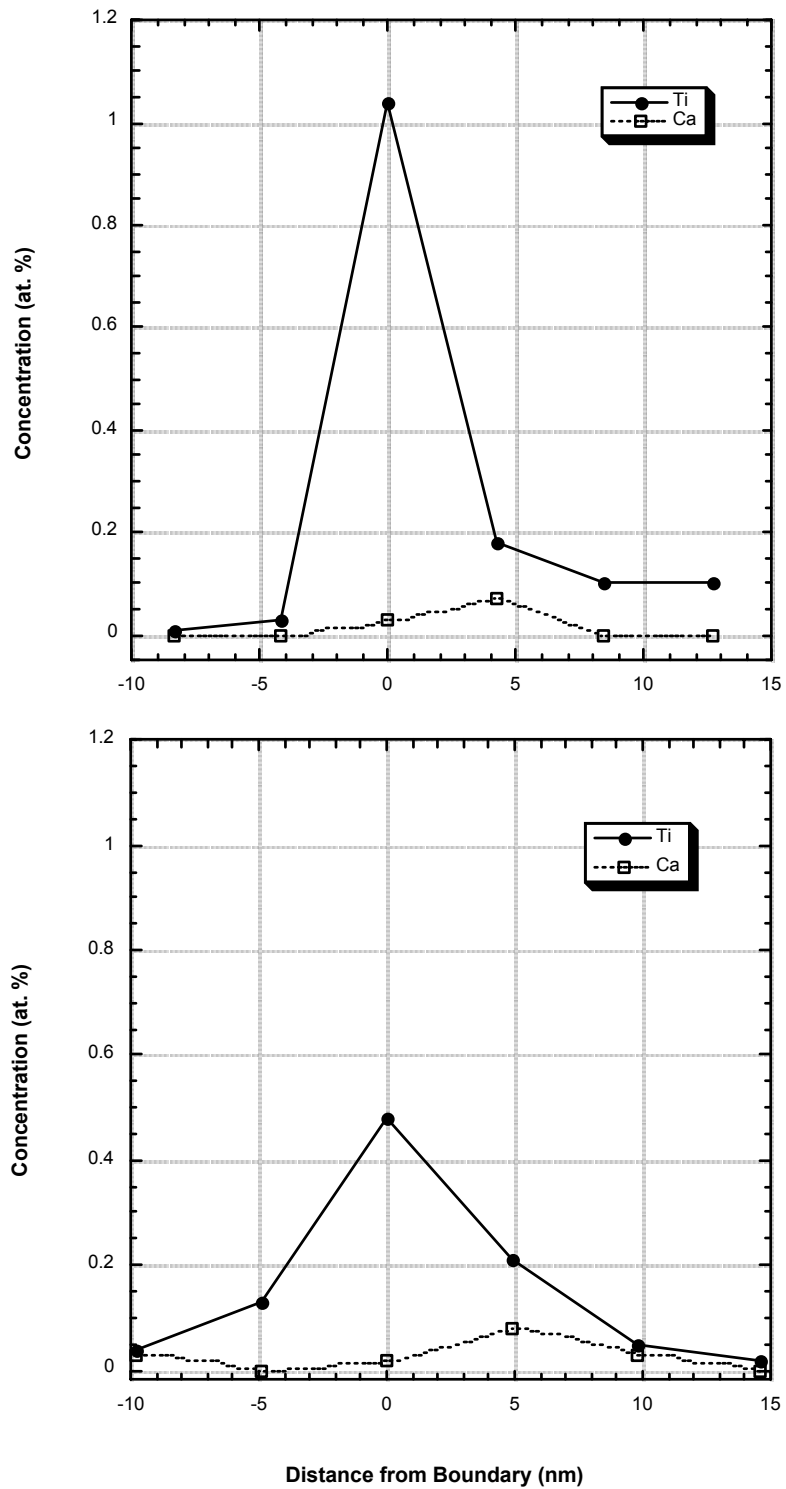


Figure 5.7. EDS line profiles across (a) $(3\bar{7}40)$ and (b) $(10\bar{1}0)$ facets reveal large differences in Ti solute concentration.

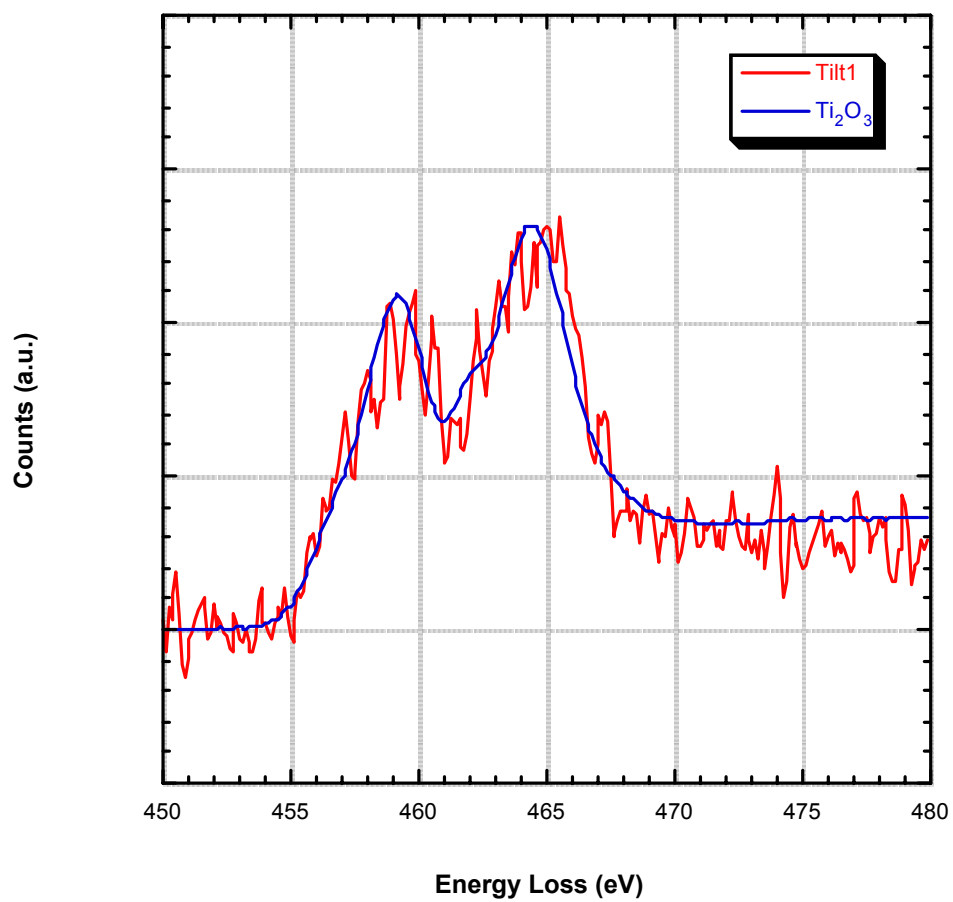


Figure 5.8. Ti L_{2,3} edge from Tilt1 boundary closely matches spectrum from Ti₂O₃ standard, confirming Ti³⁺ at the boundary.

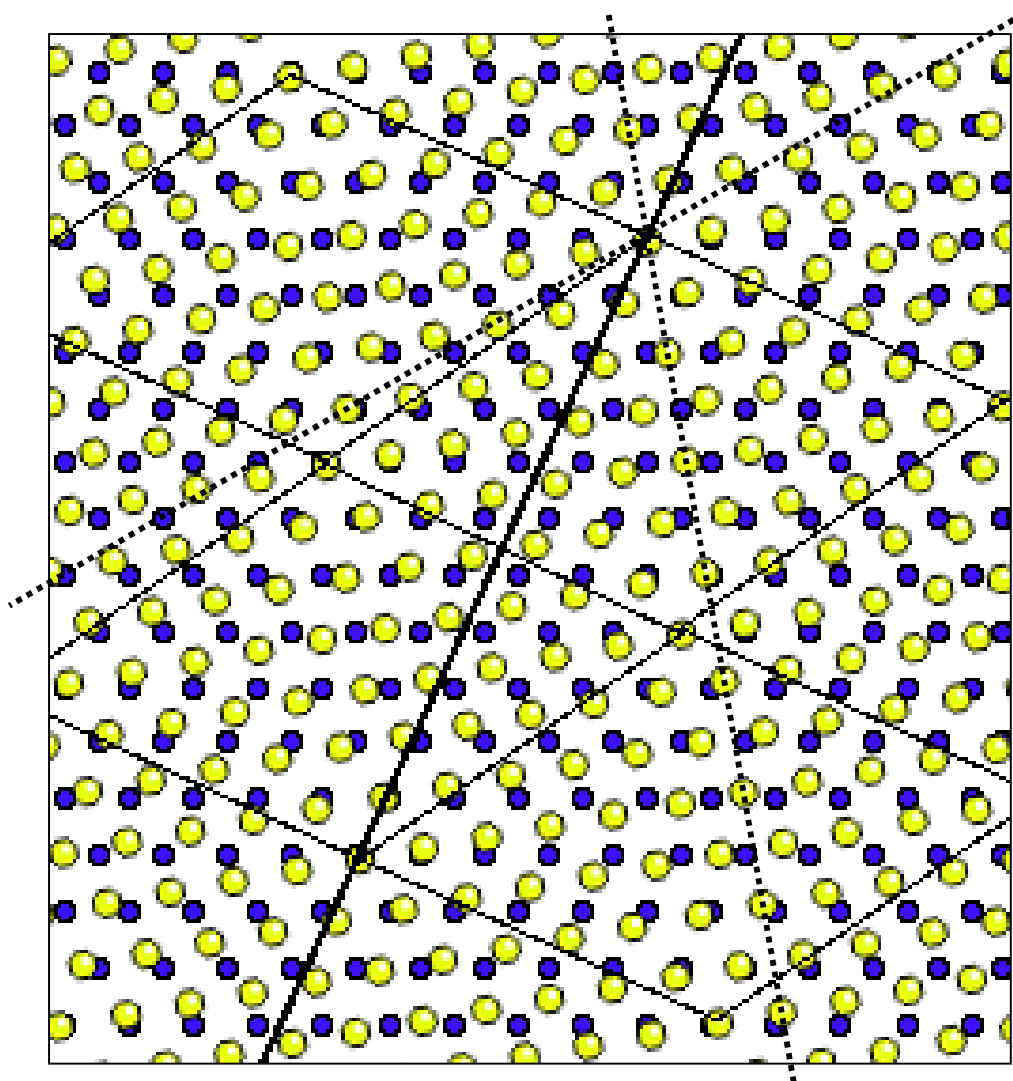


Figure 5.9. Coincidence site lattice formed by 9.8° rotation of two hexagonal arrays about $[0001]$. Thin lines identify CSL; bold line indicates $(3\bar{7}40)$ trace; dashed lines show $(10\bar{1}0)$ plane of each crystal.

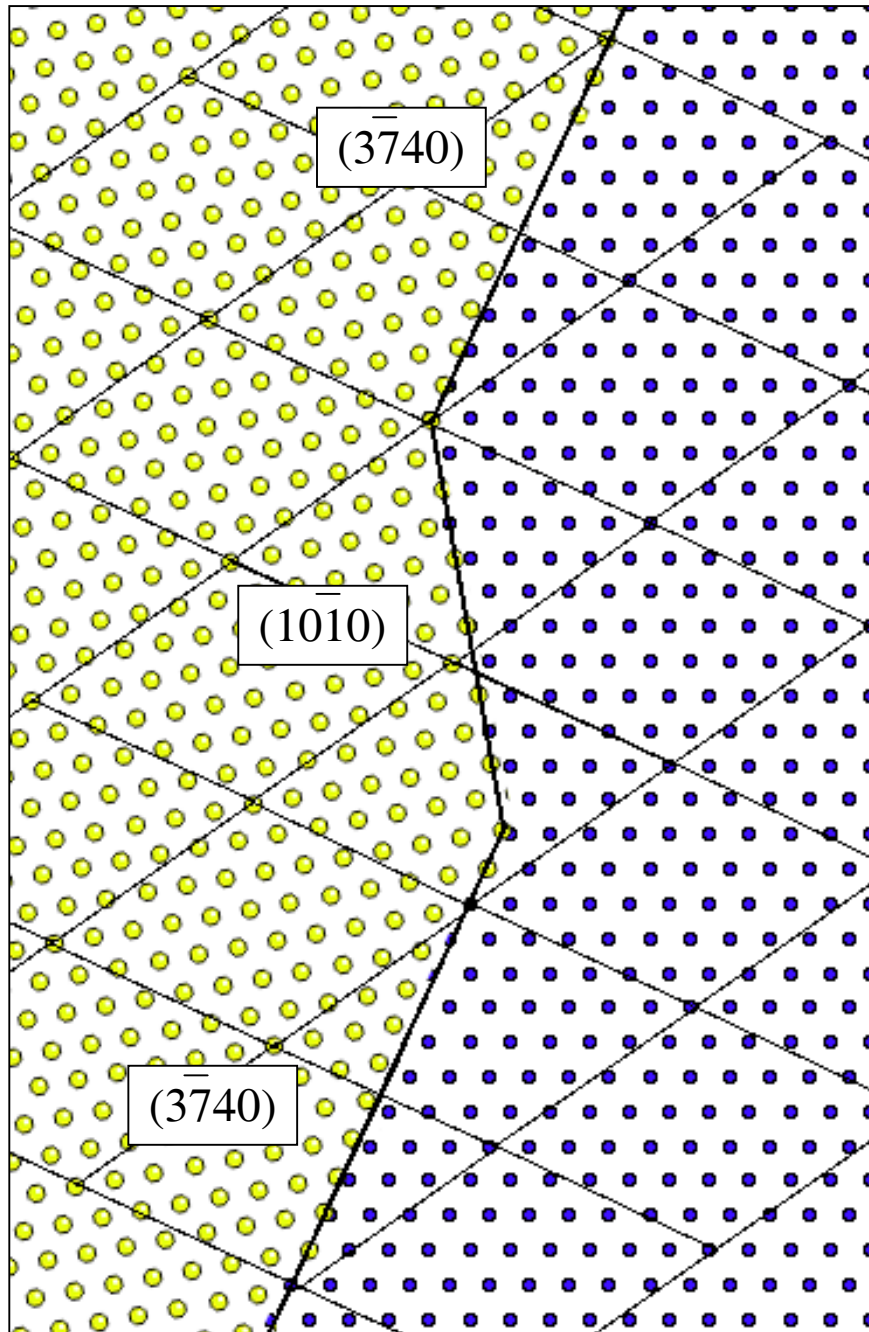


Figure 5.10. Schematic of grain boundary structure in faceted bicrystal. The $(\bar{3}740)$ planes lie parallel to high-PCSD planes of the CSL, while $(10\bar{1}0)$ does not.

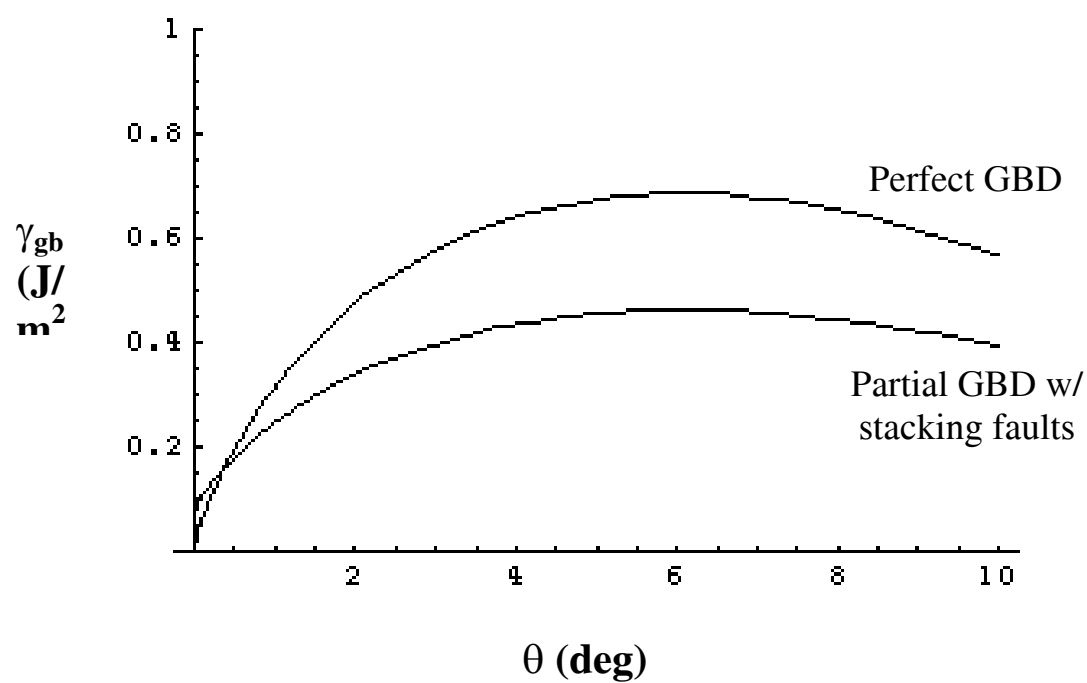


Figure 5.11. Grain boundary energy versus misorientation angle (θ) calculated for low-angle tilt boundaries in undoped sapphire, assuming either perfect grain boundary dislocations (GBD), or partial dislocations with associated stacking faults. (From [9]).

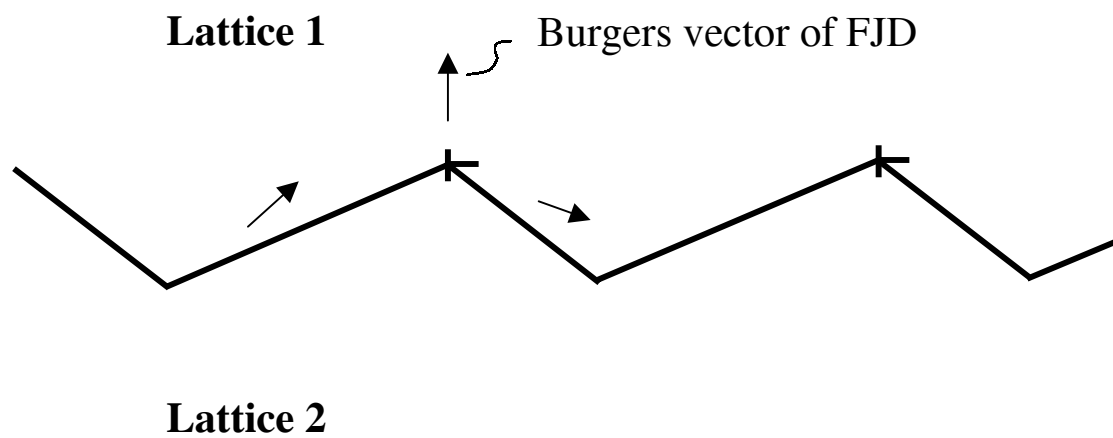


Figure 5.12. Facet junction dislocations (FJD) result from the relative displacements of Lattice 1 and Lattice 2. The Burgers vector of the FJD is determined by the difference between the two displacement vectors. (After [2]).

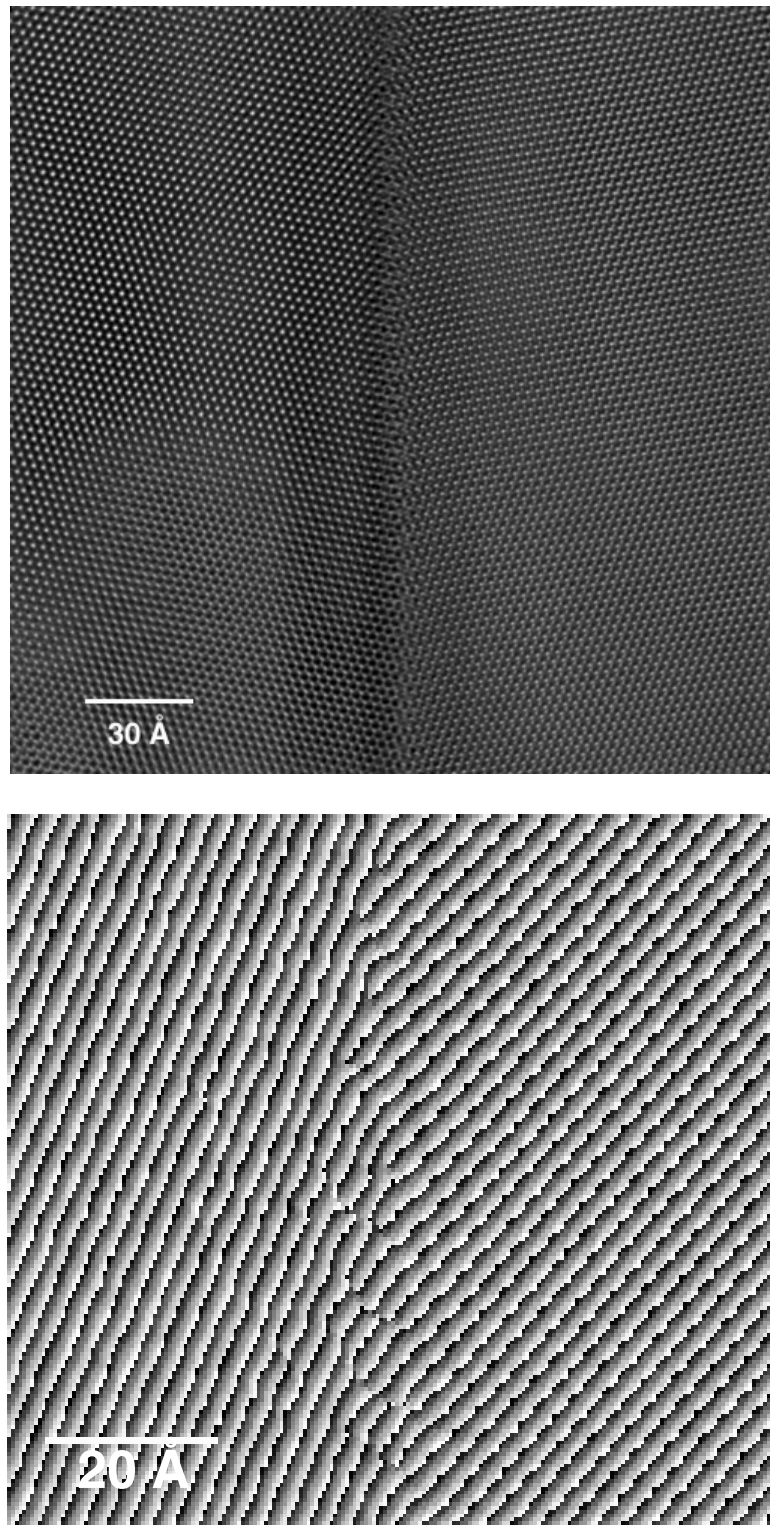
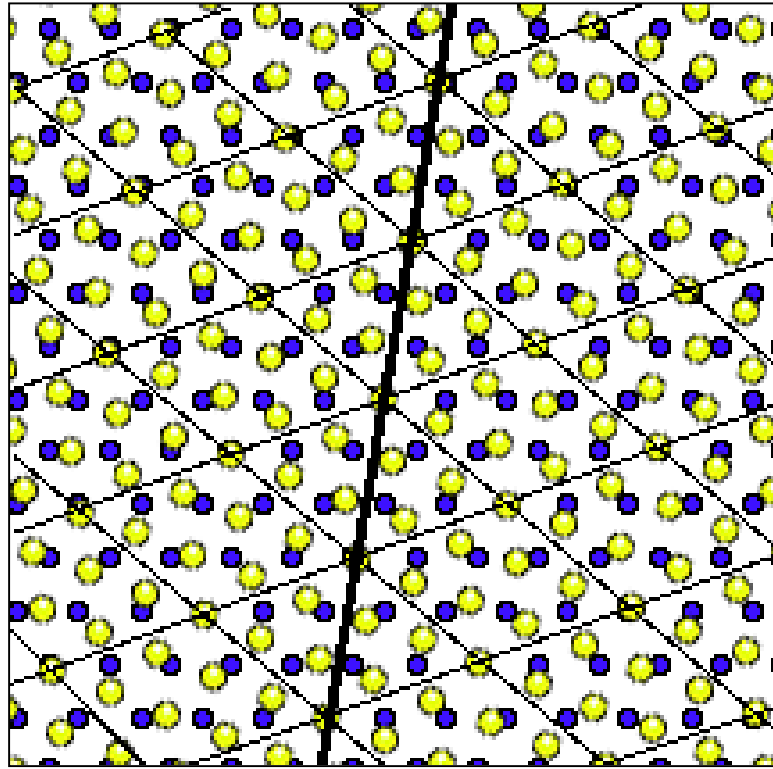


Figure 5.13. (a) Phase contrast image of air-quenched high-angle tilt boundary (Tilt15b). (b) Processed Moiré image reveals that dislocations are not periodically-spaced along the boundary plane.



$(14\bar{5}0)$

Figure 5.14. Coincident site lattice formed by 39.0° rotation of two hexagonal arrays about $[0001]$; CSL (thin lines) and $(14\bar{5}0)$ plane (bold line) are shown.

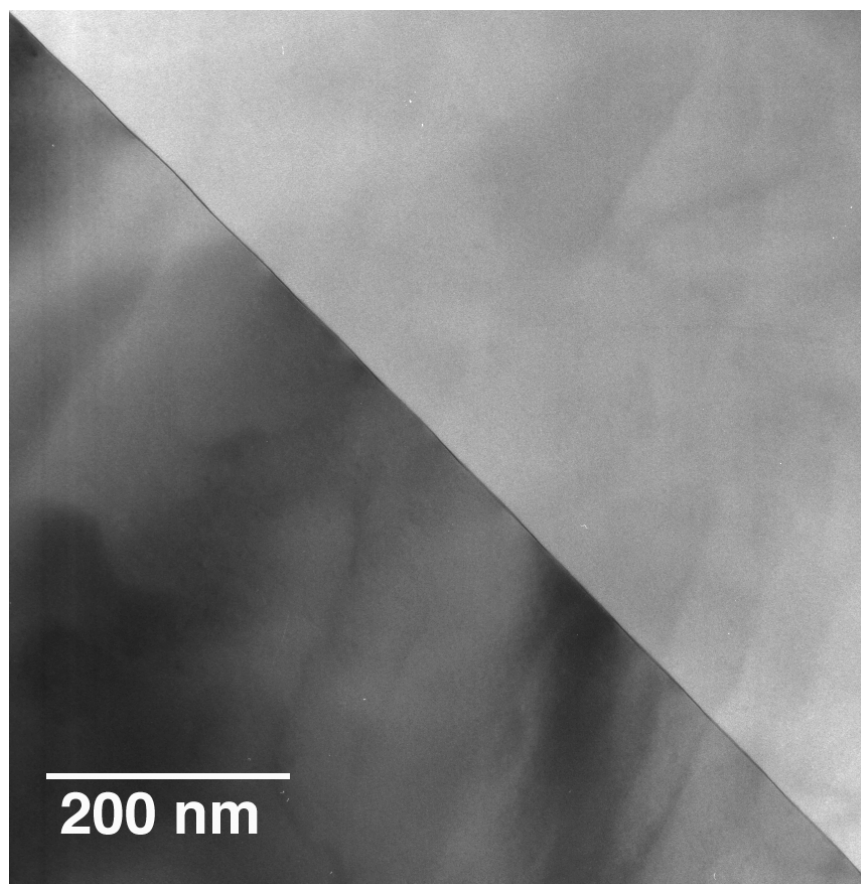


Figure 5.15. Conventional TEM image of Tilt15b shows straight grain boundary with no pronounced faceting.

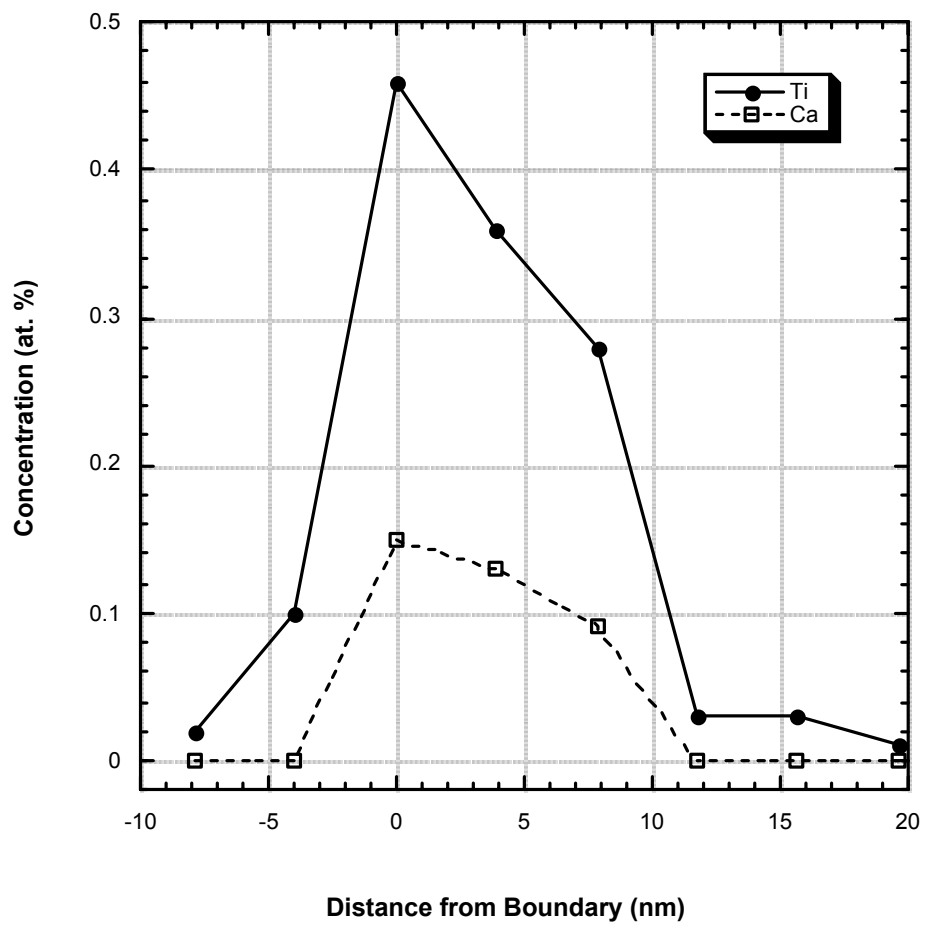


Figure 5.16. EDS line profile across Tilt15b illustrates strong Ti and Ca enrichment.

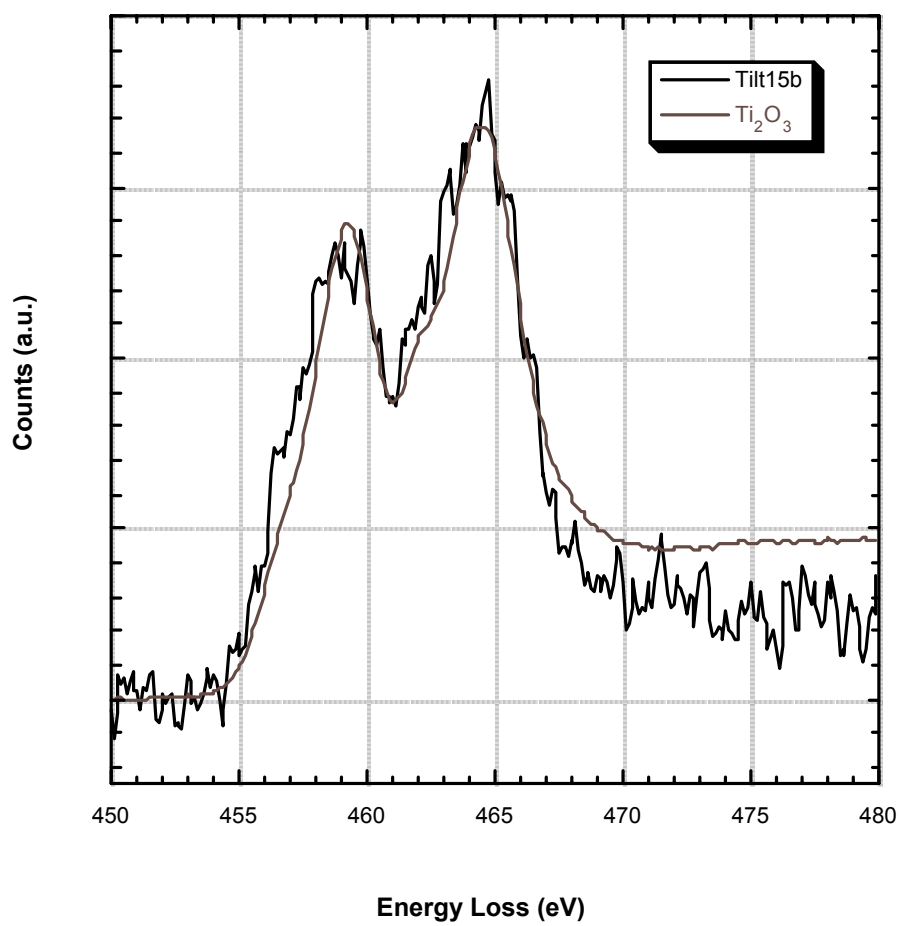


Figure 5.17. Ti L_{2,3} edge from Tilt15b demonstrates prevalence of Ti³⁺ at the grain boundary.

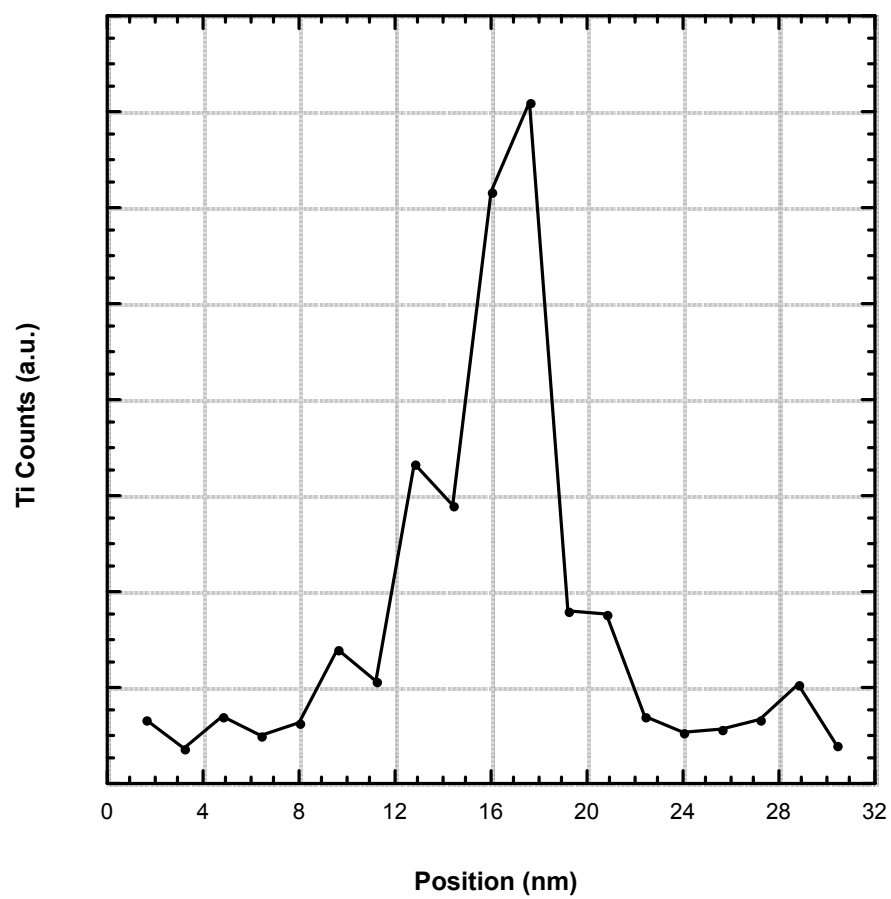


Figure 5.18. EELS line profile across Tilt15b reveals a grain boundary chemical width approximately 15 nm wide.

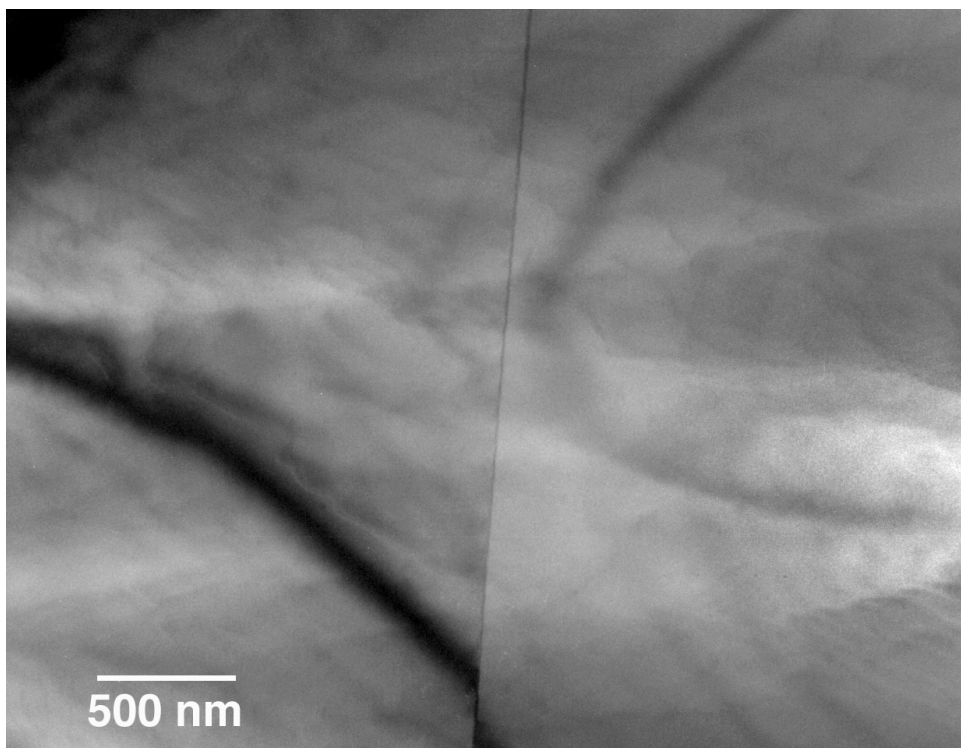


Figure 5.19. Conventional TEM image of vacuum-quenched tilt boundary (Tilt15d) demonstrates no boundary faceting.

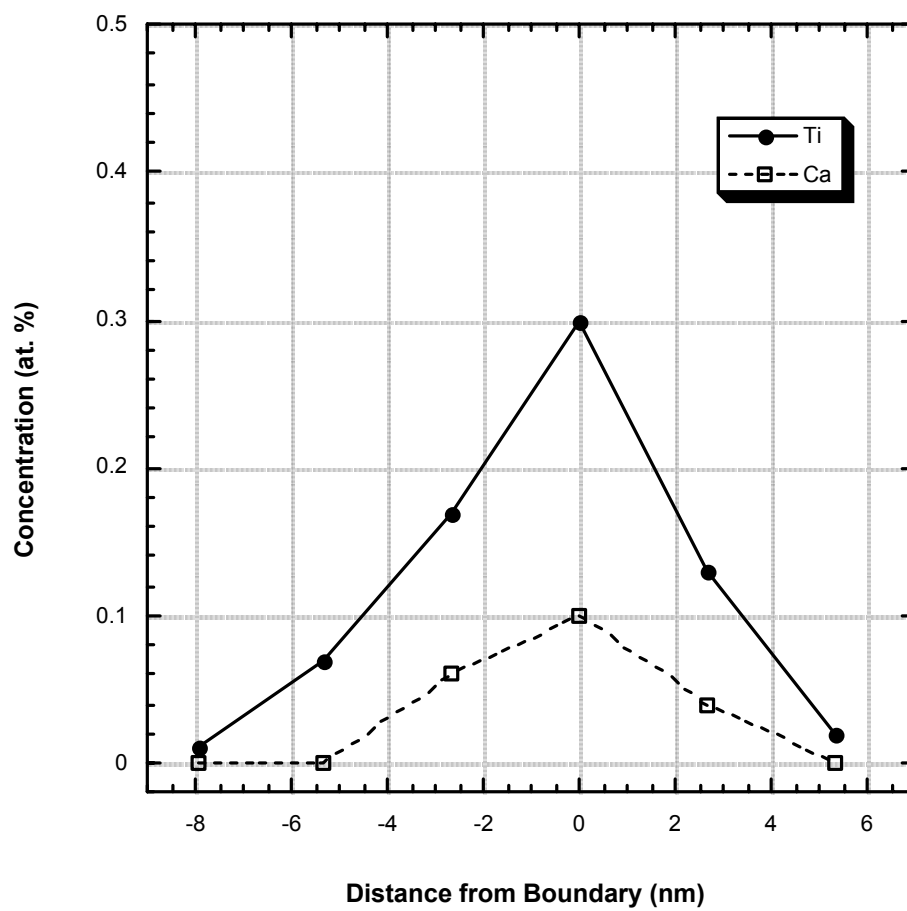


Figure 5.20. EDS line profile across Tilt15d illustrates Ti and Ca enrichment, but at concentrations slightly lower than those reported for Tilt15b.

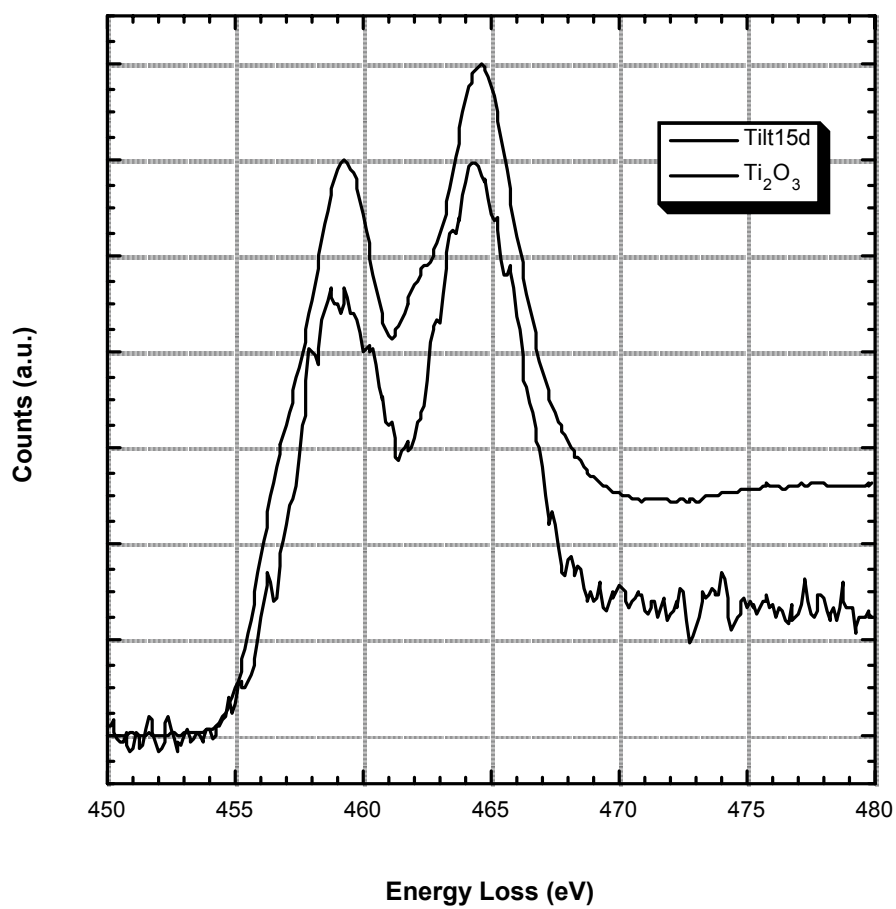


Figure 5.21. Ti L_{2,3} edge from Tilt15d confirms presence of Ti³⁺ at the grain boundary.

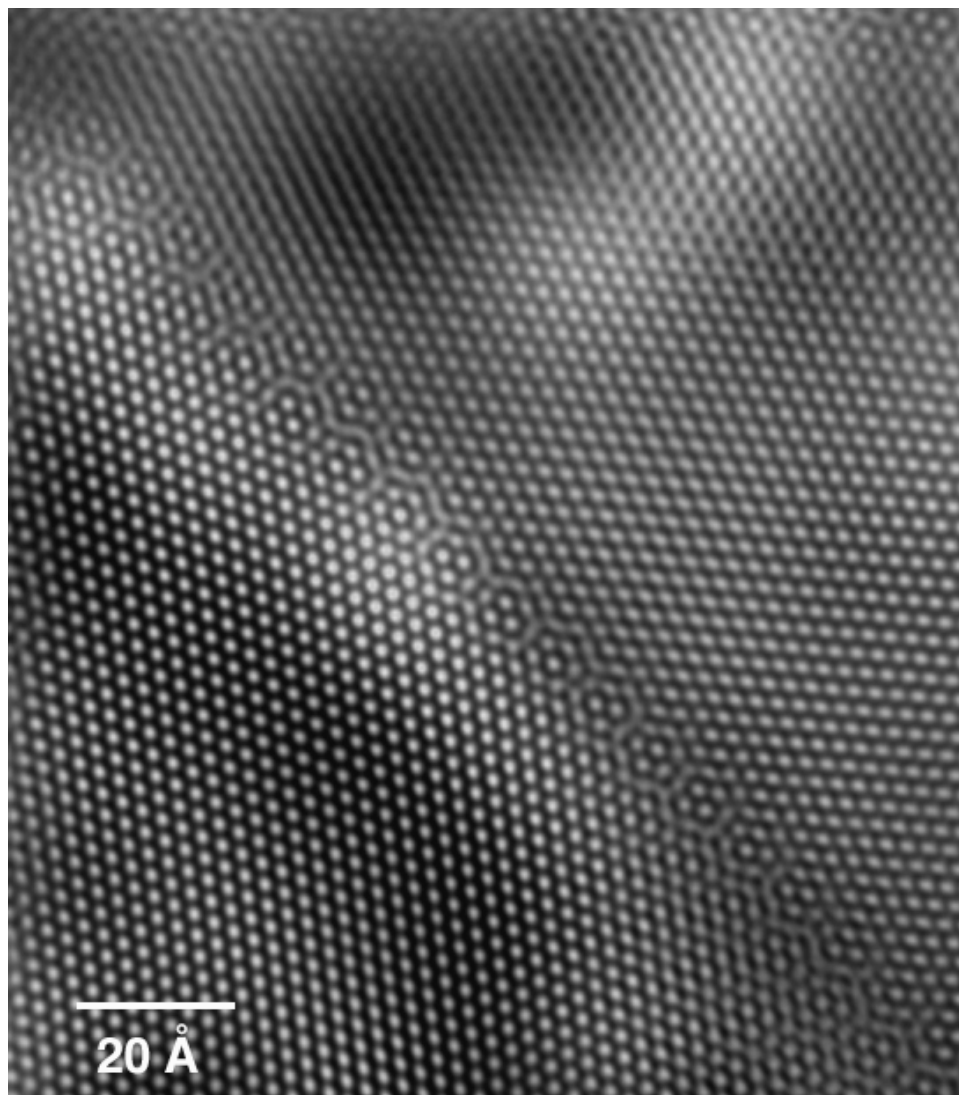


Figure 5.22. Processed phase contrast image of Tilt10 reveals a symmetric $(51\bar{6}0)$ boundary plane.

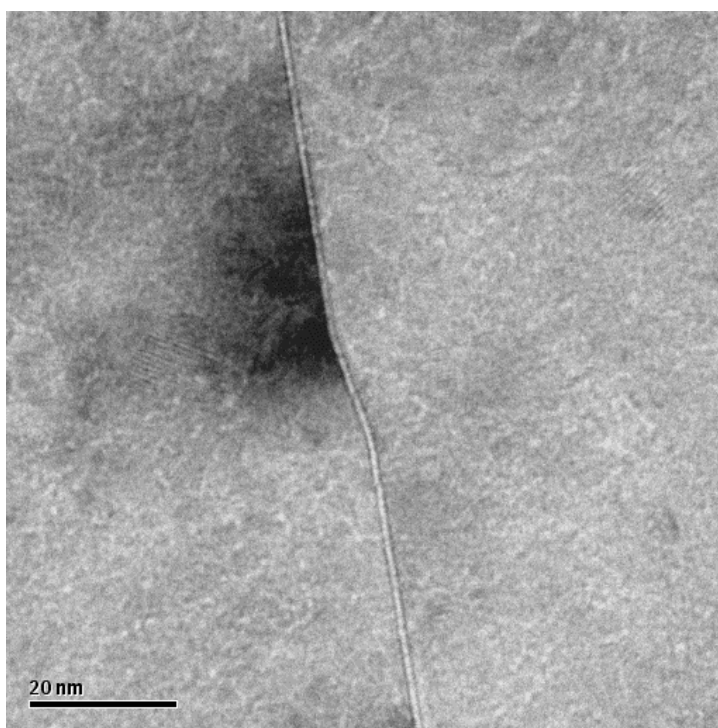
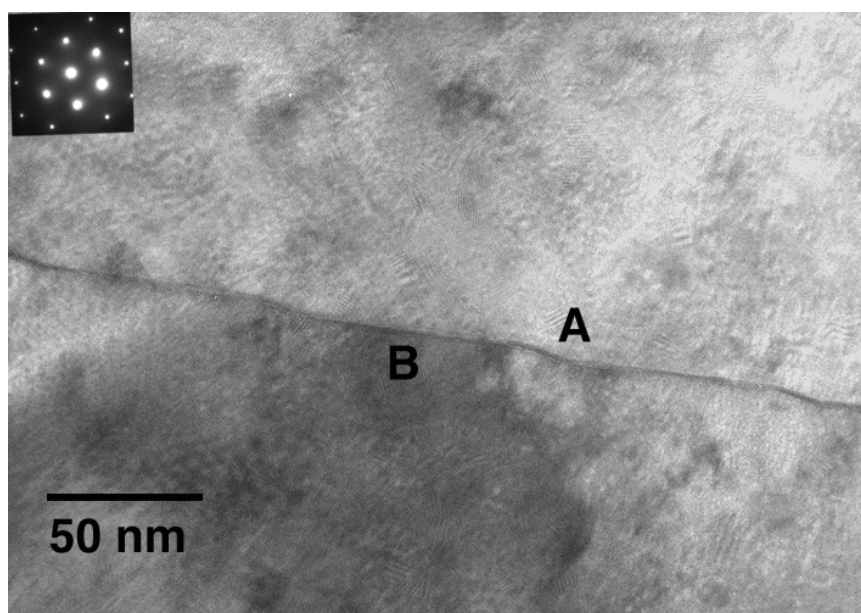


Figure 5.23. Conventional TEM images from Tilt10 demonstrate pronounced faceting of the grain boundary plane.

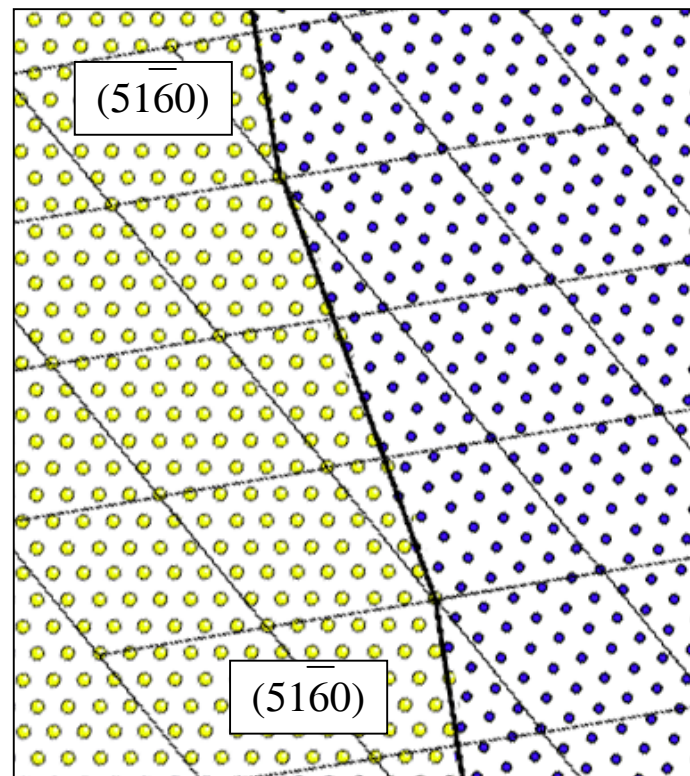
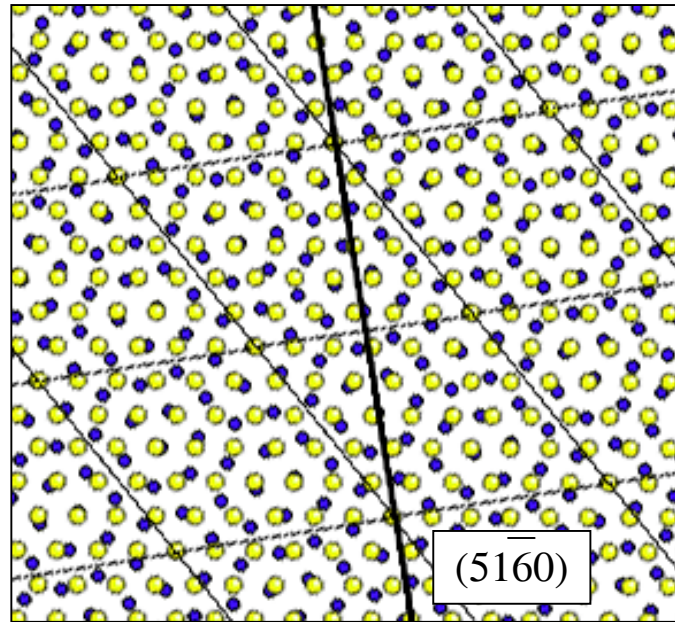


Figure 5.24. (a) CSL formed by 41.8° rotation of two lattices about [0001] shows that $(51\bar{6}0)$ plane is parallel to a high-PCSD plane of the CSL. (b) Schematic of faceted grain boundary structure shows that both facets are special planes of the CSL.

Appendix A

ISSUES CONCERNING ELEMENTAL QUANTIFICATION IN FOCUSED-PROBE MICROANALYSIS

Quantitative microanalysis using EDS must account for beam spreading that occurs through the specimen thickness. An incident probe of size d will experience broadening as it travels through the specimen, emerging at the exit surface with a size greater than d . The amount of broadening is approximated using Goldstein's single-scattering formula [1]

$$b = 625 \left(\frac{Z}{E} \right) \left(\frac{\rho}{A} \right)^{1/2} t^{3/2} \quad (\text{A.1})$$

where b is given in cm, Z is atomic number, E is beam energy in keV, ρ is the mass density in g/cm^3 , A is the atomic weight, and t is the foil thickness in cm. According to this model, beam broadening is shown to increase with $t^{1.5}$, a trend that seems to be consistent with most experimental studies to date.

The effects of beam broadening on quantitative microanalysis of grain boundary chemistry are potentially quite serious. The metallurgical community recognized this years ago and developed techniques to account for beam broadening in grain boundary microanalysis. Perhaps the most widely-used technique, pioneered by Michael and Williams [2], is summarized here.

Initially, we measure some sort of average solute concentration at the grain boundary, which is determined from the relative intensities of the elemental peaks in the EDS spectrum. However, a focused electron probe samples both the narrow solute-enriched boundary region and the matrix grains on either side of the boundary, as shown in Figure A.1. As a result, the average solute concentration that we measure is much less than the actual concentration at the grain boundary. One must account for the difference in the total volume sampled versus the grain boundary volume that effectively contains all of the solute.

If the total volume sampled by the electron beam is modeled as a truncated cone, this volume can be approximated as

$$V_t = \frac{\pi t}{4} \left(d^2 + bd + \frac{b^2}{3} \right) \quad (\text{A.2})$$

where d is the incident probe diameter and b is the amount of beam broadening. This total volume is presumably much larger than the grain boundary volume. If the grain boundary is treated as a rectangular slab of width δ , then the grain boundary volume is given as

$$V_{gb} = t\delta \left(d + \frac{b}{2} \right) \quad (\text{A.3})$$

The ratio of total volume to grain boundary volume (V_t/V_{gb}) is therefore a sensitive function of the specimen thickness and the grain boundary width. Both parameters need to be known with high precision to accurately measure a grain boundary concentration.

In metals and alloys, δ is usually assumed to be on the order of one nanometer, a value that reflects the highly localized segregation of solute species to metal grain boundaries. When large incident probes (e.g., ≥ 4 nm) are used for grain boundary

microanalysis in metals, V_t swamps V_{gb} , so the “average” or measured solute concentration greatly underestimates the true grain boundary concentration. In the case of ionic ceramics, however, the effective grain boundary (chemical) width can be significantly larger than one nanometer due to the spatial extent of the space charge region. Indeed, calculations and experiments both reveal that the space charge region (primarily responsible for solute segregation in ionic materials) ranges from 6-15 nm away from the boundary into the grain interior. This means the chemical heterogeneity defining the grain boundary region ranges anywhere from 12-30 nm in width. In the current investigation, where a 1.0 nm incident probe was routinely employed, the chemical width of the grain boundary is clearly much greater than the probe size (or even the broadened probe size), so the sampled volume should not lead to erroneous calculations of solute concentration.

Figure A.2 shows a plot of V_t/V_{gb} versus grain boundary chemical width δ calculated for Al_2O_3 at 200 keV and 1.0 nm probe size, using Eqs. A.1-A.3. For accurate quantitative microanalysis, V_t/V_{gb} should be less than or equal to one – represented by the dashed line in Figure A.2. For a very thin grain boundary width (say 1 nm), the specimen must be very thin (50 nm) in order for the total volume of the probed region to equal that of the boundary, assuming an incident 1 nm probe. As specimen thickness increases, accurate microanalysis can only be performed on wider grain boundaries (i.e. 4 nm wide at 200 nm Al_2O_3 specimen thickness). To quantify solute concentration at grain boundaries thinner than 3.5 nm in a 200 nm thick specimen, one would need to correct for the difference between V_t and V_{gb} . Fortunately, in Al_2O_3 and other ionic ceramics, effective grain boundary (chemical) widths typically exceed 10 nm, so

corrective measures are not required for accurate quantification in the near-boundary region.

However, it should be noted that accurate quantitative microanalysis of grain boundary chemistry in ionic materials is complicated by the fact that the grain boundary width δ contains a spatially-varying solute concentration, not a fixed one as was assumed in the derivations of [2]. This ultimately introduces some amount of error in the determination of solute concentration. For example, a probe positioned directly on the grain boundary core samples not only the core, but also material immediately adjacent to it. But the solute concentration profile varies dramatically with distance away from the grain boundary core. Consequently, the measured solute concentration at this location will underestimate the true solute concentration that exists right at the boundary plane. Moreover, measurements of solute concentration at the grain boundary core should be more susceptible to specimen thickness (i.e. beam broadening) effects.

Hall and Vander Sande quantified Fe solute segregation to MgO grain boundaries as a function of specimen thickness, using EDS with a 2.5 nm probe in the STEM [3, 4]. They observed little change in the spatial resolution of the composition profile as the specimen thickness increased from 80 nm to 338 nm, as seen in Figure A.3 [4]. However, slight changes in the calculated Fe concentrations were observed with varying thickness, and the change in C_{Fe} measured right at the grain boundary (as a function of specimen thickness) was quite pronounced. This is probably because the solute concentration right at the grain boundary core is peaked over a very small length scale (perhaps on the order of one nanometer or less), so beam broadening is likely to affect this region more than a region close to the tail of the (chemical) profile.

Recognizing that the composition is not uniform over the boundary width, we would ideally account for the fact that we're sampling a spatially-varying chemical profile with the focused probe. Mathematically, one needs to deconvolve the solute segregation profile from the truncated cone (beam) profile, but unfortunately, models with this degree of sophistication do not currently exist.

References

1. J.I. Goldstein, J.L. Costley, G.W. Lorimer, and S.J.B. Reed, in *Scanning Electron Microscopy 1977*, O. Johari, Editor. IIT Research Institute: Chicago, 1977.
2. J.R. Michael and D.B. Williams, "An Analytical Electron Microscope Study of the Kinetics of the Equilibrium Segregation of Bismuth in Copper," *Metallurgical Transactions A* **15A** 99-105 (1984).
3. E.L. Hall and J.B. Vander Sande, "The Effect of Sample Thickness on High Spatial Resolution Composition Profiles in Dedicated STEM," in *Thirty-Seventh Annual Meeting of the Electron Microscopy Society of America*. San Antonio: Claitor's Publishing Division, 1979.
4. E.L. Hall, D. Imeson, and J.B. Vander Sande, "On Producing High-Spatial-Resolution Composition Profiles via Scanning Transmission Electron Microscopy," *Philosophical Magazine A* **43** (6) 1569-85 (1981).

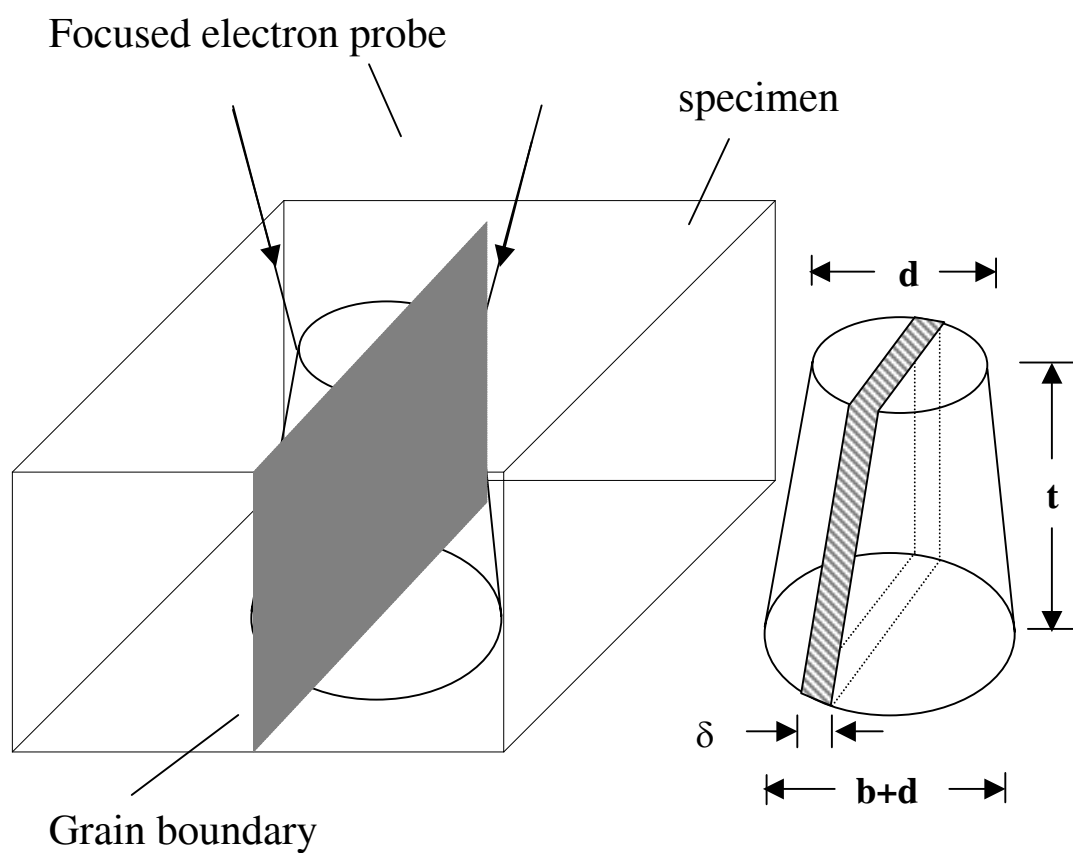


Figure A.1. Schematic showing how a focused electron probe interacts with a thin foil containing a grain boundary. The total volume V_t sampled by the beam is a truncated cone, while the grain boundary volume V_{gb} is represented by a thin slab contained in the cone.

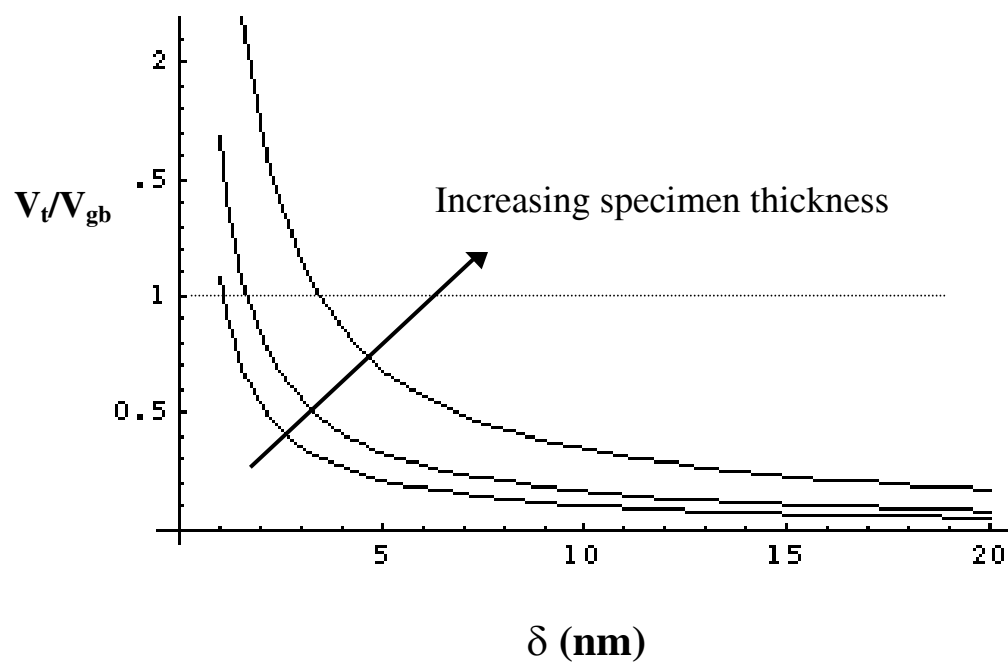


Figure A.2. Plot of V_t/V_{gb} versus grain boundary width δ calculated for Al_2O_3 at 200keV and an incident probe size of 1.0 nm. Specimen thickness increases from 50→100→200 nm.

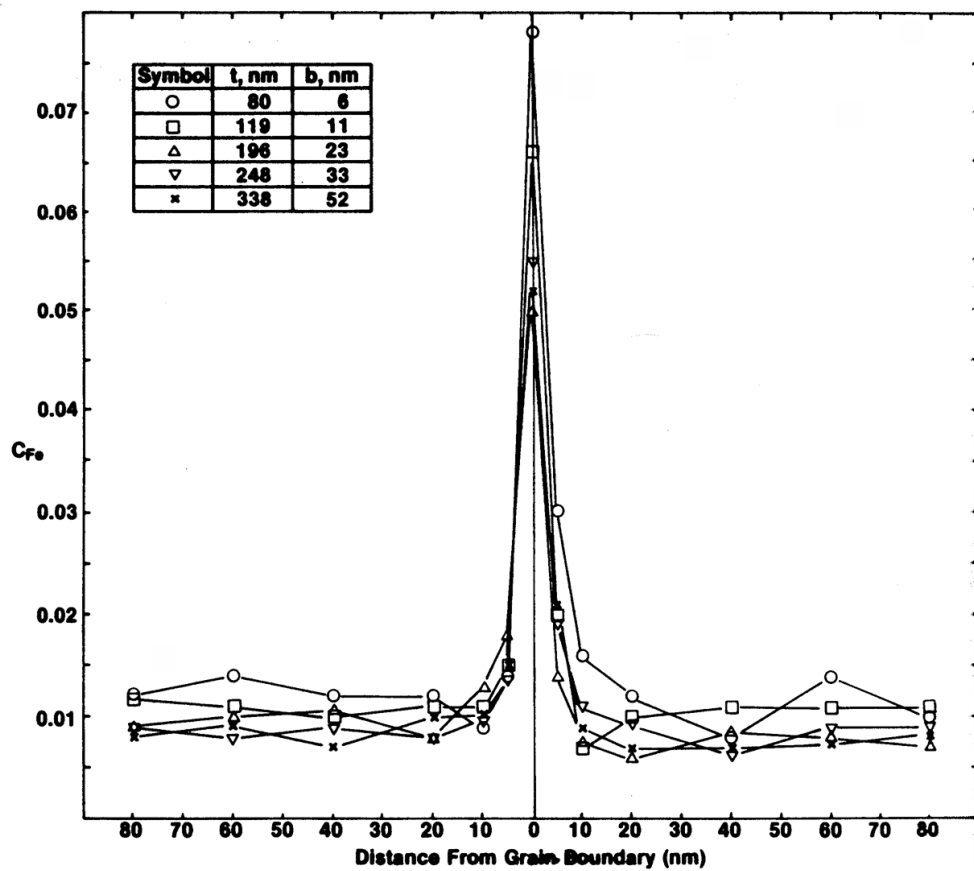


Figure A.3. Peak Fe concentrations measured at an MgO grain boundary decrease with increasing specimen thickness, due to the effects of beam broadening. (Reproduced from [4]).

Appendix B

CALCULATION OF SOLUTE DIFFUSION LENGTH DURING SPECIMEN COOLING

The distance that a cation solute diffuses during cooling from T_1 to T_2 is given by the expression

$$l = \left[\frac{k}{\eta Q} (D_1 T_1^2 - D_2 T_2^2) \right]^{1/2} \quad (\text{B.1})$$

where k is the Boltzmann constant, η is the linear cooling rate, Q is the cation migration energy, and D_1 and D_2 are the cation diffusion coefficients at T_1 and T_2 , respectively.

Unfortunately, estimation of solute diffusion lengths in sapphire are limited by a paucity of experimental data regarding specific cation diffusion coefficients D and migration energies Q in the lattice. To the author's knowledge, the only quantitative report of a diffusion coefficient for Ti solute in Al_2O_3 was given by Lagerlof et al. as $4 \times 10^{-18} \text{ cm}^2/\text{s}$ at 1400°C for Ti^{4+} [1]. Jones et al. [2] report the activation energy for defect diffusion as 3.4 eV, which should be close to the energy required for migration [3]. Because values for D and Q should depend sensitively on the overall solute concentration, using data from other studies is certainly suspect. However, for the purpose of establishing a *rough* estimate of the solute diffusion length during specimen cooling, results from other studies should be applicable.

To calculate the diffusion length of Ti^{3+} in Al_2O_3 during a rapid quench (800°C/s) from 1600°C, we first need to estimate $D(\text{Ti}^{3+})$ at 1600°C²⁵. Measured values of the lattice diffusion coefficient in Al_2O_3 for various transition metal ions range from 10^{-13} to 10^{-17} cm²/s at 1600°C, based upon extrapolated data from [4]. Assuming a value of 10^{-14} for $D(\text{Ti}^{3+})$ at this temperature, and using Jones' value for defect migration energy, the diffusion length calculated from Eq. B.1 is approximately 3 Å. Thus, grain boundary enrichment of Ti^{3+} that occurs during rapid quenching is anticipated to be quite minimal.

References

1. K.P.D. Lagerlof, B.J. Pletka, T.E. Mitchell, and A.H. Heuer, "Deformation and Diffusion in Sapphire ($\alpha\text{-Al}_2\text{O}_3$)," *Radiation Effects* **74** 87-107 (1983).
2. T.P. Jones, R.L. Coble, and C.J. Mogab, "Defect Diffusion in Single Crystal Aluminum Oxide," *Journal of the American Ceramic Society* **52** (6) 331-4 (1969).
3. W.D. Kingery, "Plausible Concepts Necessary and Sufficient for Interpretation of Ceramic Grain-Boundary Phenomena. II. Solute Segregation, Grain-Boundary Diffusion, and General Discussion," *Journal of the American Ceramic Society* **57** (2) 74-83 (1974).
4. M. Le Gall, A.M. Huntz, B. Lesage, C. Monty, and J. Bernardini, "Self-Diffusion in $\alpha\text{-Al}_2\text{O}_3$ and Growth Rate of Alumina Scales Formed by Oxidation: Effect of Y_2O_3 Doping," *Journal of Materials Science* **30** 201-211 (1995).

²⁵ Since the diffusion coefficient at room temperature is extremely small, the value in parentheses in Eq. B.1 is determined primarily by the first term, $D_1 T_1^2$.